Structural Evolution of Carbon During Oxidation

By

Angelo William Kandas

Submitted to the Department of Chemical Engineering
In partial fulfillment of the requirements of the degree of

Doctor of Philosophy

at the

MASSACHUSETTS INSTITUTE OF TECHNOLOGY

June, 1997

Author .....
Department of Chemical Engineering
May, 22, 1997

Certified by .....
Adel F. Sarofim
Lammot Du Pont Professor of Chemical Engineering Emeritus
Thesis Supervisor

Certified by .....
John B. Vander Sande
Cecil and Ida Green Distinguished Professor of Materials Science
Thesis Supervisor

Accepted by.....
Robert E. Cohen
St. Laurent Professor of Chemical Engineering
Chairman, Committee for Graduate Student

Structural Evolution of Carbon During Oxidation

By

Angelo W. Kandas

Submitted to the Department of Chemical Engineering on
May 22, 1997 in Partial Fulfillment of the Requirements for the
Degree of Doctor of Philosophy in Chemical Engineering

Abstract

The examination of the structural evolution of carbon during oxidation has proven to be of scientific interest. Early modeling work of fluidized bed combustion (FBC) showed that most of the oxidation reactions of interest occur in the micropores. This work has focuses on the evolution of macroporosity and microporosity of carbons during kinetic controlled oxidation using Small Angle X-Ray Scattering (SAXS), CO_2 surface areas, and High-Resolution Transmission Electron Microscopy (HRTEM) analysis.

Simple studies of fluidized bed combustion of coal chars has shown that many of the events previously considered to occur due to fragmentation may in fact be an effect of "hidden" or nonaccessible porosity. This thesis uses a modified shrinking core model to examine the effect of macropore size on the combustion of large (4-8 mm) coal particles in the FBC. Modeling work, supported by experimental evidence, has shown that even though complete penetration of the particle interior by oxygen may occur for large pores, micropores will not be completely penetrated and will act as diffusive barriers. These barriers shield the interior of the particle from oxidants, and increases in reactivity (CO_2 production) are the result of barriers being destroyed, revealing "fresh" carbon to the system.

The generation of a combustion resistant grid used in the HRTEM, coupled with SAXS and CO_2 measurements of the surface areas, and SAXS fractal analysis has confirmed that soot particles shrink during their oxidation. The shrinkage is the result of an overall change in structure. This structure becomes, on a radial basis, much more ordered near the edges, while the center itself becomes transparent to theHRTEM beam, implying a lack of structure in this region. Although complex, the oxidation of soot has distinct identifiable stages. The first is a devolatilization/combustion of absorbed hydrocarbons to increase surface area by exposure of pores and surface roughening. This surface roughening continues during oxidation with simultaneous densification (shrinkage) until a maximum density/surface roughness is reached at approximately 60% conversion.

The HRTEM techniques developed for examination of soots have also been applied to Spherocarb, an artificial char(Analabs) used in combustion studies. The Spherocarb ordering increases during oxidation, where average lattice parameters increase by 50% during reaction, accompanied by minor decreases in d_{002} lattice spacing. The densification (shrinkage) of Spherocarb and other carbons at low temperature can be attributed to this ordering. Assuming that these orderable fringes react in a manner similar to graphite fringes implies that the

reactivity should go down as the structure becomes ordered and edge carbons are destroyed. However, the reactivity of Spherocarb actually increases during reaction when normalized with the remaining mass and surface area. This increase in reactivity is possibly due to 1) increased catalytic effects, 2) defect site retention, and/or 3) chemisorption effects. The overall trend suggested by the ordering/reaction data indicates that low temperature ordering is not a process that is akin to "annealing." It is instead a process that must be modeled differently of high temperature oxidation where annealing will play a role, but also where other factors must also be considered. This has important implications for the extrapolation of low temperature structural studies to higher temperatures.

Thesis Supervisors: Adel F. Sarofim
Lammot Du Pont Professor of Chemical Engineering Emeritus

John B. Vander Sande
Cecil and Ida Green Distinguished Professor of Materials Science

Acknowledgments

I would like to extend a great deal of thanks to all those who aided me in this work. I could not have been accomplished this thesis without the collaborative efforts of others. First among those were my advisors, Adel Sarofim and John Vander Sande. They have not only guided me on the path of knowledge, but also encouraged me to explore beyond this path into other aspects of life. I stand in awe of their ability to provide insight and guidance on all aspects of this work. I would also thank my thesis committee, Janos Beer, Jack Howard and Yiannis Levendis, for their comments and advice.

This work has been further aided by a great many others. Lenore Rainey performed much of the early microscopy (and image analysis) for this work, and any ability with the TEM that I have learned I owe to her. Tony Modestino provided invaluable advice on virtually all the experimental parts of this thesis. I would also like to thank the support staff, among them Gabrielle Joseph, Linda Mousseau, Arline Benford, Bhengy Jackson, and Emmi Snyder for not only their assistance, but their ready supply of cocoa and coffee. Emmi ability to answer any question on MIT was a great convenience.

I would also like to thank numerous coworkers who have contributed to this thesis. Arpad Palotas and Christian Felderman helped to create the microscope computational analysis programs. My co-authors, Ezra Bar-Ziv, Issac Kantorovich, and Xue Zhang, saved me a lot of time with their work in Israel. Arpad and Ghokan Senel also spent numerous late nights with me working on the analysis of soot. Gernot Kramer was immense help in setting up the FBC, and I am still in awe of his organizational ability. Atsushita Morihara not only helped with the FBC, but he arranged for an enjoyable summer job in Japan. Bin Jiang and Jiang Hua Fong also helped not only with the FBC, but also with their challenging questions. I would also like to thank my UROPs, Lin Yang helped immensely with the early formulation of the combustion resistant grid, while Matt Stevens helped with many FBC runs.

I gratefully acknowledge the Department of Energy and Environmental Protection Agency for funding this research.

I would also like to thank my fellow graduate student, Jon Allen, who provided a sounding board for many of my ideas. Not only did he provide a wealth of technical expertise, but he also provided for countless hours of conversation into the late hours. He also helped keep me thin by being my tennis partner and eating all my chocolates.

I would also like to thank the numerous friends I have made here at MIT. My fellow Practice School inmates, Antonia von Gottberg, Dominque Rodriguez, Matt Tyler, Ashley Shih, Mike Kwan, Ridwan Rusli, and Jon Allen helped to keep me sane and actually enjoy the experience. My fellow cumbustors, Scott McAdams, Tao Feng Zhen, Carlo Procini, Bill Grieco and Tim Benish helped to keep the home fires burning.

Matt Holman, Howard Pan, and numerous others made my learning Japanese something to look forward. I would also like to thank my fellow officers of the MIT Anime club, especially Seungtaek Choi, who provided not only a place to watch Japanese animation, but also friendship. I also can't forget my fellow poker playing friends, Roger, Dave, Roy, Silvio, Mattheos, Maria, Harsono and Suman. These and numerous other friends made for some interesting times, some of which I would actually like to repeat.

I would especially like to thank Roy "I am Dogbert" and Maki "Why is my husband so loud" Kamimura, Dave "I am the Man in Black" Oda, Harsono "IHTFP" Simka, and Linnea "Are we there yet" Anderson. They shared their lives with me, and made my years in Cambridge filled with a great deal of fun and happiness.

Finally, I would like to thank my parents and sister for their support and love throughout this thesis.

> "If you do not expect the unexpected, you will not find it, for it is not to be reached by search or trail."
>
> Heraclitus of Ephesus (535? - 475? BC)

Table of Contents

Table of Figures

List of Tables

CHAPTER 1

1. Introduction

Coal is an extremely heterogeneous material that is difficult to characterize. Coal is fossilized organic matter formed by geological processes and is composed of a number of distinct organic entities called macerals and lesser amounts of inorganic substances (minerals). The macerals of coal consist principally of carbon with various amounts of hydrogen and oxygen, ranging from ~50 wt % carbon to over 95 %. Char is the product of pyrolysis of coal, and is considered to be formed as an intermediate in combustion after the devolatilization of the coal.

The reaction of carbon (char) with oxidizing gases is controlled by the following steps:

(1) Mass transfer by diffusion of gaseous reactants from the bulk gas to the carbon surface.

(2) Adsorption of reactants on the surface.

(3) Surface reactions and formation of adsorbed product.

(4) Desorption of products.

(5) Diffusion of products to the bulk gas.

The kinetics of carbon oxidation are determined by the slowest step. This determination is based on process parameters (temperature and pressure) and carbon properties (active site concentration and catalytic effects).

At higher temperatures, the reaction may be controlled by diffusion of reactants to the external surface of the particle (Regime III)[1]. At lower temperatures, the rate determining step is due to surface kinetics (Regime I). At intermediate temperatures, the reaction may be controlled

by both the chemical processes and diffusion through the pores and the external surface boundary layer (Regime II).

One measure of the overall chemical kinetics of the heterogeneous carbon reactions with oxidizing gasses is calculated by the following

$$R_O = -\frac{1}{W_0}\frac{dW}{dt} \tag{1}$$

where R_0 is the overall reactivity at temperature T, W_0 is the initial mass and dW/dt is the rate of weight loss. Another measure of the kinetics is the instantaneous rate of reaction normalized by the actual, rather than the initial mass of the carbon,

$$R_t = -\frac{1}{W_t}\frac{dW}{dt} \tag{2}$$

where W_t is the actual mass at time t. The intrinsic reactivity is expressed per unit surface area and is given by

$$R_i = -\frac{k_i P^m}{A} \tag{3}$$

where R_i is the intrinsic reactivity, k_i is the intrinsic rate constant (related to temperature by the Arrhenius expression, $k = A\, e^{-E/RT}$), P is the partial pressure of reactant gas, m is the true reaction order., and A is the surface area. The overall reactivity, R, is related to the intrinsic reactivity, R_i, by

$$R_O = \eta A_t R_i \tag{4}$$

where η is the degree of gaseous penetration and A_t is the total surface area. For reactions under pure kinetic control, $\eta = 1$, indicating complete penetration of all pores.

The physical properties of carbon at various temperatures or mass totals can be experimentally evaluated accurately, but the "reactivity" of carbon is difficult to measure with precision. Smith[2] compiled intrinsic reactivities of large numbers of carbons and compared them, finding differences of up to four orders of magnitude for the same temperature (see Figure 1).

The intrinsic reactivity of carbon is a function of the gas used, and a surface area evaluation method is necessary. The measurement of the surface area available to a reacting gas molecule is not a straightforward task. Methods of physical adsorption of gases to obtain isotherms and their interpretation often indicate pore volume rather than surface area.

The measurement of surface area is most usually determined by gas adsorption measurements using various modifications Brunauer-Emmett Teller theory[3]. A clean surface is prepared by outgassing in vacuum, and then the gas (normally nitrogen or carbon dioxide) is admitted in precise amounts. The amount of gas adsorbed is calculated using pressure differentials. From the isotherm of the gas adsorption, a value of the surface area can be inferred[4]. Another measure of surface area is active surface area (ASA), measured by chemisorption of oxygen on clean carbon surfaces,[5] which measures the active sites available to reaction.

The surface area can also be measured by the use of Small Angle X-ray Scattering (SAXS), of which a typical experimental setup is shown in Figure 2. SAXS data is produced by the interactions of X-rays with variations in the electron density caused by inhomgenaities in the scattering medium on a scale of 0.5 to 200 nm. Using SAXS, one is able to measure micro- (width less than 2 nm), meso- (width between 2 and 50 nm) and macropores (width greater than

50 nm).[6] For porous solids, the greatest change in electron density is assumed to be at the solid void interface, although for most chars the presence of ash complicates this assumption. Evaluation methods for obtaining the surface area from SAXS data include the Debye equation, Porod's Law and the Guinier equation. Although all three theories use different assumptions, the three theories use plots of the intensity of scattering in one form or the other to obtain an estimate of the surface area (see Chapter 4).

The surface area measurements are actually a measure of the structure of the carbon. For most chars, the surface area is predominantly in the micropores, while the pore volume is predominantly in the macropores.[7] Microporous carbons have a very disordered structure as revealed by High Resolution Transmission Electron Microscopy (HRTEM).[8] The various models proposed to describe the microstructure differ in detail, but the essential feature of all of them is a twisted network of defective carbon layer planes cross-linked by aliphatic bridging groups.

Transmission electron microscopy provides a means of obtaining high-resolution images of carbonaceous material. Figure 3 provides a schematic of a typical TEM microscope. The preparation techniques for TEM are quite difficult, as it is necessary to obtain very thin sections of carbon less than 10 nm of uniform thickness (See Appendix A). Proper preparation can allow direct imaging of the layer planes in carbon materials, which reveals the complexity of the most regular structures, and shows ordering down to the nanometer level,[9] as shown in Figures 4 and 5. Figure 4 shows an anathraphene graphite and is a prime example of d_{002} structure of graphite, although one can not measure the length of the lattice fringe (La) due to its extreme length (see

Appendix A). Figure 5 shows the layering of the turbostratic carbon, although the random orientation of the carbon is not conducive to simple analysis as in Figure 4.

The more ordered parts of carbon structure are essentially graphitic. Small volumes have graphitic like structure, as exhibited in Figure 6. However, the presence of defects, distortions, and hetero atoms destroys the regularity, resulting in disordered media. Little energy is needed to slide the graphitic layers over one another due to the weak Van der Waals forces holding the layers together. Twisting the layers of Graphtec carbon like paper so that they are not aligned with one another is possible leading to structures which have roughly parallel and equidistant layers but with a random orientation, the so called "turbostratic" carbon, an example of which is shown in Figure 5. Heat treatment of some of these disordered carbons can lead to decreases in these defects and subsequent increase in the graphitic nature of the carbon, as depicted in Figure 7.[10] The study of these defects is important to the understanding of mechanisms of gasification and oxidation.[11]

The reason for the extensive study of graphitic ordering and its effects on oxidation is that the edge carbon atoms have been shown to be more reactive than basal plane carbon atoms.[12] Geometrically, as the oxygen (or other gasifying agent) approaches the graphite lattice, it can undergo reaction either at the edge of the basal plane or on the basal plane itself. Rates at the edges are 10^2 to 10^3 times faster on the edges than on the basal plane.[9] Even under high temperatures where diffusional control begins to affect overall reactivity (T = 1100 and 1500K), the oxidation rates of edge carbons are still 10 to 29 times higher[13] than those for basal plane carbon.

An analogous ordering appears to happen even at low temperatures. Hurt[14] observed that during oxidation of Spherocarb and sucrose char under Regime I conditions, diameter decreased substantially. This observation was confirmed by others using carbons as disparate as soot,[15] form coke,[16] and bituminous coal char.[17] Hurt speculated that this was due to an atomic rearrangement of the carbon during oxidation. Extensive turbostratic ordering was shown concurrently with lowering of reactivity for laboratory scale pulverized combustion at 2000K.[18] Further investigations found that much of the residual carbon in industrial boilers consisted of highly ordered carbon.[19] However, the link between low temperature densification and high temperature ordering during oxidation is not clear. Since models of char combustion assume a static structure, the source of this rearrangement and effect on reactivity is important to examine in light of the increasing use of lower temperature burners. Structural rearrangements will potentially affect reactivity, fragmentation behavior, and ultimately, char burnout, which will in turn play an import part in particle emission and control strategies.

This study explores the effects of structure upon the reactivity of model chars. The effect of large macropores on the combustion time of large coal particles in an FBC is explored in Chapter 2, showing that large variations in CO_2 combustion profiles may result from simple pore distribution arguments. The structural evolution of soots during oxidation is examined with SAXS, CO_2 absorption, HRTEM, and a new technique for examining nanometer size objects before and after significant combustion, and is discussed in Chapters 3-5. The structural evolution of Spherocarb, a compound frequently used as a model char is discussed in Chapters 6 and 7, showing that the fine structure as measured during oxidation increased, and is a useful concept in understanding issues such as fragmentation. Furthermore, this structural ordering can

effect the reactivity of carbon. However, the relationship between low temperature carbon ordering and reactivity is complex, due to effects such as catalysis, defect retention and chemisorption issues.

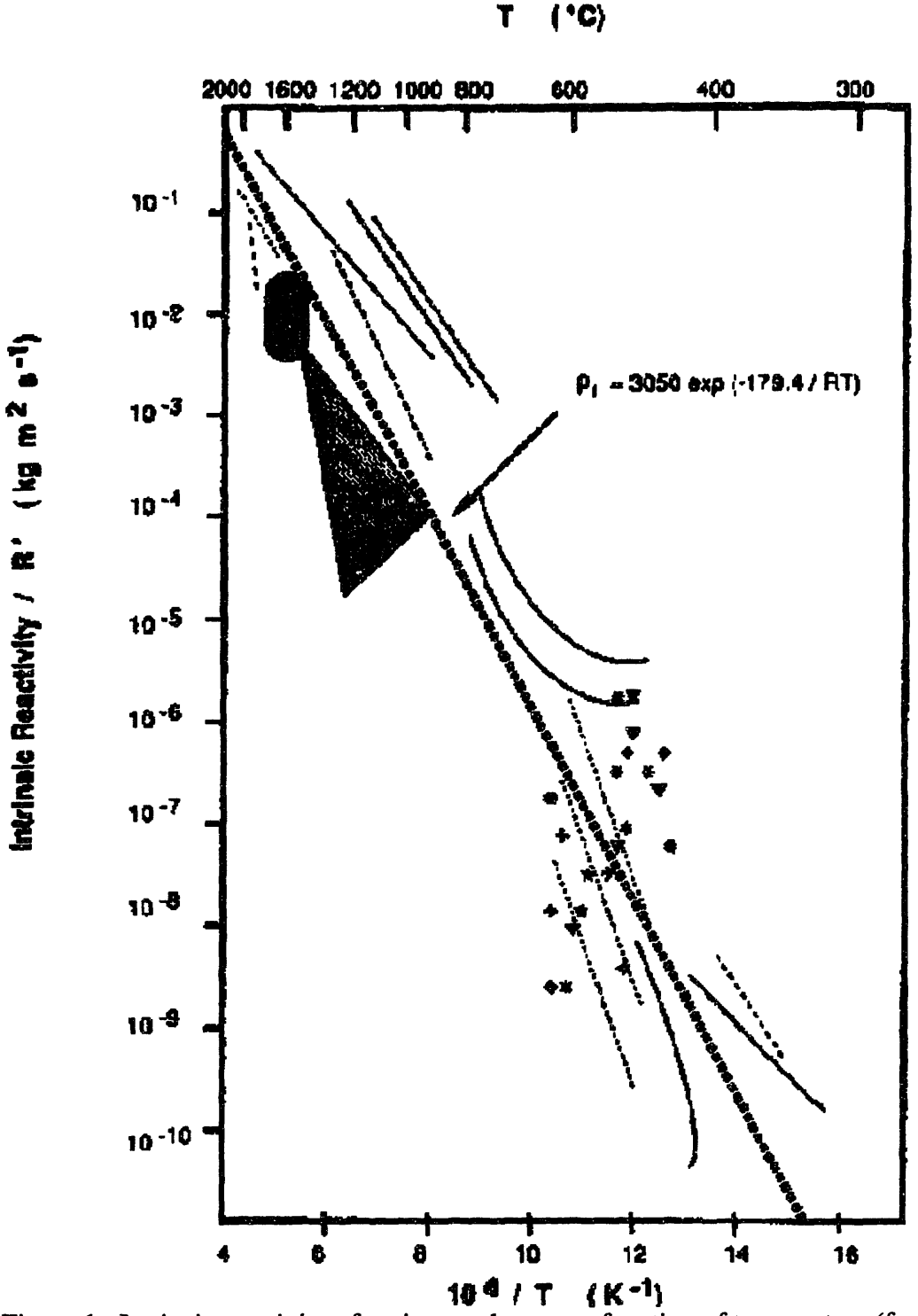

Figure 1. Intrinsic reactivity of various carbons as a function of temperature (from Smith et al[2]).

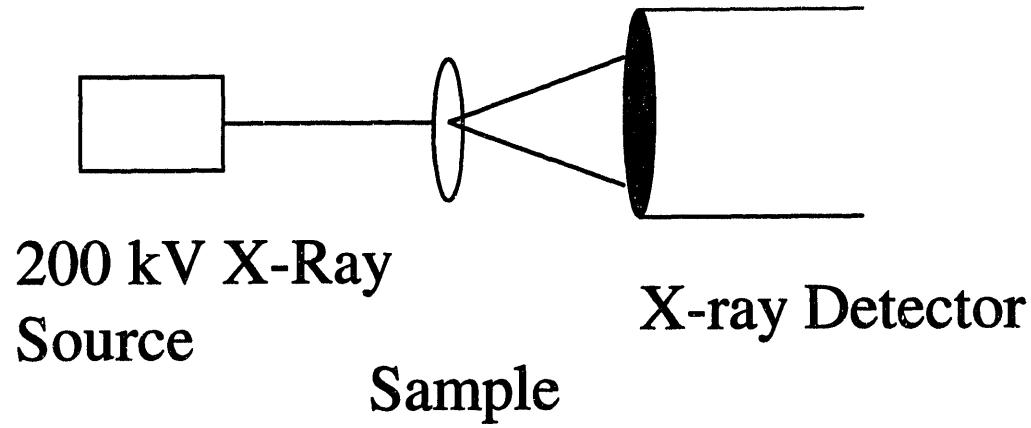

Figure 2. Schematic of SAXS apparatus.

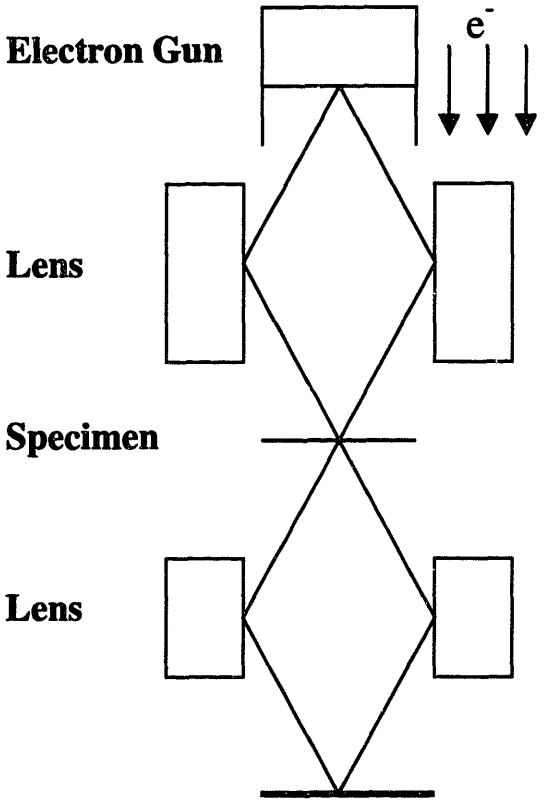

Figure 3. Schematic of a TEM microscope.

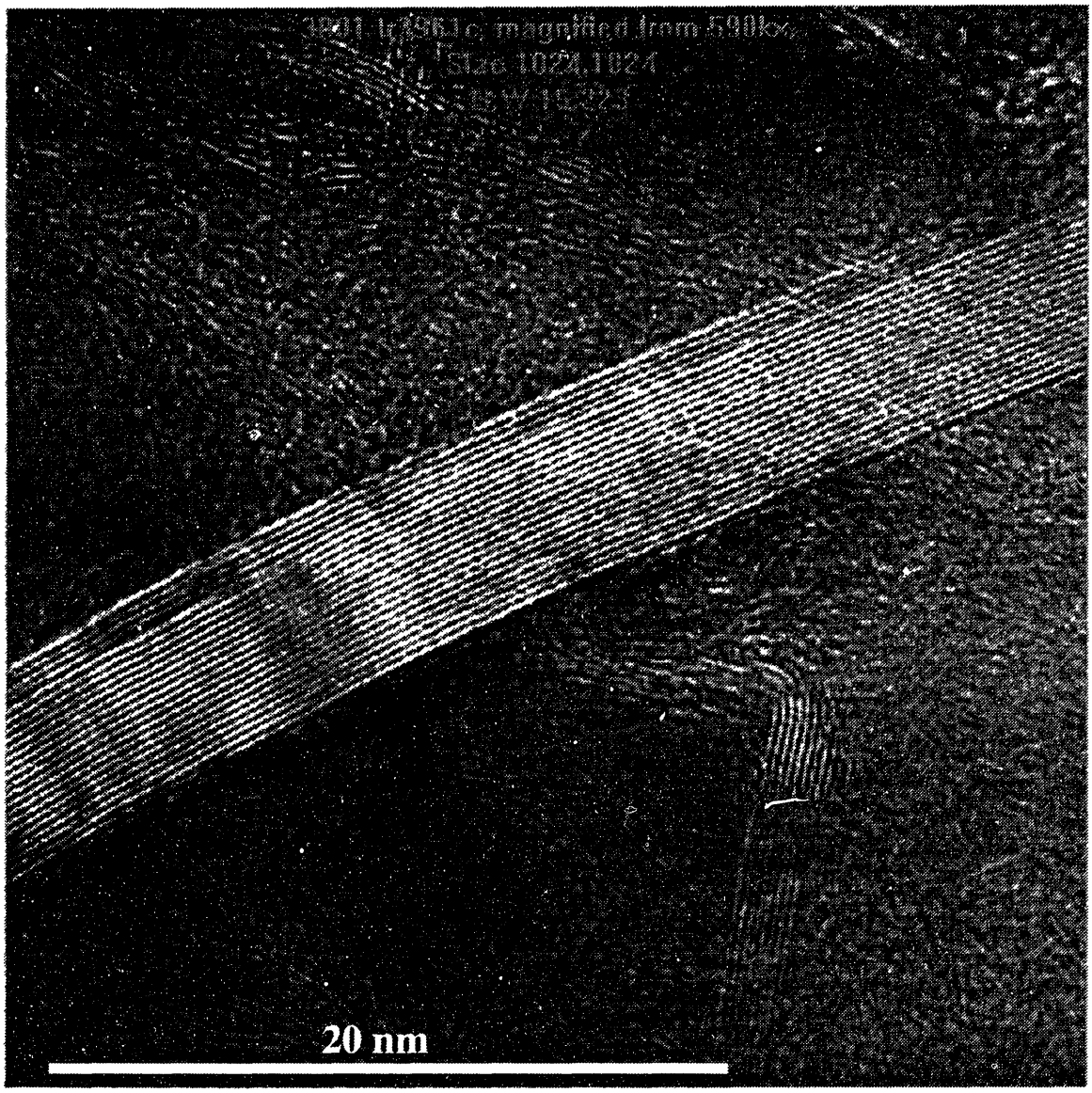

Figure 4. An ordered graphitic TEM structure produced commercially with anathraphene, 590 kX original magnification.

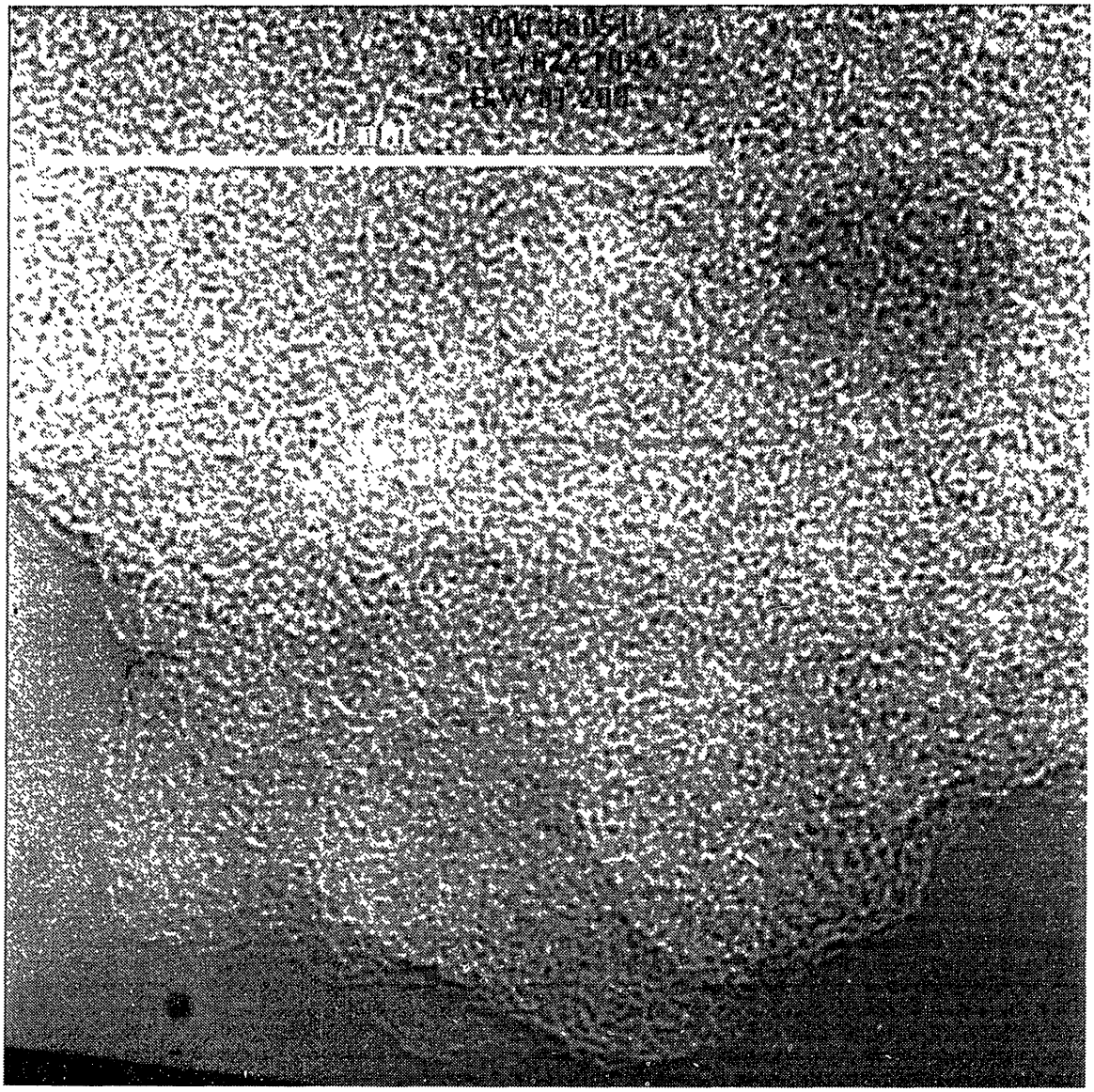

Figure 5. TEM image of a carbon with turbostratic like structure (Spherocarb, 590kX original magnification).

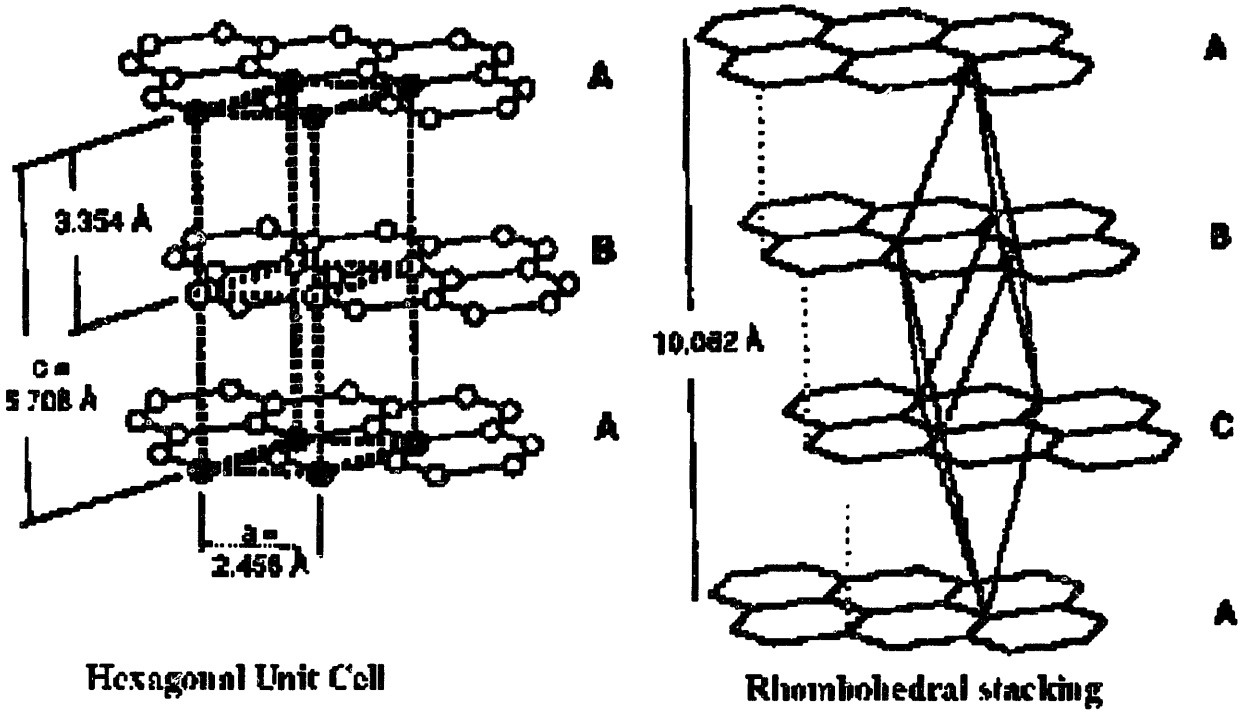

Figure 6. Diagram of perfect structure of consisting of hexagonal or rhombohedral stacking of the perfect hexagonal planes of graphite (from Marsh, 1993[9]).

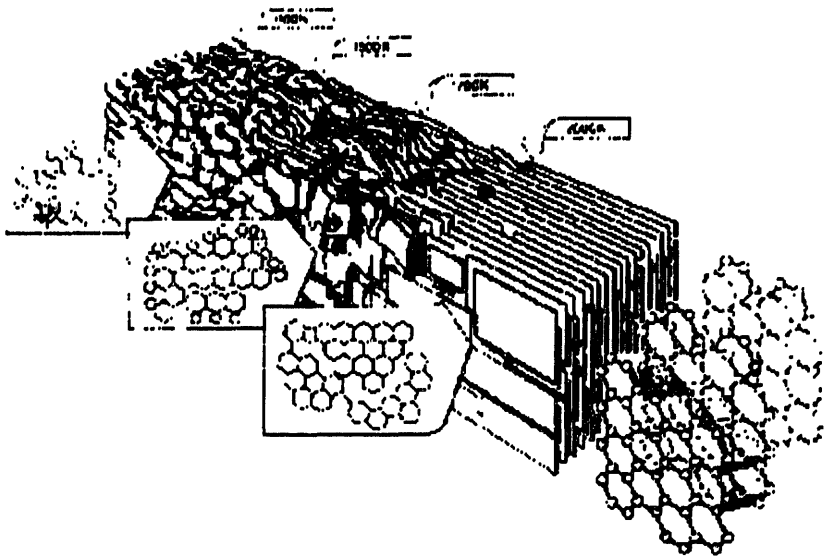

Figure 7. Generation of local graphitic level in carbons by heat treatment from Marsh et al[10]. As heat treatment temperature increases from 1000C to 2400C, ordering increases.

CHAPTER 2

2. Evolution Of CO_2 During Combustion In A Fluidized Bed: Random Pore Model

2.1 Introduction

Fluidized Bed Combustors (FBC) are becoming increasingly important as a system for generation of electricity with low cost pollution controls, especially in developing nations such as China. The system consists of a bed of char fluidized with oxidizing gasses, to which various pollution controlling additives, such as limestone, may be added. Prediction of the carbon content in fluidized beds is important because carbon losses in the bed are proportional to the carbon loading, because of carbon's role in the reduction of nitrogen oxides formed in the bed, and because of the importance of carbon content for final ash disposal. The carbon load is proportional to the carbon particle burnout time, which is, in turn, related to the particle diameter raised to a power between 1 and 2. Fragmentation and attrition, which produce smaller particle sizes, will thus decrease the burning time and the carbon content.

Evidence for fragmentation in fluidized beds has been provided by showing the variation in products of combustion of single coal particles. Sundback et al.[20] explained this variation by postulating fragmentation of a single char particle, using CO_2 profiles to obtain the size and number of coal fragments evolved during reaction. However, Zygourakis and Sandmann[21] explained the same behavior by the use of a discrete structural model, in which the reaction rate increased sharply when the reaction front reached large internal cavities that were previously unavailable for reaction, even under complete kinetic control (Regime I). In this present study

this approach is modified to simulate the variation in CO_2 emissions from single burning coal particles by using a simple system of pores, randomly distributed throughout a spherical char particle. Only the penetration depth and initial pore sizes are used as structural model parameters. The model results are examined by comparing the random factor to two different types of coal in a laboratory scale fluidized bed.

2.2 EXPERIMENTAL

Batch combustion experiments were performed in a small-scale quartz glass bubbling fluidized-bed reactor (FBC) with an inner diameter of 57 mm. A bed of silica sand (particle size 150-212 μm) with a bed height of approximately 50 mm was fluidized by oxygen in helium. A nondispersive infrared (NDIR) detector was used to measure the overall conversion of carbon to CO_2. An attached Fourier transform infrared (FTIR) spectrometer equipped with an MCT detector and a low-volume gas cell of 223 cm^3 was used to monitor CO_2, CO, and CH_4 exhaust gasses. A complete schematic of the system is given in Figure 8.

The oxygen concentration in the inlet gas stream was varied from 2-8% by use of mass flow controllers. The flow rate was set to 2.5 L/min at STP (298 K, 1 atm) conditions. Single coal particles, 5-10 mm in diameter, were burned at temperatures between 973 K and 1123 K. An analysis of the coals used in this study is given in Table 1. All measurements of the off-gas indicated that, except during the devolatilization step, the CO and CH_4 accounted for less then 1% of the original amount of fixed carbon in the coals tested.

In order to obtain samples for size distribution analysis for the pores of the char burned in the FBC, a small cage was constructed of #40 steel mesh and suspended in the FBC using nichrome metal tubing. For initial devolatilization samples, the cage was embedded in the FBC

silica sand, and He gas was used to fluidize the bed. The sample coal was inserted into the bed and after 2 minutes, the cage was lifted to the top of FBC and the sample was allowed to cool to room temperature under inert gas flow. This process was used to retrieve Newlands and Illinois chars at up to 75% conversion. The total surface areas of the retrieved chars where analyzed using an ASAP 2000 (Nicolet) automated nitrogen BET.

To obtain an average macropore size for the initial, devolatilized chars, the chars were then mounted in epoxy (Buehler, Epo-thin epoxy) and allowed to cure. Once curing was accomplished, top portion of each sample was removed by grinding the epoxy/char until the center of the char particle was reached. The epoxy/char was then polished, and the resulting epoxy mounted char was then optically imaged and average pore size was determined.

Property	Newlands Coal	Illinois #6 Coal
Volatile Matter (%)	26.49	36.19
Fixed Carbon(%)	56.07	50.97
Total Carbon (%)	58.83	65.1
Ash (%)	17.44	12.84
Nitrogen (%)	1.2	1.05

Table 1. Proximate and ultimate analysis of Newlands and Illinois coal.

2.3 RESULTS

The data shown in Figure 9 is representative of a typical CO_2 profile of coal burned the fluidized bed. The high initial peak of off gasses between 0 and 2 minutes in Figure 9 is due to the devolatilization of the coal particle when it is initially introduced into the bed. The devolatilized coal char is then oxidized slowly in the FBC, with random variation seen from the "average" value of the CO_2 production. The smooth profile at high conversions is due to the

multiple fragments, which are generated toward the end of the run when attrition effects are large.

The CO_2 combustion profile for the Newlands coal is given in Figure 10. The data between devolatilization profile and the final stages of combustion was fit to a linear profile, and an average "noise" factor was computed by simply taking the difference from a best fit of the CO_2 profile using the linear range from about 1 minute after devolatilization is over to approximately 60% conversion. The profile indicates a relatively smooth combustion characteristics, with little deviations from the average combustion values(approximately $\pm$3 %, defining the average as the best fit of the data). Increasing the oxygen content of the feed gas simply accelerates the combustion process, and does not affect the "noise" level.

The Illinois #6 coal, shown in Figure 11, has two typical types of deviations. One is a "jump" to a higher combustion rate, which can be attributed to a single event that radically changes the reactivity (CO_2 production) of the system. A similar effect was observed by Sundabk et al., and attributed to large fragmentation events. The secondary "noise" is like the noise reported for Newlands coal, but in the range of $\pm$ 5%. This secondary "noise" also significantly decreases after a "jump" to higher combustion rates.

The nitrogen BET surface area of the cage retrieved chars were measured and the change in surface area is given in Figure 12. The surface area profiles indicate a decrease in surface, due to either (1) increase in the pore size (causing a decrease in area) due to combustion, or (2) a combination of increasing ash content and "sticking" of the silica sand to the particle. However, while the absolute surface area is changing, the area of the meso/macropores remains constant, suggesting that the increase in pore size may be the most important factor.

Examination of the epoxy mounted devolatilized char, as given in Figure 14 and Figure 15, gives an average macropore size of 0.15 mm for the Newlands coal. The Illinois #6 char had an approximate pore size of 1.4 mm if one excludes the large cenospheric centers of the particle, which as shown in Figure 15 had an approximate size of 5 mm in diameter and accounts for a great deal of volume of the char. Roughly 1/3 of the particles examined showed cenospheric properties, while the rest of the coals had pores similar to the pore walls of the Illinois # 6outer char edge.

2.4 DISCUSSION

According to the works of Zygourakis[22,23] and Perlmutter[24,25,26,27], even in the kinetically controlled regime, not all the porosity is accessible at a given time, due to pore blockage. As the blockage is cleared, new regions are exposed that can significantly increase reactive area. The simple CO_2 evolution model developed here follows an approach similar to the Zygourakis model, but we cannot assume strict Regime I (kinetic control) conditions. Different pore sizes will have different depths of penetration. For FBC conditions, complete penetration is expected with large pores, even for large (7mm diameter) particles, while for small pore sizes (D <10nm), diffusion effects predominate, leading to a Regime II (diffusion and kinetic control) combustion.

One may numerically calculate the extent of this penetration by calculating the penetration depth of the oxygen for an assumed pore size. Smith[2] gave the penetration depth for a pore size of r_p as

$$L = \left(\frac{r_p D_{eff} C_{O_2}}{4 R_{chem}} \right)^{\frac{1}{2}} \tag{5}$$

where r_p is the pore radius, D_{eff} is the effective diffllusivity of the gas (O_2) of given concentration C, and R_{chem} is rate of reaction of the char. The factor L/D may be assumed to give a rough estimate of the effectiveness factor of the char combustion.

The penetration depth as a function of pore radius and temperature is calculated and given in Figure 13 as a function of particle temperature and pore size. For the conditions examined in our study, the temperature ranged from 950-1150 K, while the particle diameter ranged from 5 mm to 10 mm. Under these conditions, the penetration depth is smaller than the particle size for micropores, but for macropores, the penetration depth is of the same order or greater than the particle size. Due to the low penetration of gasses in the micropores, they essentially act as a blocking region to diffusion. Therefore, one can conclude that reactant gasses do not penetrate the micropores and that they serve only as reaction sites for the gasification of the char. The macropores, with their large penetration depths, act as pathways for diffusion, if they are not hidden or blocked by micropores. Thus, the variation in CO_2 generation may be the result of simply reacting away the blocking shells of micropores and exposing macropores.

To quantitatively test this hypothesis, a simple model was designed. Under the FBC conditions studied, we are typically in Regime II for large particles, where only partial penetration of the char is achieved. The base model we assume is the classic shrinking sphere model (Regime III), with variations to account for the penetration of the particle by reaction gasses. Distributed throughout the sphere are a number of "pore" spheroids of uniform size that are penetrated to allow for access to the interior of the char particles . The spheroids are distributed randomly under the criteria that

$$\varepsilon = \frac{n\ R_{pore}^3}{R_{char}^3} \qquad (6)$$

where n is the number of pores needed to generate the appropriate porosity, and R_{pore} and R_{char} are the pore and char radii respectively. To simplify the model, the following assumptions are also made about the pores: (1) the pores are independent of each other; (2) the pores do not grow during reaction and, (3) the pores only participate in the reaction if the reaction front of the shrinking sphere passes through them. Of the assumptions, the first is the severest, as it does not allow for development of pore networks, although large pores may be thought to model large pore networks. A representation of the char model using these assumptions is shown in Figure 16. The dark line in Figure 16 represents the reaction zone, or penetration depth. In the system are distributed 3 types of pores; 1) pores that are completely hidden to the reacting gas, 2) pores that are in the reaction zone, and 3) pores that have been destroyed during oxidation.

Using the pseudo-shrinking core model, one can assume for the basis of this analysis that the reaction rate, r, is proportional to the char surface area exposed during reaction (Regime I),

$$r = kA_{char}C_{O_2} \tag{7}$$

where k is the kinetic parameter, the dependence on oxygen concentration, C_{O2}, is assumed to be linear, and A_{char} is the accessible surface area of the char. This is in effect assuming that the concentration profile of reactant gas in the system, instead of gradually being consumed to 0 concentration in the center of the particle, is instead a step function that abruptly drops past the pore penetration depth.

Under the shrinking sphere assumption, there is no ϕ and θ dependence on the rate of combustion due to uniform combustion, so the evolution of surface area over time reduces to a one-dimensional problem of radius r. However, added to the area from the external surface of the char is the area from the penetrable pores, giving a total surface area of

$$A = 4\pi R_{char}^2 + \Sigma 4\pi R_{pore}^2 \quad (8)$$

where the term on the left represents the external surface of the char and the summation on the right is taken over all the pores that are involved in the reaction. The complete source code for the model may be found in Appendix D.

Using a constant radial decrease, one can numerically calculate curves for the evolution of the surface area with pore radius. From the surface area profile and using the reaction paramters calculated by Goel et al.,[28] one may then use Equation (7) to calculate the rate of CO_2 production, as given by Figure 17 as a function of R_{pore}. With very small pores, a constant surface area is developed that decreases with R. However, as the radius of pores increases, surface area peaks are generated due to the revelation of pores. These peaks become relevant at pore radiuses of approximately 0.5 mm. While this may seem large, the char particles have original diameters of approximately 7 mm in diameter. It should also be noted that the spherical pores can be inferred to model "pore" regions, not just pores. These pore regions would be clusters of smaller pores that are initially inaccessible but exposed during reaction.

While it is difficult to test the model against real FBC data, as the model essentially describes "randomn" noise, one can test pore size distribution of the sample during conversion.. As can be seen in Figure 12, the surface area decreases with increasing conversion, and most of this loss in area occurs in the micropores. This is indicative of the evolution of true surface area and a preferential consumption of smaller sized pores (micropores), in agreement with the assumption that all reactions take place in smaller pores micropores.[29] However, BET nitrogen surface area only examines the finer pores, and not large (macro-) pores.

Another option to test the efficiency of the model is to measure the initial pore size distribution of the coal after devolatilization by mounting char samples in epoxy and sectioning

the coal. The epoxy mounted samples of chars after 2 minutes of devolatilization are shown in Figure 14 and Figure 15 for an initial coal size of 5-7 mm. The Newlands coals had an average pore size of less than 0.15 mm in diameter as measured optically, with the largest pore area being approximately 2 mm near the center of the particle. The Illinois #6 coal, in contrast, tended to plasticize a great deal during devolatilization, resulting in a greatly expanded particle size. As seen in Figure 15, this expansion resulted in the formation of large cenospheric like particles, with large cavities internal to a relatively nonporous outer layer. However, as can be seen in Figure 15, not all particles formed large cenospheres. Furthermore, accurate measurements of the pore distribution of the sample is difficult due to the inability of the epoxy to penetrate the relatively nonporous outer shell, resulting in a crushing of the char pore walls, rather than a grinding of material. The crushed hole in the center of the particle had a width of 4 mm, approximately 50% of the size of the particle. Furthermore, examination of exposed pores within the shell revealed larger pores in the 2-3 mm range enclosed by sturdy walls.

Although the maximum pore size (2-3 mm) measured in the chars was larger than the pores examined in the model, a comparison of the model analysis with measured pore distribution/CO_2 profiles is encouraging. The Newlands char, with its small pores has very little variation in the combustion profiles associated with the oxidation of its char. Furthermore, its relatively well developed pore network means that inaccessibility will not be much of a problem. In contrast, the Illinois #6 char, with its large pores, is subject to a large degree of variability. The "jumps" may be due to revelation of the cenospheric center and the beginning either a large fragment or of an inner/outer shell combustion. The importance of penetration is seen in average

noise before and after a "jump," where the average "noise" level falls, probably due to the fact that all pores are accessible, although this is difficult to prove at the late stages of combustion.

2.5 CONCLUSIONS

Experimental measurements of the variation of CO_2 generation during combustion of chars in an FBC have been performed. A model of the combustion of char in Regime II has been developed to explain the variation in CO_2 generation during the combustion of char particles in a FBC. The model assumes that there is no penetration of the particle by reaction gasses except for regions were porosity is evident. The model adequately explains the variations seen in the production of CO_2 for pore sizes greater than approximately 0.5 mm. Comparison with pore sizes for Newlands and Illinois #6 chars shows that the criteria for relatively large variations in CO_2 production for a single char particle during combustion in an FBC may be met by chars with pores that are inaccessible to initial reactants.

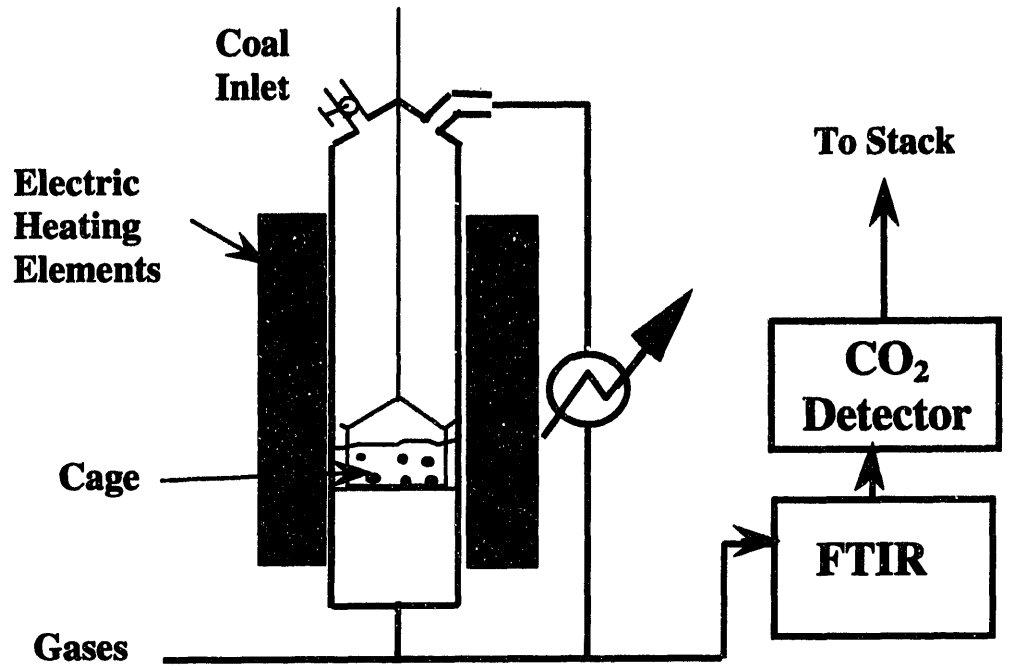

Figure 8. Schematic of Fluidized Bed Combustion apparatus and attached off gas analysis mechanisms.

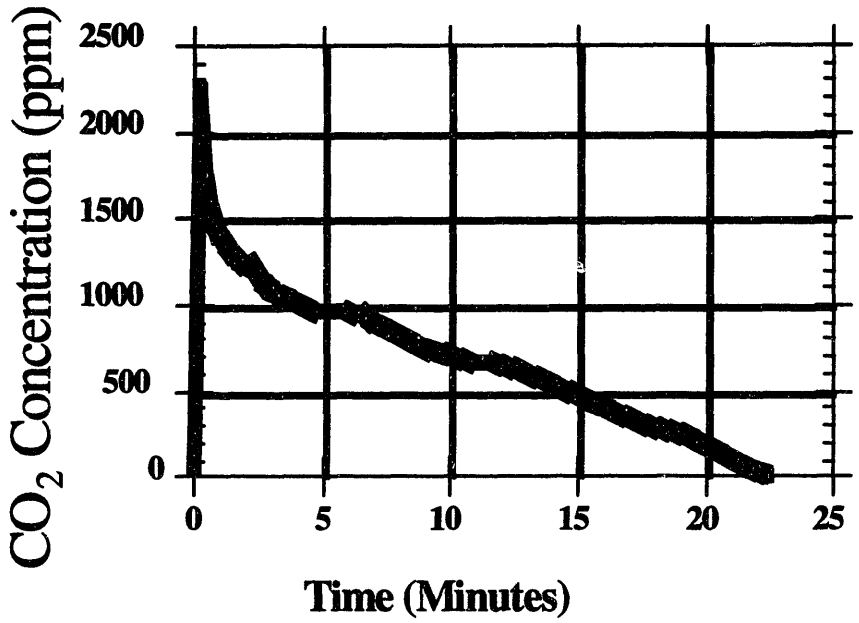

Figure 9. Typical profile of CO_2 off gas during combustion of Illinois Coal #6, 1025K.

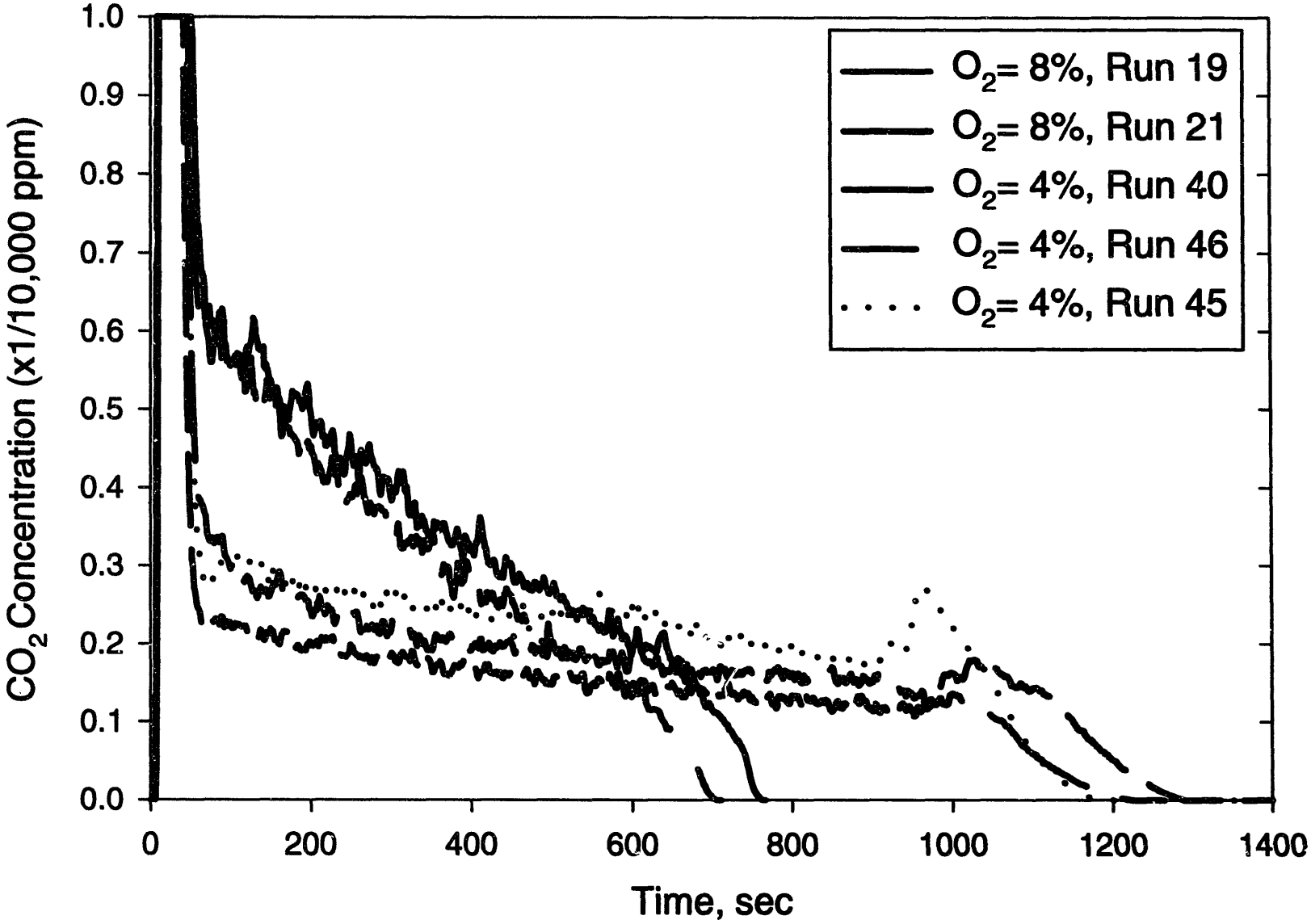

Figure 10. CO_2 Concentration profiles for combustion of Newlands Coal at 1023K

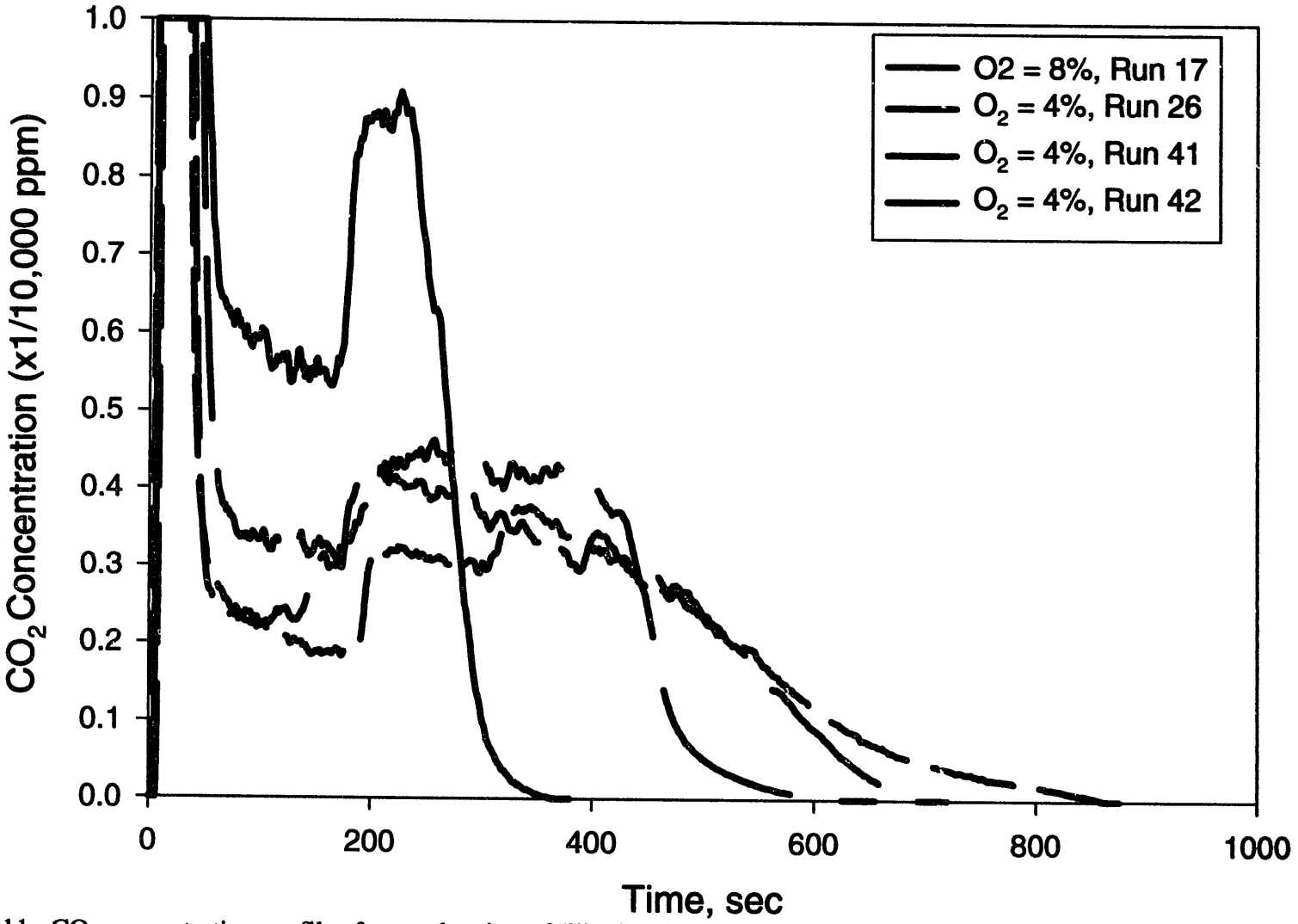

Figure 11. CO_2 concentration profiles for combustion of Illinois #6 at 1023K, 4-8% O_2.

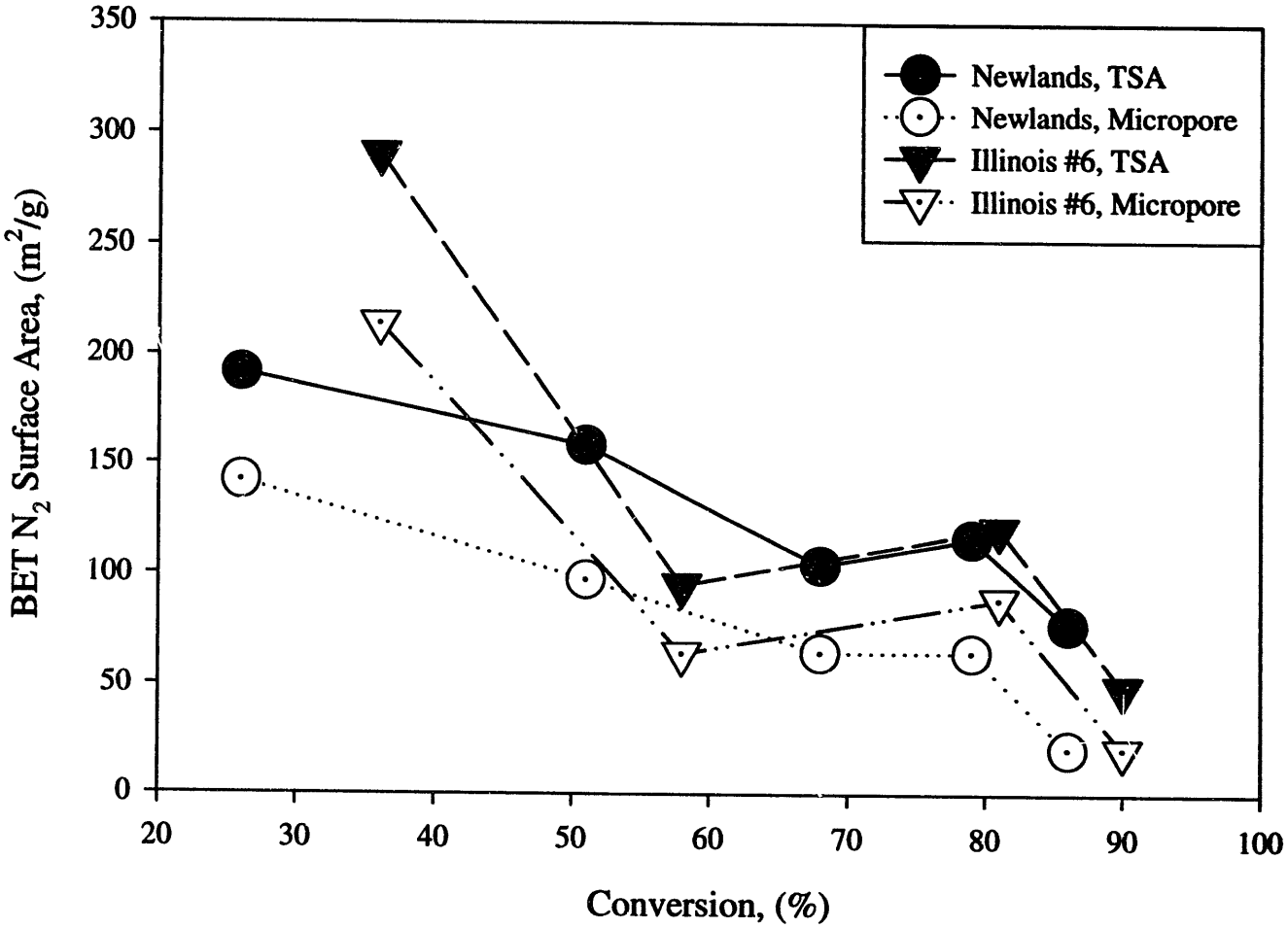

Figure 12. Evolution of Surface area of Illinois #6 and Newlands chars during oxidation in 4% Oxygen.

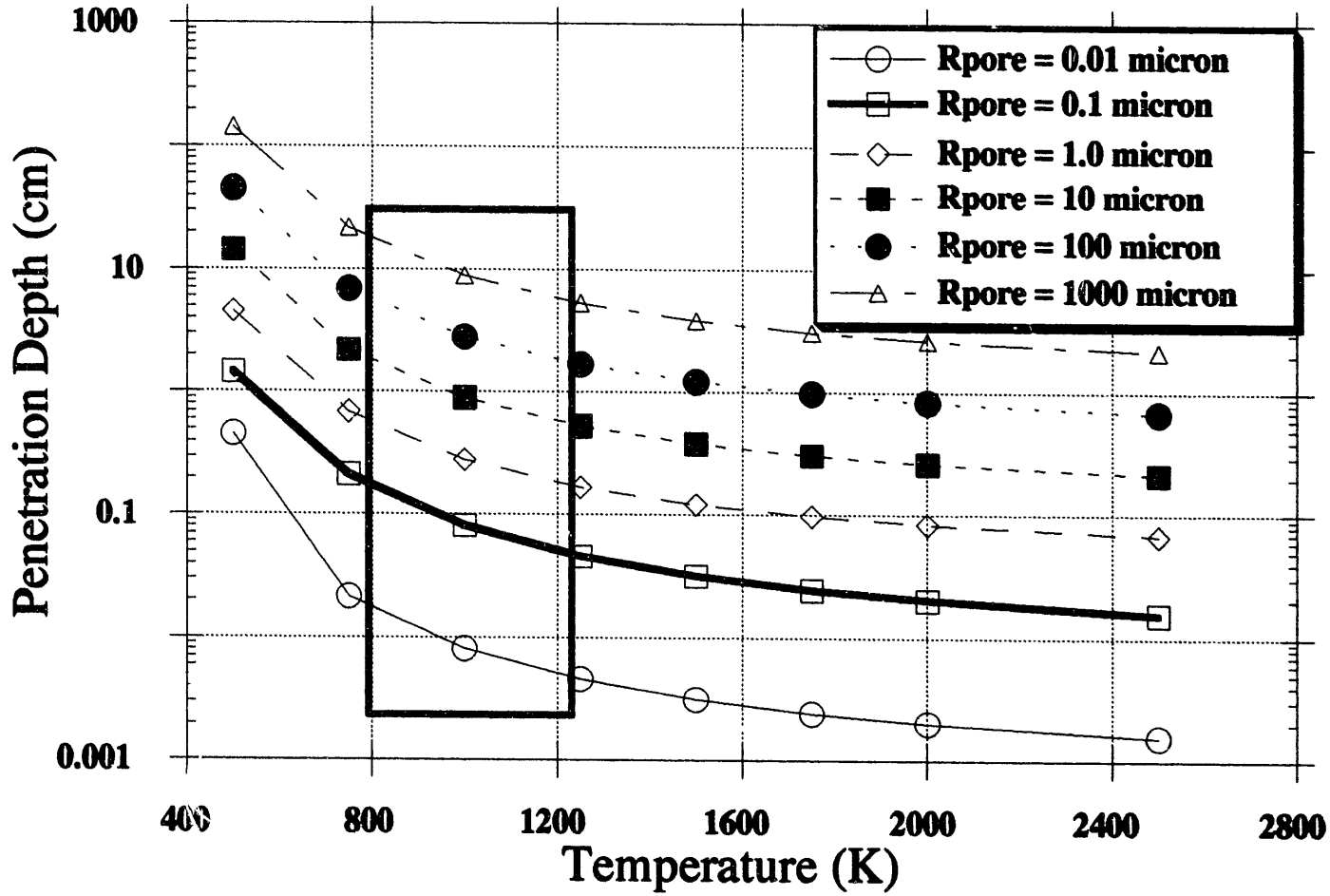

Figure 13. Penetration Depth as a function of temperature. The box represents the FBC conditions of this study.

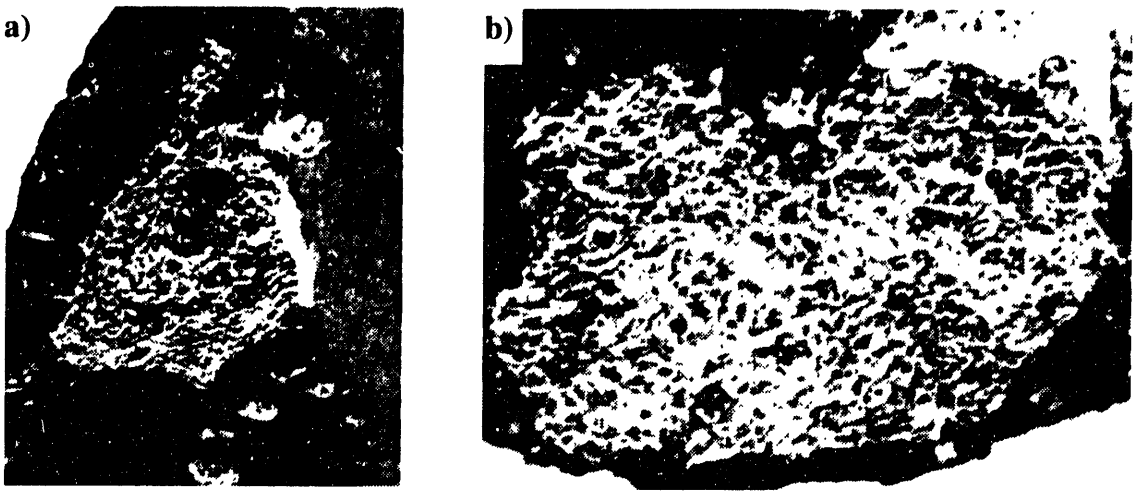

Figure 14. Epoxy mounted samples of Newlands Coal char, devolatilized at 1023K for 2 minutes in the FBC. Original images size a) 4.1 mm and b) 4.3x7.2 mm. The gray regions represent the char, while the black dots represent actual pore voids, and the white regions represent smaller pores. The pores are seen to be small, with pores sizes in the range of 0.1-0.15 mm. While the pores are small, the network(white lines) is quite extensive.

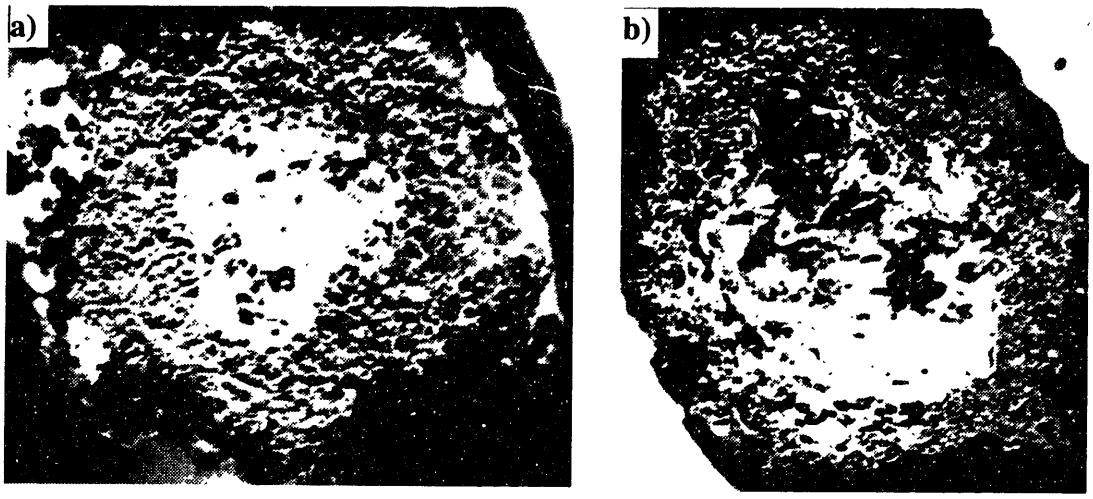

Figure 15. Epoxy mounted samples of Illinois #6 Coal char, devolatilized at 1023K for 2 minutes in the FBC. Original image size a) 8mm and b) 10mm. The Illinois #6 char has an extremely large cenospheric cavity in the center, of approximately a) 4mm and b) 6mm surrounded by a relatively nonporous char region, with large variation in pore sizes from 0.05 to 0.3 mm.

BLANK PAGE

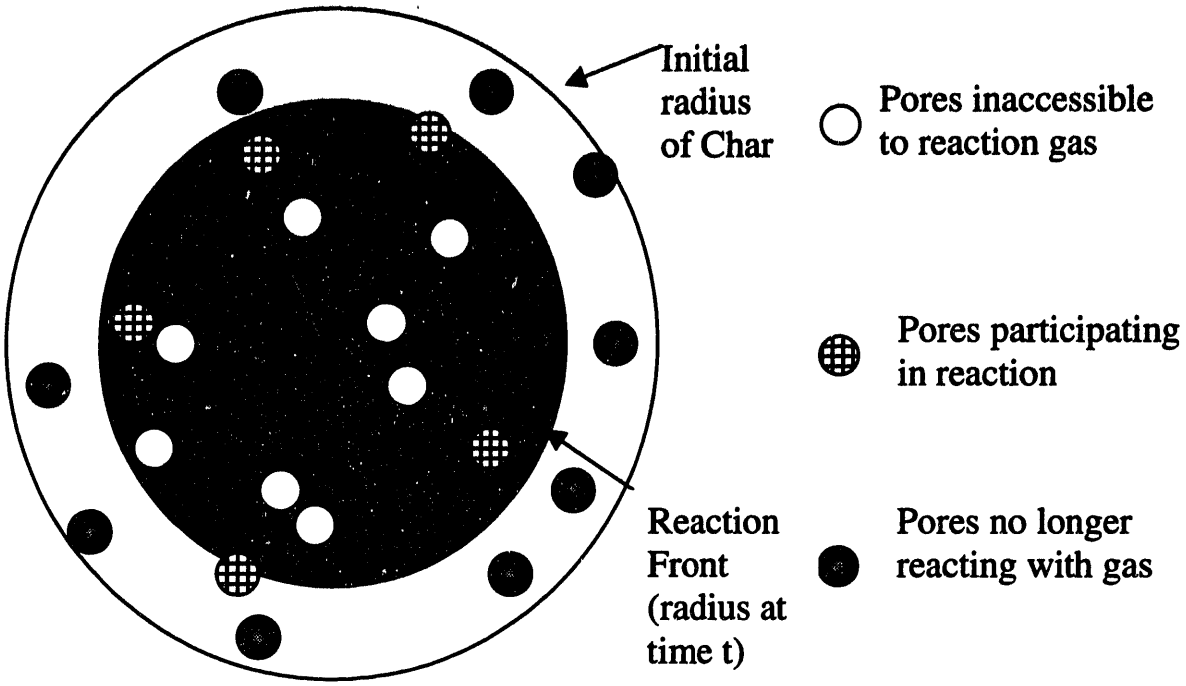

Figure 16. Schematic of Pore Model.

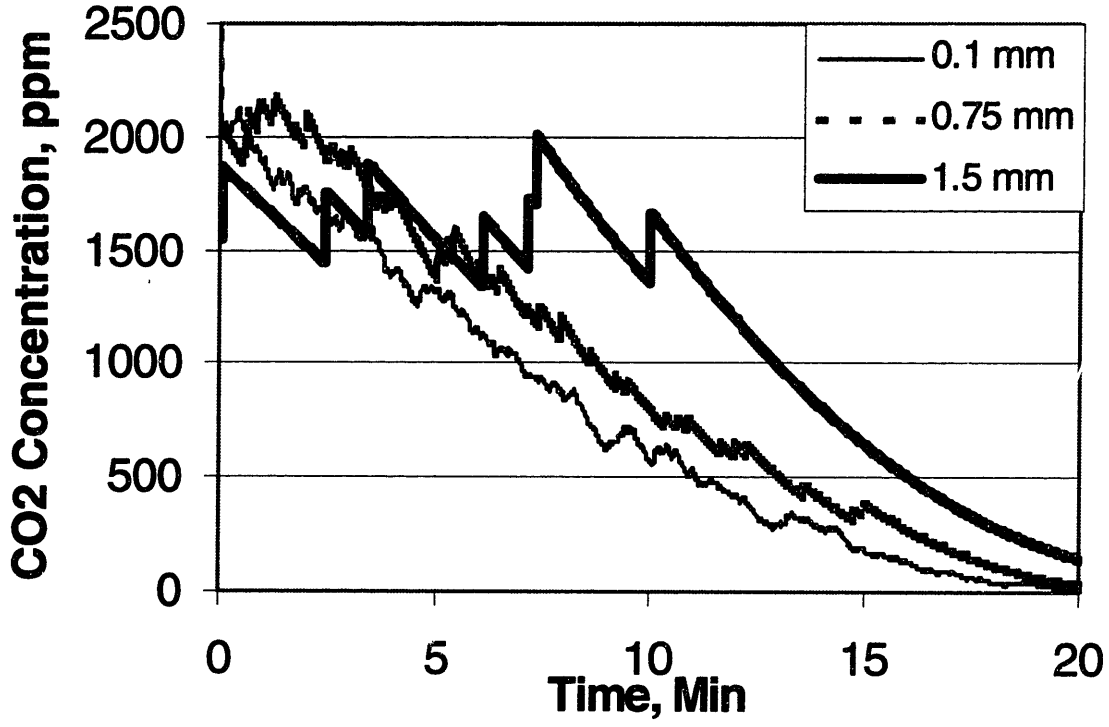

Figure 17. Evolution of CO_2 profiles as a function of pore diameter.

CHAPTER 3

3. Soot Surface Area Evolution During Air Oxidation As Evaluated By Small Angle X-Ray Scattering And CO_2 Adsorption

3.1 INTRODUCTION

Soot is produced by incomplete gas-phase combustion of fossil fuels and other organic matter.[30] While soot is emitted from numerous sources, the desire to control soot emissions from diesel engines has resulted in research into the performance of filters designed for exhaust collection systems. The collected soot is then burned off, thus there is in an interest in the oxidation reactivity of diesel soot. This oxidation process is also important particularly for the production of carbon black, where high oxidation is used to generate high surface area material. Furthermore, due to some of its structural similarities to highly reacted carbons, soot is a good model for investigating carbon reactivity. Therefore, a better understanding of the evolution of surface areas of soots during oxidation is desired.

Pore structure descriptions in carbon combustion studies have generally been used as a common parameter in reaction characterization. However, for soots, little is known about how the surface area and other physical properties vary during the reaction process. While soot is generally considered a non-porous material, some researchers have reported the existence of porosity. Neoh, et al.[31] found evidence for increases in soot microporosity during oxidation as measured by N_2 adsorption, much larger than the hypothetical unconnected sphere surface area, suggesting this difference was due to micropore development. Wicke and Grady[32] also reported

that thermal desorption of the soot-oxygen complex formed by pre-adsorption of oxygen atom at 298 K produced a significant increase in soot porosity. Smith and Polly[33] found a six-fold increase in surface area for oxidation of large carbon black particles, which they attributed to porosity development, although their carbon blacks were relatively large (200 nm). Du[34] found rapid increases of soot area at greater than 20% conversion in oxygen (going from an initial CO_2 surface of 121 m^2/g to over 800 m^2/g at 70% conversion), concluding that this was due to the reacting away of a blocking "shell" layer. After removal of this layer, internal micropores become accessible, causing a rapid increase in surface area. Du also found that the rate of reaction was proportional to the surface area up to 70% conversion. Bonnefoy, et al.[35], also reported a linear rate of mass loss for various carbon blacks and soots doped with catalyst, along with an increasing surface area (N_2) with conversion, ranging from a start of 100 m^2/g to 600 m^2/g at 50% conversion[36].

Another characterization method for soots and carbon blacks is offered by fractal geometry that characterizes structural heterogeneity by use of fractal dimensions.[37] As a general trend, high surface area soots (carbon blacks) will give high fractal numbers, while low surface area soots will give low fractal numbers, where the fractal number represents the degree of roughness, with 2 meaning a smooth surface and 3 a highly irregular one.[38] There is a wide range in the reported fractal dimensions of soot. Xu et al.[39] found that the fractal dimension of graphitized carbon black was 2.0 ± 0.01, corresponding to a smooth surface, regardless of carbon black grade. Ismail and Pfeifer[40] found similar results for carbon blacks and aerosils that had not been subjected to graphitization, conforming to a fractal dimensions of 2.02 ± 0.04. Darmstadt et al[41] found that as pyrolysis pressure was increased, the fractal dimension of rubber grade

carbon black decreased from a high of 2.6 to a low of 2.47, indicating a smoothing out of the surface due to carbonaceous deposits and possible reordering of the material.

The examination of the microstructure of soot is also important to further explain the morphological changes that soots undergo during oxidation. Ishiguro[42] proposed that the observed rise in surface area (from a nitrogen surface area of 52 to 296 m^2/g), and the corresponding decrease in diameter, was due to the growth of crystallites with a turbostratic structure, and subsequent stripping of the outer layer due to tensile stresses. However, Hurt[43] has proposed that this process is due to the actual densification of the soot particles. This has important implications concerning the modeling of the combustion of soot. Using Ishiguro's hypothesis, one would expect to model soot combustion as a shrinking core model, while Hurt's model implies that complete penetration of soot by oxygen occurs. Both processes will affect the surface area of the soot due differences in crystallite size, and examination is warranted.

This Chapter examines the surface area changes generated by oxidation of soot in air. In order to examine the surface area of the soot, Small Angle X-Ray Scattering (SAXS) and CO_2 gas adsorption methods were used. The SAXS measurements have the advantage of detecting total porosity, giving a surface profile for the entire sample, while the CO_2 measurements describe only the accessible regions of the sample. Furthermore, the fractal nature of the soots is also examined to aid in understanding their morphological evolution.

3.2 EXPERIMENTAL

Two distinct soots were used in this study. A commercially generated diesel soot from the National Institute of Standards (abbreviated as NIST soot, catalog number 1250), collected by filtration of diluted diesel exhaust, offers a high degree of material conformity and was used

due to its low ash content. Furthermore, it has been used in environmental absorption studies, and an assessment of its surface properties during combustion is desirable. The second soot (termed NEU soot) was collected during runs made at the Northeastern University, Boston diesel engine emissions program. The latter soot was collected in a ceramic monolith filter, and subsequently blown off by a high-pressure air stream. The ash content of the soot was high, due to fuel additives and possibly due to contamination by the ceramic filter. However, possibly due to a long residence time (a few hours) in the filter at a substantially high temperature (573 K), the volatile matter was significantly lower than the NIST soot. A collection of pertinent information for both soots is given in Table 2

Experiments were also performed on Spherocarb, a synthetic char furnished by Analabs that has been widely used in combustion studies. Spherocarb is a relatively pure carbon (97% C, 2% H, 1 % O), with little contamination by metals and other impurities. Furthermore, the Spherocarb's high surface is an ideal standard for testing methodologies.

Reactivity and surface area determinations were carried out in a standard Cahn 113 TGA system with an attached electronic acquisition system described elsewhere.[34] Approximately 25 mg of soot was devolatilized in inert Helium atmosphere at 1173 K for 15 minutes after a heating rate of 40 K/min. Subsequently, the devolatilized soot, termed 0% conversion, was cooled to 773 K in approximately 20 minutes. The inert atmosphere was then switched to air, and oxidation proceeded isothermally. After oxidation to the desired conversion level, the sample was cooled to room temperature in an inert helium atmosphere.

Material	NIST SOOT	NEU SOOT	Spherocarb
% Moisture (at 383 K)	5.6	0.5	0.7
% Total Volatile Matter (at 1073 K)	31.5	14	-
% Ash Content	0.96	6	780 ppm
He Density (g/cm^3)	2.1	2.04	2.1
CO_2 Surface Area, as received (m^2/g)	49	96	1000
CO_2 Surface Area, after devolatilization (m^2/g)	273	367	-
SAXS Surface Area, as received (m^2/g) [a]	156	207	1240
SAXS Surface Area after devolatilization (m^2/g)	344	280	-
External Diameter after devolatilization	36 nm	27 nm	150 μm
External Area (m^2/g)[b]	110	150	<1

Table 2. Physical Properties of Carbon Examined, and surface area for starting materials.

The average primary particle size was estimated by use of a transmission electron microscope (TEM). The soots were ultrasonically suspended in ethanol and deposited onto a carbon coated TEM grid. A Joel 200 CX TEM electron microscope operating at 200 keV was used to image the soots at typical magnifications of 100-150 kX. The resulting micrographs were digitized using a Powerlook II scanner, and the diameter of the soots were measured and averaged using the image-processing program Semper 6P. The diameters for the devolatilized soots are included in Table 2. TEM micrographs of representative samples are shown in Figure 18.

---

[a] Based on an apparent density of 1.5 g/cm^3 for the soots, 0.83 g/cm^3 for Spherocarb.

[b] Assuming a spherical particle, the external surface area is $\frac{\pi D^2}{\rho \pi D^3/6} = \frac{6}{D\rho}$ where D is particle diameter and ρ is particle density.

The surface area of the oxidized sample was measured gravimetrically by using CO_2 adsorption. The gravimetric method has advantages over the volumetric method more commonly used today. It can accurately measure surface areas in smaller amounts of sample due to the sensitivity of the TGA, and both reaction rate and surface area can be measured by in the same TGA without moving the sample. The method consisted of introducing increasing concentrations of high purity CO_2 in He (0, 0.1, 0.2, 0.35, 0.5, and 1.0 mole fractions respectively) into the TGA, and recording the subsequent weight change due to CO_2 adsorption. At least 45 minutes were allowed for equilibrium to be established for each point of the CO_2 isotherm. The weight change was then corrected for buoyancy effects due to different gas densities, and the CO_2 surface area was then calculated. Full details may be found in Du[44].

SAXS experiments were also done on each oxidized soot sample. The X-ray scattering experiments were carried out on a Nicolet two-dimensional position-sensitive detector with an associated Rigaku rotating-anode generator operating at 40 kV and 20 mA which provided Cu Kα (λ = 0.154 nm) radiation. The primary beam was collimated by two Ni mirrors, which allowed for the X-ray beam to be focused onto a small beam stop. A sample to detector length of 28.5 cm was used for all samples. Full details may be found in Kofinas.[45]

3.3 THEORY

3.3.1 CO_2 Surface Area Characterization

Characterization of the micropore capacity of the samples was estimated by application of the Dubinin- Polanyi (DP) equation[46] to CO_2 adsorption at 296 K,

$$\log V = \log\frac{\Delta W}{W_o} = \log V_o - k\left(\frac{R\,T}{\beta}\right)^2 \log^2\frac{P_o}{P} \qquad (9)$$

where V is volume absorbed at pressure P, ΔW is the change from starting weight W_0, β is the affinity coefficient, k is a surface property constant, while the saturation pressure P_o is evaluated by the correlation $P_0 = 10^{-874.34/T + 4.7386}$ atm. After using the DP equation to determine the intercept V_0, the specific micropore surface area is calculated from

$$S_{sp} = \frac{V_0 N_0 \sigma_{CO_2}}{M_{CO_2}}, \tag{10}$$

where N_0 is Avogadro's number, M_{CO_2} is molecular weight of CO_2, while σ_{CO_2} is the cross-sectional area of a CO_2 molecule (taken as 24.3 nm^2).

3.3.2 Small Angle X-Ray Scattering (SAXS) Characterization

SAXS intensity profiles have been used in several studies to determine the pore structure in carbons.[47-51] Levendis and Flagan[47] used SAXS to characterize the micropores of carbon spheres of controlled porosity. Foster and Jensen[48-49] used SAXS to investigate carbon pore structure evolution during CO_2 gasification. Guet et al[50] characterized the structure of different carbons activated by steam and CO_2 using SAXS. Hua et al[51] used SAXS along with contrast matching to compare the porous structure of various carbons and inorganic materials. The advantage of SAXS is it ability to measure open porosity and more importantly, closed porosity which is not measurable by gas adsorption techniques.

The basic property measured in all SAXS studies is the scattering intensity (I) of X-ray radiation caused by differences in electron densities of each phase. The surface area of a solid may be evaluated in the so called Porod region for larger angles of SAXS by assuming a randomly distributed porosity throughout a uniform solid.[52] The Porod approximation holds as h

$\rightarrow \infty$ (where $h = 4\pi \sin\theta / \lambda$, and 2θ equals the angle of scattering of the x-ray beam), For collimated optics, Porod's law becomes

$$I(h) = \frac{2\pi \Delta\rho_e^2 S}{h^4} \tag{11}$$

where S is the total surface area of matter contained in volume V, and $\Delta\rho_e$ is the difference in electron density. To avoid the use of absolute intensity measurements, which are difficult to obtain, the intensity may be normalized by the invariant Q_0, or the total integrated intensity given by

$$Q_0 = \int_0^\infty h^2 I(h)\, dh = 2\pi^2 (\Delta\rho_e)^2 \frac{\Delta V}{V} \tag{12}$$

where $\Delta V/V$ is the volume fraction of scatterers.

The evaluation of the invariant Q_0 must proceed carefully. The lower limit is not a significant problem, as $h^2 I(h)$ is small as h tends to zero, although it must be extrapolated due to the presence of the beam stop. At higher values of h, the small I(h) can be influenced by extraneous sources. Therefore, the numerical integration was divided into three parts,[53]

$$Q_0 = Q_1 + Q_2 + Q_3 = \int_0^{h_{min}} h^2 I(h)dh + \int_{h_{min}}^{h_{max}} h^2 I(h)dh + \int_{h_{max}}^{i\infty} h^2 I(h)dh. \tag{13}$$

where Q_2 is evaluated from the measured scattered intensity $I(h)$ between h_{min} and h_{max}, corresponding to the minimum and maximum scattering vectors of the measured scattering curve. The integration from h_{max} to infinity was calculated using Porod's approximation for intensity.

Extrapolation for small angles was accomplished by using the Guinier approximation. As $h \rightarrow 0$, the Guinier region is reached and the scattered intensity exponentially rises as

$$I(h) = V \Delta\rho_e^2 \exp\left(\frac{-h^2 R_g^2}{3}\right) \tag{14}$$

where R_g is the electron radius of gyration about the center of electronic charge.

The total specific surface area (S_{sp}) may then be evaluated as

$$S_{sp} = \frac{\pi \varepsilon \ (1-\varepsilon)}{\rho} \frac{\lim_{h\to\infty} h^4 I(h)}{Q_0} \tag{15}$$

where ε is the porosity and ρ is the apparent density of the sample.

Another measure of the surface irregularity is the fractal dimensions of an object. True fractal objects are scale-invariant or self-similar, in that they look similar at all levels of magnification. The earliest work in fractal analysis has shown that the degree of surface roughness, or irregularities can be expressed by the parameter D_s,[54,55] where $2 \leq D_s \leq 3$. D_s may be taken as a measure of the space filling ability of the surface.[37] For an Euclidean, perfectly smooth surface, $D_s = 2$, and the value of D_s increases with the degree of surface irregularity, and for a very rough, disordered surface, the value of D_s approaches 3.

The roughness is further classified by defining a surface fractal object, which is rough on a length scale small compared to its radius, e.g., rough pore boundaries in a porous solid.[56] The intensity scattered on fractal surfaces is proportional to a negative power of the wave vector h for $h\xi_s > 1$,

$$I \propto h^{-\alpha} \tag{16}$$

where ξ_s is the correlation length for surface fractal behavior. In other words, ξ_s is the upper limit of the length range in which the surface is fractal. For materials with a surface fractal nature,

$$\alpha = 6 - D_s \tag{17}$$

When $D_s = 2$ (smooth surface), the intensity is proportional to h^{-4}, the Porod's Law dependance.

3.4 RESULTS AND DISCUSSION

3.4.1 Reactivity Measurements of Soot

During devolatilization in the TGA, volatile matter was driven off until a constant weight was reached. This freshly devolatilized material was termed 0% conversion, and oxidation proceeded at 773 K in air. The reaction rate was calculated by normalizing the rate of change in mass by initial sample mass (g/g-min) on a dry ash free basis,

$$R = -\frac{1}{w_{C,0}}\frac{\Delta w}{\Delta t} \tag{18}$$

where $w_{C,0}$ is the initial mass of carbon and $\Delta w/\Delta t$ is the weight change in time interval Δt. The intrinsic reactivity was computed by dividing the reaction rate by the specific surface area at time t and correcting for conversion, X, of the initial carbon, or

$$R_i = R\left(\frac{1}{S_{sp}}\right)\left(\frac{1}{1-X}\right) \tag{19}$$

The variation of the reactivity with conversion is plotted in Figure 20, while the change in the intrinsic reactivity is plotted in Figure 21. For the NIST soot, a relatively linear rate of mass loss was observed, followed by a leveling off of reaction rate at higher conversions. The NEU soot passed through a maximum rate at approximately 30% conversion. Both the NEU and NIST soots had, assuming first order kinetics, rate constants of 0.15 s^{-1}at 30% conversion, in good agreement with Bonnefoy et. al.,[35] who reported rate constants between 0.06 to 0.2 s^{-1} for diesel soots. The high initial rate for the NIST soot may be a function of loosely bound organic matter that is not devolatilizable in an inert atmosphere, or as Ishiguro described, the soluble organic fraction.[42]

3.4.2 Surface Area

The original and oxidized products were characterized by CO_2 to determine the specific surface area. The Dubinin-Polanyi plots were all fitted to straight lines with minimum correlation coefficients well above 0.997 for all tests, an example of which is shown in Figure 23. The resulting CO_2 surface areas calculated using Equation 10 are plotted in Figure 24. As shown in Figure 24, there is approximately a two fold increase in surface area during oxidation. The greatest increase in surface area occurs during the initial devolatilization step. Surface areas then rose to a maximum surface area at around 50% conversion for both soots. However, while the surface areas of the NIST soot remained essentially constant above 50% conversion, the NEU soot exhibited a loss of surface area. The most plausible explanation for this is that the ash content plays a significantly greater roll in the surface area calculations as reactions proceeds (at 80% conversion, ash makes up approximately 25% of the sample). Furthermore, the accompanying small, but measurable decrease in surface areas at higher conversions for the NIST soot may also be evidence of Hurts' densification phenomenon at higher conversions as proposed by Hurt.

The significant overall increase in surface area during devolatilization and oxidation can be explained in two ways:

1. Micropores are created in soot particles during oxidation, or
2. The micropores are inherently contained in the soot particle, but are inaccessible. Devolatilization and oxidation reacts away the shell that initially blocks these pores, making them accessible and increasing porosity.

To check these hypothesis, SAXS measurements, which have the inherent ability to measure total porosity, were performed.

3.4.3 SAXS MEASUREMENTS

SAXS profiles of the converted soots were measured at each conversion level. The resulting two dimensional profiles did not exhibit any isotropic effects, so the average intensity at each value of h was found by radially integrating the circular profiles measured by the 2-D detector to eliminate noise. Typical profiles are shown in Figure 23 for the NIST and NEU soot data. Intensity data were corrected for background noise for by using the high h range to obtain the correct background subtraction factors and treated with the aid of a set of programs furnished by Glatter[57,58].

The Guinier plots for typical runs are shown in Figure 25. The linear range is quite broad for most samples, suggesting that there is a narrow pore size distribution. Typical h_{min} values were approximately 0.25 nm^{-1}, and the intensity for values of h less than h_{min} were obtained by extrapolating the data using Equation 14. The applicability of Porod's Law was checked by plotting h^4I versus h^4, as shown in Figure 26. The invariant plot does not show significant variation from Porod's law at high h, exhibiting an approximately constant h^4I value. At very high values of h, the plots exhibited a higher variation in h^4I, due probably to the small intensity values as compared to other sources of radiation in this range.

To check the SAXS systems, and compare a well behaved carbon to obtained results, SAXS experiments were also done on Spherocarb, a high-surface area synthetic char. The intensity curve of the Spherocarb scattering is given Figure 27, while the inset shows the well-

behaved Porod's Law region. The SAXS resulting calculated surface area of char was 1200 m^2/g. This value is above the typical CO_2 value reported for Spherocarb as 850-1000 m^2/g, which is to be expected as SAXS can measure inaccessible porosity.

The invariant was calculated using the Guinier and Porod's approximations to extend the integration region from zero to infinity. The surface areas of the soots were then calculated using the Porod's law approximation given in Equation 11. However, the porosity and density of the soot particles are essential components in this analysis to obtain specific surface areas. Unfortunately, small sample sizes precluded accurate measurement of these factors. Therefore, three alternate density/porosity variations are assumed to give the limits of porosity for the purposes of calculating surface area. For all approaches, measured true (He) densities of 2.1 g/cm^3 and 2.04 g/cm^3 for the NIST and NEU soots were used respectively. An initial starting apparent density of 1.5 g/cm^3 after devolatilization was assumed for both soots, based on values reported in the literature ranging from 1.3 to 1.8[59] g/cm^3. The three models were:

(1) Constant density oxidation. The soot is assumed to burn at with no variation in density. As density does not vary, the porosity given by

$$\varepsilon = 1 - \frac{\rho_{app}}{\rho_{true}} \tag{20}$$

remains the same. This corresponds to reaction in Regime III, or pure external diffusion control of reaction.

(2) Constant diameter oxidation. The soot is assumed not to change size as oxidation proceeds. Therefore, density will decrease and porosity increase with increasing conversion. This assumption will break down at higher conversion levels due to collapse of the soot structure.

This assumption corresponds to reaction in regime I, or pure kinetic control, and assumes that all pores are completely penetrated.

(3) Ishiguro's[42]/Hurt's[43] diameter variation with conversion is assumed. Ishiguro investigated diesel soot oxidation under similar conditions as to this study, so the soot diameter variation can be assumed to be the same. Furthermore, TEM measurements of the NIST soot diameter during oxidation that support the theory of Hurt using an oxidation resistant grid agree well with the overall diameters of Ishiguro. (See Chapter 5.). While the underlying theory for the diameter variation is different, the overall result is the same. Normally, combustion with a diameter change would conform to Regime II or III combustion. However, Theile modulus analysis confirms that at 773 K, the reaction is in the kinetic control regime (I). Assuming that Hurt's ordering model of densification is correct, the particle will change in mass and volume during reaction as

$$\rho = \rho_0 \left(\frac{D_0}{D_t} \right)^3 (1 - X_t) \tag{21}$$

The results obtained using these three assumptions are plotted in Figure 28 for each soot sample, along with the CO_2 areas measured by adsorption for comparison. As can be seen in the figures, there is a striking variation between the results obtained for the three different cases . The constant density assumption gives relatively low values of surface areas that do not vary greatly with conversion. The constant diameter assumption gives rapidly increasing surface area values, rising to over 800 m^2/g for both soots. The Hurt/ Ishiguro curve falls between the constant density and constant diameter approaches. One should also note that the relative values assumed for density can cause a great deal of variation in the actual values reported, although the trends remain the same.

Examining the NIST CO_2 and SAXS area curves (Figure 28), one trends notes that there are evidently two regions where the agreement in trends is evident, below 40% conversion and above it. Below 40% conversion, all assumptions other than the constant density approach give the same upward increasing trend. However, past 40% conversion, only the constant density approach gives trends that are qualitatively the same between the two area evaluation methods. The NEU soot also follows a similar trend, with the constant density approach again yielding a relatively flat surface area profile. However, the surface area profiles for all three methodologies provide trends that agree somewhat with the CO_2 surface area, including the decrease in surface area past 50% conversion.

The fractal nature of the soot surfaces was calculated on a length scale (= 2 π/h) of 1 to 40 nm, ranging in size from the micropores to the diameter of the soots, and is given in Figure 29. Both soots have low fractal dimensions initially, with dimensions slightly less than 2, in reasonable agreement with the results of Xu et al.[39] The reason the values are less than 2 is probably due to mass fractal nature of the entire soot agglomerate, and not individual particles. Devolatilization of the soots increases the surface roughness of the system, but the surfaces are still relatively smooth. The smoothness of the soots is probably due to aromatic layers that are deposited and loosely held on the surface of the soot during soot generation, of which devolatilization causes their pyrolysis.

The introduction of oxidant to the system radically alters the surface roughness of the soot, as indicated in Figure 29. The fractal dimension increases from about 2.2 for the devolatilized soot to about 2.7, even at very low levels of oxidation. The fractal dimension then increases with oxidation, up to a maximum of 2.9, very near the theoretical limits for a solid.

Both soots follow the same trends, although the NEU and NIST soots differ somewhat at high conversions, probably due to the impurities in the NEU soot. The high fractal numbers for soot surface roughness are comparable to the range of surface roughness obtained by Sahouli et al[60] for vacuum pyrolysis generated carbon blacks (range 2.69-2.91). The high degree of surface roughness also agrees well with Ehrburger-Dolle et al.,[61] who found that high surface area furnace carbon blacks exhibited surface fractal properties while low surface areas did not exhibit fractal character ($D_s \cong 2$).

That the SAXS surface area calculated assuming a constant density gives the trend that agrees best with the CO_2 data is troublesome, as penetration depth analysis would indicate complete penetration of all pores at 773 K. The constant density assumption would indicate that the diameter remains constant during reaction. However, the diameter does change significantly, as evident in direct measurements of the soot diameter.[42,43] The disagreement between the two calculated areas may be addressed by examining Figure 28. Assuming a relatively small error, the two methodologies do not significantly diverge before 40% oxidation. Examination of the actually volume variation of the soot in Chapter 5 reveals that while the diameter does vary significantly from the constant density and diameter slopes at lower conversions, the density change begins to slow and parallel the constant density line at higher conversions. This is indicative that only very small changes in density, if at all, are possible at higher conversions, and oxidation then proceeds with constant density.

3.5 CONCLUSION

Reaction of soots at 773 K was performed in air to various conversion levels and surface were measured be SAXS and CO_2 adsorption. The surface area as shown by CO_2 absorption

increased by a factor of two as the soots were oxidized. SAXS areas could also vary dramatically for our soots, depending on the model assumed for the density variation with conversion.

The combined analysis of the SAXS, CO_2 adsorption and TEM data indicates that during the initial stages of combustion, the soot is capable of structurally transforming and densifying, and the soot structure may be broken down into 3 distinct stages.

The soot, as received, contains numerous "light" hydrocarbons that surround the skeletal soot structure, as illustrated in Figure 30. Devolatilization will remove the adsorbed compounds, revealing some of the skeletal structure and introducing porosity. The introduction of oxygen then further facilitates removal of hydrocarbons that are lightly bonded to the soot structure, revealing at last the connected soot skeletal structure. This structure is subject to the densification phenomena, structurally ordering during oxidation, until complete burnout is achieved.

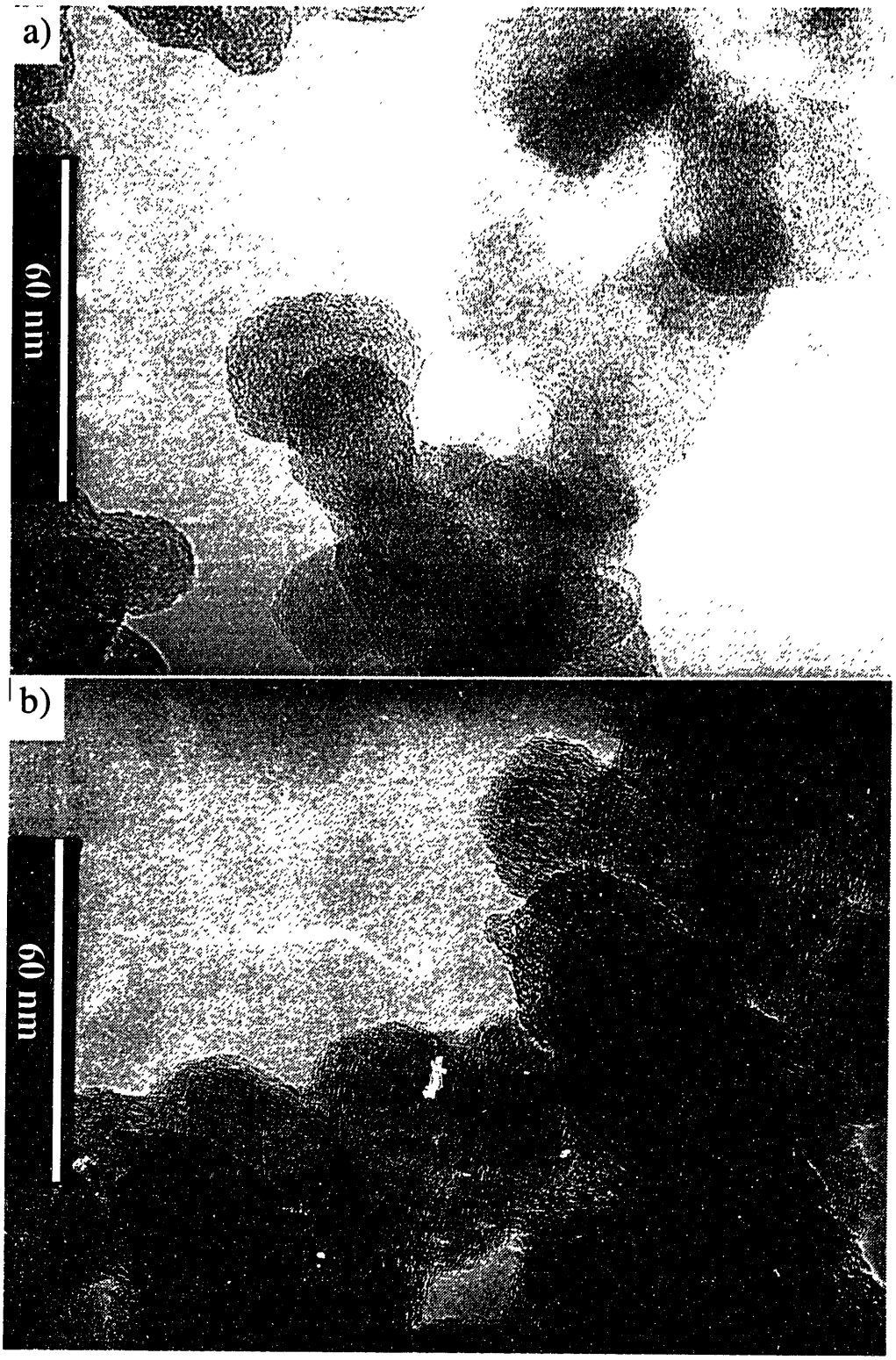

Figure 18. TEM images of the soots used in this study; a) NIST and b) NEU.

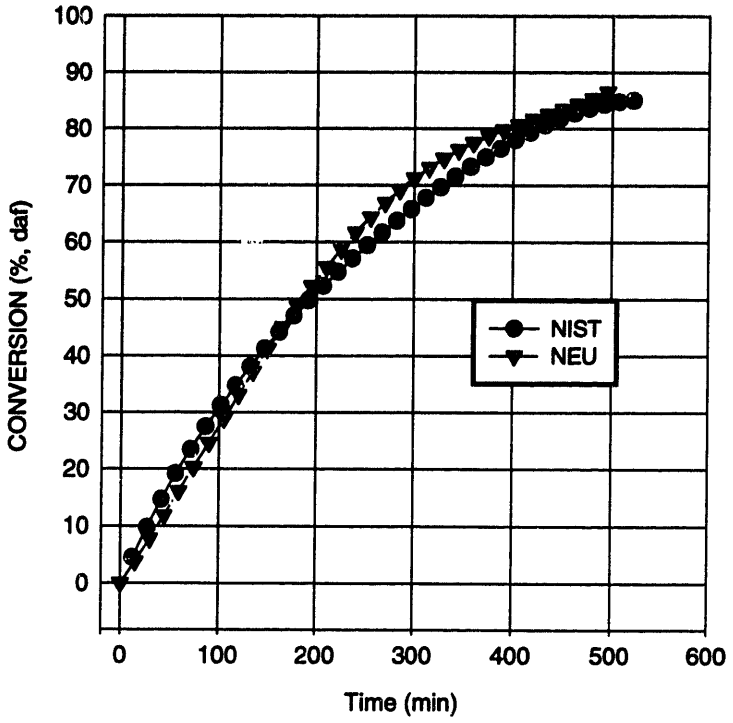

Figure 19. Conversion as a function of time for soots.

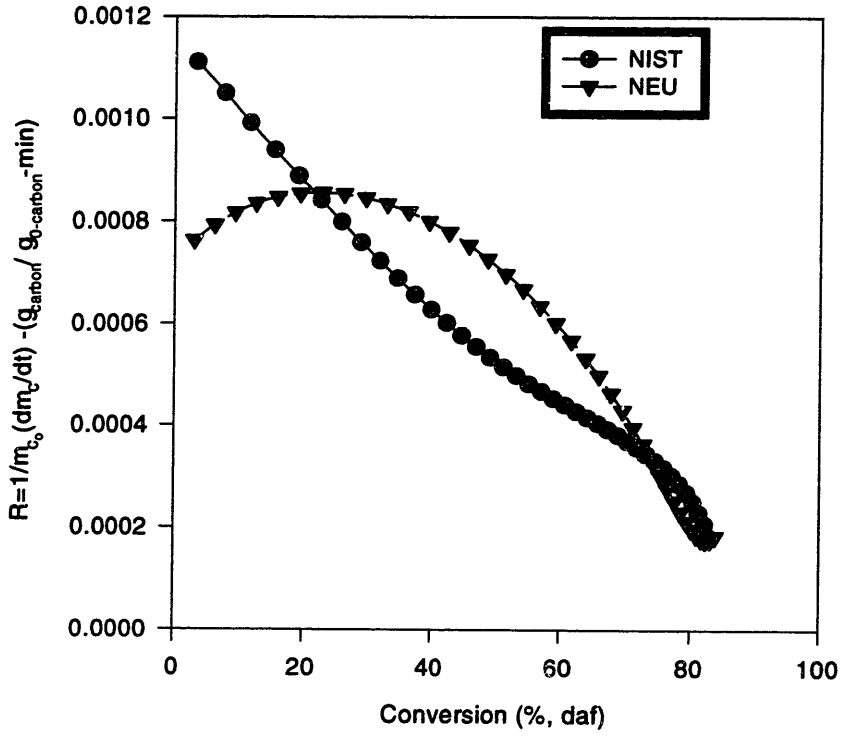

Figure 20. Variation in reactivity as a function of conversion.

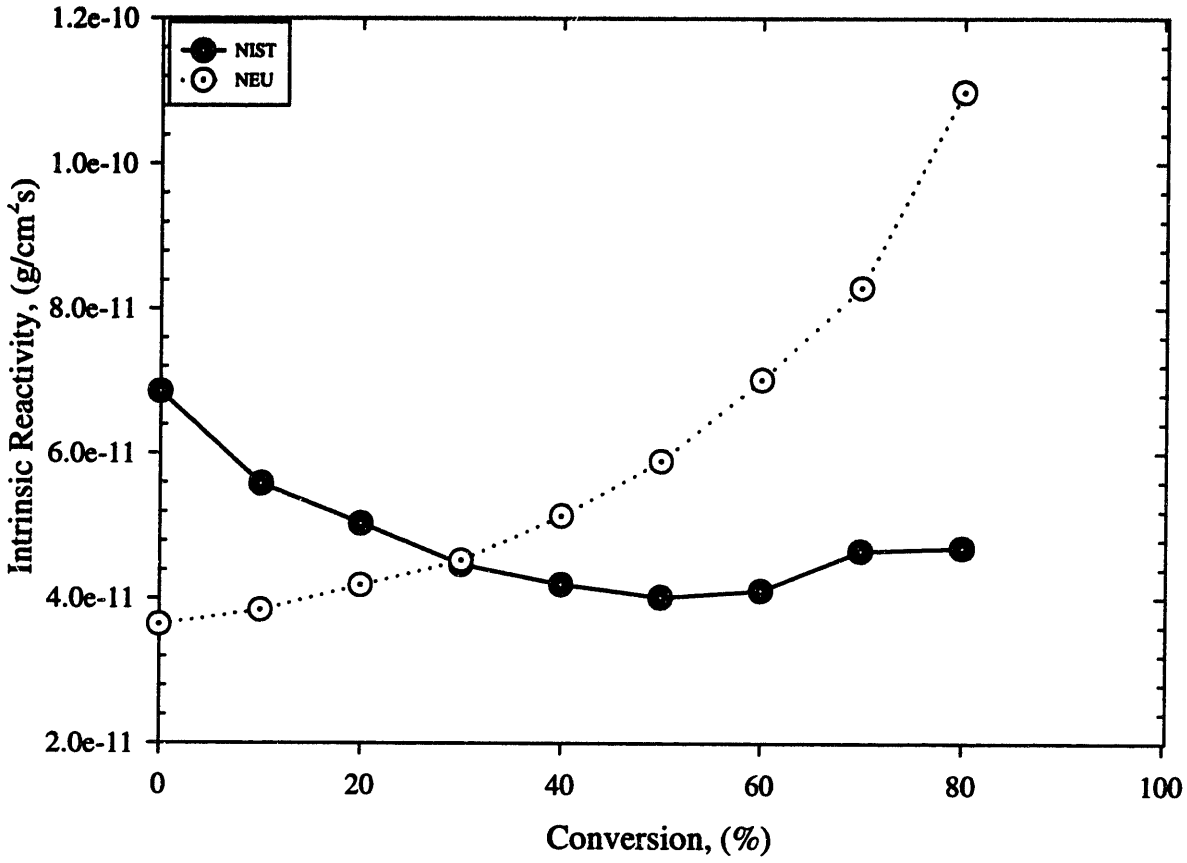

Figure 21. Intrinsic reactivity of soot, normalized with CO_2 surface area.

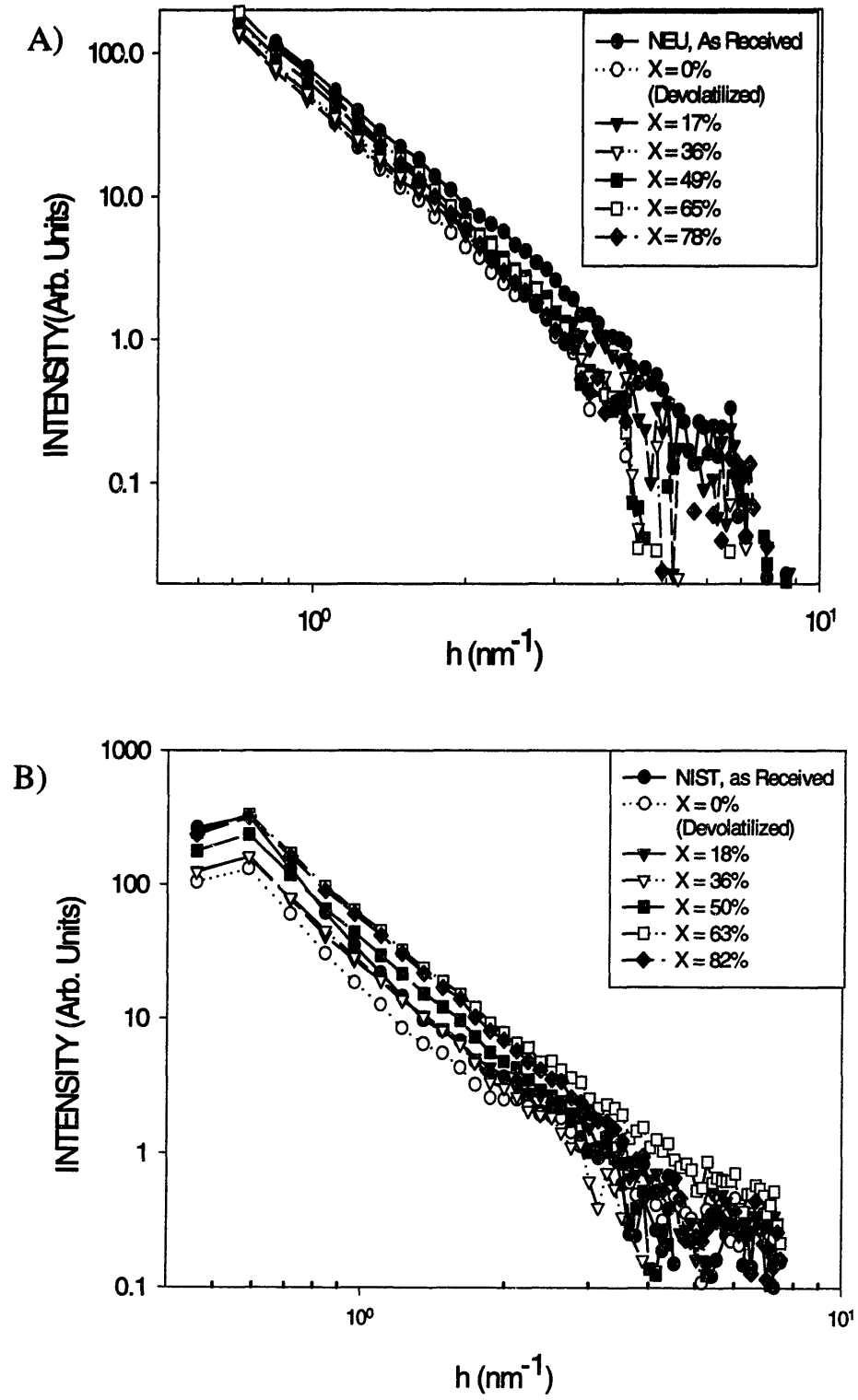

Figure 22 Typical SAXS profiles for (a) NEU and (b) NIST soot.

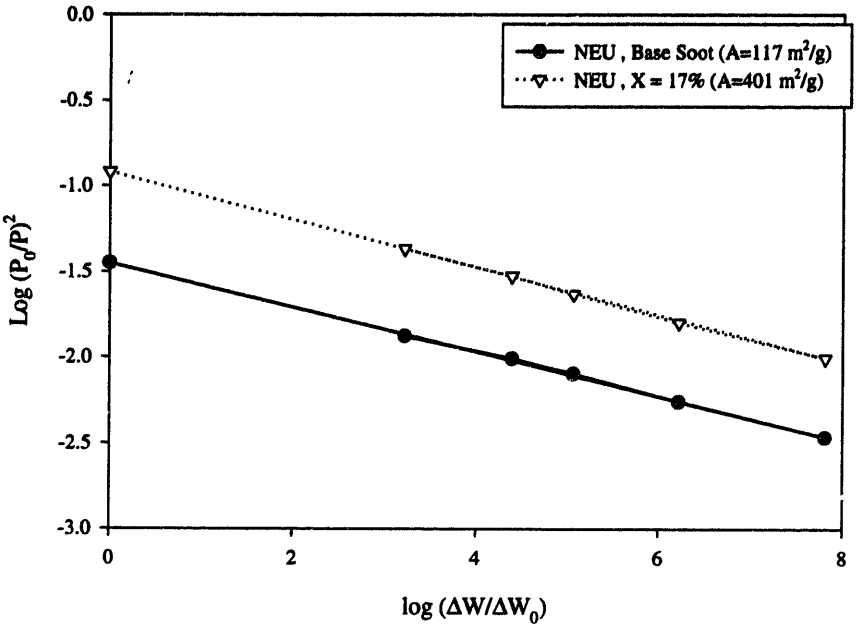

Figure 23. Dubinin-Polyani example plots.

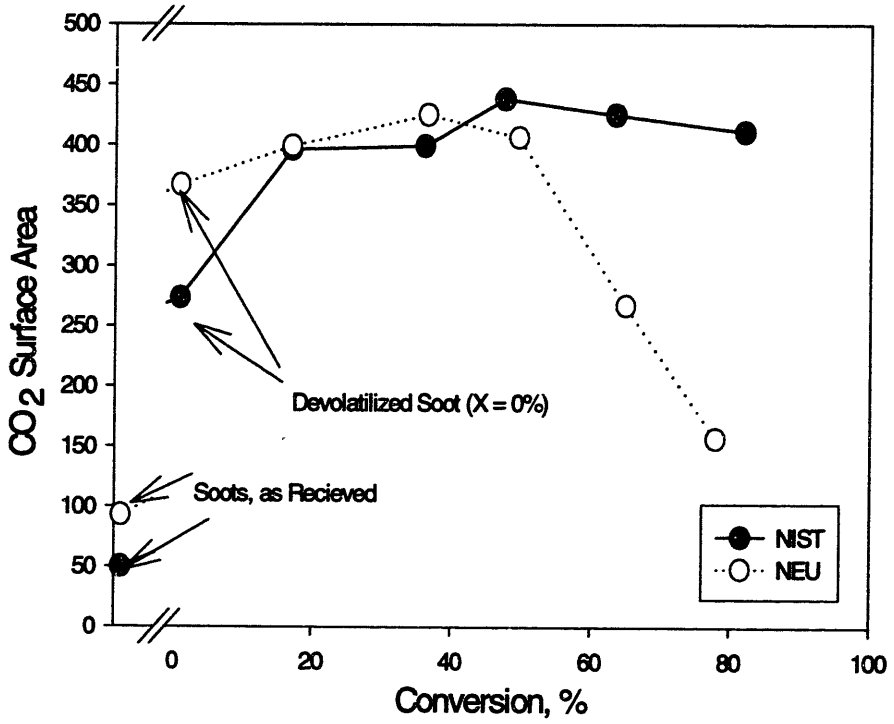

Figure 24. Evolution of CO_2 surface area with conversion. The points shown before zero conversion represent the soots as received (no treatment).

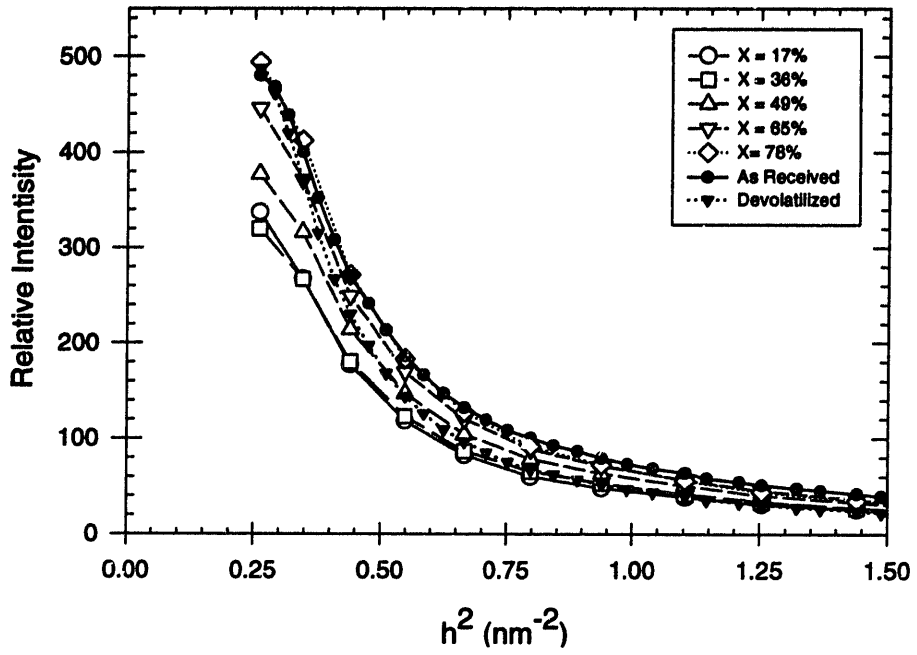

(a)

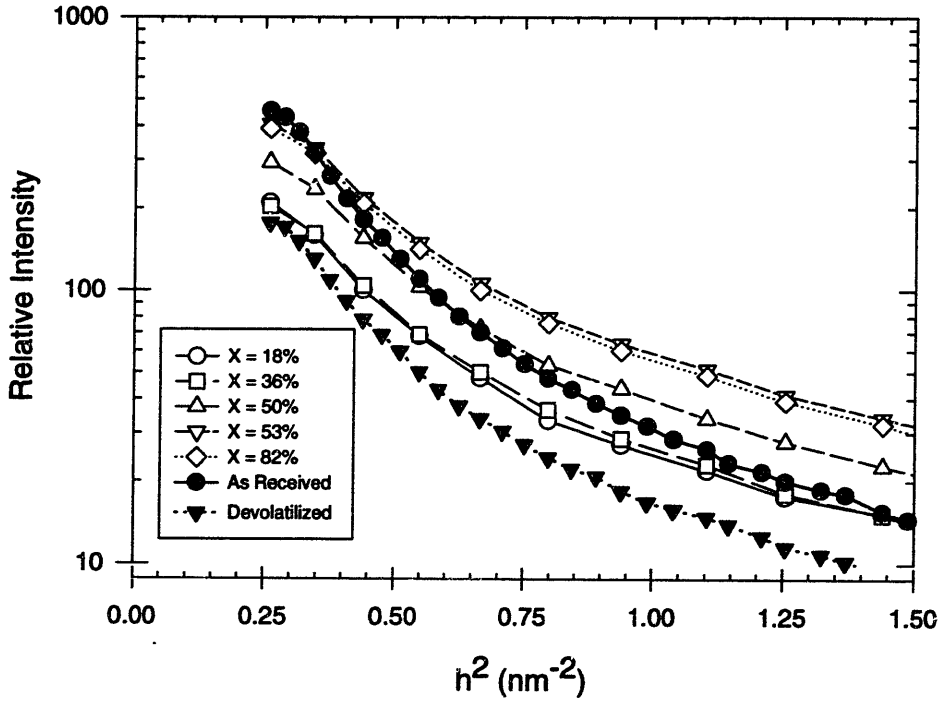

(b)

Figure 25. Guinier plots for (a) NEU Soot and (b) NIST soot as a function of conversion

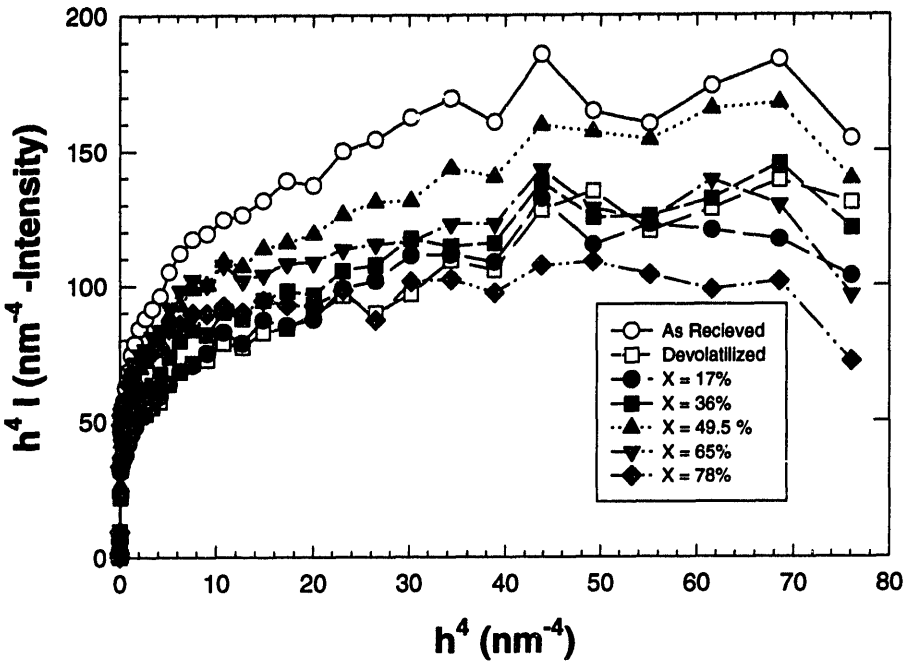

(A)

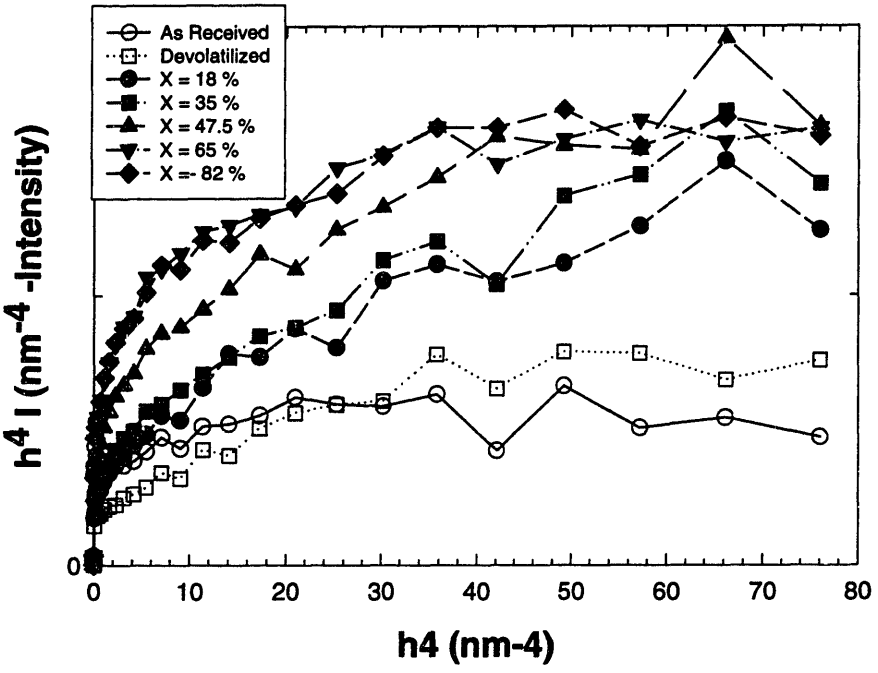

(B)

Figure 26. Porod invariant plots for (a)NEU and (b) NIST soots as a function of conversion

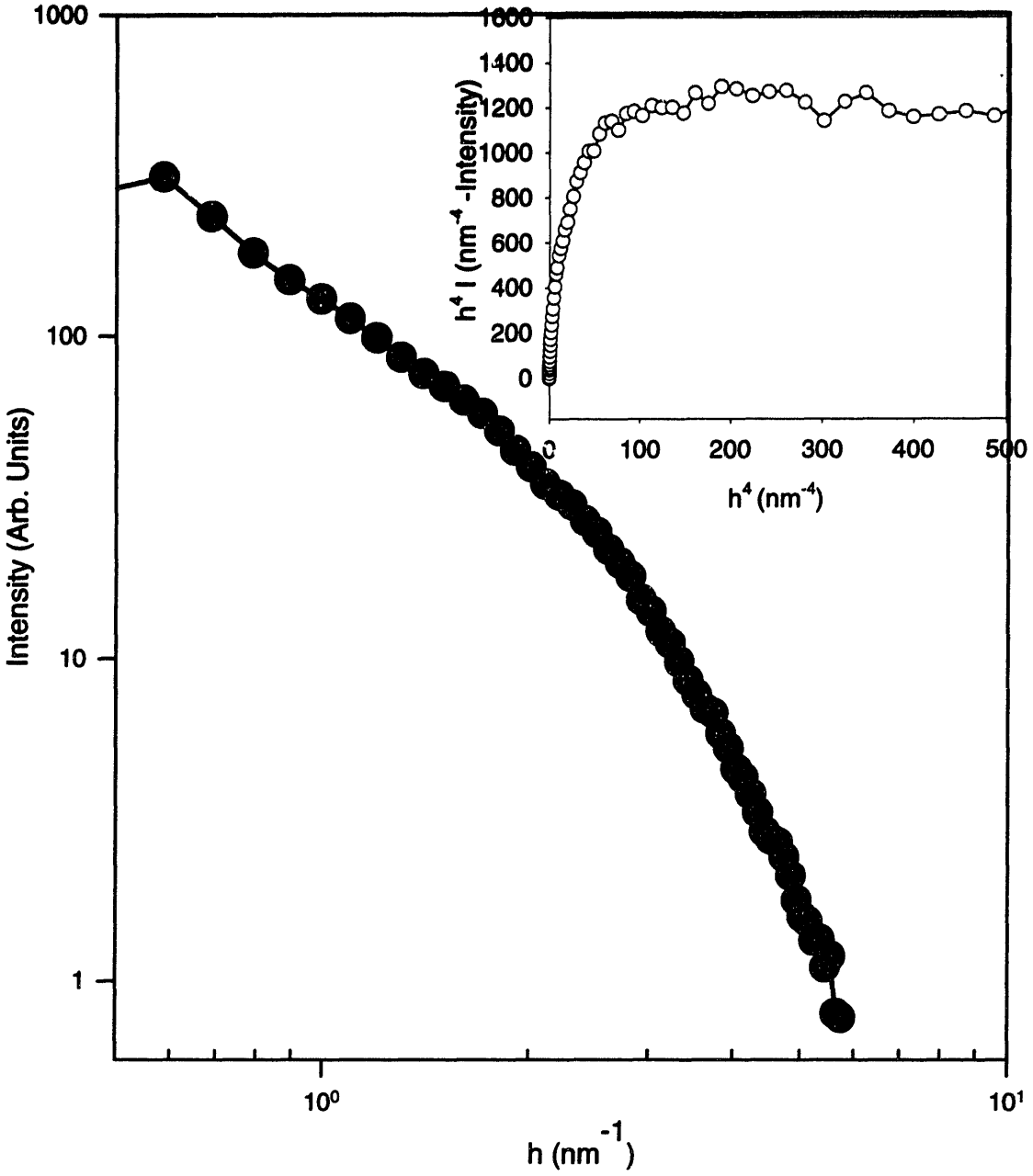

Figure 27. SAXS profiles of Spherocarb.

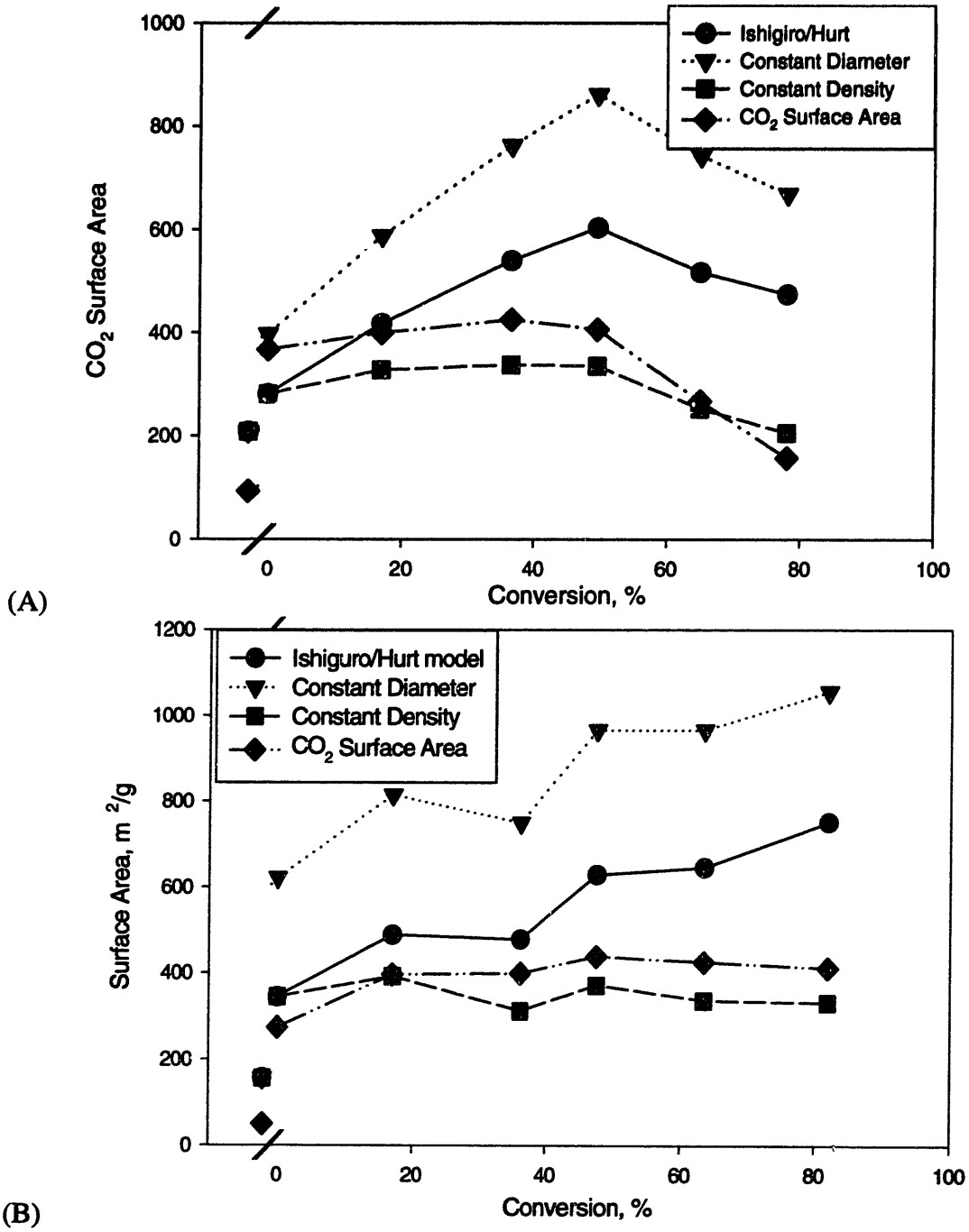

Figure 28. Variation in SAXS calculated surface areas for (a) NEU and (b) NIST soots assuming constant diamter, constant density, and the Ishiguro/Hurt variation in structure.

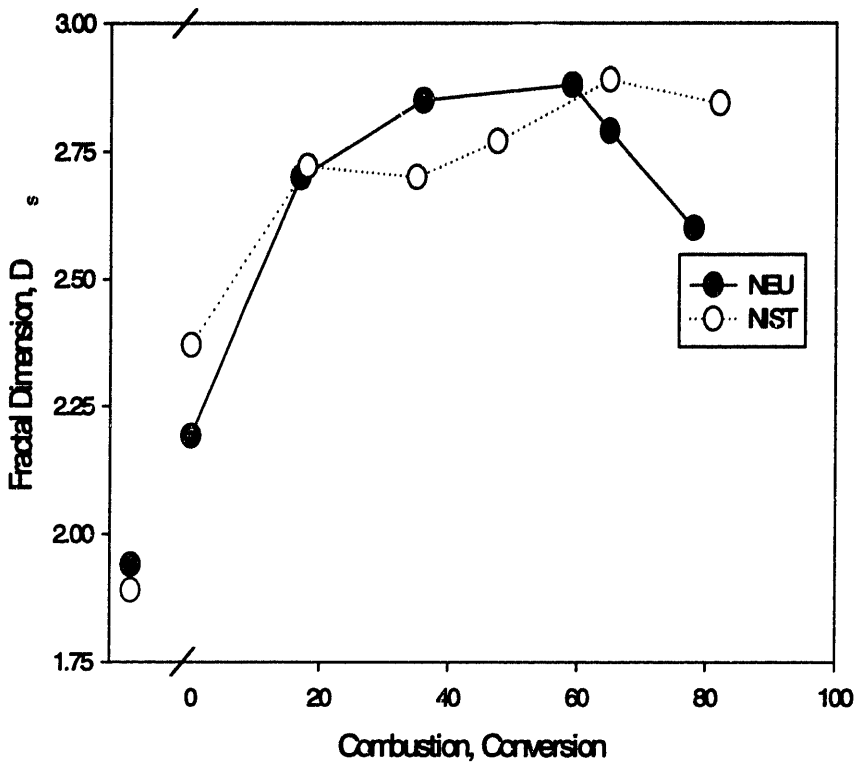

Figure 29 Fractal evolution of Soot. Devolatilization increases the fractal character of the soot, while oxidation increases its character even more.

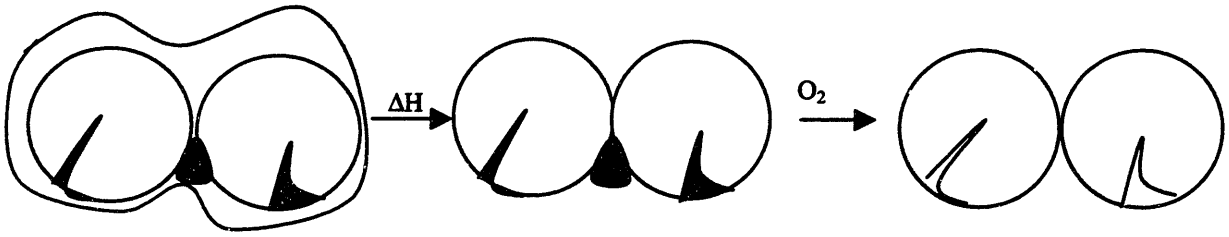

Figure 30. Idealized Soot particle. a) smooth, covered with hydrocarbons, b) devolatilized, with hydrocarbons filling selected areas, such as dark "pores" and c) Oxidized, with only skeletal structure.

CHAPTER 4

4. Generation of A Combustion Resistant Grid: Application To Single Particle Studies

4.1 INTRODUCTION

A large variety of carbonaceous solids are of interest in combustion, including soots, cokes from liquid-fuel combustion and chars from high temperature decomposition of organic solid precursors. The oxidation of these solids can occur uniformly throughout the solid under certain conditions, notably for low rates of reaction, small particle size, and high porosity. For small particles in the nanometer size range, it is difficult to experimentally distinguish measurements that occur at a single particle level from bulk phenomena. An observation of interest is gasification induced densification, in which structural rearrangements result in particle contraction during oxidation. This densification phenomenon was inferred from the studies of particles in the 20 nm to 13 mm range, including Spherocarb,[62,63] Pittsburgh #8 coal,[64] form coke,[65] and soot.[66] Hurt et al.[67] attributed the densification to the microstructural rearrangement of the carbons due to oxidation, but had no direct corroboration of these changes.

Ishiguro et al.[66] observed the reduction of primary particle diameter during the oxidation of diesel soot at 500°C. They attributed this particle size reduction to surface ablation of the particles due to surface tension effects. Ishiguro et al. also provided high resolution electron micrographs and EELS data from the soot at different extents of oxidation, supporting the theory that increased ordering (graphitization) of the soot occurs with increased degree of oxidation.

Data concerning the evolution of the size and microscopic structure of the same soot particle during oxidation would be useful in resolving this issue.

Heckman and Harling[68] obtained transmission electron microscope (TEM) micrographs of the same carbon black particles before and after oxidation, but did not report the details of their experimental procedure. Heckman observed that the key to the methodology is the development of a sample holder that will withstand oxidation and allow imaging of soot particles at the same location on a TEM grid after the soot particles have been subjected to different amounts of oxidation external to the microscope.[69] Controlled atmosphere electron microscopy (CAEM) for examining carbon during oxidation has been developed but so far only with lower resolution microscopes.[70] Higher resolution microscopes use electron energies which can cause structural rearrangements for the long reaction times involved for chemically controlled soot oxidation;[71] therefore CAEM cannot be used to pursue structural changes at high resolution.

A modification of the Heckman procedures for obtaining and processing a labeled TEM grid that survives oxidation has been developed. The generation of this grid and its application to the study of soot shrinkage during oxidation are the subject of this chapter.

4.2 SAMPLE PREPARATION

Standard TEM grids are available in a variety of materials, consisting typically of a thin metal mesh with an overlaying amorphous carbon layer that provides sample support. For examination of carbon structure in which the amorphous carbon layer would interfere with sample characterization, a lacy carbon layer grid is preferred. The carbonaceous material to be imaged is examined by imaging only the portion that extends over the holes of the lacy carbon. The very thin carbon layer, however, is quite fragile, readily reacting under slightly oxidizing

conditions, destroying the structure of the grid and its usefulness as a sample holder. The problem of fragility was solved by coating the grid with a deposit of non-reactive aluminum (oxide)

The grids, obtained from Ted-Pella Inc., were labeled nickel grids for location assistance, coated with lacy carbon with typical hole diameters of 300 nm. The grids were then coated on both sides with approximately 7.5 nm to 10 nm of aluminum using a thermal evaporator; thickness was confirmed with a profiler. This thickness was the minimum needed to provide a robust "sandwich" to protect the grid structure. After coating, the grids were subjected to a temperature stabilization period, typically 1 hour at 900K in air after a mild (10K/min) heat ramp in a thermogravimetric analyzer (Cahn, model 113 TGA). The mild heat ramp allowed for an evening out of the aluminum coating, which can deposit unevenly or in large crystal domains. The high temperature oxidizing environment allows for further stabilization of the aluminum (MP 930K) by formation of aluminum oxide (MP ~2300K). The stabilization step also acted as a first-pass removal method for grids that were not capable of withstanding elevated temperatures, probably due to uneven metal deposition, which may leave carbon exposed to the oxidizing environment. The sample examined was NIST diesel particulate matter (NIST item 1650), a standard diesel soot used in environmental studies. The NIST soot was devolatilized at 1173K for 15 minutes in order to minimize particle movements that could arise due to outgasing of volatile material. The NIST soot was then ultrasonically suspended in ethanol and deposited dropwise onto the prepared grid. The grid and deposited soot were then subjected to a "thermal shock" step consisting of a rapid heating(50K/min) in inert gas to above the reaction temperature

(823K). This allowed thermal stability of the agglomerates to be achieved in order to minimize changes in the agglomerate structure due to heating in subsequent steps.

After stabilization, the sample was examined using either a Joel 200CX TEM or an Akashi/Topcon 002B, both equipped with LaB_6 filaments operating at 200 keV. For a typical sample, 4-5 regions were identified and photographed at magnifications of 100-150 kX, along with lower magnification micrographs used for identification of the proper grid location in later microscopy work. The grid with deposited sample was then oxidized at 773 K in air using the thermogravimetric analyzer (TGA). The conversion level was calculated using a control sample of the same material to measure the change in oxidation level versus time, since the amount of sample was too small in comparison to the grid weight to allow for measurement of weight loss. After oxidation, the grid was again imaged with the electron microscope, locating regions photographed before oxidation. Typically, only one or two of the regions had soot agglomerates that were identifiable in the preoxidation images, probably because of temperature induced movement of the agglomerates, which are held to the grid only by electrostatic forces. The micrographs were then digitized using Adobe Photoshop® with attached scanner (UMAX model II) and analyzed with Semper 6P®.

4.3 RESULTS

TEM micrographs of the same region taken before oxidation and after oxidation to 40% weight conversion are shown in Figure 31 and Figure 32. Individual soot particles, such as those at point A and B, were selected for the purpose of examining structural changes during oxidation. Comparison of the two figures shows that the agglomerate itself has retained much of its overall shape. The upper portion has moved from its attachment point C in the pre-oxidation

micrograph to point D in the post oxidation micrographs, resulting in a change in the overall orientation of the agglomerates without loss of overall structure.

In Figure 33, the soot primary particle at Point A has been isolated. The pear shaped region is the result of the overlapping and fusion of two primary particles. The particle diameter is measured using software tools, and the differences in diameters are obtained. The plot of the overall trends in particle volume (assuming a spherical volume) is given in Figure 34, along with comparisons of the data from Ishiguro[15].

While only the pear-shaped particle was measured in the subregion (Figure 33), there are important trends to note from the entire region. The first is that the overall structure is maintained. Even though a large fraction of sample has been oxidized, there is little change in the structure that is not due to rotation or shrinkage. This indicates that the particle is burning without removal of outer layers, since the agglomerate does not lose its shape. One would expect that primary soot particle connectivity would not be retained after oxidation if surface layer recession were occurring. That shrinkage occurs throughout the agglomerate is evidenced by the increase in the number of soot primary particles in the subregion (Figure 33) indicating that shrinkage has occurred not only for the measured particle, but also for the entire soot agglomerate.

The usefulness of the technique is exhibited in Figure 35, showing a highly oxidized sample. The same soot agglomerate is imaged before and after oxidation to 90% by weight. Due to the high degree of oxidation, loss of the particles due to structural breakdown is severe, and the same primary particle may not be identified with a reasonable degree of accuracy, limiting the usefulness of this methodology. However, the primary particles are from the same

agglomerate, minimizing possible differences in the primary particle history, reducing the error associated with measurement of microscopic particles.

4.4 CONCLUSIONS

A combustion resistant grid has been used to examine the shrinkage of single soot particles during kinetically controlled oxidation. The retention of soot agglomerate shape and structure agrees well with the hypothesis that soots undergo homogeneous shrinkage during oxidation.

The examination of soot is only one potential application of this grid, and studies with different materials may be of interest. While only low oxidation temperature experiments were performed, the aluminum oxide grid structure can withstand higher temperatures, and may be of use as a collection grid during in-situ combustion studies.

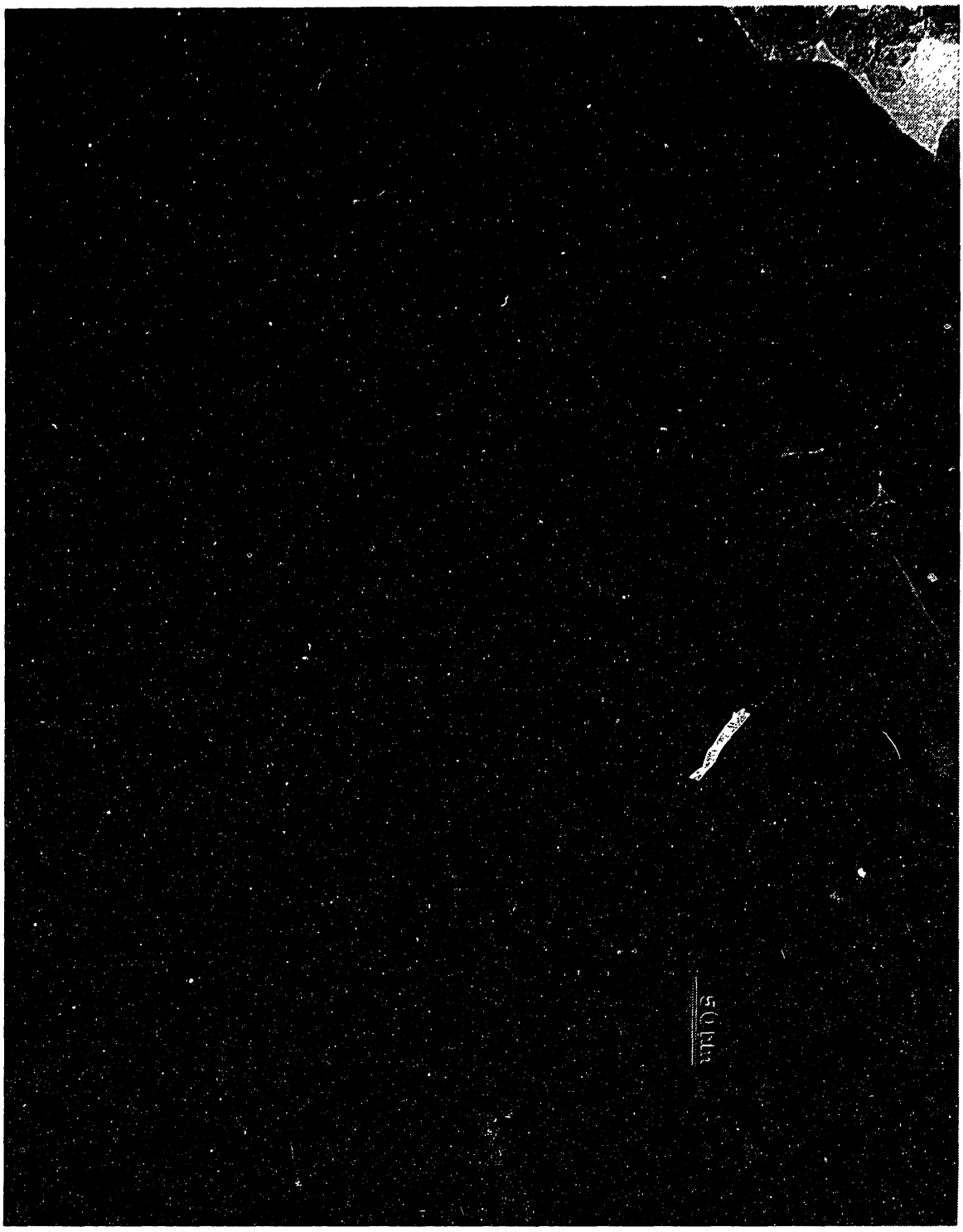

Figure 31. TEM micrograph of NIST soot before oxidation (original image: 200keV, 120kX magnification).

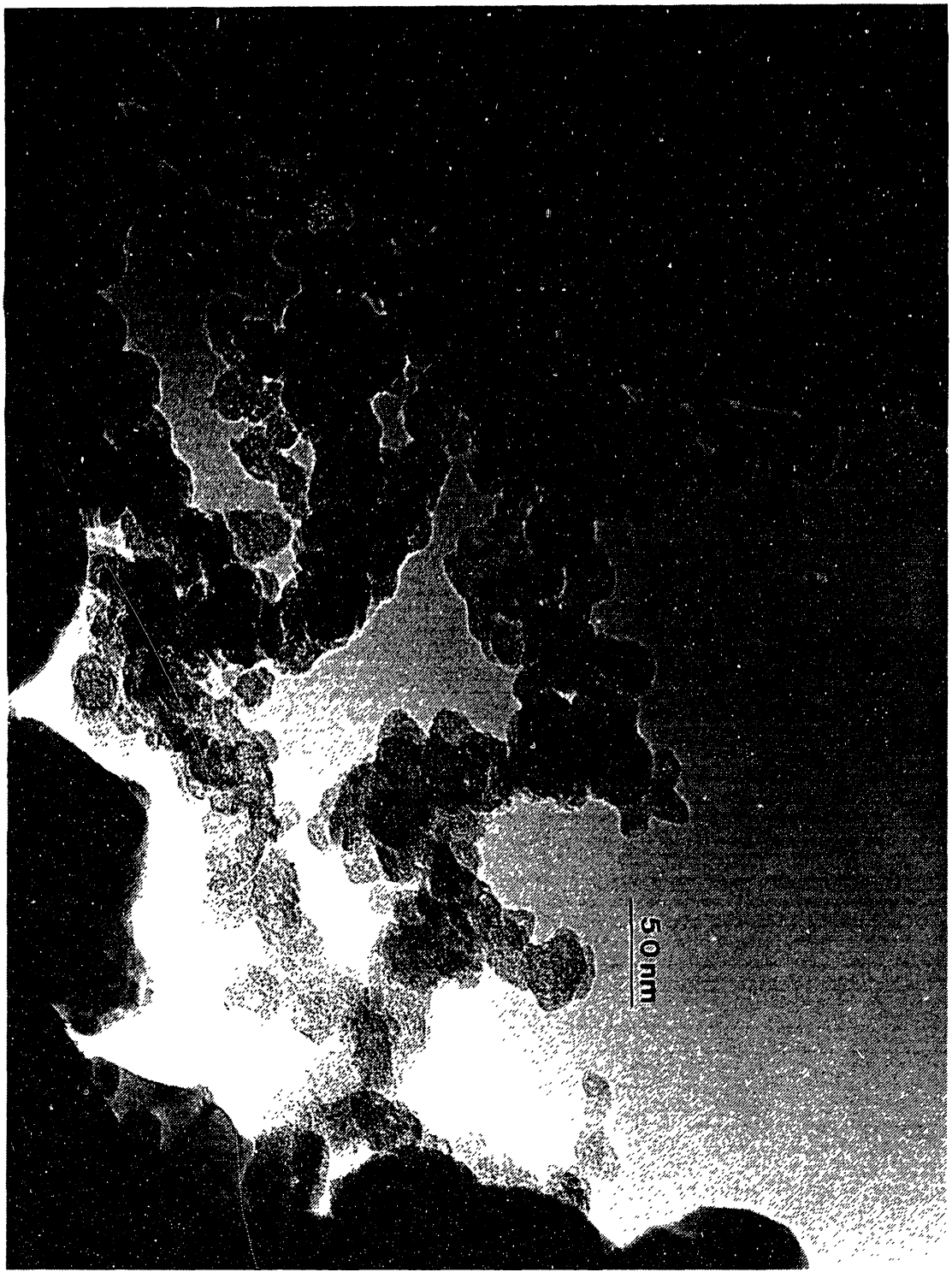

Figure 32. TEM micrograph of NIST soot after oxidation to 40% conversion (original image: 200keV, 120kX magnification).

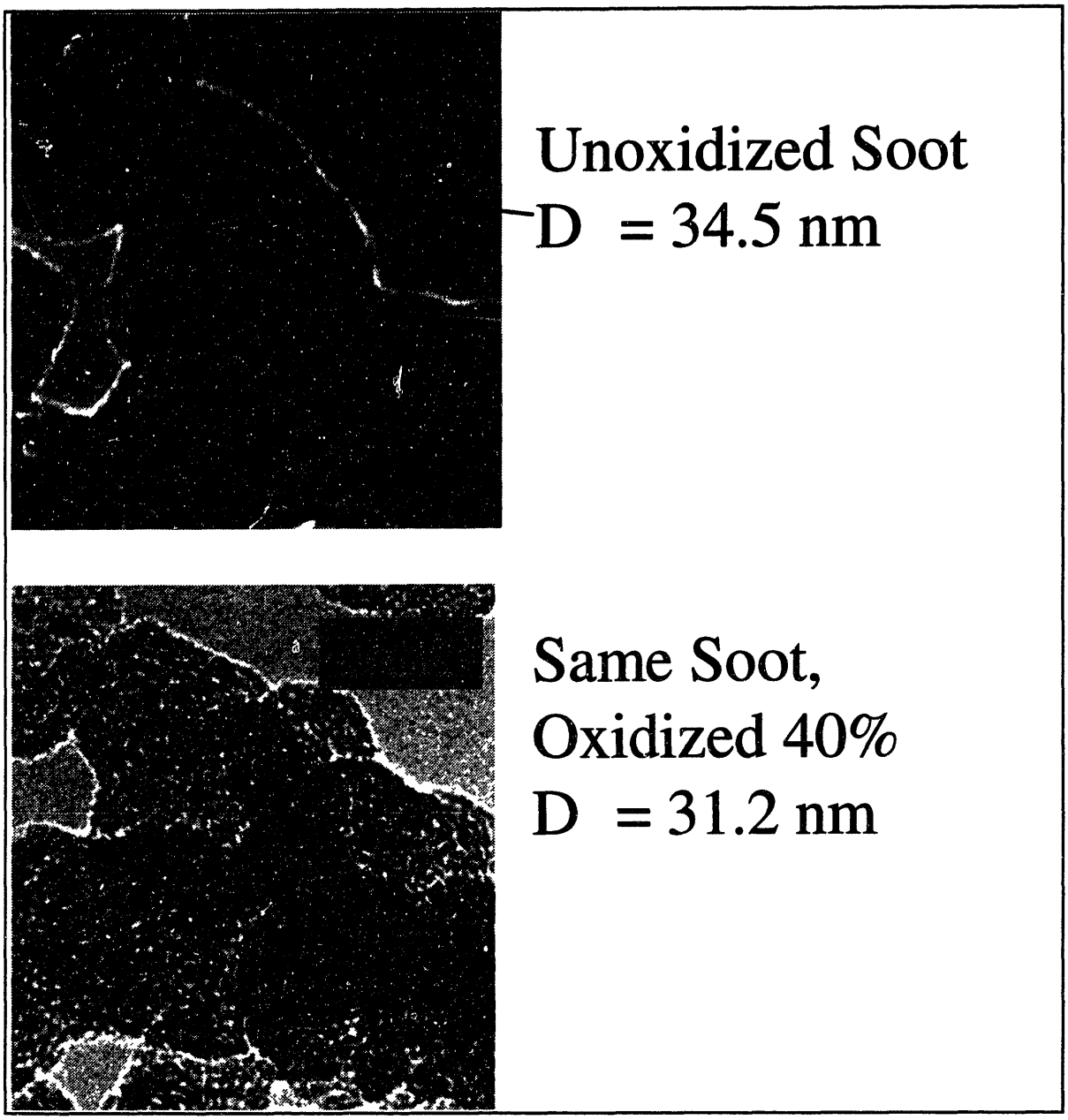

Figure 33. Magnification of Region A of Figures 1a and 1b. Shrinkage of the primary particles that make up the pear-shaped particle is evident.

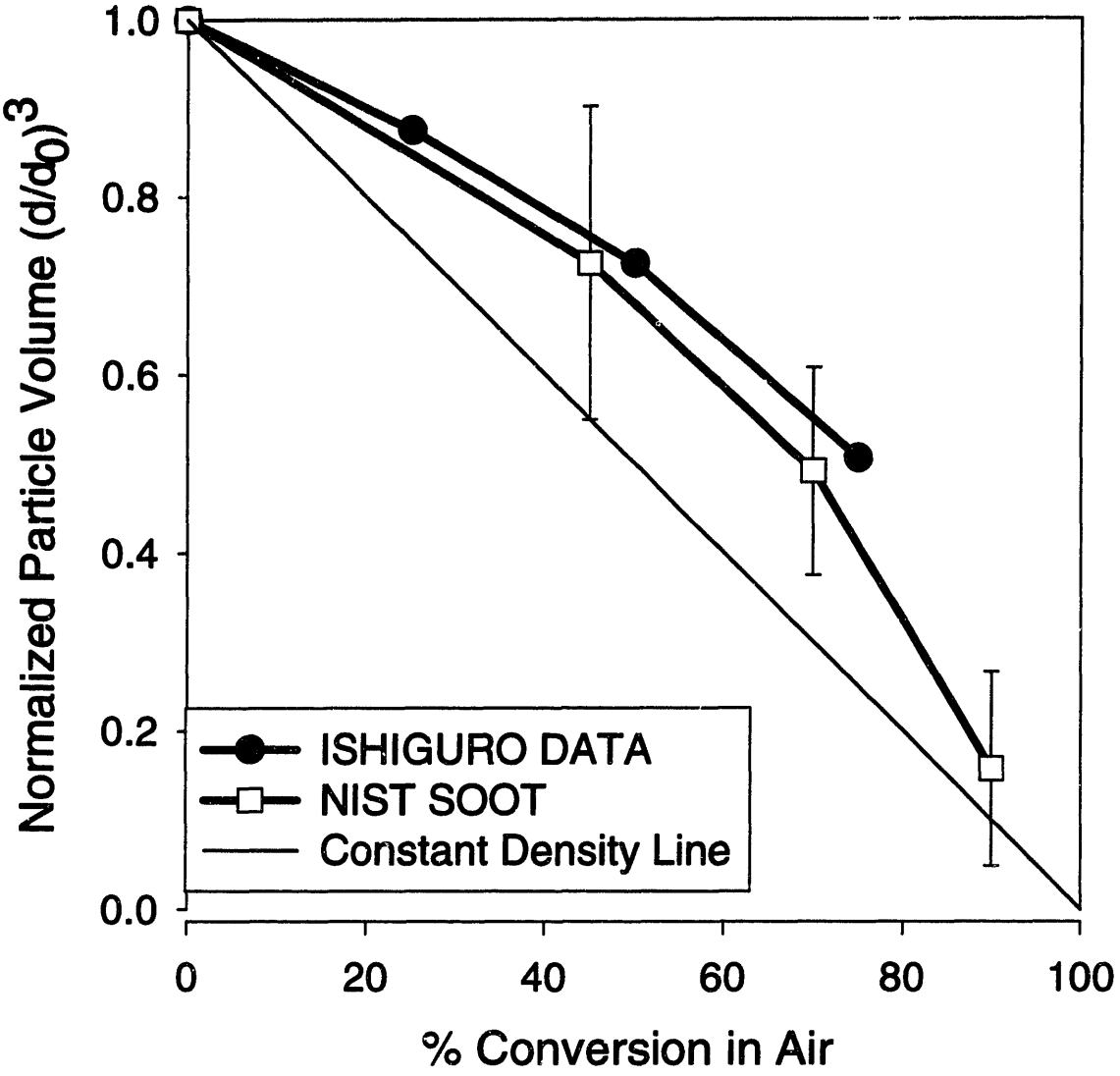

Figure 34. Comparison of sample data using Ishiguro's data and the data generated using the grid. The error bars represent the maximum variation in diameter observed.

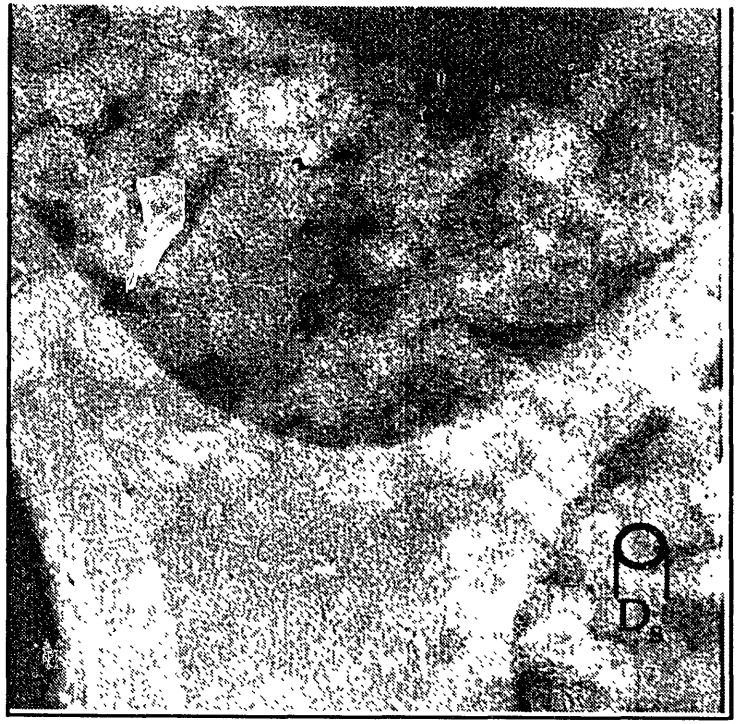

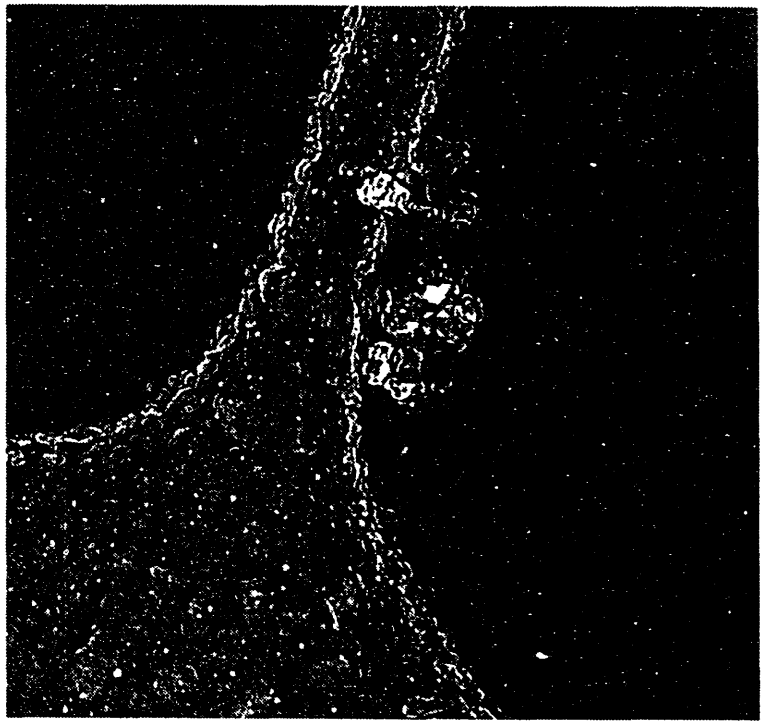

Base diesel soot on carbon grid

$D_{soot} = 23.7 \pm 4.1$ nm

90% weight conversion

$D_{soot} = 12.8 \pm 4.2$ nm

Figure 35. Very high conversion of soot on the TEM grid. The high oxidation level makes comparison difficult, but some regions are isolatable. The "bumps" seen on the grid are due to aluminum migration during extended periods of oxidation

CHAPTER 5

5. Radial Distribution Of Soot Structure Obtained With High Resolution Transmission Electron Microscopy

5.1 INTRODUCTION

Widely used techniques used to measure porosity and surface area, such as gas absorption (N_2, CO_2) and Small Angle X-Ray Scattering (SAXS), when performed on particulates such as soot, yield average sample characteristics, but do not provide details on the variation of the physical structure within a particle. The morphology of carbonaceous materials is the direct result of their oxidation history.[9] One result of oxidation is that certain carbon blacks yield cenospheric (hollow) particles, suggesting that the outer layers are less reactive than the core. Another result is the observation of large increases in the surface area of soot after only a small fractional oxidation (50 to 400 m^2/g for ethylene soot going from 0 to 20% conversion,[72] and 50 to 300 m^2/g for Regal 600 carbon black for the same level conversion[73]) . This can be attributed to "blockage" of the internal area of individual particles by a relatively impervious shell of carbonaceous material.[72,74]

Diesel soot consists of spherical primary particles, approximately 20-30 nm in diameter, that are aggregated in grape-like clusters of 1 to 2 mm, as seen in Figure 31.[75] In diesel engines, soot forms in the fuel-rich pockets and may undergo oxidation before being released to the atmosphere. The basic structure of soots is formed in these pockets from large poly-aromatic hydrocarbons (PAH) compounds that coalesce and deposit onto single particles. Using High-Resolution Transmission Electron Microscopy (HRTEM), it has been found that under different

loads, diesel engines emit structurally different soots.[76] It also has been found that an increase of lattice ordering and a decrease in primary particle size is the result of oxidation of soot.[66] Similar results have been observed for carbon black.[77]

The purpose of this study is to examine the effect of oxidation on the microstructure of soot. The consequences of radial variation in the structure of soot as function of oxidation will be examined by analyzing the soot structure using a recently developed methodology based on image analysis of high resolution transmission electron micrographs.

5.2 EXPERIMENTAL AND ANALYTICAL METHODS

Diesel emissions are complex in structure and composition. Electron microscopy (HRTEM) coupled with image-analysis techniques that apply high level computer software has been used to analyze the structure of a diesel soot that has been exposed to oxidizing conditions (air, 773 K). A standard soot generated by the National Institute of Standards and Testing, NIST, was used for this study. The sample, NIST 1650, corresponds to a medium load diesel engine exhaust with collection by dilution followed by filtration.

In order to minimize interference from the polycyclic aromatic hydrocarbons (PAHs) absorbed on the soot surface, the soot was devolatilized in an inert helium atmosphere by heating at 50K/min to 1173 K. The soot was held at 1173 K for 15 minutes until a constant sample weight, measured by a standard Cahn 113 thermogravimetric analyzer (TGA) was obtained. The sample was then cooled at a cooling rate of approximately 40 K/min, and then oxidized in air at 773K using the TGA to 70% mass conversion. Another sample was treated in a furnace for 1 hour at 1500 K in a covered graphite crucible, with a sample weight change of approximately 40% due to pyrolysis and/or mild oxidation.

A small portion of each sample was ultrasonically suspended in ethanol and deposited dropwise on a lacy carbon TEM grid. An oriented gold crystal was used as a calibration standard and subjected to the same techniques as the diesel soot samples. The use of a specifically oriented gold crystal allows only the lattice locations in one plane to be diffracted. Thus, precise measurements of the lattice distances may be made and compared to the experimental samples.

An Akashi/TOPCON 002B transmission electron microscope with an LaB_6 filament operating at 200 KeV was used to produce high resolution images of each sample. The micrographs were digitized with a UMAX PowerLook II model scanner operating at a scanning resolution of 993 dpi. The high level language computer software, SEMPER 6P™ (Synoptics, LTD., Cambridge, UK), developed especially for image analysis, was then used to manipulate the digitized images in order to extract data that could be used to characterize each soot sample. Optical diffraction patterns showing the periodic patterns present were generated from these images (see Appendix A and B). The optical diffractogram is a power spectrum calculated by squaring the modulus of the Fourier transform. Intensity profiles characteristic of the range of contrast in the diffractograms were then produced. A series of "filters" were also applied to the digitized soot images to eliminate noise and isolate the significant structural data from the image. The extracted structure then becomes the basis for statistical analysis. A complete explanation of the technique used may be found in Appendix B.

After image processing, the lateral extent of fringes, L_a, and interlayer d_{002} spacing were quantified. The angular dependence of the structures was also be measured, and was used to obtain the center reference axis of the primary soot particle so that the mean of the orientation of

all structural elements was as close to zero as possible in order to get as accurate a measurement of the soot center as possible.

The lateral extent of fringes is defined as:

$$La = AB\sqrt{m_{max}} \quad (22)$$

where m is the principal second moment of area. A second moment is a mean square of all pixels about a line through the center of area of a structural element (fringe). The principal second moments are the second moments with respect to a pair of mutually perpendicular axes in directions that achieve minimum and maximum moments. The constant B is a physical conversion factor from pixels to Angstroms. The factor A, usually between 3 and 4 depending on the shape of the object in question, was determined experimentally to be 3.56 1/pixel.

To get the characteristic interlayer spacings for the sample, the total area of the fringes was determined with minimal filtering, which corresponds to eliminating repeated frequencies below 0.3 nm and above 0.5 nm. Then, in order to eliminate differences in illumination between each sample, the intensity range was narrowed and shifted to a position in which the number of fringes showed a maximum as a function of intensity.[77,78,]

5.3 RESULTS

The electron micrographs in Figure 36 show the turbostratic (randomly orientated carbon atoms layers) lattice structures of the untreated and oxidized diesel soots, respectively. In Figure 37, a portion of the base soot has been masked off using the image analysis software in order to isolate the soot particle for comparison purposes. An example of the structural data extracted from the soot images after a series of filters is shown in Figure 38.

Care was taken to eliminate any regions of overlap between adjacent primary particles. The overall distribution of lattice lengths for each particle, along with a comparison of lattice length as a function of radius is shown in Figure 39. The average lattice lengths were 1.53 ± 1.0, 1.55 ± 1.2, and 1.58 ± 1.1 nm, for the untreated, 773 K and 1500 K soots, respectively. The large errors associated with these readings are the results of a non-gaussian nature of the system.

5.4 DISCUSSION

The extracted soot images of the two different conditions that we have examined were compared to the results for the unoxidized soot. The average lattice length for all samples was approximately 1.5 nm, although there is there is a difference in the distribution of lattice lengths of each sample. It is important to note that the untreated soot has more individual lattice fringes due to its much larger area than the oxidized samples (approximately 2 times), making comparisons difficult. However, as temperature/oxidation conditions increase, the lattice length tends to shift toward a bimodal distribution, with a large concentration of shorter lengths, and increasing number of longer lattice lengths.

Another method of comparing the samples is to examine the radially sectioned averages, as shown in Figure 39. The average is plotted in bin sizes of 2.5 nm, along with the average lattice length from a radius of 0 to the radius r. Each of the soot samples has as a small average lattice length in the center and increases to a maximum value near the edge of the soot before again beginning to decrease. The unoxidized soot starts with an average lattice length of approximately 1.2 nm, and slowly increases to a maximum of about 1.6 nm near the edge of the soot particle. This is similar to the results of Lahaye and Prado[75] who observed that the layer

planes of soot are oriented around some randomly distributed centers in the particle, much like an onion[75].

In contrast, both of the treated soot samples have higher maximum values for the radial section, but start with lower center values for the radially sectioned average lattice length, although the relative error is large for these samples due to the low number of fringes in the center. The actual average for all samples is about the same due to the high total number of small fringes for all particles. This transformation due to oxidation is similar to the work of Buseck et al., who showed an ordering of the structure of amorphous coke with increasing annealing temperatures and increasing linearity of the coke precursors when imaged by TEM.[79]

For all of the soot samples, the lattice fringe length decreases near the edge. While this may be due to interference from other particles that influence the average, careful examination of Figure 38 reveals otherwise. As the edge of the particle is neared, the extracted structure reveals fewer long lattice lengths and more indentations where no ordered structure can be seen. This may be due to the carbon not being oriented in the direction of the electron beam, so that the Bragg angle condition necessary for diffraction and viewing of the structure is not satisfied. However, these edge carbons may also be the area "blocking" layers observed in surface area studies of soot.[72, 74] The blocking layer appears to be structures that have not completely coalesced into an extended structure, although they are stable to highly thermal conditions (eg, the 1173 K devolatilization). Another possible explanation is that during formation of the soot, high temperature oxidation only effects the outer layers of the soot particle, leaving an imperfect structure at the surface of the soot particle.

We were unable to compare the interlayer spacing differences between the center and edge layers. Except for the unoxidized case, we were unable to experimentally measure any lattices in the center of the particle. This is either indicative that the interior of the particle has been preferentially oxidized, as indicated by Heckman and Harling,[68] who observed a hollowing out of particle cores during oxidation, or the center of the particle cannot be imaged due to the absence of Bragg conditions (see Appendix A). The untreated soot case had the same interlayer spacing of 0.344 nm between the center and edge of the soots, in good agreement with Marsh et al.[9] who found that the interlayer distances were the same in the core and the periphery of the primary particle. It is interesting to note that there is a considerable difference in the standard deviation of the spacing. We measured roughly twice as many fringes on the edge of the soot, yet the standard deviation increased from 0.014 nm in the center to 0.018 nm near the edge. This may indicate that the chemical species involved in formation of the soot differ between nucleation and outer edges, either in absolute size of the species or in its orientation. The difference may also be due to high temperature exposure time differences during formation, since the center of the soot particle is expected to a longer residence time during formation at higher temperatures than the outer edges, allowing for the system to adopt a more energetically favorable structure.

The differences between the untreated and oxidized soots show a difference between nucleation and growth species, which supports some formation theories. If one assumes that preferential oxidation takes place in the center, one can conclude that the center carbon solids involved are fundamentally different in either their structural or chemical properties. The concept that at inception the particles should be considered liquid droplets[80] would seemingly

only apply to the initial 1-2 nm particle due to the disordered, small lattice structure found in the center of the particle.

5.5 CONCLUSIONS

Differences in the carbon structure of soot has been shown to be a function of radius for unoxidized soot. Oxidation of the soot alters the structure of the soot. Near the center of untreated soot the structure is disordered with short lattice lengths predominating. As the radius increases, the fringe length increases, becoming more ordered. This ordering with radius increases as oxidation level increases. The increased ordering is caused by oxidation that allows reacts away blockages to internal ordering

The generation of a hole in center of the soot particles during oxidation agrees well with results of past researchers. If this is not a TEM artifact, this indicates that the species involved in the formation of soots differ between the center and edge of the soot particles. Furthermore, this hole generation would mean that there is complete penetration of the soot particle by oxidation, indicating that what few pores there are provide adequate diffusion pathways.

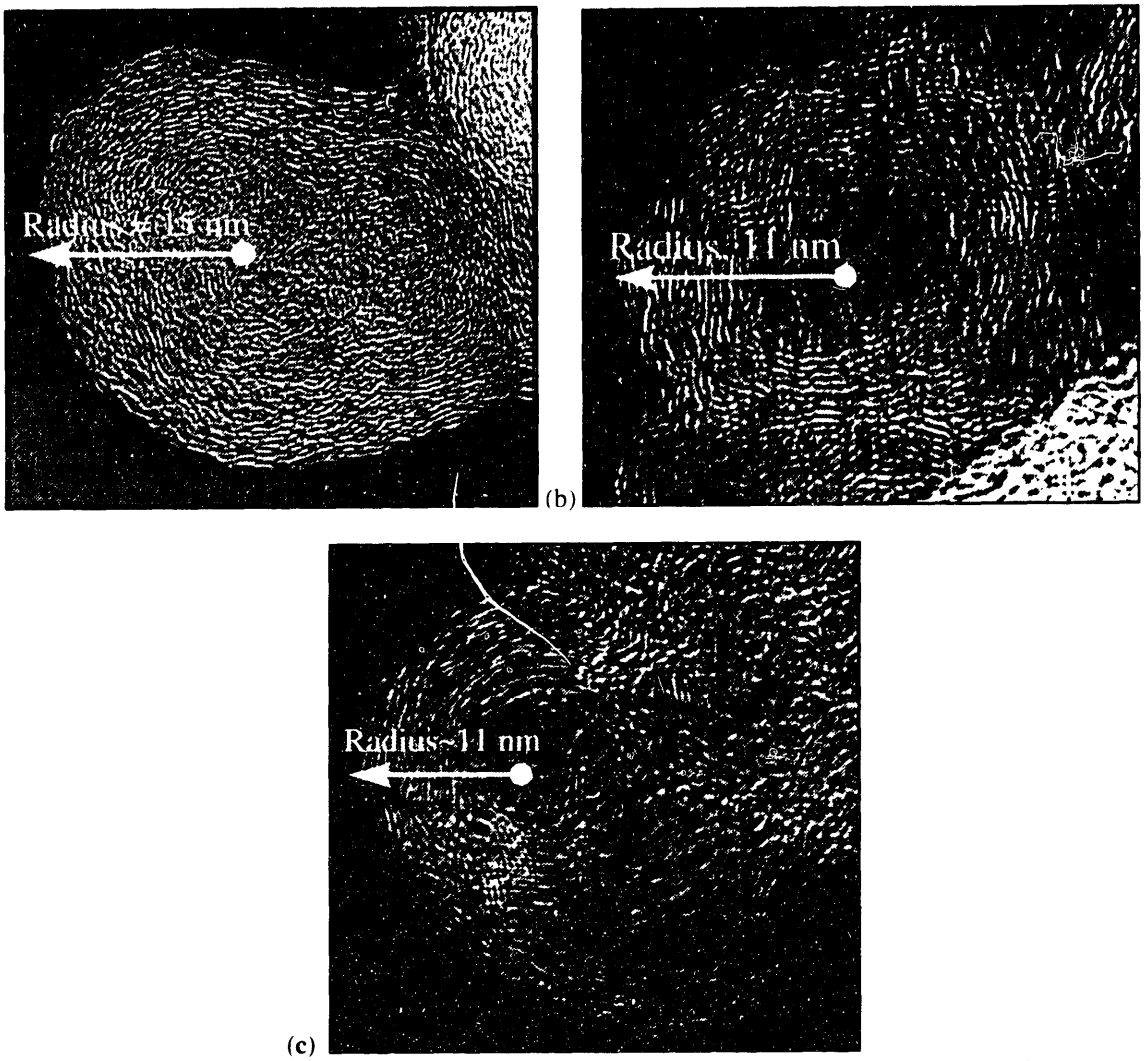

Figure 36. Digitized TEM images of soot. (a) Initial soot (b) Soot Oxidized at 500°C for 1 hour (Weight conversion = 70%); (c) Soot Oxidized 1 hr, 1500K(X ~40%)

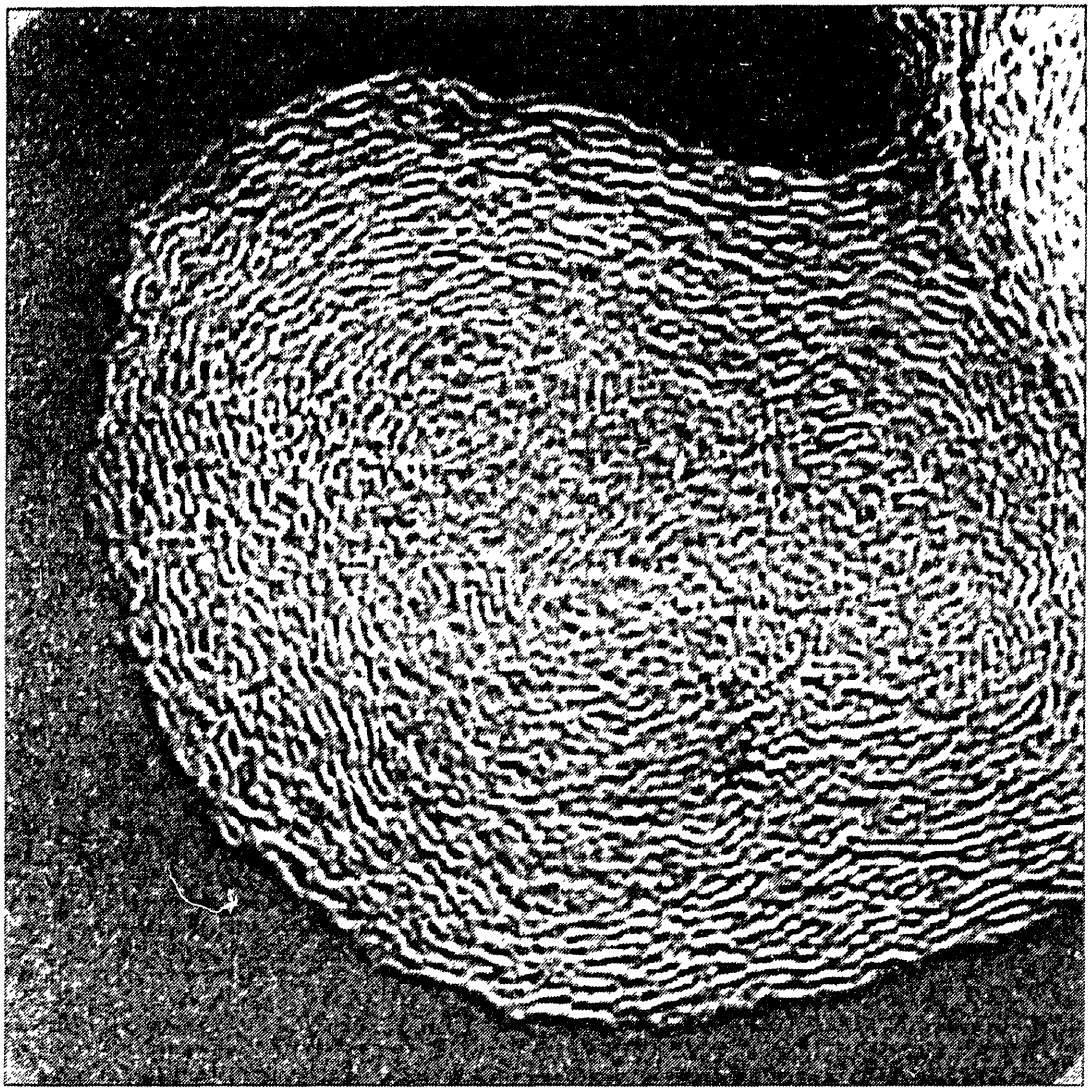

Figure 37. Isolated Soot particle of Figure 1a used for analysis.

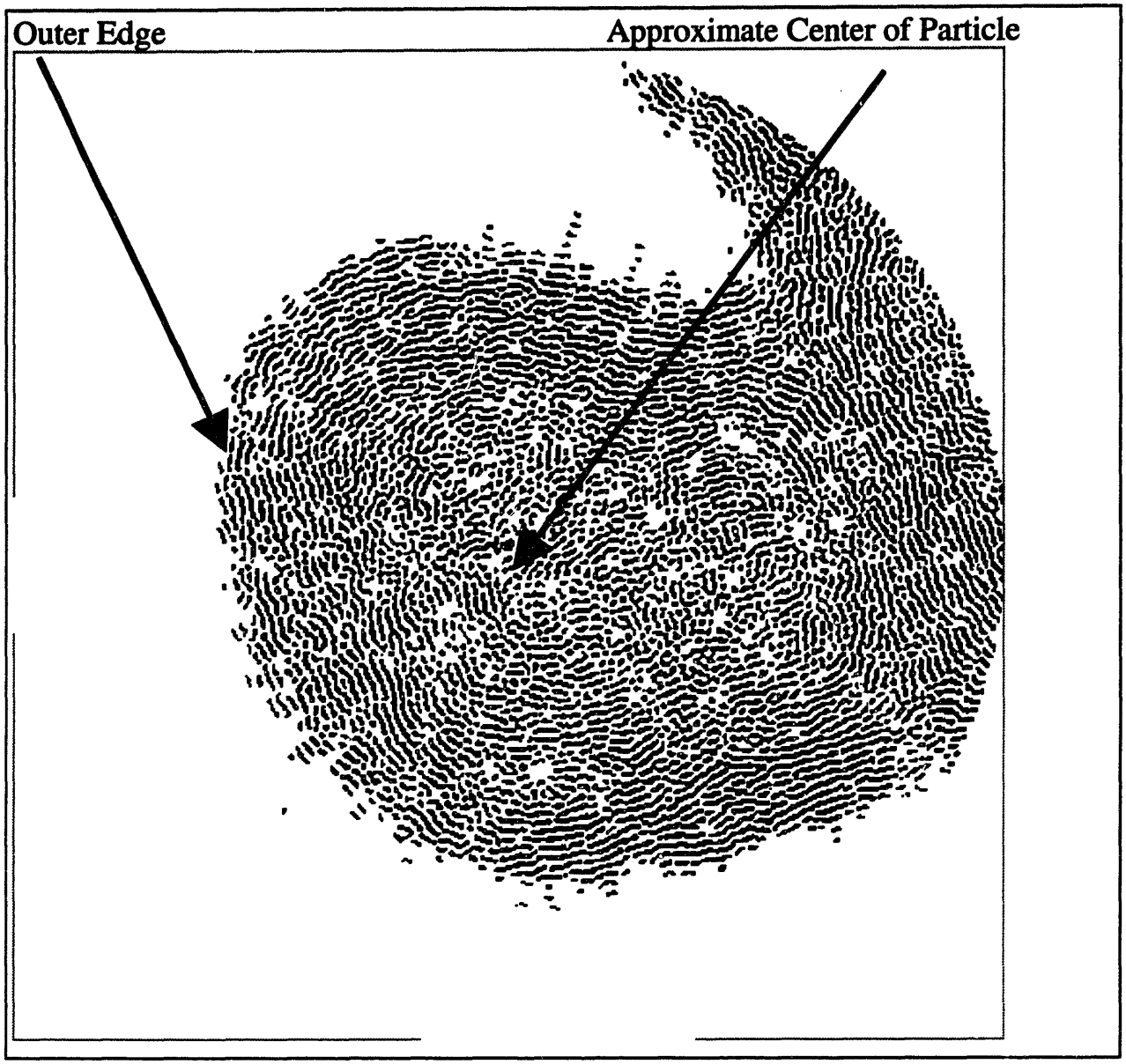

Figure 38 Extracted Structure of Figure 37 showing lattice fringes. The outer edge shows more variation than the middle shells.

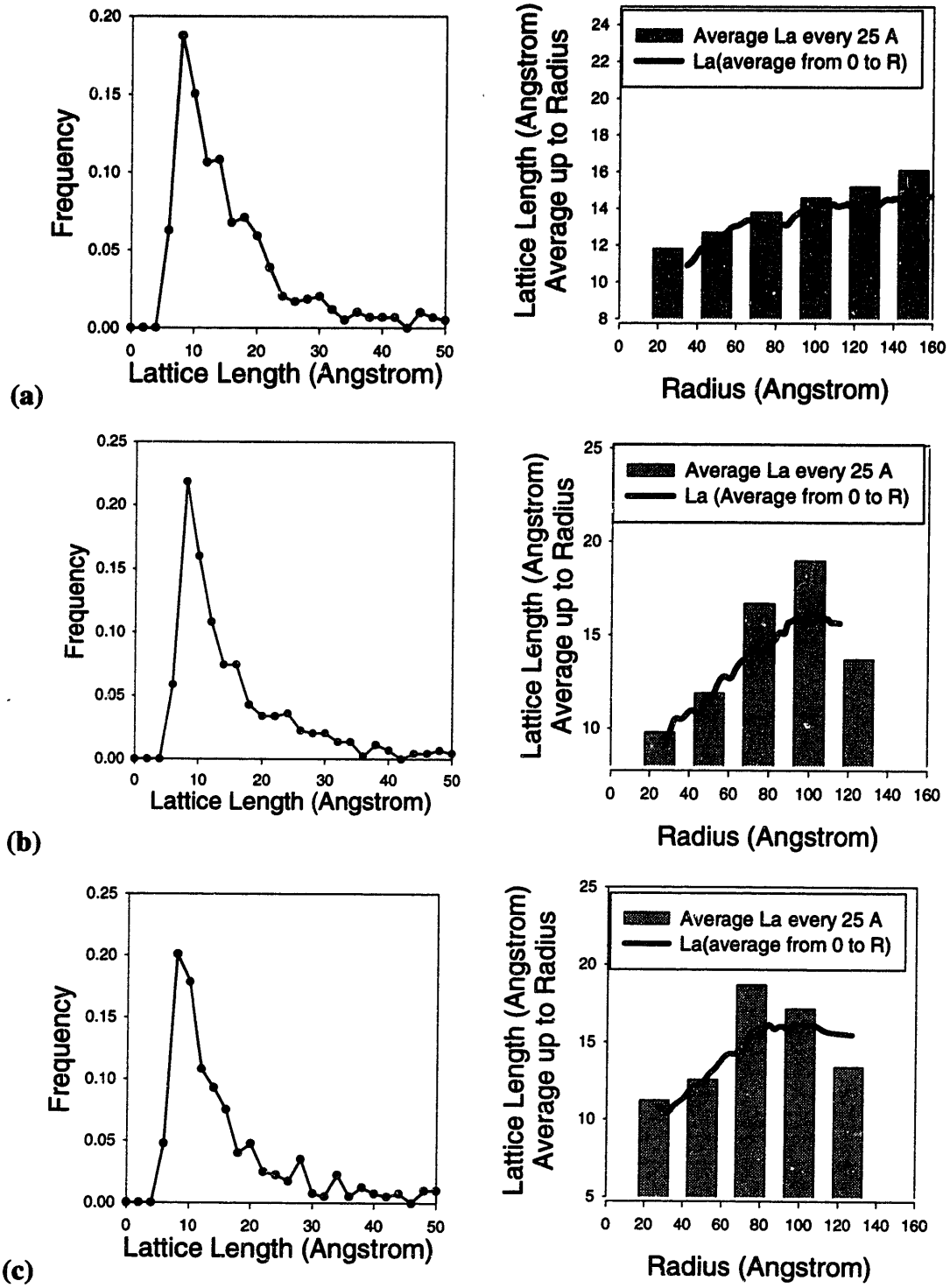

Figure 39. Overall distribution of lattice lengths for (a) base soot; (b) oxidized, 500 K; and (c) oxidized, 1500K.

CHAPTER 6

6. Structural Changes of Char Particles During Chemically Controlled Oxidation[c]

6.1 INTRODUCTION

Changes in particle structure during carbon oxidation are of importance because they can influence particle sizes and shapes, which in turn influence reaction times. Moreover, the changes in structure influence particle fragmentation, which affects combustion by changing the particle size, and has a major impact on the number and size of fly ash particles produced per coal particle[81,82]. There are several mechanisms of char fragmentation, including percolative fragmentation, in which oxidation increases the porosity until the interconnectivity of the solid matrix is interrupted; fragmentation resulting from the enlargement of macropores until they interconnect and the particle breaks up; and attrition, fragmentation resulting from mechanical forces acting on weakened parts of a char particle. Reports of fragmentation in the combustion literature date back to the study of Davis and Hottel[83] on the oxidation of carbon spheres and include the studies of Walker et al.[84] and Dutta et al.[85]

The focus in this chapter is on the changes in the particle structure during char oxidation in the chemically kinetically controlled regime (Regime I) and its impact on fragmentation. A useful reference point is percolation fragmentation, the theory of which has been developed for materials with a uniform pore size, for which various theories predict that the fragmentation occurs at porosities of around 0.7.[86] Kerstein and Niksa[86] carried out experimental

[c] Based on a paper published in the 26th Symposium (International) on Combustion, 1996.

measurements on large carbon disks, 52 mm in diameter and 1.5 mm thick, and observed that the samples disintegrated into very fine fragments at the predicted critical porosity. They showed that this process is reproducible. However, coal chars tend to have a wide pore size distribution, ranging from the micropores, having dimension of 2 to 3 nanometers, which account for most of the internal surface area to the macropores, having dimensions in the tens of micrometers, which often account for the major fraction of the porosity. For macroporous solids, the enlargement of macropores can lead to fragmentation as the particle continuity is interrupted. This was shown early for diffusion controlled reactions and, more recently, by Weiss and Bar-Ziv [87] and Zhang et al.[88] in synthetic char particles (Spherocarb) of 200 μm diameter reacting under chemically controlled conditions. Modeling of the combustion of char that includes aspects of pore enlargement connected to fragmentation was carried out by Kang et al.,[81] Salatino and coworkers,[89,90,91] and by Kantorovich and Bar-Ziv.[92,93] The problems in applying theory to chars are complicated by two factors. The first is the wide range of pore size distribution. The second is that the char particles shrink due to densification, a phenomena which has a major impact on particle porosity.

The purpose of this chapter is to present the structural changes during oxidation to high porosity of a synthetic char, Spherocarb. Spherocarb particles have the advantage of being essentially ash free and spherical, while having a high initial porosity in the range 60-80%, distributed approximately one-third/two-third between micro- and macro-porosity, respectively.[94] Studies of the structural change of Spherocarb were carried out in two laboratories: (i) at Ben-Gurion University, where single particle experiments were carried out in an electrodynamic[87,95] chamber; and (ii) at MIT, where TGA experiments were performed and

samples were characterized by high-resolution transmission electron microscopy (HRTEM). The results of these studies provide insights on how the macroporosity and microporosity evolve with increasing conversion under Regime I conditions and how this evolution impacts fragmentation.

6.2 EXPERIMENTAL

6.2.1 Electrodynamic Chamber (EDC) Experiments

Observation of the detailed process of fragmentation of single highly porous char particles in Regime I were carried out in an improved EDC. The EDC and its diagnostic systems has been described in detail in recent publications,[87,95,96,97] and will not be discussed here. In these experiments a particle was heated vertically from below by a CO_2 laser beam. The DC voltage, responsible for the levitation of the particle, is proportional to the vector sum of the gravitational, photophoretic and free convection forces.[87,95-97] The three forces were uncoupled by periodical interruption of the laser.[97] The DC voltage was measured every second by a data acquisition system and a CCD camera recorded continuously the shadow of the particle for size and shape measurements. Freeze-frame capabilities and shutter control facilitated the digital analysis of individual images. A Mutech corporation model IVP, frame-grabber board was used for image analysis. Size calibration was carried out by measurements of a 155 ±1 μm diameter wire, which was placed across the center of the EDC.

Particle density was measured at zero conversion by the drag force on a particle due to imposed flow, also described by Weiss.[87,95] Figure 40 (top) presents the ratio of the drag force to weight of a polystyrene particle and a Spherocarb particle (ΔV is a voltage difference of flow and non-flow voltages, and V_0 is initial voltage without flow). The line shape depends on the flow

field within the chamber (as has been shown by D'Amore et al.[98]) and the magnitudes are inversely proportional to ρd^{2}.[87] Since the density of the polystyrene is known, the density of the Spherocarb can be obtained from the slope of a plot of $(\Delta V/V_O)(\rho d^2)$ for polystyrene vs. $(\Delta V/V_O)d^2$ for Spherocarb as shown in the lower half of Figure 40, which yields a density for the Spherocarb particle of 579 ± 2 kg/m^3. This method is valid for spherical particles. During char oxidation, as the particles become aspherical, the density of particles are obtained from ratio of mass (obtained from the DC voltage) and volume (obtained from the images of the particle from two perpendicular angles).

6.2.2 TGA and HRTEM Measurements

Spherocarb particles at various conversions were produced by reaction in a thermogravimetric analyzer in air at a temperature of 773 K. Carbon conversions were determined by analyzing the weight versus time. The initial sample weight was approximately 10 mg.

For HRTEM observation, the oxidized samples were ground for 5 minutes in a ball mill or a mortar and pestle for higher oxidation samples were sample size was limited. The resulting powder was then ultrasonically suspended in ethanol and deposited dropwise on lacey carbon TEM grids(Ted Pella). An Akashi/TOPCON 002B transmission electron microscope with an LaB6 filament operating at 200keV was then used to record high resolution (590 kX) images of each sample.

The images were digitized, and an image analysis software (SEMPER6P, Synoptics Ltd., Cambridge, UK), developed specifically for applications to high resolution electron microscopy was used to manipulate the stored images in order to extract characteristic Spherocarb structure.

Characterization was accomplished using a Fourier Transform of the TEM images to establish periodicities. By then applying a mask to remove unwanted noise in the image, the annulus was reverse transformed to obtain a gray filtered image. This image was then converted to a two color 'extracted structure' by setting a threshold value for the pixel intensity. This extracted structure was the basis for the statistical analysis of the lattice length, L_a, and d_{002} carbon spacing.[99]

More than one hundred oxidation experiments were carried out in air and in pure oxygen, with moisture and without it, at temperatures varying from 700 K to 1000 K in the EDC for conversions up to 80%. Another twenty-two experiments were conducted up to nearly complete conversion. The experiments in the TGA were carried out in air at 773 K for conversions up to 96 percent. The structural transformations observed are summarized below.

6.3 RESULTS

6.3.1 Particle Size and Shape

In all experiments involving the EDC, the particle underwent non-uniform shrinkage. The initially spherical particle transformed into a disk at 50-60% conversion. It was observed that the particle rotated frequently up to about 40% conversion, with a consequent uniform shrinkage. At higher conversions, the particle only flipped occasionally and non-uniform shrinkage started, as observed previously.[87,96,97] The frequency of flips decreased noticeably when the particle evolved into a disk at about 60% conversion. At higher conversion (above

85%) the particle became one of the following three shape types: type I - a disk without a hole; type II - a disk with one or more holes; type III - an opened disk. Figure 41 shows the three types at high conversions (from two perpendicular sides) together with images of the initial particles.

In the TGA experiments, the particles maintained their spherical symmetry to high conversions (see Figure 43). The differences between particle shapes after oxidation in the EDC and the TGA are due to the non-uniform heating of particles in the EDC[97]. This non-uniform heating, induced by the laser directed from below, results in a preferential reaction of the lower side of the particle, and explains the shape and the flipping of the particle as it becomes unbalanced, and the eventual formation of a hole in the center.

The results in the EDC and the TGA both show the dramatic shrinkage of the particles at high conversions. This is consistent with the previously reported densification of carbon during Regime I gasification or oxidation[43,100]. The rationalization for the densification was that the oxidation or gasification reactions induced reorganization of the fine structure leading to loss of pores and contraction of the microporous regions. This hypothesis was tested in this study by the use of HRTEM to study the changes in micro structure of the char with increasing carbon conversion.

6.3.2 Fragmentation

The particles chosen for this study had high initial porosities (61 - 78%). From the percolation theory for particles with uniform pore sizes, the particles started with porosities exceeding the critical value or should have fragmented after very little conversion. For more than 100 experiments carried out with conversions up to 80%, none showed fragmentation. For

22 experiments (listed in Table 2) in which the conversion approached completion (up to 99% conversion), five particles experienced minor fragmentation, and about half developed holes in the center of the particle. A particle break up is shown in Figure 46, which presents a typical conversion vs. time curve with a sequence of shadowgraphs depicting the shape development of a Spherocarb particle of 204 micron diameter at various conversions, oxidized in air at T=920 K (experiment number e7-281, in Table 2). The particle conversion was obtained from the weight loss of the particle assuming that the charge remained constant, a good assumption at this temperature.[95] The initially spherical particle turned into a disk at about 60% conversion. Spatial dimensions of the particle are included in the figure. The projected images from two perpendicular directions at 88% conversion show that the disk diameter decreased to 0.75 of the initial particle diameter, while the thickness decreased to 0.62 of the initial diameter, and a hole appeared around the center of the disk. The hole grew with increasing conversion and, at about 98% conversion, evolved into an opened ring. Further burning caused the particle to break into two fragments. The image at this conversion shows one half of the broken ring. In fact, both halves were suspended in the chamber after fragmentation. These two fragments were oscillating around the center at a large distance from each other. Since only one could be suspended in the center, the field parameters (AC and DC amplitudes and AC frequency) were adjusted such that one of the fragments drifted away and the other was kept. This fragment continued to oxidize and eventually broke into two other fragments at higher conversion.

Table 2 summarizes the results of only the experiments that were carried out to high conversions. In these 22 experiments only five particles fragmented. One can see that fragmentation occurred only for those particles that developed opened disks—Type III particles.

However, not all particles that developed holes fragmented, but only those in which the progress of the reaction produced shapes in which the particle continuity was broken.

Fine Structure

The results of the images abstracted from the HRTEM using image analysis are shown together with the parent samples in Figure 43. The spacing between the fringes in the picture is around 0.34 nm, slightly larger than that expected for graphites. The images showed increased order with conversion. A quantitative measure of the increased order in the system is provided by the lattice length L_a of the 'graphitic planes' in each sample. These are shown in Figure 44 for the original Spherocarb and high conversion (95%) particles. At high conversions there is systematic increase in the fraction of large lattice lengths. The interlattice spacing also decreased slightly. The peak in the distribution function for the original Spherocarb particles was at 0.34 nm, whereas at the high conversion (95 %) the peak had shifted to about 0.33 nm (see Figure 45). This ordering of the micoporous structure has important ramifications for the fragmentation of the particles.

6.4 DISCUSSION

In order to understand the lack of fragmentation at high conversions in these experiments one needs to examine the separate behavior of macro and micro pores. Changes in total porosity of the particles versus conversion were obtained for six experiments from the changes in particle mass and volume. The initial values and final values of the porosities were obtained by assuming the dense phase had the density of graphite (2.2 g/cm^3), a reasonable assumption since the interlattice spacings of the Spherocarb were similar to that of graphite. The results in Figure 46, demonstrate that although the porosity increase is less than would be expected in the absence

of particle shrinkage, it is sufficient to provide final porosities in the range 0.83-0.87, in excess of the percolation threshold of about 0.7 for a homogeneous material.

If the material is considered to have a bimodal distribution, then one can assess the probability of exceeding the percolation threshold in either the macro-porous or micro-porous regions. With about one-third of the porosity of Spherocarb particles being in the micro-pores and two-thirds in the macro-pores,[95] the initial macro-porosity is in the range 40-50%, well below the critical value, and the micro-porosity is half that value. The results of Hurt et al.[94] show that the macro-features, including macro-pores, in chars shrink in proportion to the shrinkage of the entire particle; therefore, the macro-porosity is expected to stay constant during conversion. The micro-porosity will therefore increase but the values, obtained as the difference between the total porosity and the macro-porosities(~0.4-0.5), will always be well below the threshold value of 0.7. Therefore the lack of fragmentation of the Spherocarb particles even at high conversions can be explained by the bimodal pore distribution, by noting that the micro-porous and macro-porous regions maintain their integrity since neither reaches a porosity equal to the percolation threshold.

The formation of holes in the center of the particle was a result of the uneven heating of the particle resulting in the local acceleration of the reaction rate. When the holes break through the walls of the particle, a ring is obtained and the further selective reaction can result in the fragmentation for selected particles as was observed.

The results presented in this chapter on the changes in the macro-structure and micro-structure of carbons can provide guidance to the development and refinement of models (e.g,

references 88, 92, 94). These model improvements should include changes in the ordering that lead to shrinkage and the changes in the pore structure of chars with oxidation or gasification.

6.5 SUMMARY AND CONCLUSIONS

The data that was obtained in the EDC showed that fragmentation is of less significance than might have been inferred from simple percolation theory. The information on the micro-structure of carbons provides insights on the reordering of the carbon structure which results in the densification of the chars and the preservation of the structural integrity of particles. No fragmentation was observed in the entire Spherocarb particle structure in numerous experiments carried out in the EDC. Experimental porosity data show that the total porosity increased from initial values of 0.6-0.76 to final value of 0.83-0.88. For the initial polymodal pore size distribution of Spherocarb, the macro-porosity is well below the critical porosity of 0.7. Therefore, consumption of carbon inside the particle was compensated by reordering and shrinkage so that the percolation threshold is not attained for the entire particle. It was observed that holes were formed at 65% to 96% conversion in thirteen experiments. These holes are a consequence of non-uniform rate of reaction obtained under non-uniform laser heating. The expansion of such holes led to fragmentation in a few cases, but this mechanism of fragmentation is quite distinct from percolative fragmentation.

Evidence is provided from the examination of the microstructure of particles at different conversion that the shrinkage is the result of the increased ordering of the graphite-like microstructures in carbons with increased carbon conversion. The change in microstructure will be discussed in detail in the next chapter.

Table 3. Summary of results of Spherocarb particles oxidized in EDC, in air at various temperatures (values in parenthesis in density column is porosity in %), where T is temperature, d_o is initial diameter, ρ_o is initial density, ε_o is initial porosity.

Exp. no.	T (K)	d_o (μm)	ρ_o (g/cm^3)	ε_o	Hole formed at conversion	Fragmented at conversion	Shape type at final burnout
e7-271	930	247	0.76	0.65	83.8	89.8	3
e7-273	880	172	0.58	0.74	86.1	none	3
e7-281	920	204	0.59	0.73	87.7	97.5	3
e7-312	900	176	0.59	0.73	none	none	1
e7-314	900	177	0.71	0.68	none	none	1
e7-315	940	200	0.78	0.64	95.9	none	2
e8-11	910	198	0.61	0.72	none	none	1
e8-12	940	189	0.45	0.80	70.9	95.1	3
e8-14	860	206	0.50	0.77	90.8	none	2
e8-21	850	212	0.58	0.74	91.0	none	2
e8-22	880	215	0.85	0.61	none	none	1
e8-23	870	187	0.78	0.65	none	none	1
e8-24	910	205	0.48	0.78	66.3	none	2
e8-31	870	219	0.68	0.69	none	none	1
e8-32	850	176	0.71	0.68	66.0	none	2
e8-33	970	187	0.63	0.71	82.8	none	2
e8-34	940	186	0.69	0.69	none	none	1
e8-41	920	185	0.51	0.77	none	none	1
e8-51	930	185	0.56	0.75	91.1	92.6	3
e8-52	900	177	0.53	0.76	none	none	1
e9	780	205			86.0	97.0	3
e10	830	205	.579	.74	64.7	none	3

Type 1 is a disk without a hole.
Type 2 is a disk with one hole or more.
Type 3 is a disk that opens.

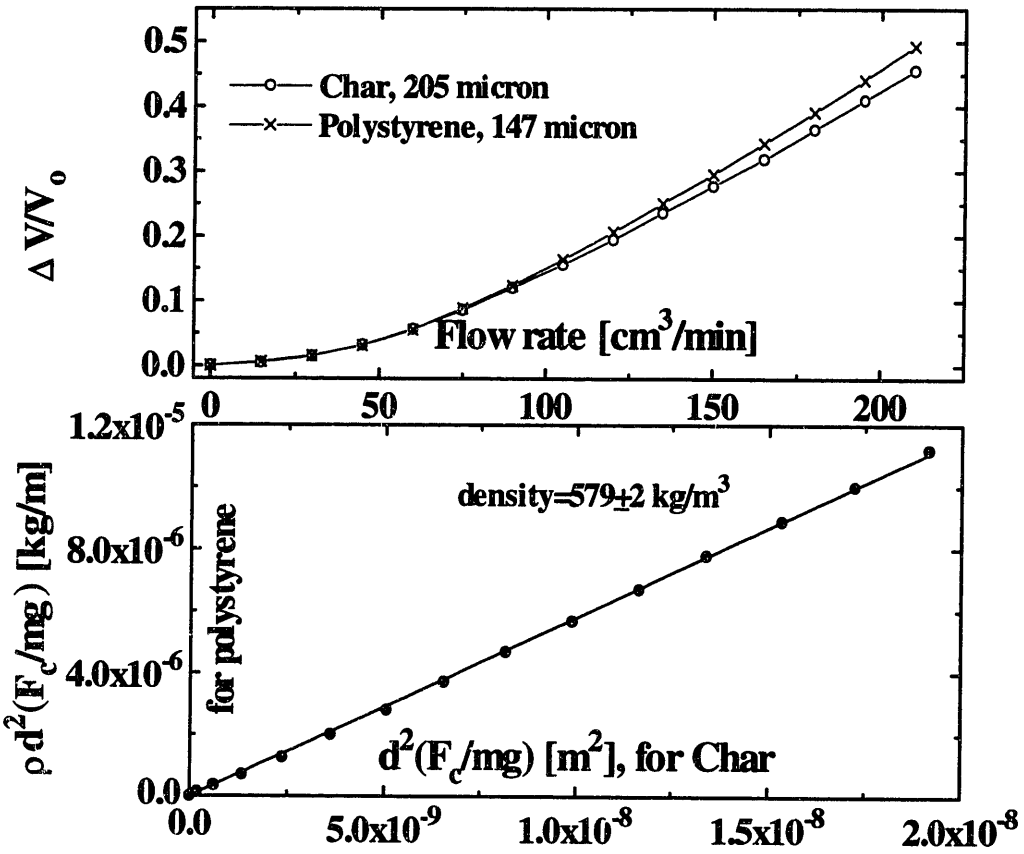

Figure 40. Top - ratio of drag force to weight ($F_d/mg=\Delta V/V_o$) vs. flow rate for polystyrene particle (x) and for Spherocarb (o) particles. Bottom - $(F_d/mg)\rho d^2$ of the polystyrene particle vs. $(F_d/mg)d^2$ of the char particle, and best fit (solid line).

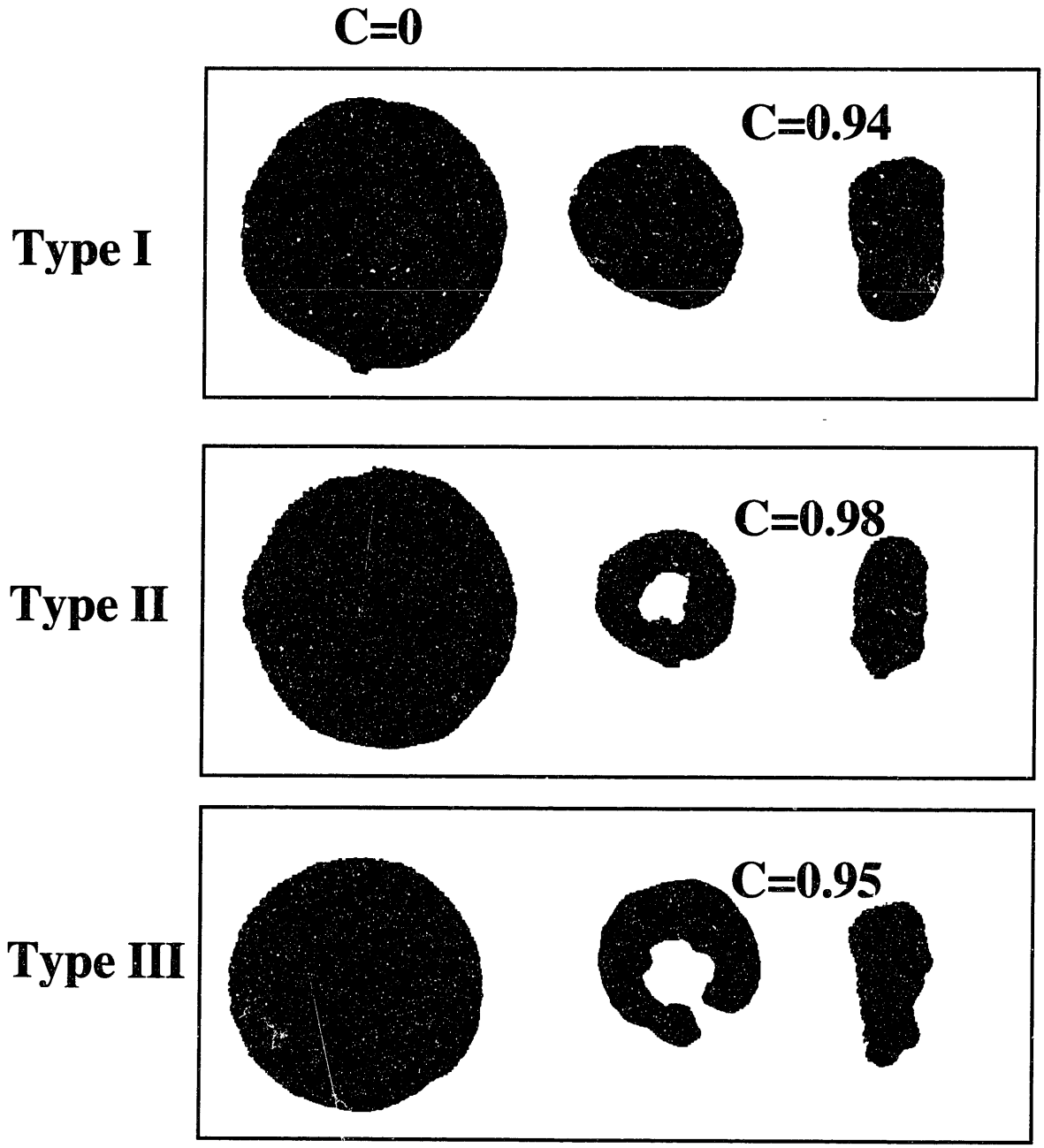

Figure 41. Examples of three types of shapes of initially spherical particles at high conversion. Type I - a disk without a hole at 94% conversion. Type II - a disk with one hole at 98% conversion. Type III - an opened disk at 95% conversion. The left sides of each panel are the initial particles, while the right sides are the particle from two perpendicular sides at high conversion.

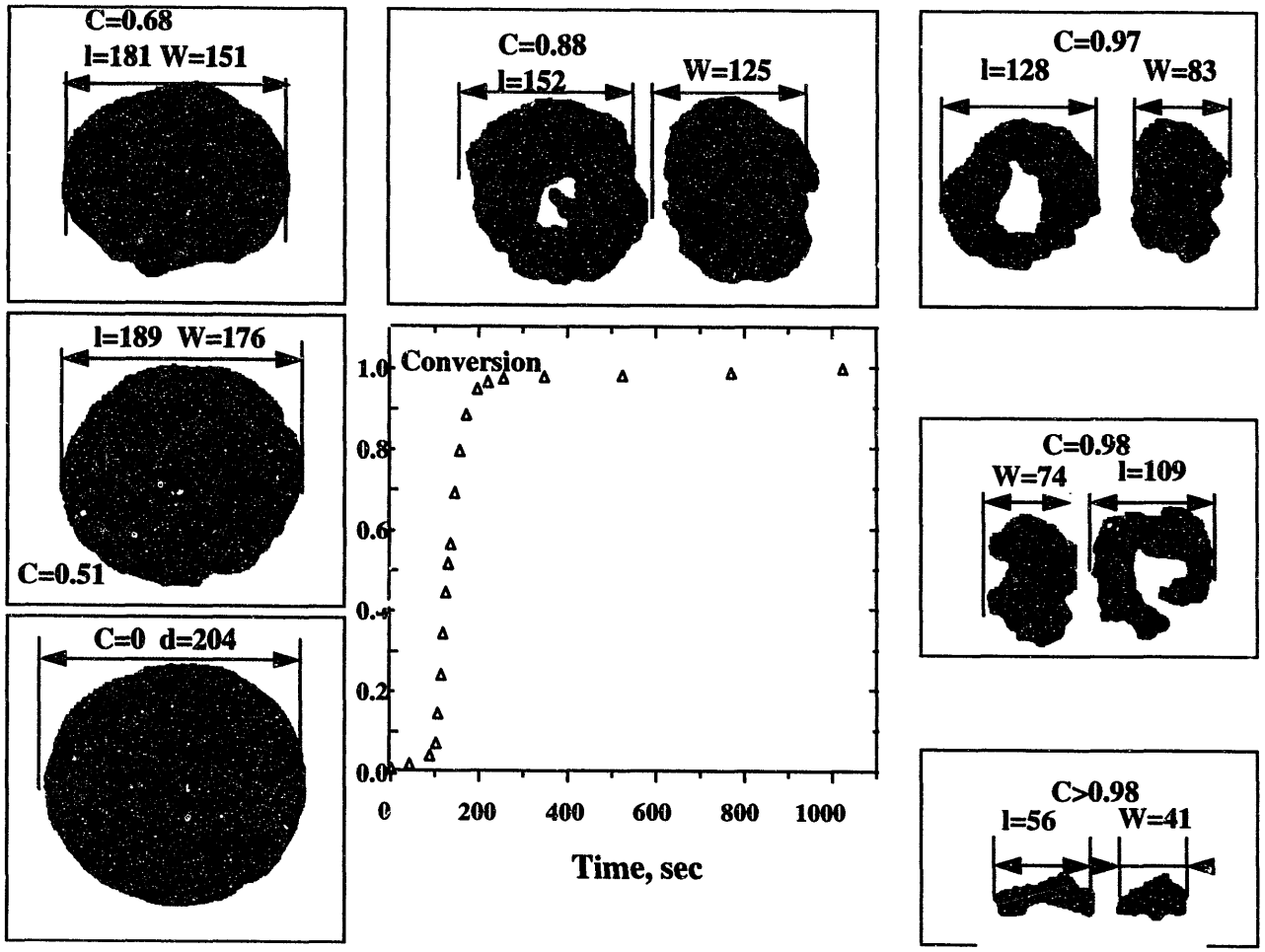

Figure 42. Conversion versus time and a sequence of shadowgraphs presenting the evolution of shape of a 204 μm Spherocarb particle oxidized in air at 920 K as a function of conversion; C is conversion, l is length, and w is width in μm.

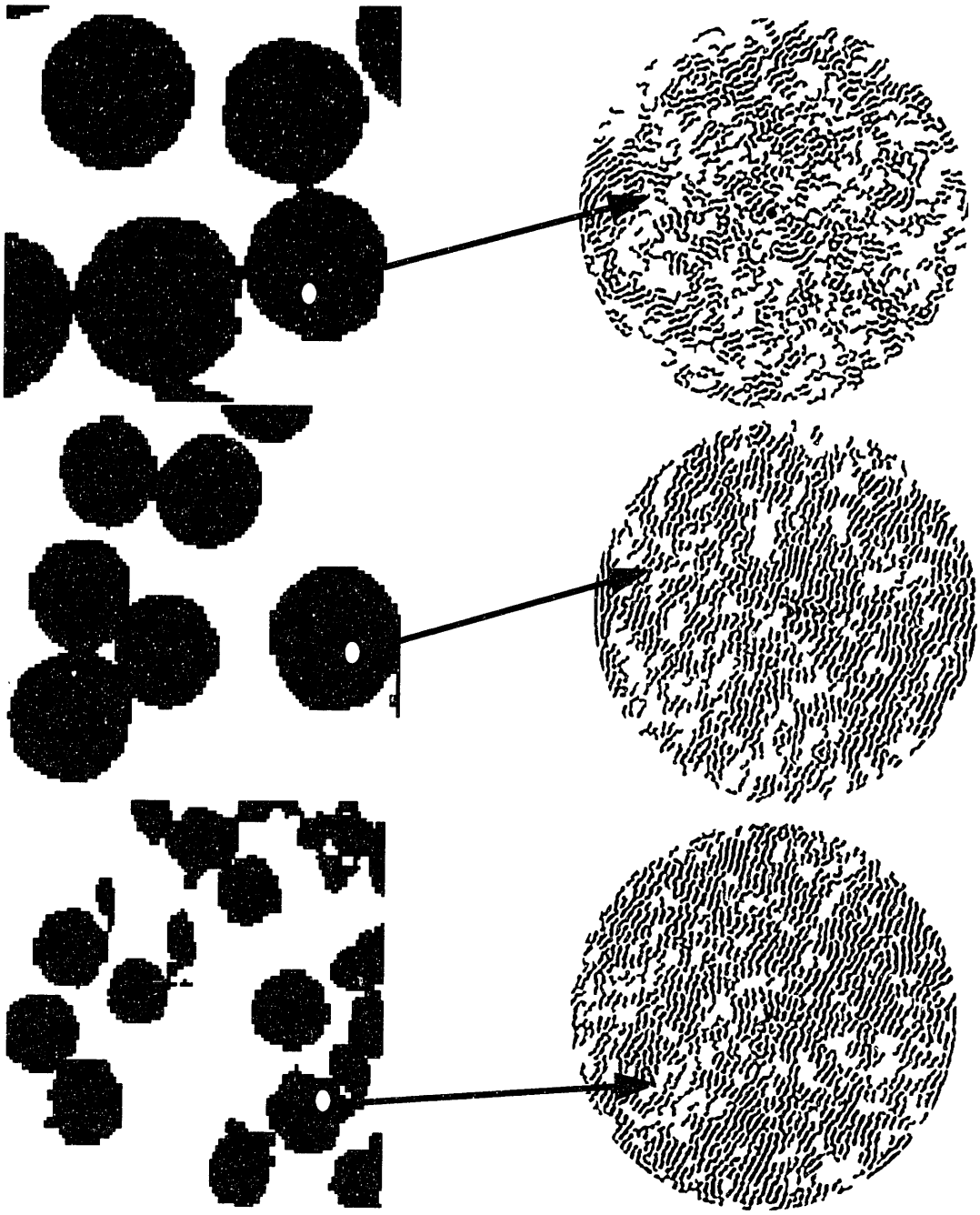

Figure 43. Shadowgraphs of Sphercarb Particles (initial diameter 160 μm) reacted in air at 773 K and the HRTEM structures for each sample: top, 0% conversion; middle, 44% conversion; bottom, 95% conversion.

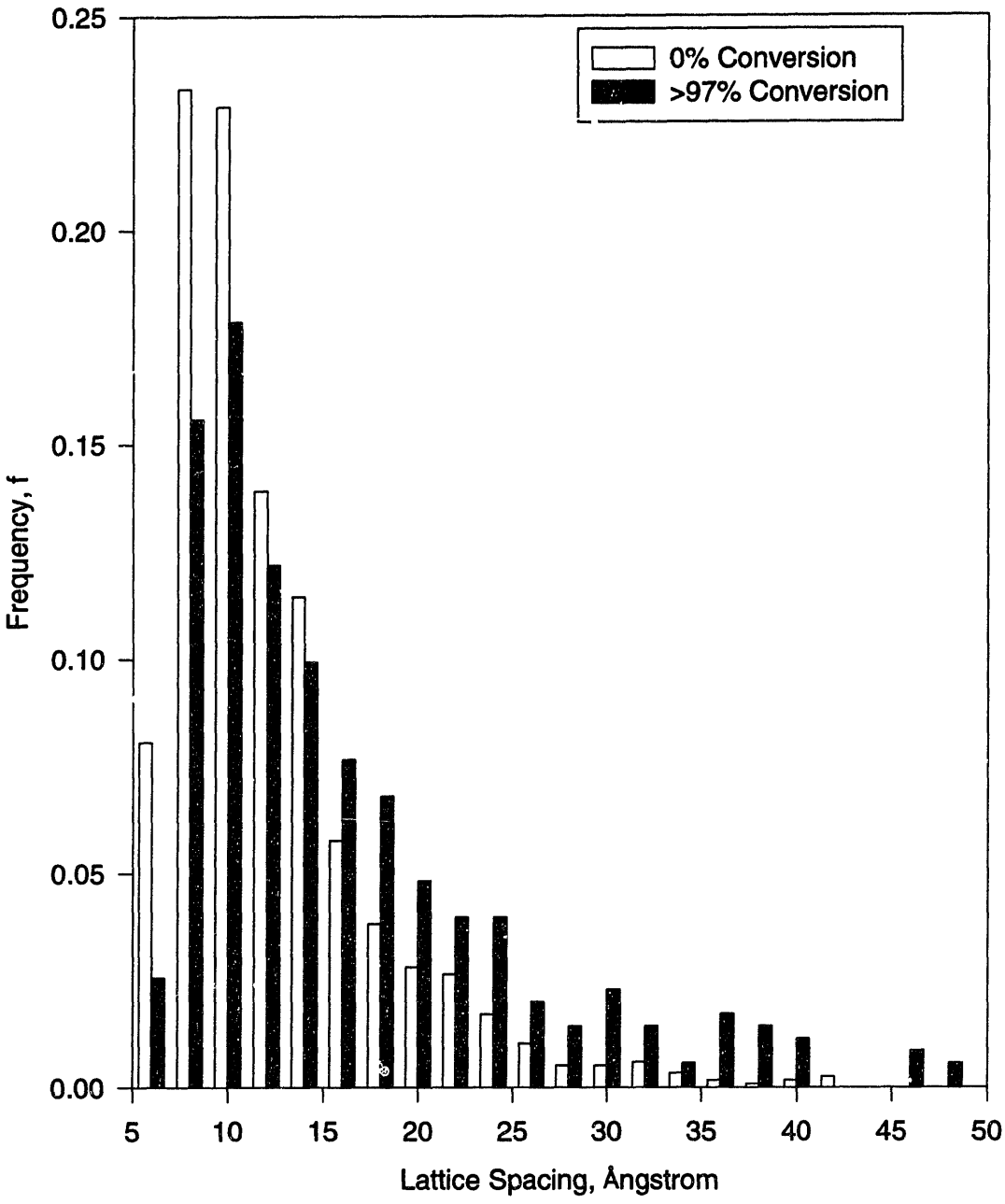

Figure 44. Distribution of lattice lengths L_a(in Å) for Spherocarb particles at zero and greater than 95 percent conversions by oxidation.

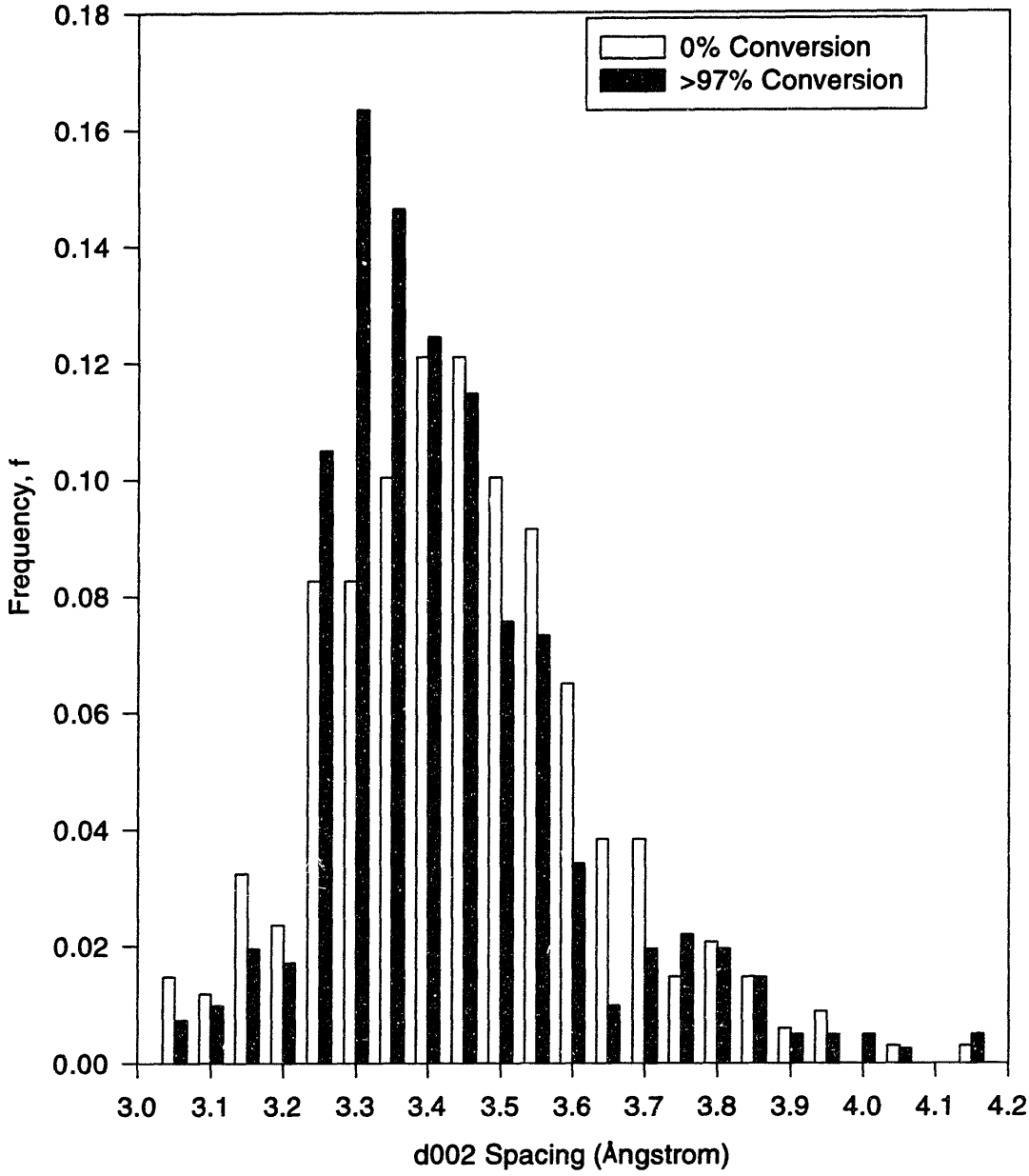

Figure 45. Distribution of interlattice spacings d_{002}(in Å) for Spherocarb particles at zero and greater than 95 percent conversions by oxidation.

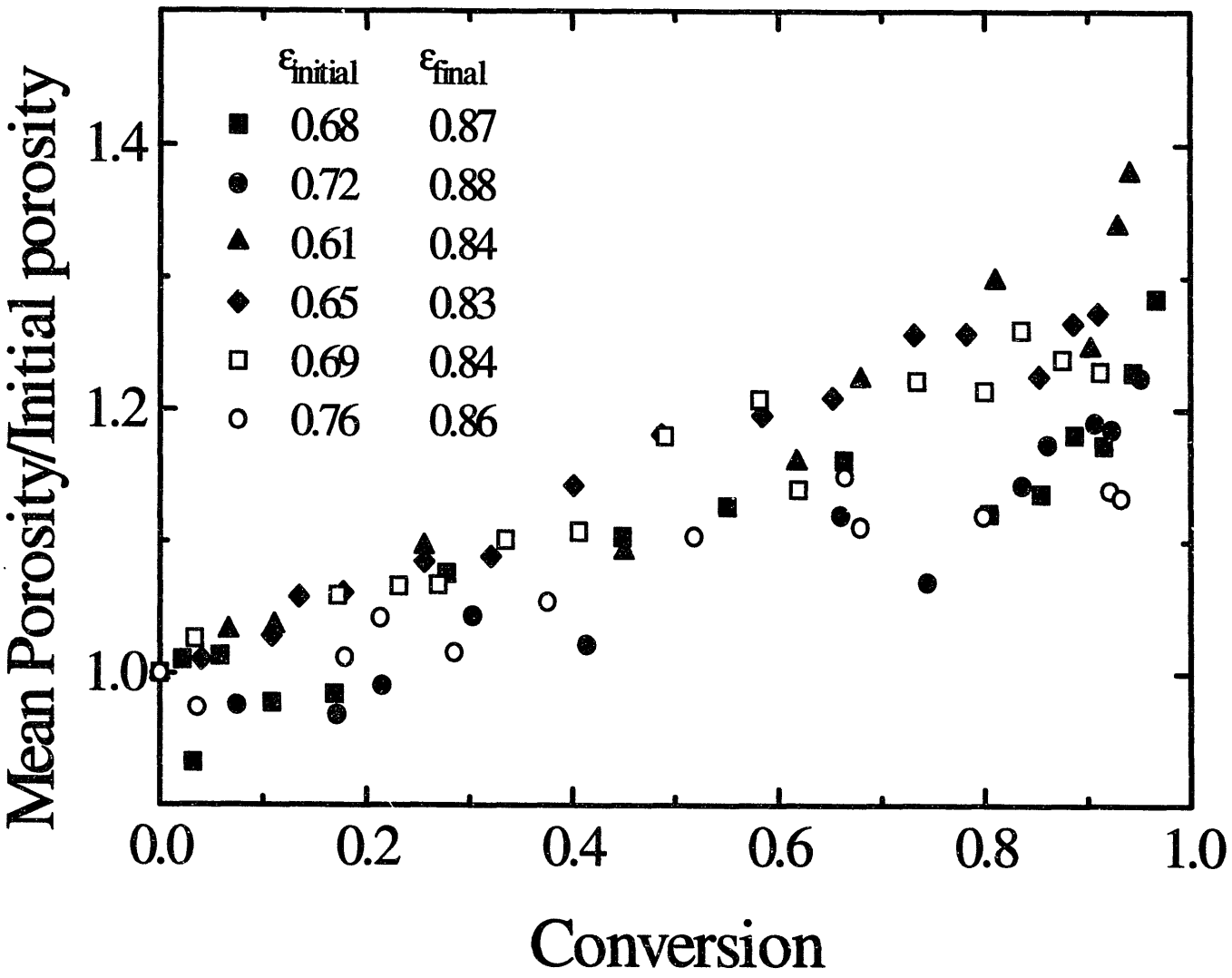

Figure 46. Ratio of porosity to initial porosity versus conversion. Initial and final porosities are indicated in the figure.

CHAPTER 7

7. Effect of Carbon Microstructure on the Rate of Low Temperature Oxidation

7.1 INTRODUCTION

The combustion of coal char can, depending on char temperature, occur in three regimes. At low temperatures, the reaction rate is controlled by the kinetics of the surface reaction of carbon with oxygen. The oxygen can diffuse throughout the pores of the particle faster than the surface reactions, so the oxygen concentration is uniform throughout the porous particle (Regime I). At intermediate temperatures, the reaction rate increases to the point that diffusion of oxygen through the pores is comparable to the surface reaction (Regime II). At even higher temperatures, the reaction rate is controlled by boundary layer diffusion to the particle surface (Regime III). In Regime III, only a thin layer of char will oxidize, leading to the classic shrinking sphere model. In Regime I, the carbon loss will occur uniformly so that diameter stays essentially constant while the density decreases linearly until conversion is nearly complete. As oxidation nears completion, percolative fragmentation will begin to occur at about 70% conversion (although for Spherocarb this limit is much higher, as seen in Chapter 5).[86]

In char oxidation studies at temperatures low enough (T < 900 K) to be in Regime I, Hurt et al[100] observed that some chars, notably Spherocarb and sucrose char, did not gasify at a constant diameter as expected, but instead "shrank." Shrinkage has been observed in various other studies[101,102,103] for highly porous synthetic chars oxidized in regime I. It has been shown[104] that shrinkage is a general phenomenon occurring for a variety of carbonaceous

materials for feature sizes ranging from tens of nanometers[105] to 70 mm.[106] The observed shrinkage either means that the coal structure has changed, as postulated by Hurt and others, or that the particles did not burn in the kinetically limited regime. Hurt et al. also observed that external features, such as the diameters of surface pores, decreased in size at the same rate as the particle diameter. If the reaction was occurring without shrinking, the pore diameters would be expected to enlarge as the particle reacted.

Hurt et al.[104] speculated that as the char loses carbon, atomic rearrangements account for the loss of pore volume in the fine pores. These atomic rearrangements lead to the graphitization accompanied by an increase in the density. This is consistent with the observation of Levendis et al.[107] that little graphitization occurred when synthetic char was heated in nitrogen. However, oxygen accelerated the graphitization of the synthetic char, and this graphitization increased as oxidation temperature was increased. Thus, there is evidence that as chars react in oxygen, the carbonaceous material undergoes graphitization.

The extent of graphitization is of importance to the modeling of char oxidation. Oxidation of graphite occurs mainly at the prism faces in uncatalyzed reactions, although basal plane defects cause pitting corrosion, creating additional prismatic faces during gasification.[108] It has been found that the reactivity of graphite prism planes is an order of magnitude higher than for that of the basal plane.[109] Suuberg showed that the graphitization (heat treatment at $T > 2500$ K) of coals will, in general, decrease the reactivity of the carbons, as well as showing a decreasing the surface area with increasing heat treatment temperatures. Davis et al.[110] found that for pulverized coal ($T > 1800$ K) oxidation, three dimensional graphitization did not occur due to insufficient reaction time, but rather graphitization lead to the growth of regions of

turbostratic order. This growth in turbostratic order was accompanied by decrease in char reactivity.

Using techniques recently developed to quantify high-resolution transmission electron microscopy (HRTEM), one can examine the microstructural changes of Spherocarb during oxidation. This chapter examines the microstructural evolution of Spherocarb for oxidation in Region I, and using simple population balance modeling, derives the differences in lattice oxidation rates as a function of oxidation, and give possible explanations for the change in reactivity with conversion.

7.2 EXPERIMENTAL METHOD

Spherocarb particles were oxidized isothermally to different extents of conversion at 773 K in air (flowing at 100 ml STP/min) using a Cahn 2000 TGA with attached data collection equipment. Carbon conversions were determined by analyzing the weight versus time, starting from an initial sample weight of approximately 10 mg. An analysis of the Spherocarb used in these experiments is given in Table 4.

Table 4. Spherocarb Properties.

Average bulk density (g/cm^3)[111]	0.56-0.63
Helium density (g/cm^3)[111]	2.10-2.15
BET Surface Area (m^2/g) [111]	860-1000
CO_2 Surface Area (m^2/g)[112]	870
Carbon Content (%)[113]	96.84
Hydrogen Content(%)[113]	0.73
Oxygen Content (by difference) (%)[113]	2.43
Ash Content (ppm)[14]	760

For comparison purposes, X-ray diffraction analyses were performed on the initial Spherocarb with a Rigaku diffractometer equipped with a rotating copper anode ($\lambda = 0.154$ nm). The ground Spherocarb was mounted on low-background quartz. The samples were corrected for background noise by subtraction of a baseline measurement, an accurate enough method for amorphous materials.

An Akashi/TOPCON 002B transmission electron microscope with an LaB_6 filament (spherical aberration coefficient of 0.5 mm) operating at 200 keV was used to record high resolution images of each sample. The light field images provide detailed information on the crystalline structure of the carbon materials. The resolving power of the HRTEM allows one to distinguish individual graphitic layers oriented perpendicular to the image plane, and if properly focused, to extract information on the interlayer spacings. The lattice-fringe images yield information on the degree and nature of crystallinity in the carbons. Usually, HRTEM requires the generation of thin sections that are difficult to prepare. For this HRTEM study, optically thin regions of char particles were prepared grinding the sample for 4 minutes in a ball mill previous to any oxidation in order to minimize possible grinding artifacts. After grinding and oxidation in the TGA, a small portion of each sample was ultrasonically suspended in ethanol and deposited dropwise on a lacy carbon TEM grid. Thin edged sections of sample were found at moderate magnifications (see Figure 51), and then photographed at high magnifications (590 kX), Representative samples are reproduced here for discussion (Figure 52 and Figure 53)

To calibrate the microscope, an oriented gold crystal was used and subjected to the same image analysis techniques as the Spherocarb samples. The use of a specifically "oriented" gold

crystal allows only the lattice locations in one plane to be diffracted. Then, precise measurements of the lattice distances may be made and compared to the experimental samples.

After HRTEM imaging, quantitative information on the structure of the particles was determined by measurements using commercial software (SEMPER 6P,™ Synoptics, LTD., Cambridge, UK). The samples were digitized with a UMAX Powerlook II model scanner (scanning resolution 1200 dpi, 993 used). The high level language computer software, SEMPER 6P,™ developed especially for use with high resolution electron microscopy, was used to manipulate the stored images in order to extract data for each Spherocarb sample. From these digitized images, optical diffraction patterns were generated. The optical diffractogram is a power spectrum calculated from the modulus of the Fourier transform.

The power spectrum provides an important check of the instrumental defocus. Millward and Thomas[114] indicated that quantitative interpretations cannot be justified except under rigorous conditions of microscopy (correct defocus) which generate adequate contrast-transfer properties in the electron-optical system. Crawford and Marsh[115] and Johnson and Crawford[116] emphasized this by showing that serious artifacts may arise in carbon-fringe images at improper defocus, usually in the form of contrast reversals and information gaps. The power spectrum also provides a check for proper astigmatic correction, as the randomly oriented Spherocarb should not show orientation preferences.

Intensity profiles characteristic of the contrast range of the diffractograms were then produced. A series of "filters" was also applied to the digitized images to extract only the significant structural data (between 0.3 and 0.5 nm in spacing) from the image while eliminating unwanted characteristics. This then becomes the basis for statistical analysis of the structures.

The parameters that can now be quantified are the lateral extent of fringes (L_a), fractional coverage (C), and interlayer spacing (d_{002}). The lateral extent of fringes is defined as:

$$L_a = A \cdot B \sqrt{m_{max}} \tag{23}$$

where m is the principal second moment of area. The second moment is the mean square of all pixels about a line through the center of area of a structural element (fringe). The principal second moments are the second moments with respect to a pair of mutually perpendicular axes in directions that achieve maximum and minimum moments. The constant A represents the carbon fringe shape factor that was found to be 3.56 pixels.[128] The constant B is the pixel/Angstrom conversion factor, equal to 0.4336 A/pixel for a scanning resolution of 993 dpi. To get the characteristic interlayer spacing value for the sample, first the total area of fringes was determined with minimal filtering, which corresponds to eliminating repeated frequencies below 0.3 nm and above 0.5 nm. Then, in order to eliminate possible differences in sample image illumination, the intensity range was narrowed and shifted to a position in which the area of fringes showed a maximum. The fractional coverage is then simply the ratio of total area of fringes in this two-color image with the maximum to total area of image,

$$C = \frac{\text{Area of Dark Fringes}}{\text{Total Area Processed}} \tag{24}$$

The fractional coverage is typically in the range of 25-35%. Of the parameters tested, the fractional coverage is the measurement most subject to user "bias," as it is a strong function of the area chosen, and can only be used as a parameter in well defined situations.

The best method for determining the characteristic interplanar (d_{002}) spacing for a sample has proven to be calculation of the distance between parallel fringe pairs.[117] As a first step, the fringes, from the intensity calculations above, are filtered to remove pairs that are not within a

physically realistic distance from one another (in our case, 0.3-0.5 nm, although most d_{002} spacing is between 0.33 and 0.42 nm). Each fringe I is characterized by a center of area P_I and the orientation of its long axis, α_I. The calculation of the distance d_i between the parallel fringes i and i + 1 is then performed with the following formula

$$d_i = \frac{m_i \cdot (x_{i+1} - x_i) - (y_{i+1} - y_i)}{\sqrt{m_i^2 + 1}} \tag{25}$$

$$m_i = \tan\left(\frac{\alpha_i + \alpha_{i+1}}{2}\right) \tag{26}$$

where (x_i, y_i) and (x_{i+1}, y_{i+1}) are the coordinates of P_i and P_{i+1}, respectively. This calculation is repeated for as many pairs as possible in order to obtain statistically meaningful values. The interplanar spacing can then be specified by a mean and standard deviation, or a distribution function if there is more than characteristic peak. An example of the lattice and d_{002} spacing is given in Figure 47, while full details of this technique may be found in Palotás.[128]

7.3 RESULTS

A typical weight loss curve is shown in Figure 48 for the complete oxidation of Spherocarb. The calculated reactivity of the Spherocarb is given in Figure 49 for normalization by both initial weight and instantaneous carbon content, along with the Spherocarb surface area determined by Dudek.[118] The intrinsic reactivity of the Spherocarb may be calculated by assuming complete penetration of the Spherocarb particles, and dividing by the surface area, and is given in Figure 50. The initial weight normalization oxidation rate of 3 mg/g_0-min agrees well with the data reported by Hurt[62] and Gavalas[64] for Spherocarb, with a high degree of repeatability. As plotted in Figure 50, the reactivity, when normalized for remaining amount of carbon, actually goes up during reaction. This plot shows an initial induction period (thought to

be due to water desorption[119]) where reactivity increases rapidly, followed by an increasing reactivity rate.

Typical TEM micrographs for each Spherocarb conversion level examined with the HRTEM are given Figure 52 and Figure 53, showing the turbostratic structure of Spherocarb at 0, 25, 50 and 75% oxidation. Circular portions of Figure 52 and Figure 53 were masked off using the image analysis software in order to isolate sections for analysis. A power spectrum was then generated from the image to show the periodicities present in the Spherocarb sample. The images were further manipulated by applying filters to extract only the significant structural data from the image while eliminating any unwanted characteristics. The masked section, power spectrum, and extracted structure are shown in Figure 55 through Figure 58 for each of the conversion levels.

The images of Figure 55 through Figure 58 are representative of the turbostratic carbon in the system. As noted by Mitchell[120] in cleaved samples of Spherocarb, there is thought to be a layer of graphitic/denser "skin" around the Spherocarb. This notion is further supported by work of Radovic and coworkers, who have noted the possibility a characteristic breakthrough that could be explained as arising from a graphitic type shell in ^{129}Xe NMR adsorption studies.[121]

A possible section of this layer is shown in Figure 59, where a sheet of graphitic carbon is visible with approximately 5-8 layers of graphitic carbon. Assuming that this skin coats the entire outer surface area of the Spherocarb, the actual mass ratio of this layer to the rest of the Spherocarb is only:

$$R_{GT} = \frac{\rho_{sphero} V_{Spherocarb}}{\rho_{graphite} A_{spherocarb,outer} L_{stack}} \approx 3.1\% \qquad (27)$$

Since this percentage is quite low, we concentrate only on the turbostratic carbon by selecting only on these areas in the microscope.

Representative lattice fringe length, fractional coverage, and d_{002} spacing distributions derived with the Spherocarb extracted structures are given in Figure 60 through Figure 63 respectively, and summarized in Table 5. It is important to note that in order to minimize variations that could arise locally in the Spherocarb, these distributions are based on a minimum of 3 observed regions, typically 2 from the same electron micrograph and an additional area as a check. The results of multiple samplings at the same conversion level is shown Figure 64 as a function conversion level. There is a great deal of scatter in the data, although the increasing lattice fringe length and mildly decreasing d_{002} spacing are evident. For comparison purposes, x-ray analysis was performed on the 0% conversion Spherocarb. The result of this analysis is given in Figure 65.

Conversion Level (%)	Average Lattice Length (nm)	d_{002} Spacing (nm)	Fractional Coverage (%)
0	1.11	0.374 ± 0.02	21.9 ± 1.1
25	1.20	0.369 ± 0.02	22.8 ± 0.6
50	1.29	0.367 ± 0.024	23.4 ± 1.0
75	1.47	0.361 ± 0.023	24.5 ± 0.9

Table 5. Average Spherocarb properties as a function of conversion

The average lattice fringe length, $L_{a,avg}$ shown in Figure 60 increases with increasing extent of oxidation. As plotted in Figure 60, most of the change in lattice structure occurs in the range of 1 to 2 nm. The greatest change in lattice structure occurs at 1.0 nm, where the fraction of lower lattice lengths decreases during oxidation, and is one of the primary causes of the increasing average lattice length from approximately 1.1 nm at 0% conversion to 1.5 nm for 75% conversion. Marsh et al[122] observed a similar increase in the lattice structure of petroleum coke, with L_a going from approximately 1 nm to 2.5 nm for heat treatment temperatures of 750 K and

1148 K respectively. Levendis et al[123] also noted an increase in lattice length with increasing oxidation temperatures for glassy carbons, with lengths increasing from 2.6 nm for temperatures of 1400 K to 3.7 nm for temperatures of 1600 K.

It is important to note that, while the increasing average lattice length that accompanies heat treatment is much greater than for the oxidized Spherocarb, no ordering at all is expected for the low oxidation temperatures of the TGA (773K). This is shown in Figure 67, where a graph of L_a as a function of heat treatment in nitrogen is shown for anthracene carbon. Until approximately 1700 K, the carbon structure remains relatively stable, while the carbon rapidly graphitizes with increasing heat treatment beyond this point. All reactions were carried out at 773 K in this study, far below the temperature of which thermal annealing results in measurable changes in the carbon microstructure. There is a possibility that localized heating may occur causing an isolated (adiabatic) graphitic layer temperature increase during combustion. Assuming an aromatic region with a length of 1 nm (molecular weight ~ 1000 g/mol, heat capacity ~ graphite = 4.5 cal/mol-K), the heat generated during conversion of a edge carbon to CO_2 (heat of combustion CO_2, $\Delta H_f \cong 94$ kcal/mol), causes less than a 250 K increase in the local temperature.

The interplanar spacings of carbon derived from the TEM images were compared to the spacings obtained using XRD as a check on the image analysis methodology. For comparison purposes, the 2θ values were converted to layer spacings using Bragg's law ($2d_{002} \sin\theta = \lambda$), and the two different methods were plotted in Figure 66. The 0% conversion Spherocarb has an XRD spacing of approximately 0.37 nm. The layer spacing obtained by analysis of the HRTEM

images was approximately 0.374 nm on average. Marsh et al[124] reported a similar discrepancy (0.35 nm versus 0.36 nm) for untreated petroleum coke.

The XRD gives a broader region of spacings, with most of the actual peak cut off in the diagram. This is due to the fact that Spherocarb has a wide distribution of spacings due to its disordered nature, causing a broadening of the peak. This broadening is also a function of the source wavelength, with λ= 0.154 nm for X-rays, and 0.029 nm for 200 keV electrons. The broadening is, according to Scherrer, a function of wavelength, given as

$$\Delta(2\theta) = \frac{\lambda}{L_c \cos\theta} \tag{28}$$

where L_c is the stacking height. Since the wavelength of the TEM is approximately an order of magnitude difference, the width of the peaks should be approximately 10 times narrower.

The change in lattice fringe spacing, d_{002}, with oxidation is shown in Figure 63 as a function of conversion. The average values for the d_{002} spacings were 0.374, 0.369, 0.367, and 0.361 nm for 0, 25, 50 and 75% conversions, respectively. These values are slightly higher than expected for graphitic carbon, but within the range of disordered carbons.[125] This value is also slightly higher than the value measured previously for Spherocarb (Chapter 5), which is probably the result of using two different batches of Spherocarb. Another possible cause of the difference is grinding. The samples in Chapter 5 were ground after conversion, while those in this chapter were ground before combustion, and grinding has been shown to cause changes in structural parameters.[126] The decrease in spacing agrees well with the decrease reported by Palotás et al.[128] for oxidized soot, where mean spacing decreased from 0.351 nm for unoxidized sample to 0.343 nm for the sample oxidized to 96% conversion. Levendis et al.[124] also found that the interlayer spacing of polymer chars decreased with heat treatment, and this effect was enhanced by oxygen.

Marsh et al., also found that the average d-spacing significantly shifted toward smaller average values with a narrowing of distribution during heat treatment of carbon black. However, no change was reported for heat treatment temperatures of up to 1273K, 500K above our reaction temperatures.

As can be seen from the extracted images of Figure 55 through Figure 58, the fractional coverage (% dark) increases with oxidation, and is plotted in Figure 61. The coverage falls into the 25-30% range for Spherocarb. The coverage, if one assumes that the fractional coverage is an estimate of the number of ordered fringes that appear per area, and assuming that this estimate can extend to three dimensions, can be taken represent an estimate of the particle density. As the fractional coverage is simply the measure of dark fringes to total examined area, the true coverage will be higher, as illustrated in Figure 62. The regions (A) between the dark lines that represent fringes are part of a continuous 3 layer stack. However, the space they occupy is not counted in the coverage, and is a source of error, especially for the turbostratic carbons that are not entirely linear.

The increase in coverage from 20 to 25% may be taken as indicative of pore closing (surface area loss) and concentration of ordered carbon. However, the "pores," regions with no fringes, shown in the extracted structure are in actuality regions of either 1) low order carbon, 2) ordered carbon not aligned with the beam to satisfy the Bragg angle, or 3) actual pores, and is subject to some error. The stacking is also seen to increase with conversion, from an average stack height of 2-3 layers for 0% conversion, up to average stack heights of 4-5 for 75% conversion, although this was not measured extensively.

In order to understand how the lattice length affects carbon reactivity, the derived lattice parameters are plotted with reactivity as a function of conversion level in Figure 68. As shown previously, the reactivity goes up with conversion. At the same time, the lattice spacing remains approximately constant, and the lattice length increases by approximately 50%. This increase is contrary to the idea that edge carbons are more reactive than basal carbons,[60,13] as longer fringe lengths are indicative of lower edge/basal carbon ratios and lower reactivity. A decrease in reactivity with fringe length was shown by Davis et al[148] for pulverized coal at high (1800K) temperatures. However, at low temperatures, Ciambelli[127,128] has shown increasing reactivity with structure for soot oxidation.

To examine this issue of reactivity, a population balance model is needed to examine how lattice fringes are changing during oxidation, as the distributions measured must be normalized for remaining carbon and other factors. The model is developed in the next section.

7.4 DISCUSSION

7.4.1 Modeling of Reactivity Using Fringe Length Change

As the Spherocarb is a relatively pure carbon, it is ideal to test whether the lattice length is a factor in the reaction rate of the carbon particles. In this analysis, we assume that the lattice length is a measure of the proportion of edge to basal carbon atoms in the Spherocarb's turbostratic structure. Marsh et al[122]suggested that these graphitic structures may line up to yield apparent lengths comparable to those of longer molecules. However, we assume that for the thin edge samples examined here, that this is not a factor (see Appendix A). Another source of possible error is that throughout this analysis, Regime I, kinetic control is assumed. The presence of an outer graphitic shell could possibly lower the diffusivity. However, reaction

studies on Spherocarb by Hurt[14] showed that for at least temperatures up to 900 K, complete kinetic control is maintained.

In order to derive a model for the oxidation of Spherocarb, one may make an analogy between the population of individual lattice fringes and the population of particles in aerosol particulate systems. Randolph and Larson[129] applied a statistical mechanical view to the conservation equations governing the size distribution of particulate systems to formulize the population balance approach of Hulburt & Katz.[130] The population balance is in effect a statement of continuity for particulate systems. In this approach, the rate of increase of the number of particles of a certain size must be related to the rate at which particles of that size are being formed and removed, and the rate at which the particles are growing. The number of particles of a certain size is expressed as a population density, n(L). The population density at size L, n(L), is defined as the ratio of the number of particles (or fringes in our case), dN, in a differential neighborhood around L, to the size of the neighborhood. That is;

$$NdL = \text{Number of Fringes in Length } L + \Delta L = n(L) \tag{29}$$

To simplify the population balance system, the following assumptions are made:

1) No generation of lattice fringes occur during oxidation. This does not imply that lattice fringes cannot grow, but that in the oxidation system we are using, any nucleation or formation of new lattice fringes is superseded by changes due to oxidation (removal).
2) The porous region where reaction takes place does not change significantly during oxidation, so diffusive effects need not be considered. This simply means that the particle burns with Regime I kinetics.

3) The rate of reaction in a given fringe length is uniform. Changes in reactivity for a fringe of a given length are due to changes in interlattice spacing and possible changes in any catalytic activity are neglected.

4) The lattice distribution may be approximated as an exponential distribution. This assumption simplifies the distribution function, at the cost of losing the variability in lattice lengths, especially at higher lattice fringe lengths. However, these lengths account for less than 5% of the total number of measured fringes. The model fits of these distributions is given in Figure 60.

Using these assumptions, the change in number of fringes in a given time interval in length L to L + ΔL, as depicted in Figure 68, becomes

$$\Delta L \frac{d}{dt}(N) = N\left(\frac{dL}{dt}\right)_L - N\left(\frac{dL}{dt}\right)_{L+\Delta L} \tag{30}$$

where the term on the left gives the time rate of change of the number of fringes. The first term on the right gives the growth into (out of) the size range of the fringe of smaller size when dL/dt is positive (negative), and the second term gives the growth out of(into) the size range to (from) large sizes when dL/dt is positive (negative).

Making use of the definition of the derivative with respect to L, one can than find that

$$\frac{dN}{dt} = -\frac{d}{dL}\left[N \frac{dL}{dt}\right] \tag{31}$$

$$= \frac{dN}{dL}\left(-\frac{dL}{dt}\right) + N\frac{d}{dL}\left(-\frac{dL}{dt}\right) \tag{32}$$

The change in lattice length with respect to time is essentially the reaction rate of the lattice fringes, and one can define a reaction rate as

$$r = -\frac{dL}{dt}. \tag{33}$$

substituting r for the expression, one finds

$$\frac{dN}{dt} = \frac{dN}{dL} r + N\left(\frac{dr}{dL}\right) \tag{34}$$

Normally, in population balance equations, one would only know r, the rate of reaction. However, in our case, the distribution functions are known from the experimentally determined HRTEM work, as

$$\frac{dN}{dt} = \text{Change in number of fringes with conversion} \tag{35}$$

$$\frac{dN}{dL} = \text{Derivitive with respect to L of the distribution function} \tag{36}$$

If one assumes that the reaction rate is constant as a function of lattice length, the solution is straightforward. However, assuming that

$$\frac{dr}{dL} = \text{Change in reaction rate of fringes with changes in L} \tag{37}$$

is not constant results in an iterative solution process.

One must now relate the TEM measurements of the fringes to the model, as the TEM only gives a representative sample, not a full measurement of all the fringes (N(L)). An estimate of the number of fringes must now be made using a mass or atomic balance. The absolute number of carbon atom, N_T, may derived by the weight of the sample and the carbon analysis given in Table 4. Once can assume that there are essentially two types of carbon in our system, an ordered carbon giving rise to TEM diffraction patterns (N_O), and a disordered, randomly oriented sample that gives rise to no lattice fringes (N_R) due to imaging limitations. Due to the limitations of the TEM that the ordered carbon must fulfill the Bragg condition for diffraction,

not all ordered carbon will appear in the microscope (given a 10° margin of error for the d_{002} planes to appear, only 10°/180° or approximately 5% of the fringes are expected to be imaged). However, as a first order approximation, we assume that all carbon present is represented in the carbon fringe image distribution, or

$$N_0 + N_R = N_T = \text{Total Amount of atomic Carbon} \simeq N_0 \qquad (38)$$

To estimate the number of fringes from the number of ordered atoms, one must know the average number of carbon atoms per fringe. To simplify the analysis, we assume that each fringe is the projection of a circular aromatic compound, with predictable fringe spacings per carbon atom, as given in Figure 70. From Figure 70, it is simple to calculate the number of carbon atoms per fringe for a given length L, CA(L). The average value of carbon atoms per fringe may then be calculated from the distribution function of each oxidation condition as

$$CA_{ave} = \sum_{0}^{\infty} n_L \, CA(L) \qquad (39)$$

From the distribution length functions, the average values for CA_{avg} were 49, 55, 69 and 91 atoms/fringe, corresponding roughly to lattice lengths of approximately 1.1, 1.2, 1.4 and 16 nm at conversion levels of 0, 44, 66, and 95% respectively,

Combining Equations 14 and 13 gives an overall estimate of the number of fringes as

$$N_f = \frac{N_O}{CA_{ave}} = \frac{N_O}{\sum_{0}^{\infty} n_L \, CA_L} \qquad (40)$$

The overall effect of the population balance may be seen as a model of the fringe change, where the number of fringes is a function of both oxidation level and structural distribution changes. The fringes at low conversions are highly concentrated at the lower lattice lengths.

However, the number of fringes decreases with conversion due both to removal of mass, and transformation of the lattice distribution to a higher average lattice length due to oxidation.

7.4.2 Modeling Results

A plot of lattice reaction rate r as a function of lattice length is given in Figure 71 for various conversion levels. The absolute reactivity of fringes increases during oxidation. At very low levels of conversion, the reactivity of each fringe is quite small, and in fact the growth of fringes becomes noticeable at a lattice length of approximately 2 nm, where the counting statistics for lattice fringes begins to break down due to lack of sample and modeling errors. However, the growth area only corresponds to roughly 5% of the fringes and is not of much importance globally.

To better understand the nature of the reactivity change, one needs to normalize the reactivity data. For comparison purposes, we assume that the reactivity of a lattice of length 0.8 nm is comparable across each oxidation level. In the model, this lattice length corresponds to the basic aromatic structural building block coronene. The normalized change in reactivity, calculated by dividing the reactivity at a length of 0.8 nm, is plotted in Figure 72. The normalized reactivity shows a fall off with increasing lattice length for all oxidation levels.

The difference in reactivity between short ($L_a < 1$ nm) and long ($L_a > 2$ nm) range order is approximately a magnitude lower for all conversion levels. This is somewhat lower than the trend of 2-3 order of magnitude differences in reactivity reported by researchers[9] for graphitic edge/basal plane reactivity. While the change in reactivity is lower, these graphite studies have carbons with a great deal more long-range order ($L_a > 5$nm) than the Spherocarb examined here.

To understand the nature of the decrease in reactivity with lattice length, Figure 71 also shows the ratio of edge carbons to basal carbons in the circular aromatic compounds assumed in the study. As can be seen, the decrease in reactivity actually occurs at a faster rate than would be expected from edge carbon effects alone, although the trend is comparable in scope. This implies that there is another process that acts to increase the reactivity of the fringes in inverse proportion to their length. Furthermore, this process must act to increase the reaction rate with increasing conversion. The actual process of oxidation is quite complex, but the following possible causes of changes in reactivity are discussed: 1) catalysis, 2) defect/reactive sites, and 3) chemisorption.

Catalytic effects could be a factor. At high carbon conversions, the absolute ratio of catalyst to carbon will increase with a consequent possibility of increasing reaction rate with conversion. This assumes that the catalyst is mobile and not being removed from the system. At the temperatures of the reactions studied here, catalyst should not be vaporized appreciably. As to mobility, catalysts have been shown to be able to "eat" grooves in graphitic layers under oxidizing conditions and low temperatures (Baker[71]). Another question that remains to be answered for turbostratic carbon is the question of "contact" and whether smaller lattices have the same reactivities (contact) with catalysts as compared to large lattices.

As shown by Hurt in Figure 73, the reactivity of acid washed Spherocarb is nearly identical with unwashed Spherocarb. This indicates that catalysis is probably not a large factor in the reactivity of Spherocarb, as would be expected with the low levels of impurities present in Spherocarb. However, this assumes that acid washing Spherocarb removes all of the impurities,

which may not necessarily be the case, as removal is highly dependant on char temperature histories. Furthermore, the possibly presence of a graphitic shell may effect removal.

The concentrating of reaction sites is an interesting possibility that bears further investigation. As can be seen by lattice variation in Figure 60, the lattice fringes are not static, but instead evolve over time, increasing in overall length. An ideal case of oxidation induced densification is shown in Figure 74. The squiggly line represents a blocking element, such as an aliphatic joining group that prevents the two basic structural units, (BSU) from closing to form an annealed molecule (Figure 74-b). At high temperatures, the removal of this blocking element will result in annealing due to atomic movement and slippage of the two BSU. However, for very low temperatures, the system may be in effect locked from closing due to interactions with other layers and linkages (not shown). Therefore, at low temperatures the removal will induce a physical shift of the BSU to become more linear and aligned, but the bonds are unable to form because of unfavorable conditions due to distance and/or misalignment of the BSU. This lack of joining may or may not be viewable in the microscope, as if the distance separating the two now separate BSU is less than 0.16 nm, the current resolution of the electron microscope, the two BSU will appear joined. This imperfect ordering phenomenon will tend to increase the reactivity of molecule due to the leaving behind of active sites.

The concentration of active sites also makes sense when one examines the data of Davis et al[148] and Palotas[128] For low temperature oxidation of diesel soot, Palotas et al. found that the reactivity per unit weight increases with increasing conversion, as in this study. Furthermore, the d_{002} structure, as in this study, became slightly narrower. In contrast, the study of Davis et al. for high temperature combustion of pulverized coal oxidation, found that the reactivity

decreasedwith conversion, while conversely the structure will became more ordered as measured by X-ray and TEM analysis. At high temperature, oxygen may accelerate the annealing processes, which have typical activation energies of 400-800 kJ/mol,[131] and begin to destroy active sites. Low temperature oxidation may not have the sufficient energy to destroy these sites, resulting in their retention.

The last factor considered is changes in the chemisorption of oxygen. The reactivity of carbon at low temperatures may be modeled as first order in surface area and coverage, yielding

$$R = kA_{carbon}\theta_{O2} \tag{41}$$

where θ_{O2} is the coverage of oxygen in the system. Schlogl et al[132] found that an increase in graphite structural perfection facilitated the dissociative chemisorption of oxygen. This is similar to the results of Yang[133] and Olander[134] where too high of a density of surface defects in all cases was detrimental for the reaction rate. This indicates that a highly disordered structure with low coordinated carbon atoms is not favorable to gasification.

Spherocarb can be seen to go through a similar state, from a highly disorganized structure (L_a =1.0 nm, L_c ~2-3 stacks) to a more ordered structure (L_a =1.5 nm, L_c =4-5 stacks). Assuming that chemisorption of oxygen increases with ordering, the reactivity will also increase. This may account for the increased reaction rate at low temperatures, where chemisorption plays an important role in oxidation. This may be seen by the measured activation energy of Spherocarb combustion, 35 kcal/mol[94], which is compareable to the desorption energy of CO (30 kcal/mol[134]) on graphite

While carbon densification is important at lower temperatures, this study implies that any reactivity effect that accompanies this densification may be fully offset by a change in the

reactivity of fringes themselves and extrapolation of this structural change to higher temperatures may not be warranted. The probable limit of this oxidative acceleration is approximately 1500 K, the point where annealing would naturally result in fringes of length approximately 1.5 nm.

7.5 CONCLUSIONS

The use of HRTEM and image analysis provides a method for examining the structure of highly disordered turbostratic carbons quantitatively. The results of this study show that the carbon lattice becomes more ordered during oxidation as exhibited both by the increased lattice lengths, L_a and decreased d_{002} spacing. This ordering results in the densification phenomena previously reported for carbons reacting under kinetic control.

The inverse correlation between structure and reactivity implies that one cannot measure the structure of carbon and expect to predict reactivity. This is because of the complex interaction between temperature history and chemisorption effects. Ordered fringes generated at low temperatures will have a higher than expected reactivity, probably due to the presence of defects that are not resolvable in the microscope. The ordering of carbon may also increase the chemisorption of oxygen, increasing the overall reaction rate.

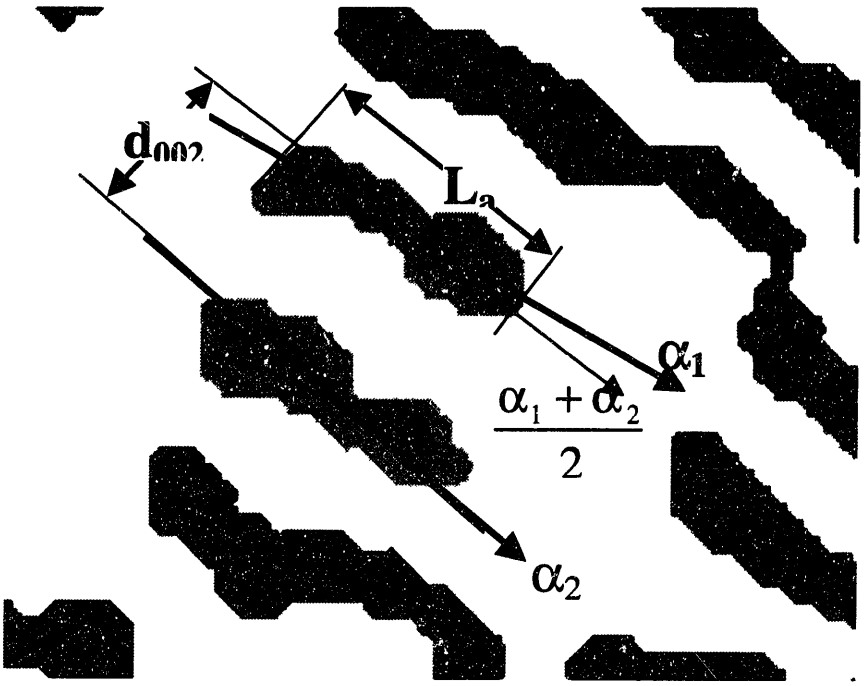

Figure 47. Magnified extracted structure showing example measurement of d002 spacing and Lattice length

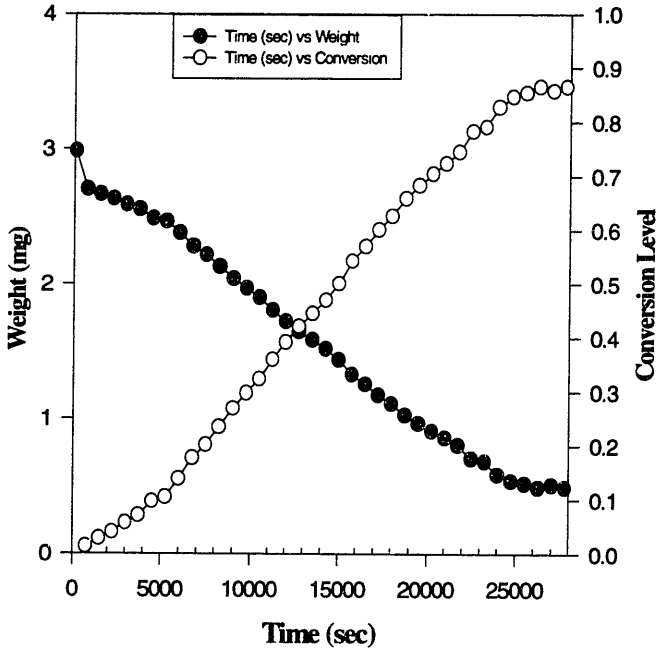

Figure 48. Weight loss of Spherocarb as a function of time at 773 K.

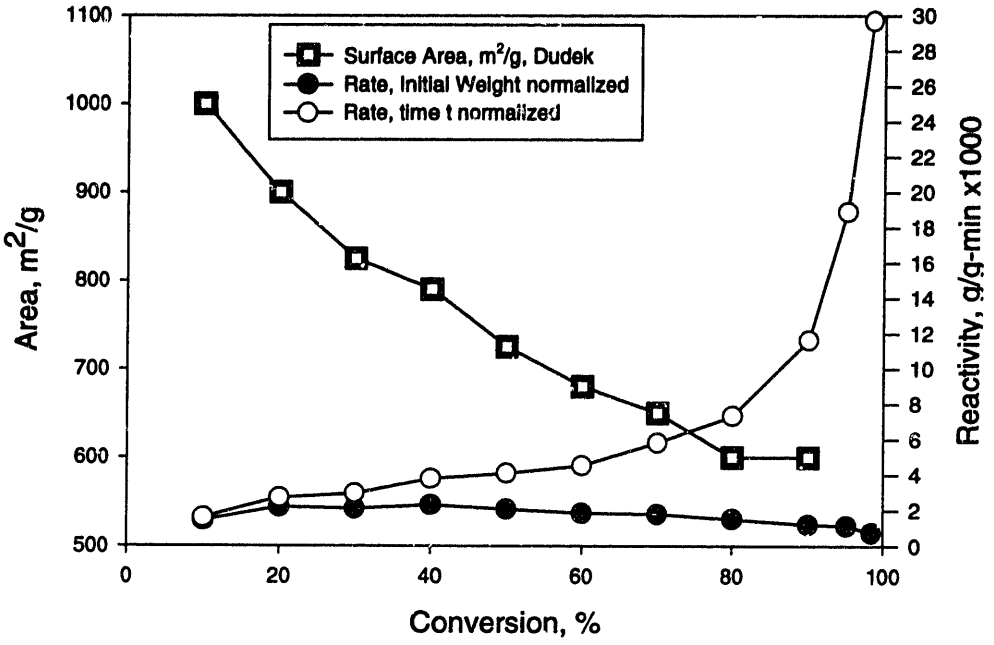

Figure 49. Reactivity of Spherocarb as a function of conversion.

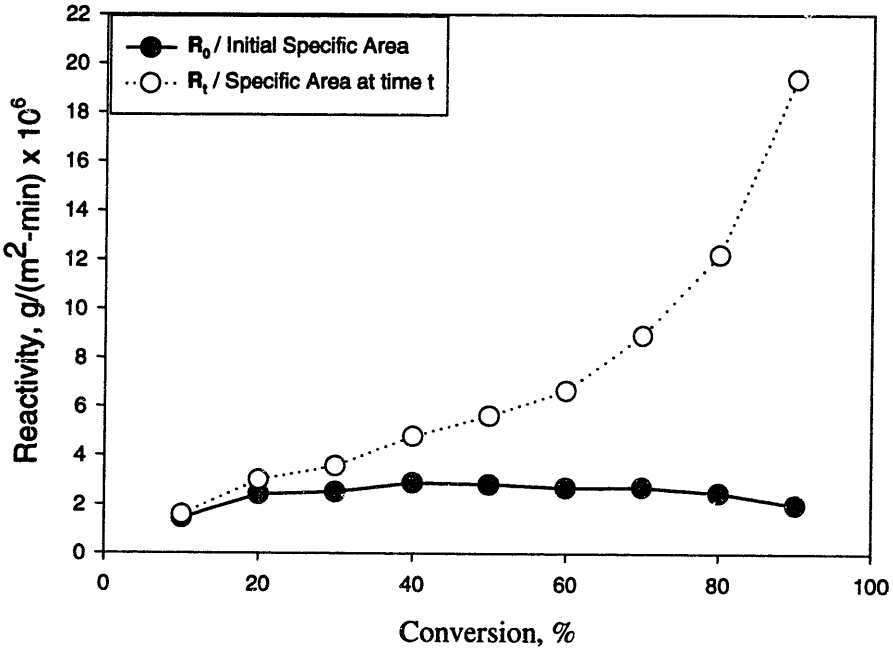

Figure 50. Intrinsic Reactivity of Spherocarb

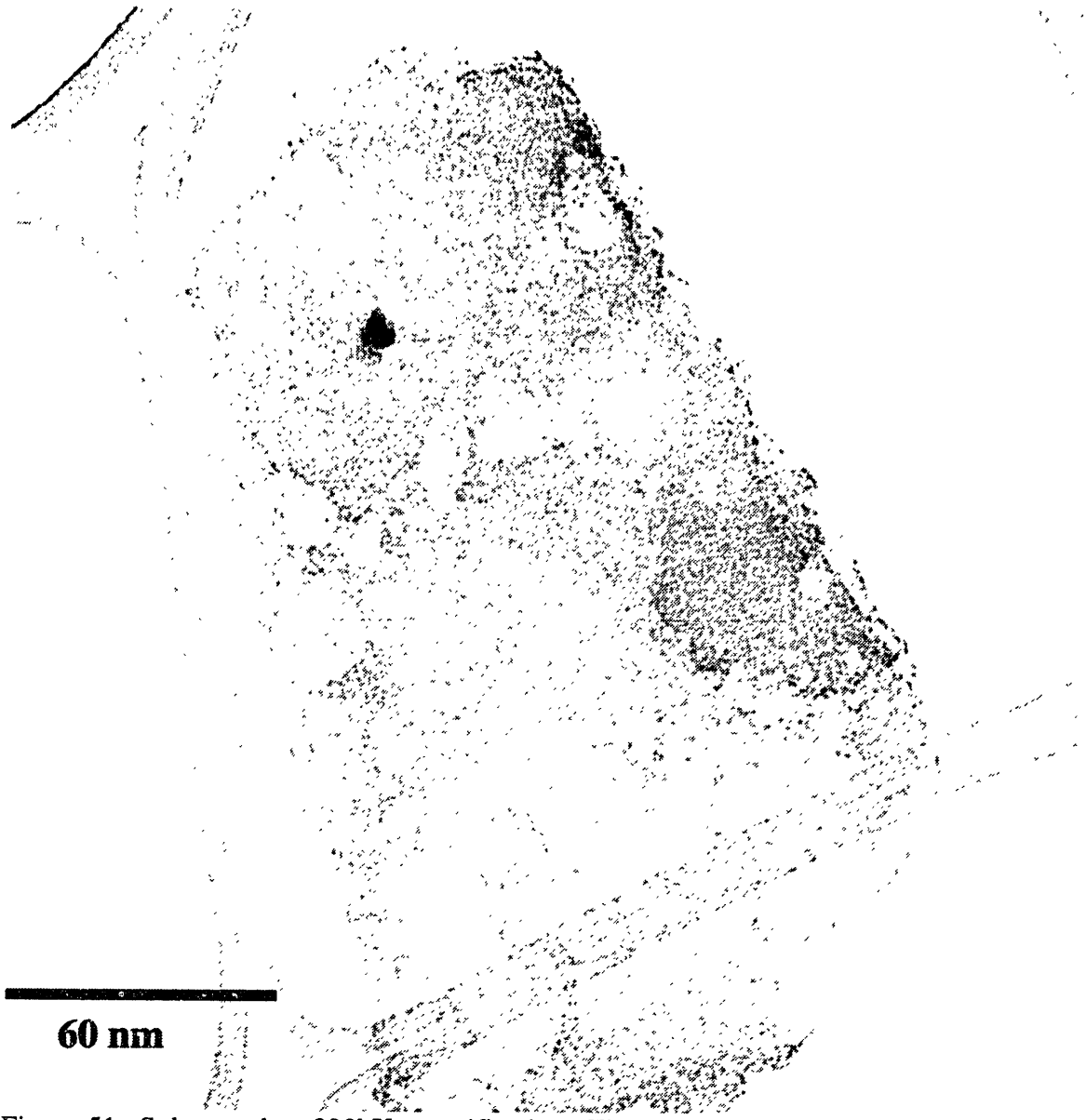

Figure 51. Spherocarb at 290kX magnification. The carbon is seen to have a number of "holes" At this magnification, these may be thought of as regions of different carbon density, or "pores." The thin regions at the edge are where useful microscopy may be accomplished.

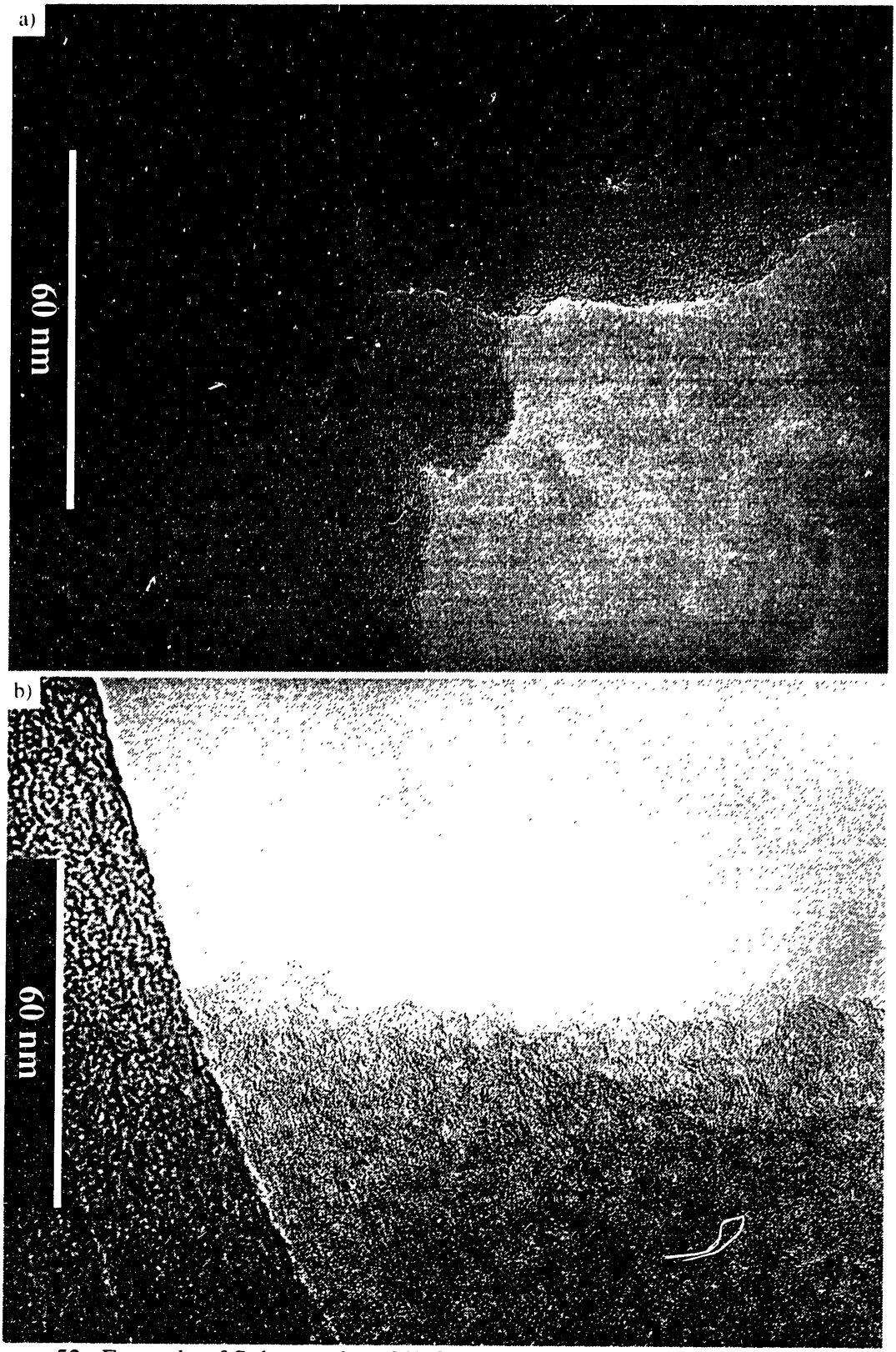

Figure 52. Example of Spherocarb a) 0% Conversion and b) 25% conversion. Original micrograph, 200 keV, 590 kX.

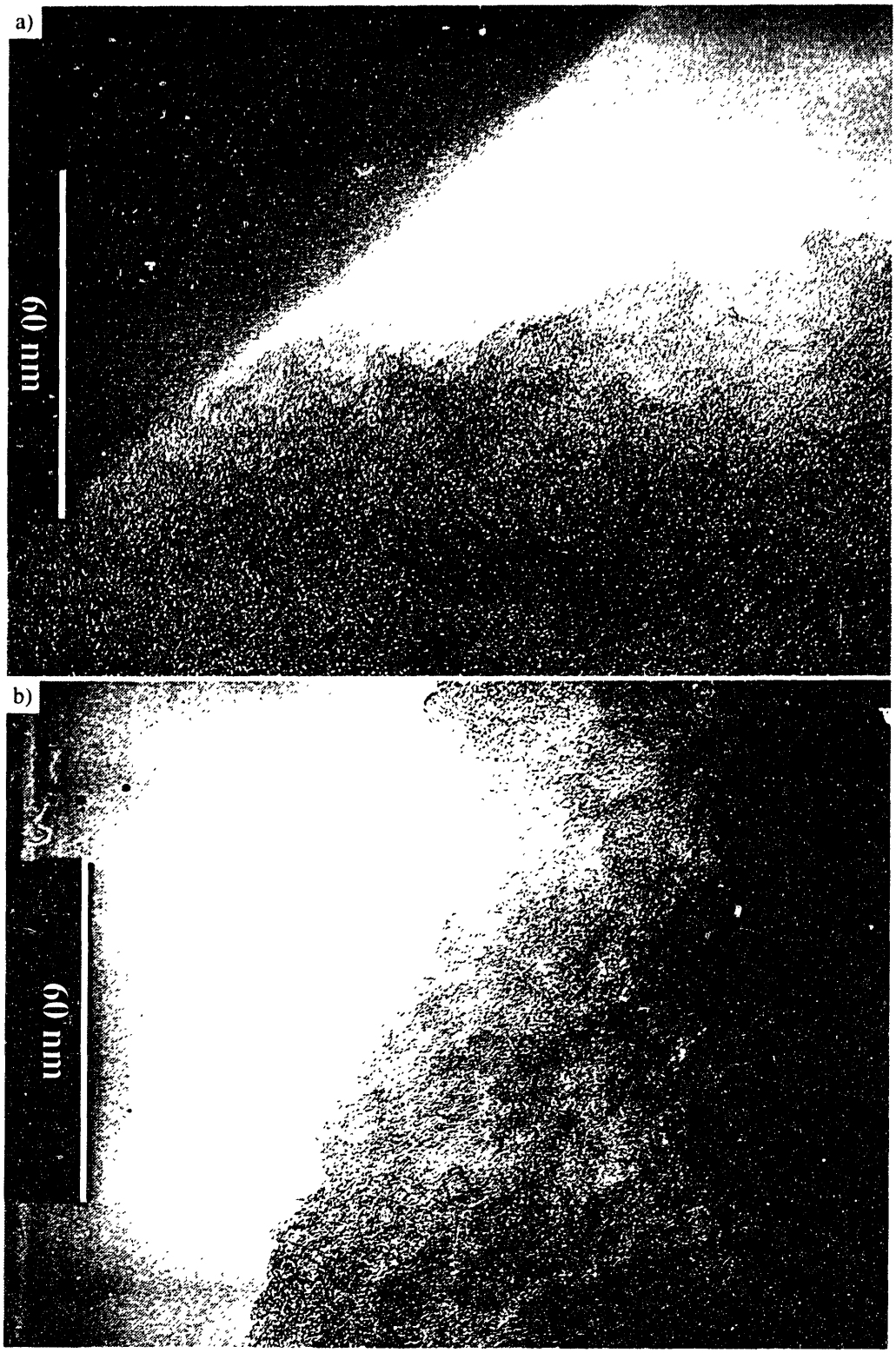

Figure 53. Example of Spherocarb a) 50% Conversion and b) 75% conversion. Original micrograph, 200 keV, 590 kX.

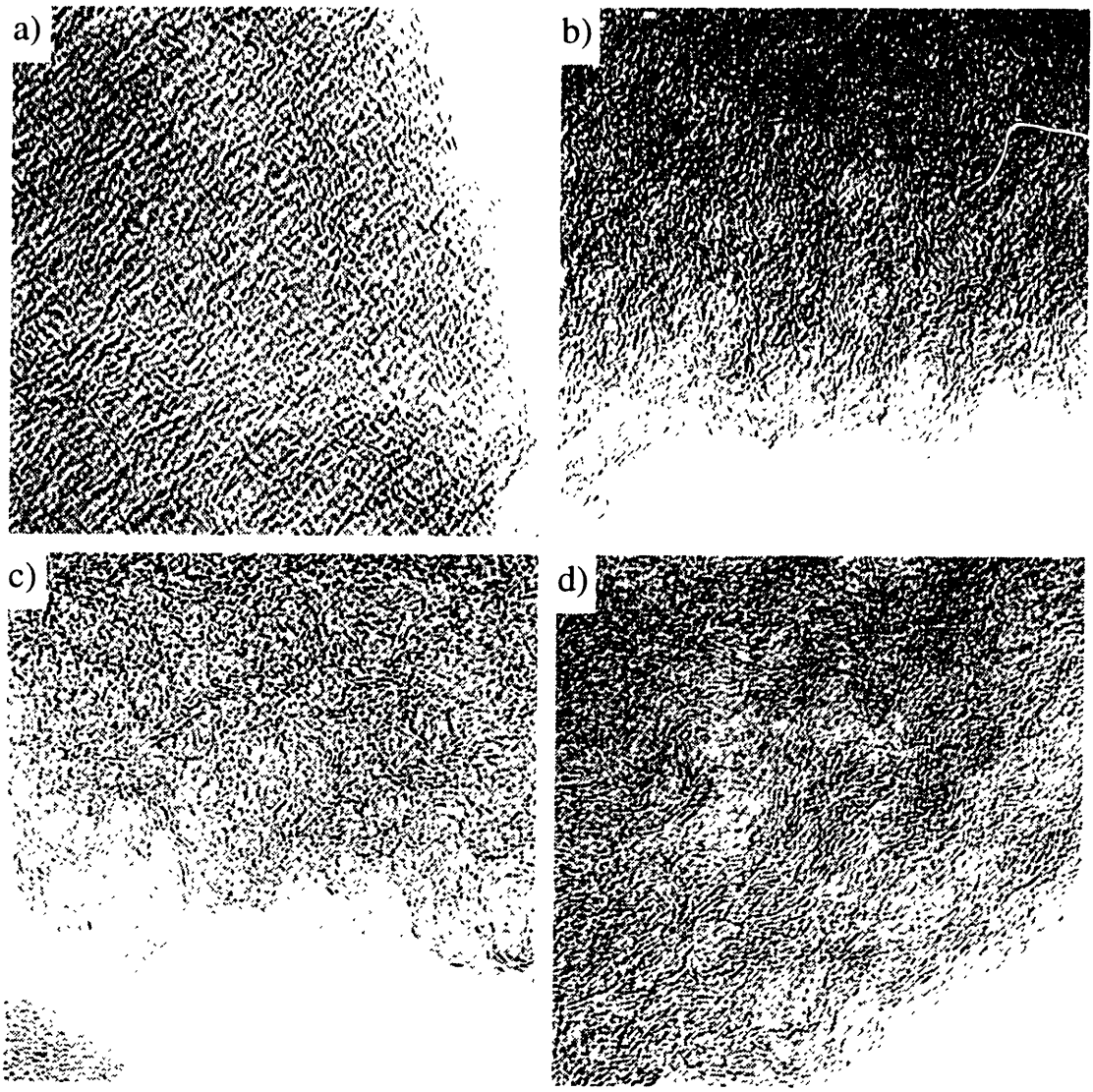

Figure 54. Magnified Spherocarb example isolated from Figure 52 and Figure 53 a) 0% b) 25% c) 50% and c) 75% conversion.

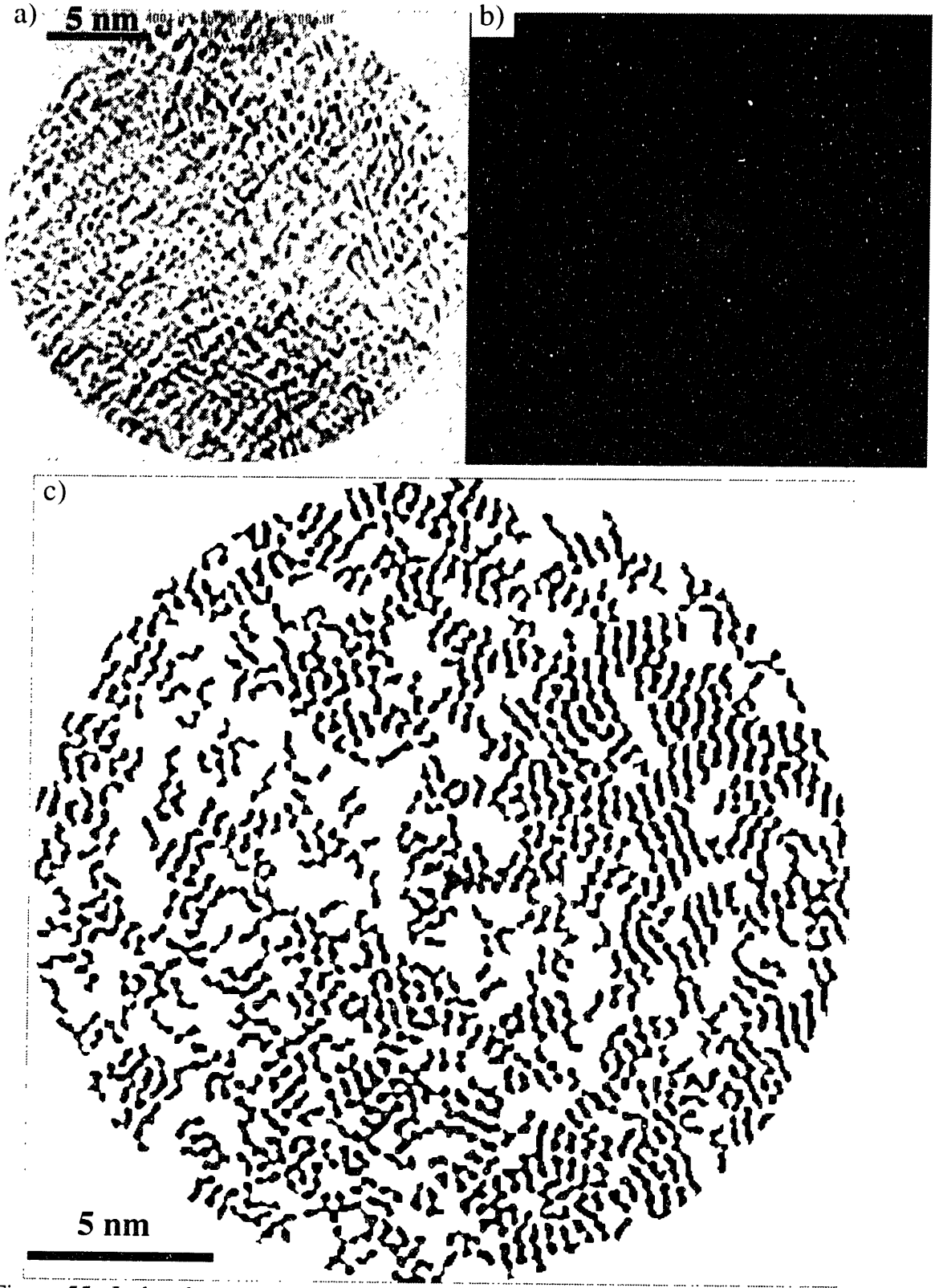

Figure 55. Isolated soot structure of Spherocarb at 0% Conversion. a) isolated structure, b) power spectrum and c) extracted structure.

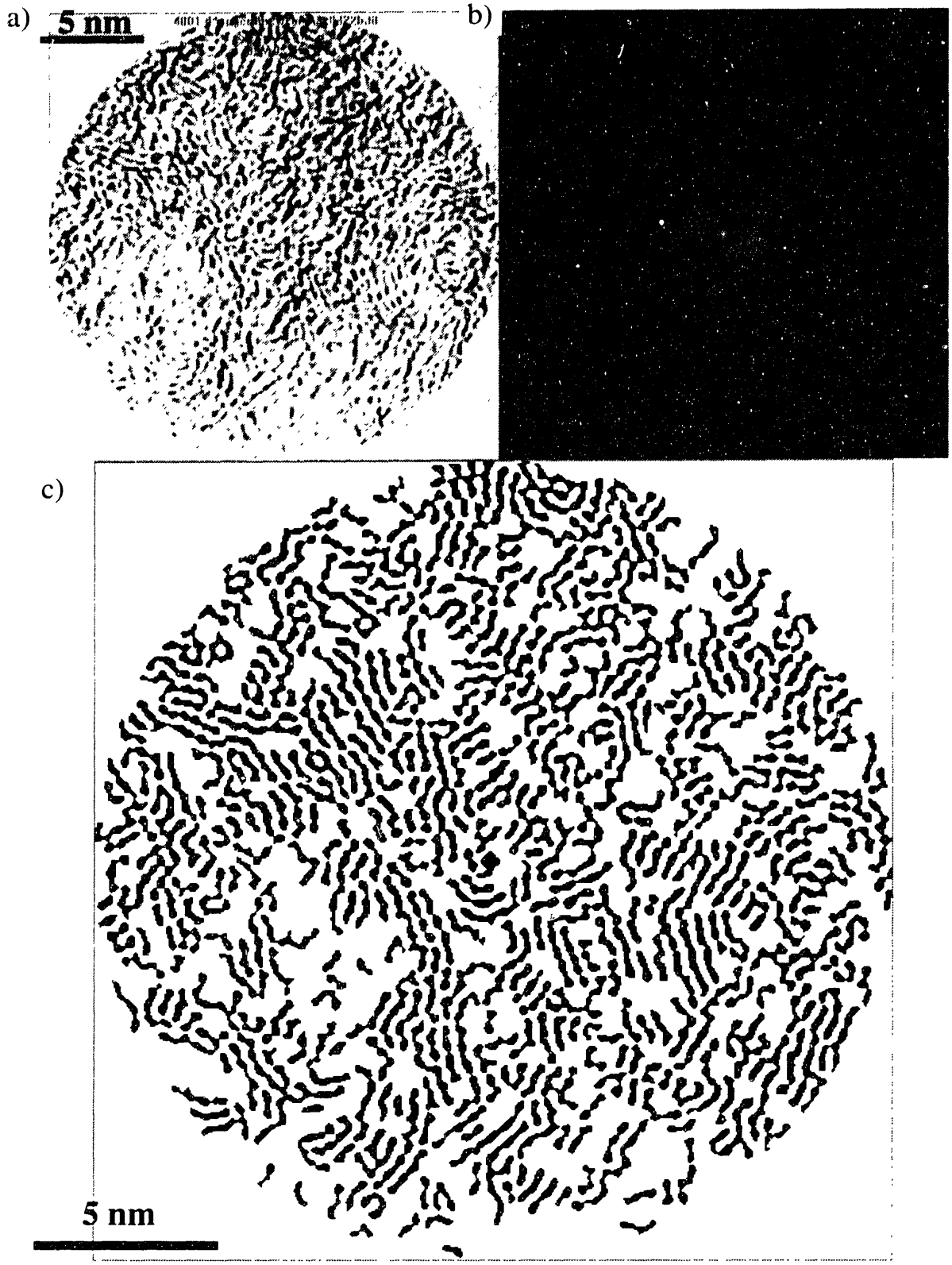

Figure 56. Isolated soot structure of Spherocarb at 25% Conversion. a) isolated structure, b) power spectrum and c) extracted structure.

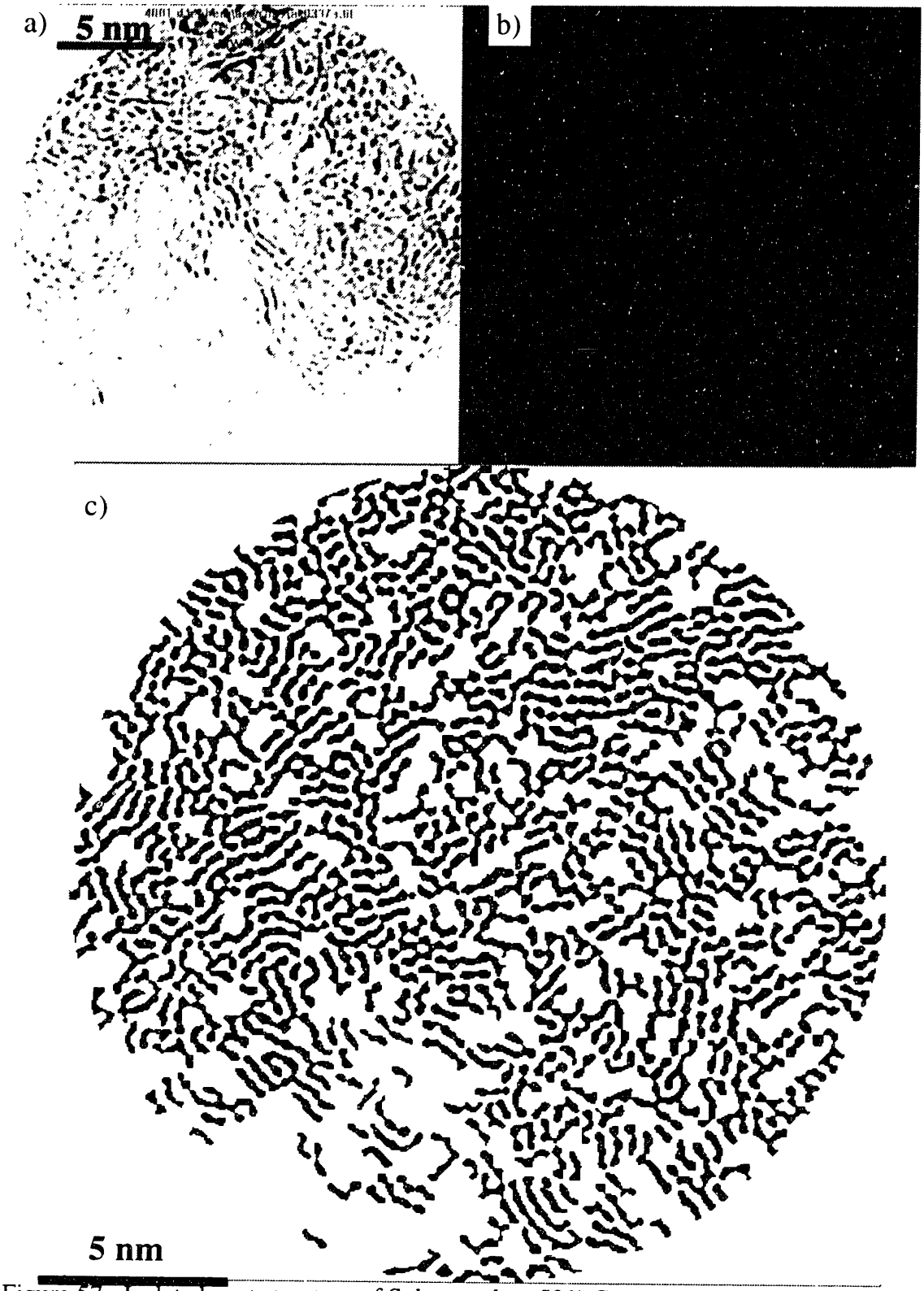

Figure 57. Isolated soot structure of Spherocarb at 50% Conversion. a) isolated structure, b) power spectrum and c) extracted structure.

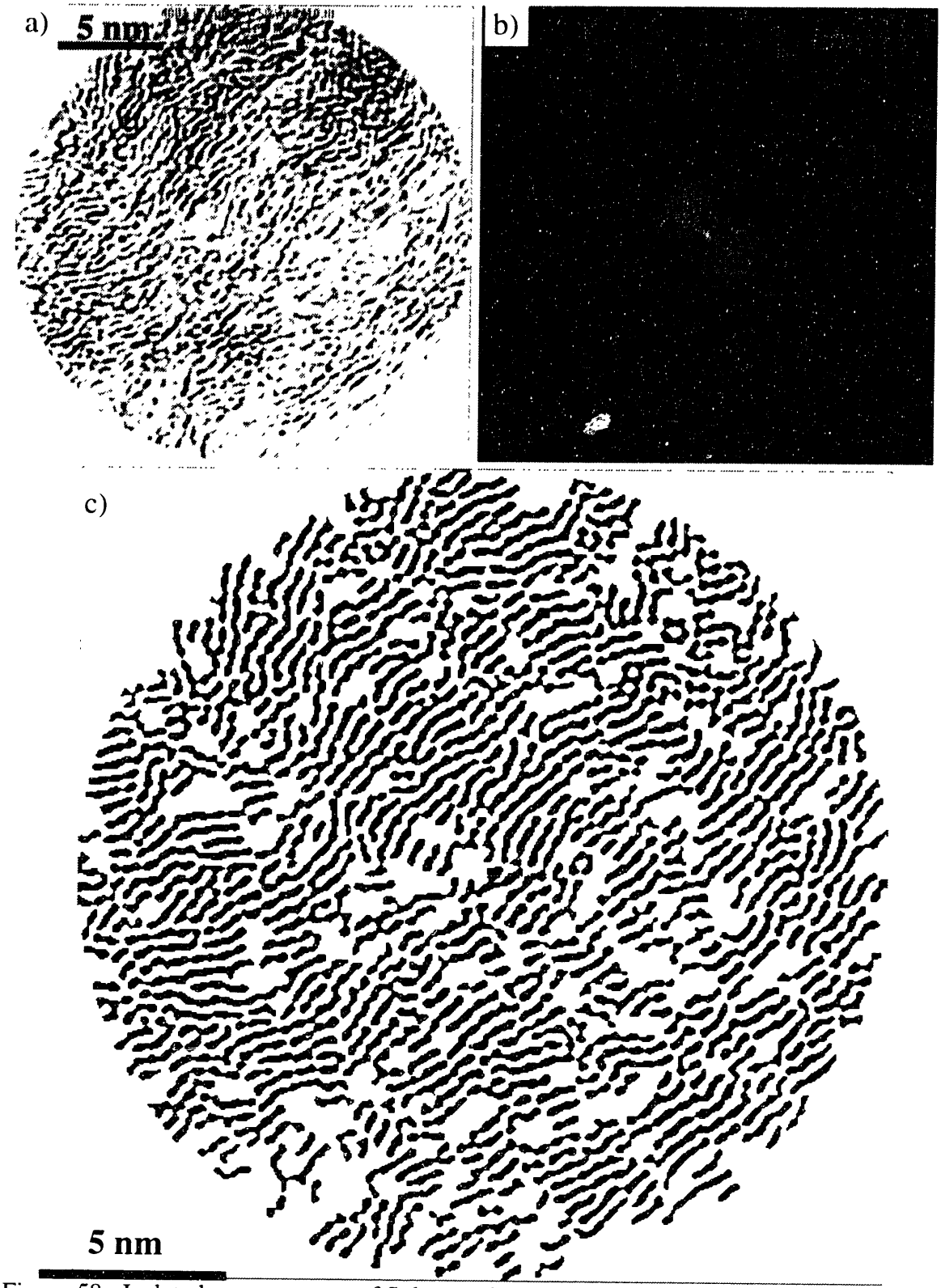

Figure 58. Isolated soot structure of Spherocarb at 75% Conversion. a) isolated structure, b) power spectrum and c) extracted structure.

Figure 59. Example of a "graphite" region in Spherocarb.

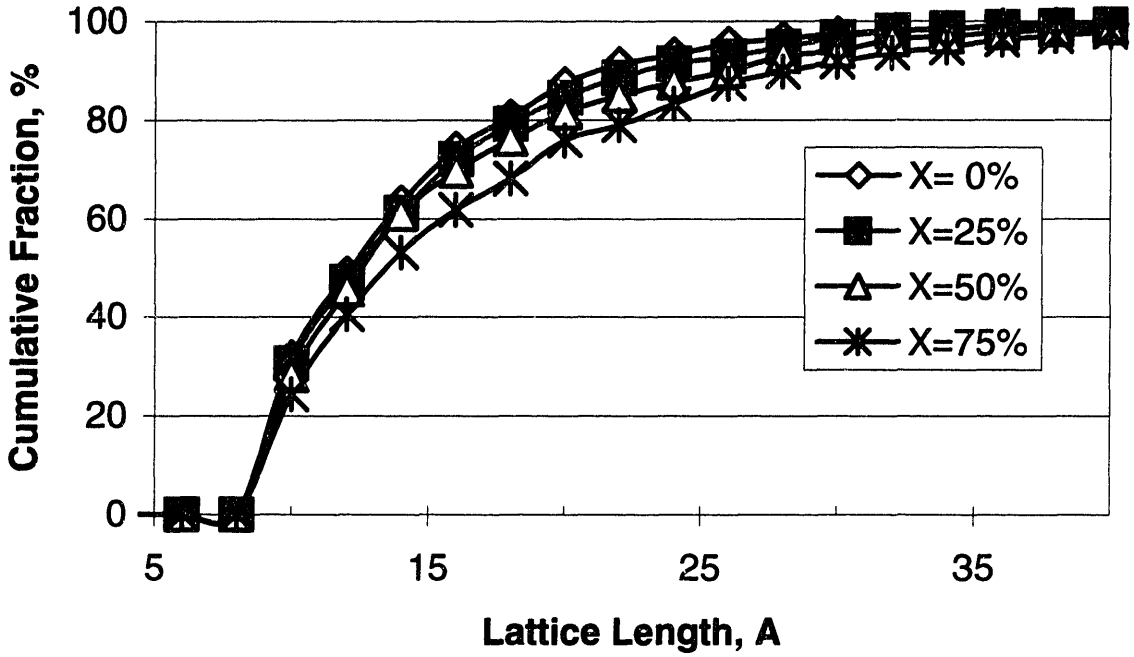

Figure 60. Lattice length variation as a function of oxidation.

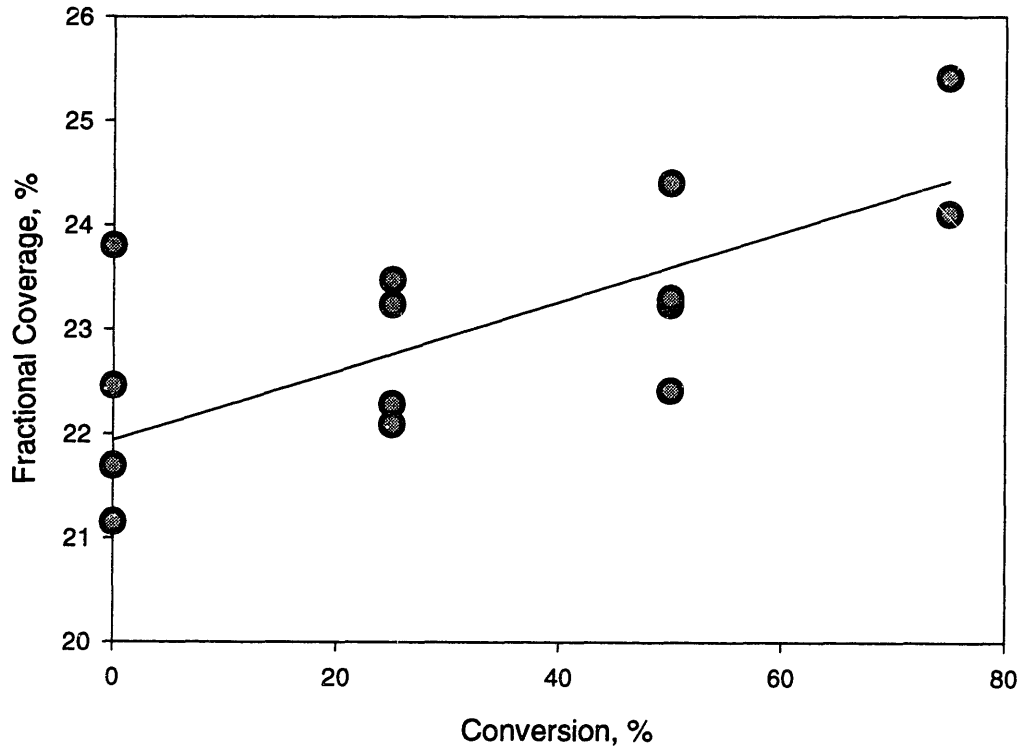

Figure 61. Fractional coverage as a function of oxidation conversion.

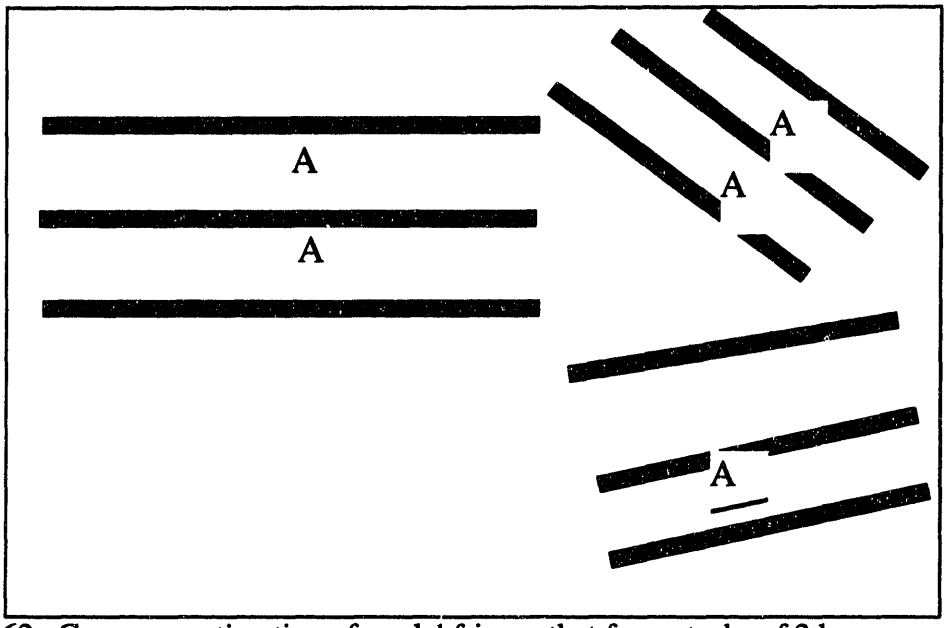

Figure 62. Coverage estimation of model fringes that form stacks of 3 layers.

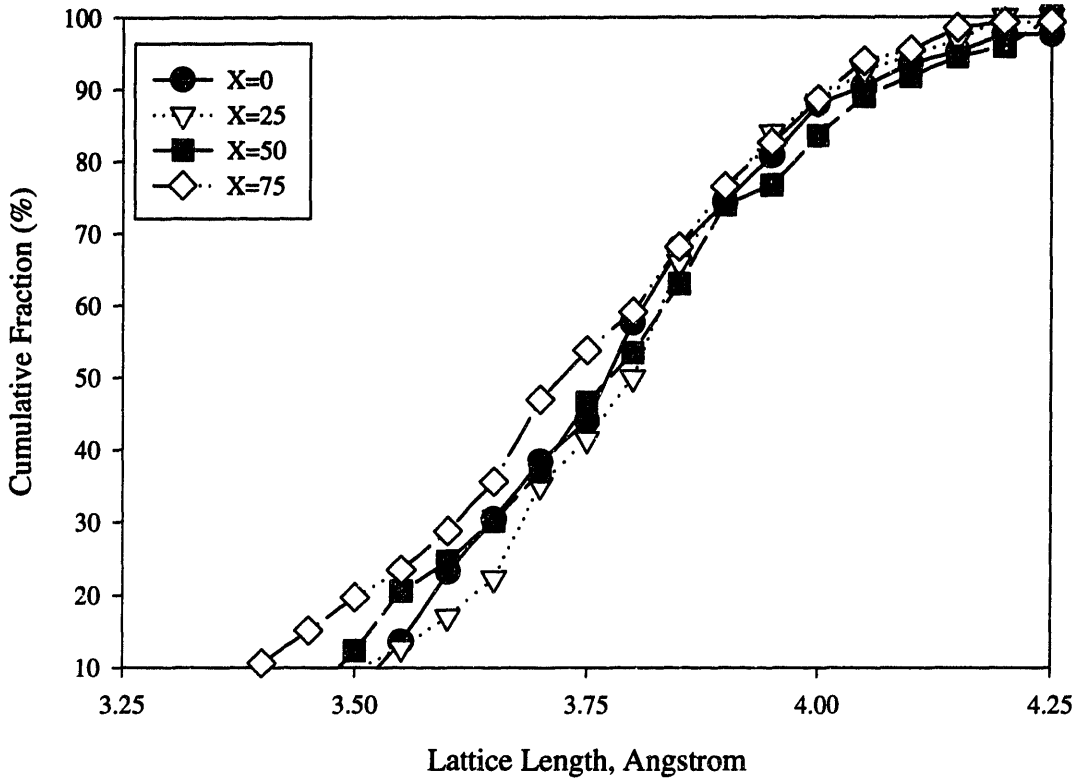

Figure 63. D_{002} spacing variation as a function of oxidation

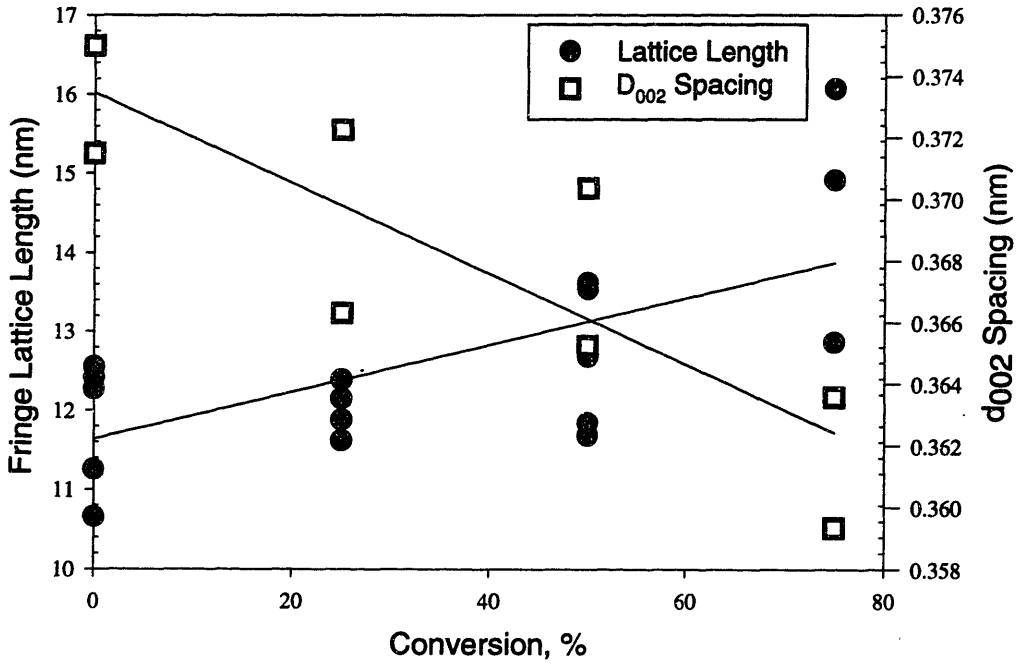

Figure 64. Variability in measurement of d002 and lattice length in multiple samples.

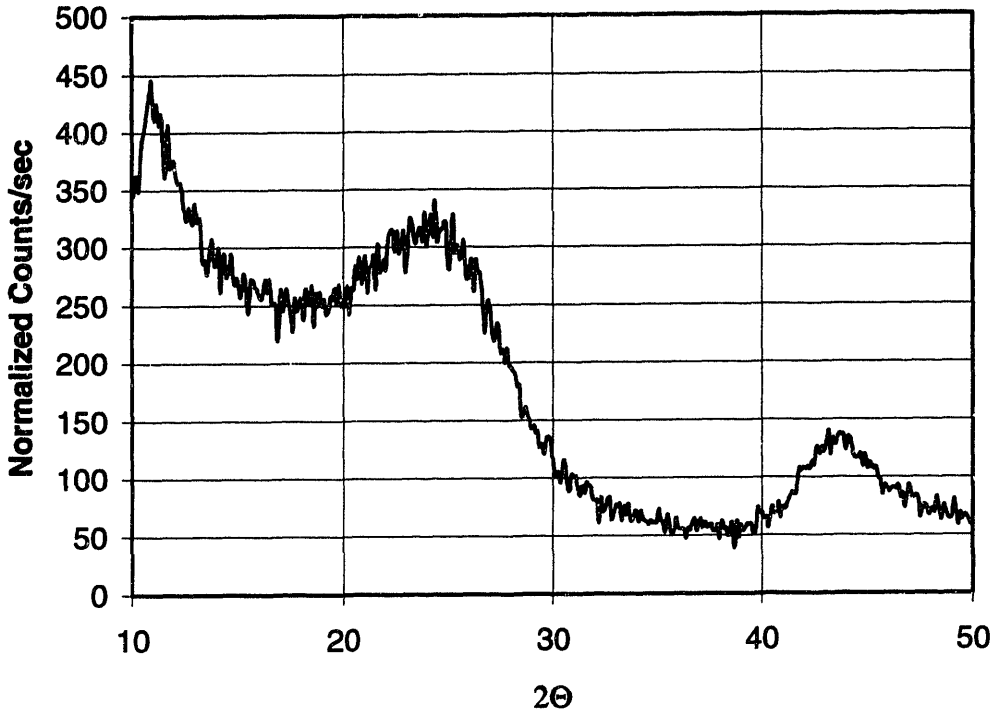

Figure 65. X-Ray Diffraction of pherocarb.

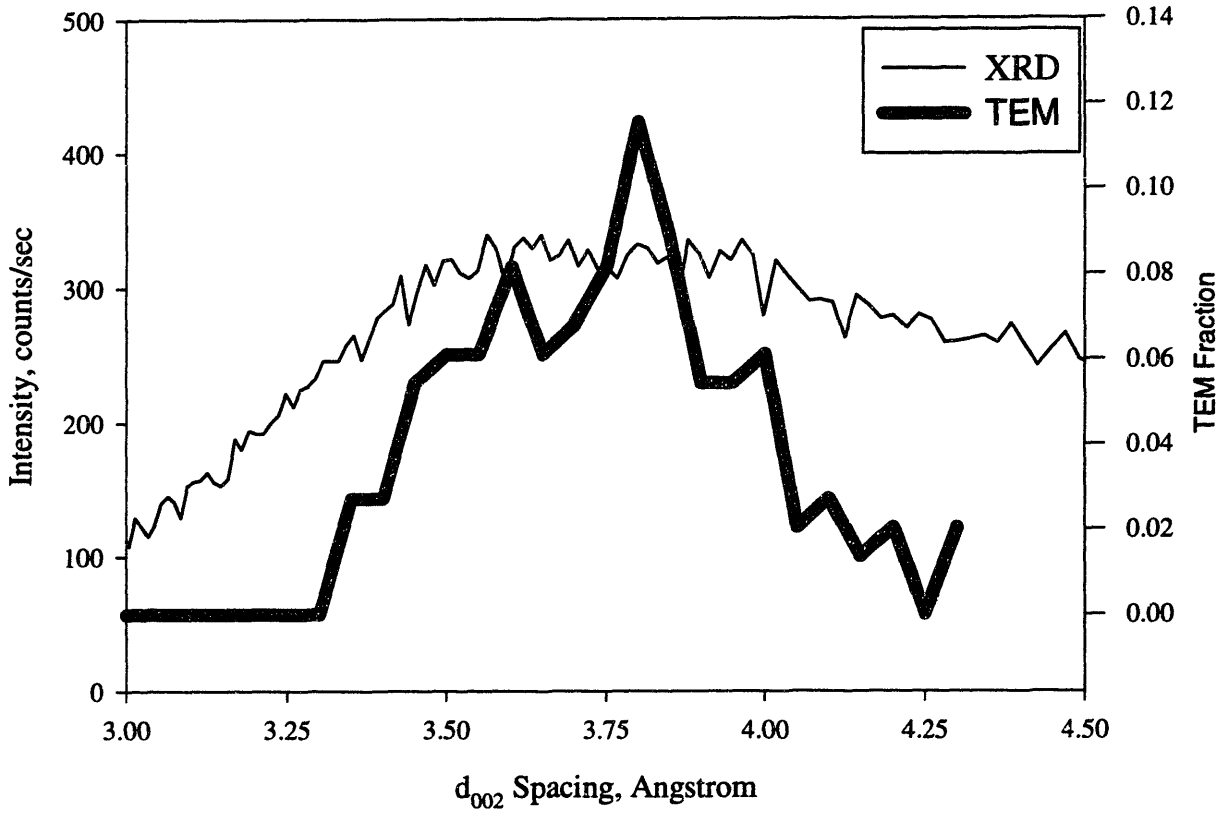

Figure 66. Comparison of d_{002} spacing of Spherocarb measured by X-ray diffraction and the TEM image analysis.

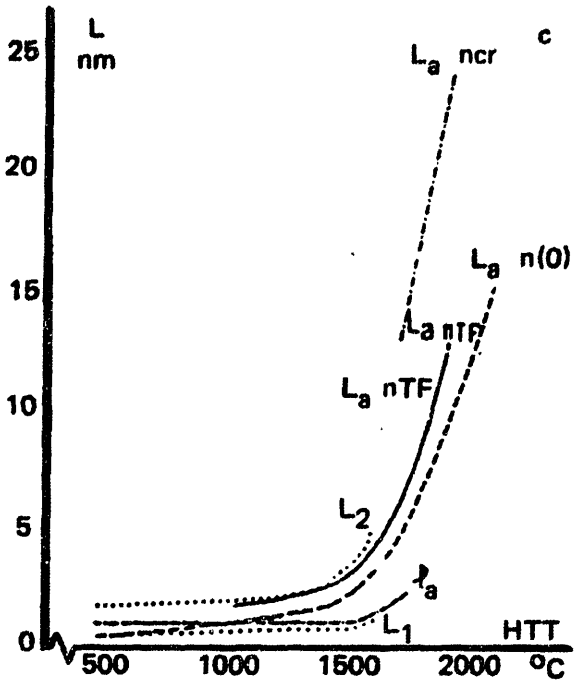

Figure 67. Effect of heat treatment on lattice lengths (Marsh et al).

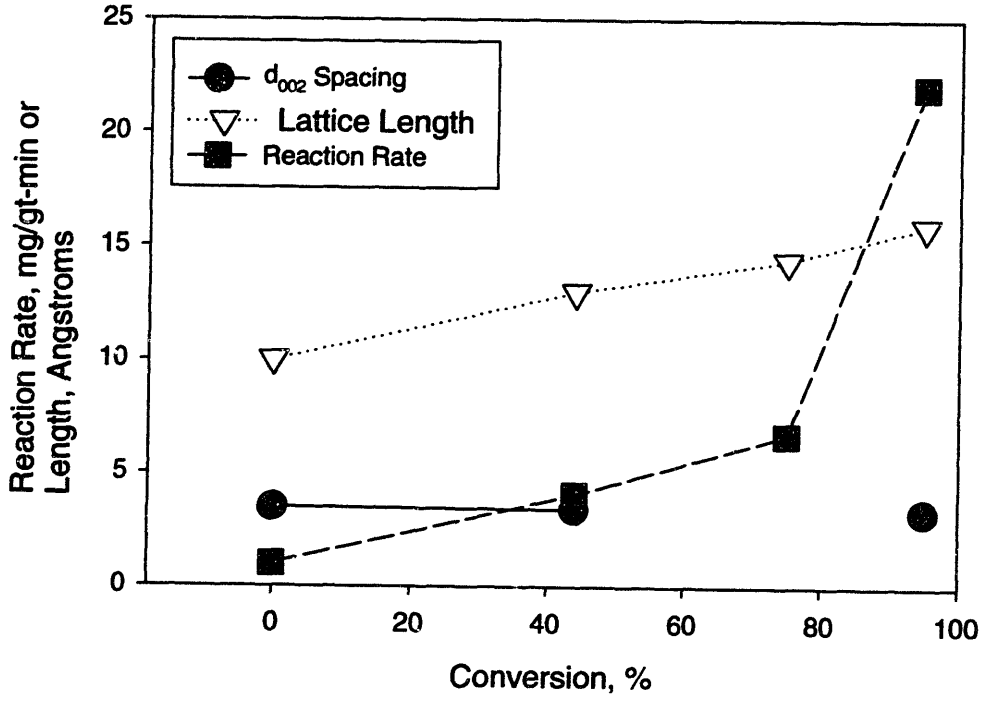

Figure 68. TEM extracted Parameters and Reactivity as a function of Conversion

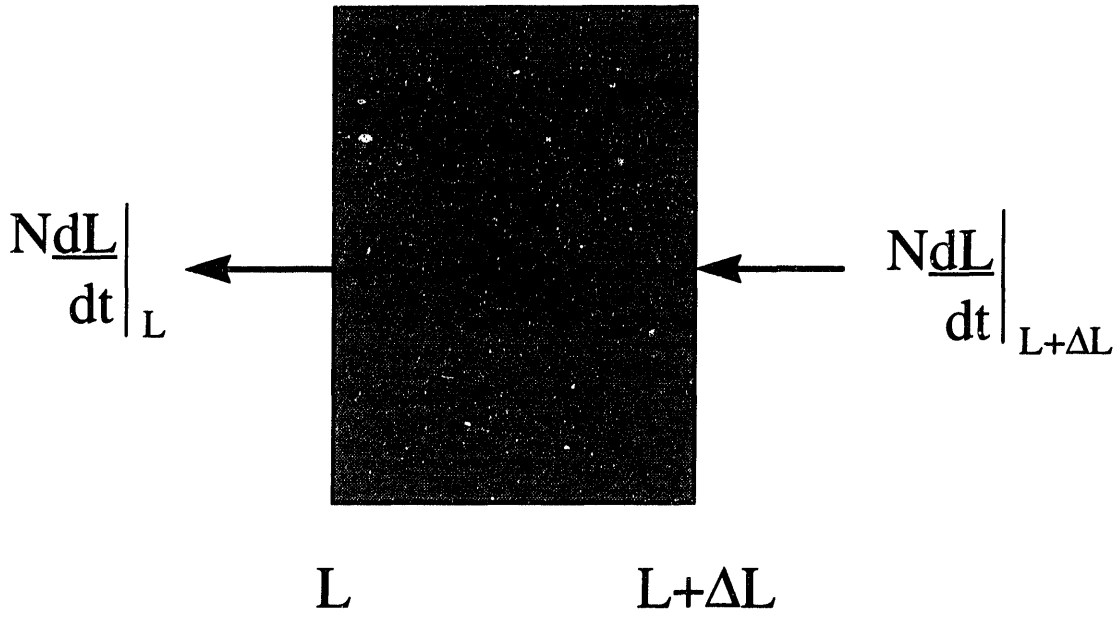

Figure 69. Population balance around L.

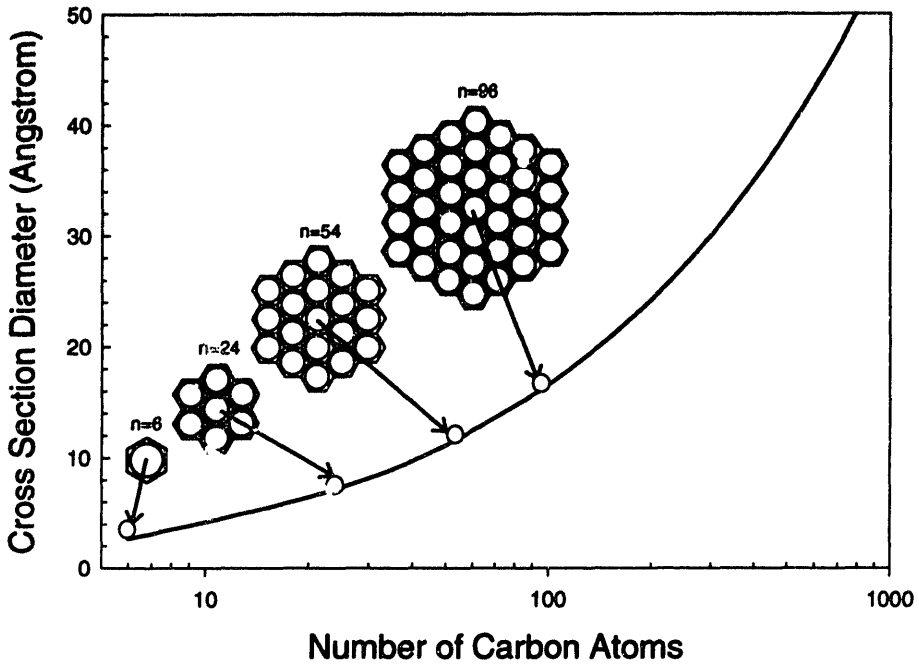

Figure 70. Variation in lattice length as a function of carbon atoms. The aromatic molecules depicted are the symmetric molecules that are assumed to represent the lengths images.

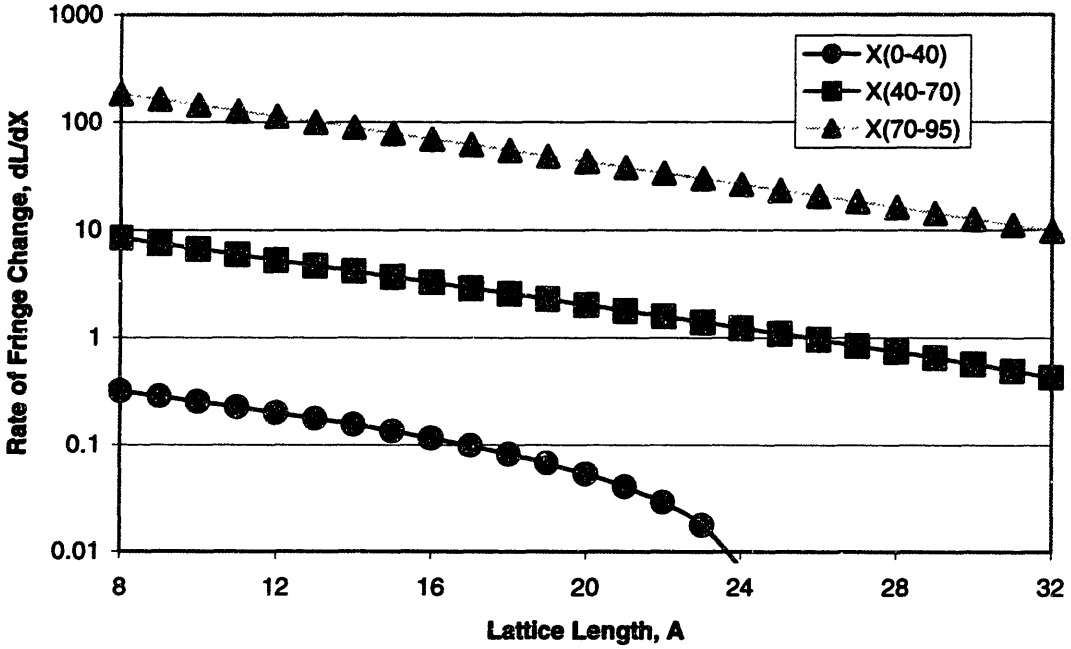

Figure 71. Reactivity of Fringe Lengths as a function of Lattice fringe length. The reactivity reaches an asymptotic value at about 15 A.

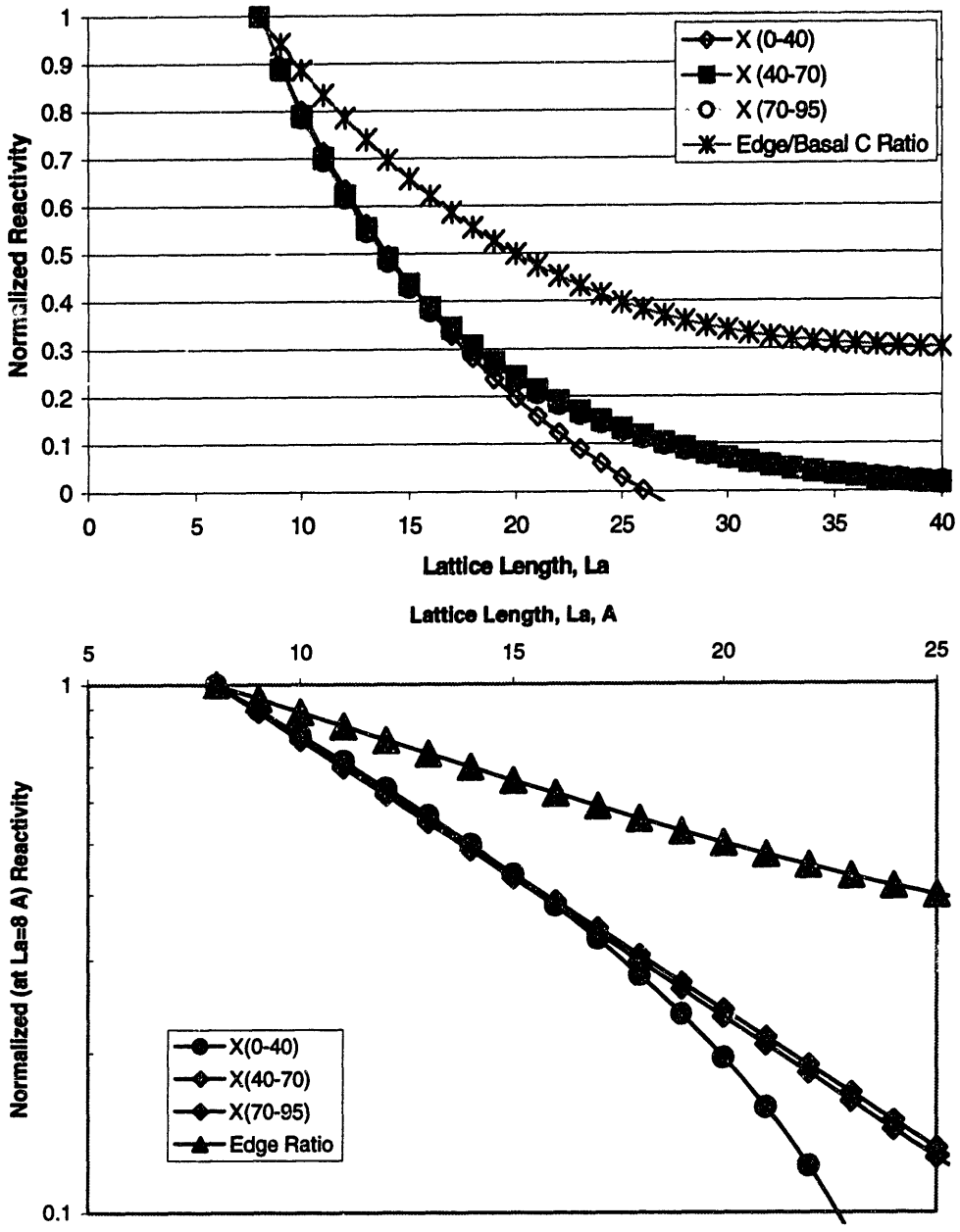

Figure 72. Reactivity of lattice fringes of Spherocarb, normalized at La = .7 nm

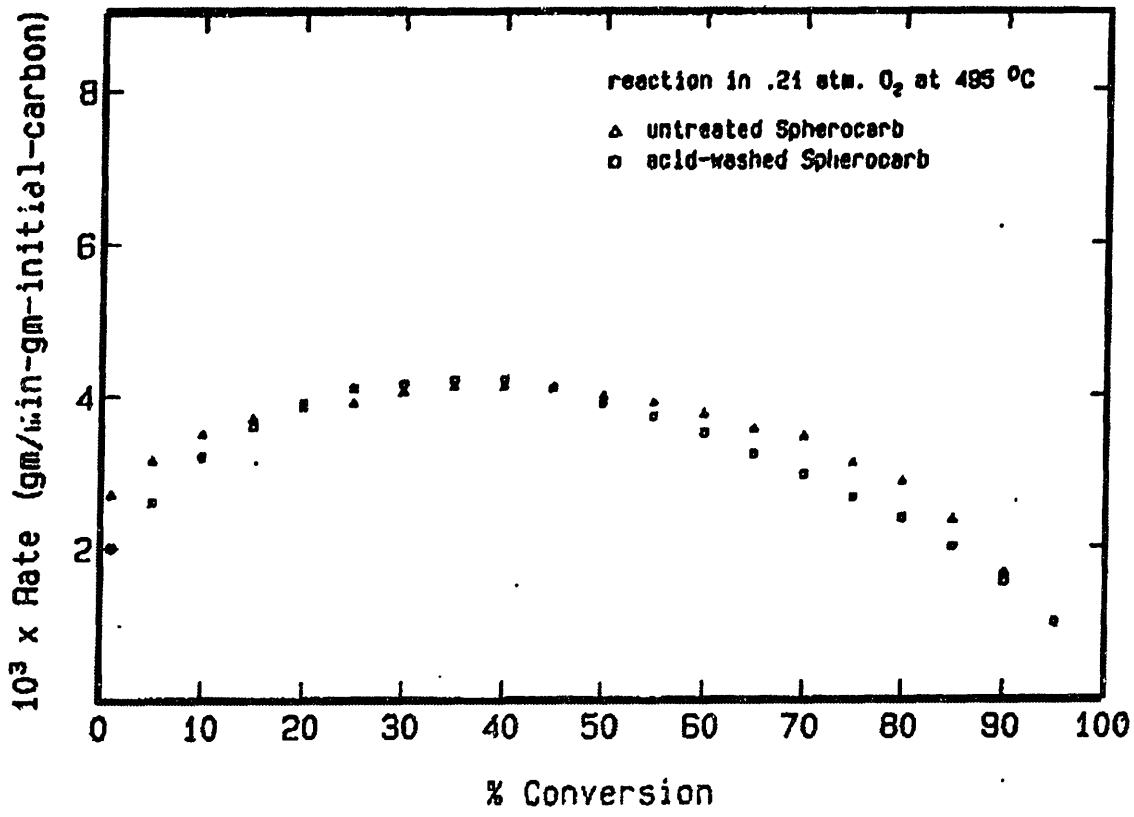

Figure 73. Acid washed Spherocarb reactivity.

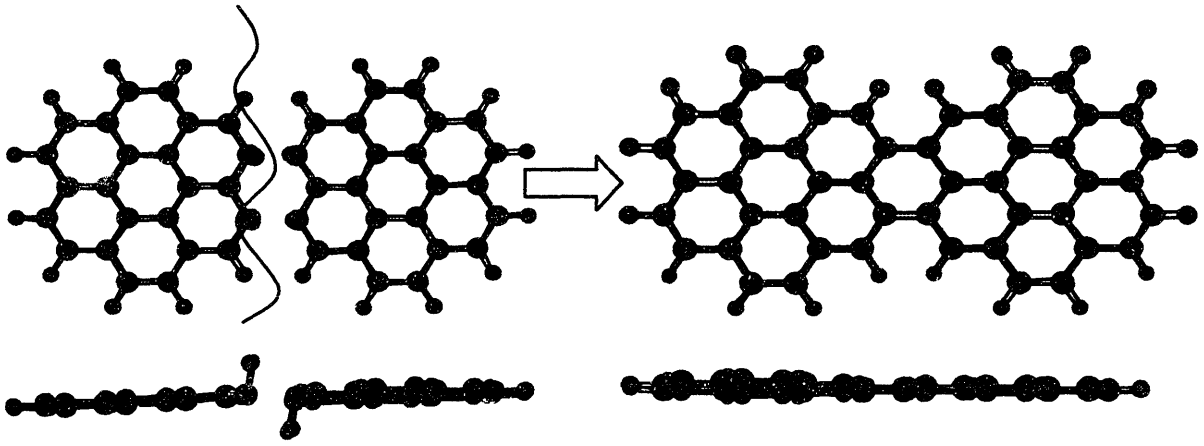

Figure 74. Ideal Case of Densification. The 2 correnene units are separated by an oxidizable element.

CHAPTER 8

8. Conclusions and Recommendations

8.1 CONCLUSIONS

A number of carbons of diverse origin have been studied in order to obtain a better understanding of the evolution of carbon properties during oxidation. Three aspects of this relationship were pursued: the role that macropores play in the combustion profile of coal char in a fluidized bed, the examination of the issue of closed and open porosity in soots, and the origin of the densification phenomenon and its effects on fragmentation.

Experimental measurements of the variation of CO_2 generation during combustion of single particles of coal char in an FBC were performed. A model of the combustion of char in Regime II was developed to explain the variation in CO_2 generation during the combustion of char particles in a FBC. The model assumed that there was no penetration of the particle by reaction gasses except for regions were porosity was evident. The model adequately explained the variations seen in the production of CO_2 for macropore sizes greater than approximately 0.5 mm. Comparison with pore sizes for Newlands and Illinois #6 chars showed that the criteria for relatively large variations in CO_2 production for a single char particle during combustion in an FBC may be met by chars with pores that are inaccessible to initial reactants.

During the modeling and experimental work involved with the FBC, it became evident from surface area evolution that, during combustion, most of the reaction was occurring in the micropores, with little reaction occurring in the macropores. This process was examined in more detail with novel techniques, including Small Angle X-ray Scattering (SAXS) and transmission electron microscopy (TEM). Two carbons were investigated, soots and Spherocarb.

Soot oxidation has many interesting combustion characteristics to recommend it for study. One such aspect is the high surface area generation during the initial stages of combustion, followed by a densification phenomenon. This densification phenomenon has been attributed to atomic rearrangements or tensile stress "peeling." A novel methodology to examine the same soot primary particle before and after oxidation was developed, and by identifying the same soot features, homogeneous rearrangement was confirmed as the source of this shrinkage.

To examine the issue of high surface area generation during low levels of oxidation, SAXS was used to examine total porosity, which includes porosity thought to be hidden by a "blocking" layer of carbon. There was a large amount of surface area generated during devolatilization of the sample, and a less pronounced generation of surface area during oxidation. Furthermore, SAXS analysis indicates that while there was hidden porosity in the soots, this porosity could not account for the generation of the large amounts of surface area developed during oxidation. However, a fractal analysis indicates that there was a large difference in the soot properties before devolatilization, after devolatilization, and after the introduction of oxygen. Before devolatilization, the soot has a smooth character ($D_s \sim 1.9$), while after devolatilization this surface becomes rougher ($D_2 \sim 2.3$). Once oxidation begins, the fractal nature of soot increases even more ($D_s \sim 2.9$). This indicates that while some of the surface area is generated due to revelation of inaccessible pores, a great deal of this area is the result of a roughening of the surface by reacting away the "blocking" layer. This outer layer of the soots is covered by short lattice length fringes, indicative of the blocking layer, and is probably formed by the deposition of large PAH molecules during the formation process.

The TEM imaging techniques originally used to examine soot[77] were applied to the model char compound Spherocarb. Spherocarb has been extensively used to model char oxidation reactions, notably in the electrodynamic balance (EDB). The densification

phenomenon has been extensively documented in Spherocarb, but only model inferences have been made. Using the TEM, distributions of the lattice fringe lengths, L_a, fractional coverage, C, and d_{002} spacings were measured. During oxidation, the d_{002} spacings tended to decrease slightly, although it was difficult to state this conclusively due to the large distribution of spacings. However, the lattice fringe lengths, an indication of the fundamental size of the basic structural unit of carbon, increased during oxidation from about 1 nm to approximately 1.5 nm in length. The fractional coverage, which can be thought of as a rough measure of order and density, increased from a value of 21.9% to 24.5%. The increase in lattice structure has not been observed previously during low temperature oxidation, although structural ordering has been observed in the residual carbon of high temperature (2000K+) commercial pulverized coal plants.[148] This transformation is the microscopic linkage between macro structural shrinkage and the actual atomic rearrangements of the Spherocarb char. This has important implications for the issue of fragmentation, as the structural transformation allows the Spherocarb to retain its shape past the theoretical percolative fragmentation limit.

While the issue of densification has been proven relatively conclusively to be accompanied with (caused) by structural transformations, the issue of how the transformation effects reactivity is not as clear. The possible presence of graphite (possibly as a shell) makes the measurement of structural transformations difficult. Analogies to graphite would indicate that large lattice fringes would have smaller amounts of edge carbon, resulting in a decrease of reactivity with structural ordering, which is the exact opposite effect observed for Spherocarb.

Population balances on the fringes further indicate that the overall reactivity of fringes increases during oxidation. This change is attributed to three possible causes:

1. Catalysis: As oxidation removes carbon, if the catalysts remains in the lattice network and are mobile, reactivity will increase as the grams of catalyst/gram carbon ratio increases.

2. While oxidation removes carbon atoms that cause structural defects, insufficient energy is present in the system at low temperatures to anneal many of the defects. Therefore, while lattice fringes lengthen during reaction, the ratio of defects to carbon mass may actually increases during oxidation, increasing the reactivity of the Spherocarb.
3. Chemisorption: It has been shown for very disordered carbons that an increase in ordering will accompany an increase in chemisorption of oxygen. Since the Spherocarb is going from an analogous low order to higher ordered structure, a similar effect may be occurring.

8.2 PARALLELS BETWEEN SOOT AND SPHEROCARB

While soot and Spherocarb char come from vastly different sources, and are treated as separate materials in this thesis, a comparison of their structural transformations does yield additional insight into various processes, such as densification, and its effect on reactivity.

8.2.1 Reactivity

The intrinsic reactivities of Spherocarb and soot are plotted in

Figure 75, along with a number of other carbons. A summary of the reaction conditions of the plotted coals is given in Table 6. All of the plots assume that there is complete penetration of oxygen into the particle interior during reaction. There is a relatively wide range of reactivities, as would be expected from the different temperatures and properties of the material represented. The range of reactivities also correspond well with the reactivity range reported by Smith et al[2] in Figure 1, although they are on the lower side of the reactivity range

As can be seen in

Figure 75, the reactivities of the soots used in this study are actually quite close to one another. While the NIST soot follows the trend "expected" for carbon, that of continued mildly decreasing reactivity with conversion, the NEU soot increases in reactivity with conversion. The

reactivity of the soots compares well to that of the soot used by Du.[34] The reactivities between the soot samples are different by an order of magnitude for the initial starting material, but equalize during reaction, indicating that the soot skeletal structures are approximately the same for these systems, but the actual hydrocarbon species that are contained in the soots are not.

In comparison, other carbons are not as well behaved in falling upon one another. The reactivity of three coals, PSOC 176,[135] Illinois #6,[136] and a Lignite[136] are also plotted in Figure 75. Disregarding the initial reactivities, which may be effected by limitations in mass transfer, heating rate, and devolatilization conditions, the PSOC 176 coal is the most highly reactive, and this reactivity does not change during reaction. Both the Illinois #6 and the lignite have changes in reactivity, with a low initial reactivity that increases with conversion. However, all three coals exhibit a relatively small change in reactivity with conversion

The reactivity of the synthetic(plain polymer-pp) chars[137] is also relatively constant with conversion, with reactivities comparable to that of the PSOC 176 char. The difference between the polymer chars (high and low porosity) is generated by the addition of carbon black to increase porosity. The carbon black also appears to act in a catalytic fashion in respect to the reactivity, although this may be also a function of the changes in surface area of the system.

The Spherocarb, while of much lower reactivity than the plain-polymer chars, also exhibits a similar increase in reactivity with conversion as the high porosity polymer char and the Illinois #6 char. The Spherocarb reactivity of this study also agrees well with the reactivity measured by other researchers, although slightly lower. However, the very large change in reactivity for the Spherocarb does not seem to match other carbons, except possibly the plain-polymer high porosity char. This may be an indication that the carbon black added to the plain polymer may act in a similar manner as the "graphitic" inclusions seen in the Spherocarb.

8.2.2 Densification

The reactivities of Spherocarb and soot are not directly comparable in an absolute sense. However, the issue of densification is directly comparable between carbonaceous systems. Plotted in Figure 76 is the Spherocarb and Soot change in volume as a function of conversion, along with size changes seen in other carbon studies.

The Spherocarb and soot studied herein have volume changes that are comparable with past measurements of chars that undergo the densification phenomenon. However, the locations of the structural rearrangements that occur are quite different for the two types of materials. As illustrated for soot in Chapter 5, the structural rearrangements that seem to cause the densification phenomena seem to occur more readily in the outer layers of the soot, most probably due to different structural properties. In contrast (Chapter 7), the Spherocarb rearrangements appear to be, except for possibly the graphitic "edges," happening throughout the Spherocarb particle.

One of the most interesting items to note is the PSOC 1451 char that is devolatilized at two different temperatures, 1200K and 1600K.[138] While both chars share some of the same properties due to the common parent coal, the densification is different for the two chars. The 1600K char does not exhibit densification, while the 1200K char does. Wong et al. attributed this to increased graphitization of the chars, as evidenced by the loss of finer pores. This would support the notion that the maximum temperature where densification would be expected to occur would be about 1300-1500K, the point where structural rearrangements (graphitization) begin to occur due to temperature effects.

8.3 RECOMMENDATIONS FOR FUTURE WORK

The issue of densification has been investigated by direct observation of carbon structural transformation in soots and Spherocarb. However, the issue of the change in reactivity with conversion is a subject well worth exploring further. While normalization by remaining carbon is not usually done in combustion experiments, it is a useful tool when following carbon reactivity evolution. The increase in reactivity that is shown for Spherocarb and NEU soot does not follow the conventional wisdom of greater order, less reactivity, and high burnout, low reactivity.

The reactivity change in Spherocarb should be followed more closely, especially at different temperatures than the ones explored here to gain a better understanding of this ordering phenomenon. Furthermore, a time-temperature series on structural ordering would allow one to obtain an estimation of the activation energy of this structural ordering, an important criteria for determining its importance to combustion modeling. The answers to the question of why the reactivity goes up may also be accomplished with a series of oxygen chemisorption experiments on the Spherocarb, as it could confirm/ eliminate one of the possible reasons for this increase.

Furthermore, a more detailed investigation on the actual structure that initially comprises Spherocarb should be performed. There is a possibility that the graphite does form a shell, and this would certainly effect diffusion in the system. If it is distributed, the assumptions used in percolative fragmentation (specifically, homogeneous material) is circumspect, and thus the issue needs to be examined.

The other general topic that should be addressed deals with microscopy. As can be seen in this thesis, there is still not an adequate theory linking TEM observations on the microscale with large macroscale combustion systems. However, the following recommendations concerning the microscopy can be made:

1) Ideally, the densification of soot should be investigated further with the combustion resistant grid, but with much larger "as received" soots. Some carbon blacks are in the 200 nm range, and would be ideal for this, assuming that they are not already extensively graphitized. A goniometer stage series, that would allow rotational movement of the soot during TEM work, would also be useful to compensate for movement of soots during combustion.

2) The TEM structure should be pursued aggressively, although perhaps not with Spherocarb due to possible heterogeneity with the graphitic inclusions observed. Again, a three-dimensionally spatially oriented data series, such as can be obtained by using a goniometer stage, would be helpful in reconstructing the skeletal frame of the Spherocarb.

Table 6. Oxidation conditions and surface areas for carbons used in Figure 75.

Sample	Temp K	Reaction Gas	Initial Surface Area (gas type) (m^2/g)	Final (Max) Surface Area (m^2/g)
Ethylene Soot, catalyzed by Ca[34]	773	Air	100 (CO_2)	650
Plain Polymer, low Porosity[137]	773	Air	2 (300) (N_2)† 59 (560) (CO_2)	
Plain Polymer +25% Carbon Black, High Porosity Synthetic Char [137]	773	Air	184 (360) (N_2)†	
PSOC 176 Bituminous Coal[135]	800	17% O_2	56 (N_2)	450
Lignite Coal[136]	701	5% O_2	488.7(CO_2)	390
Illinois #6 Bituminous Coal[136]	799	5% O_2	530.8 (N_2)	
Spherocarb Char[14]	768	Air	1000 (CO_2)	600
NIST Soot, this study	773	Air	50 (274)‡	~425
NEU Soot, this study	773	Air	93(367)‡	~400*
Spherocarb, this study	773	Air	1000 (CO_2)	600

† The higher values are after 15% oxidation
‡ The higher number represents the value after devolatilization.

Table 7. Oxidation conditions used in densification comparison of Figure 76.

Sample	Reaction System	Atmosphere	Temperature (K)
Diesel Soot, Ishiguro[15]	Furnace	Air	773
Spherocarb (Hurt) [14]	EDB/TGA	Air	768
Spherocarb(Waters)[103]	EDB	Air	800-100
Bituminous (PSOC 1451) Coal, Devolatilized at 1200K[138]	EDB	Air	800 ± 50
Bituminous (PSOC 1451) Coal, Devolatilized at 1600K[138]	EDB	Air	800 ± 50
NIST Soot, this Study	TGA	Air	773
Spherocarb, this Study	TGA	Air	773

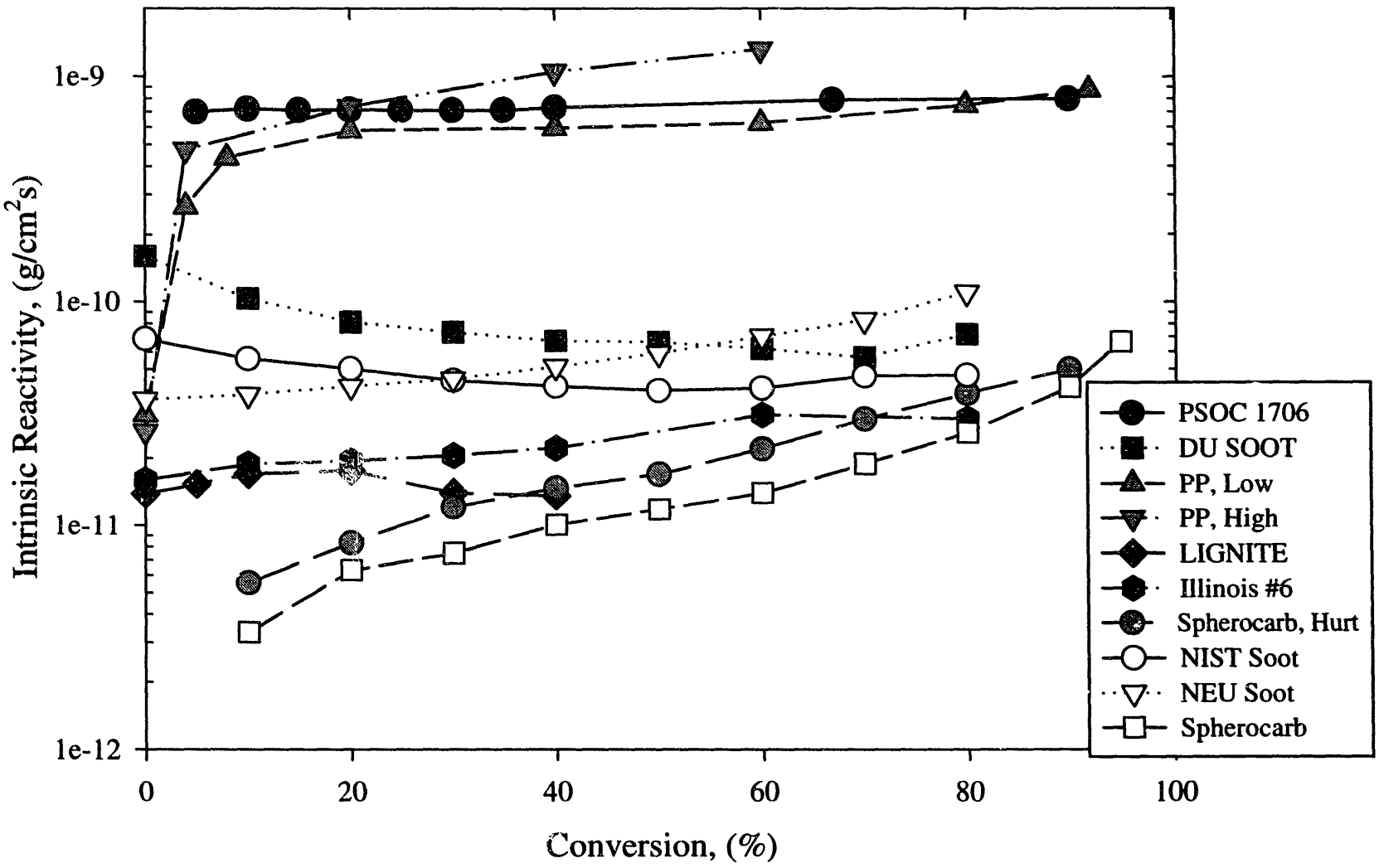

Figure 75. Intrinsic reactivity of selected carbons

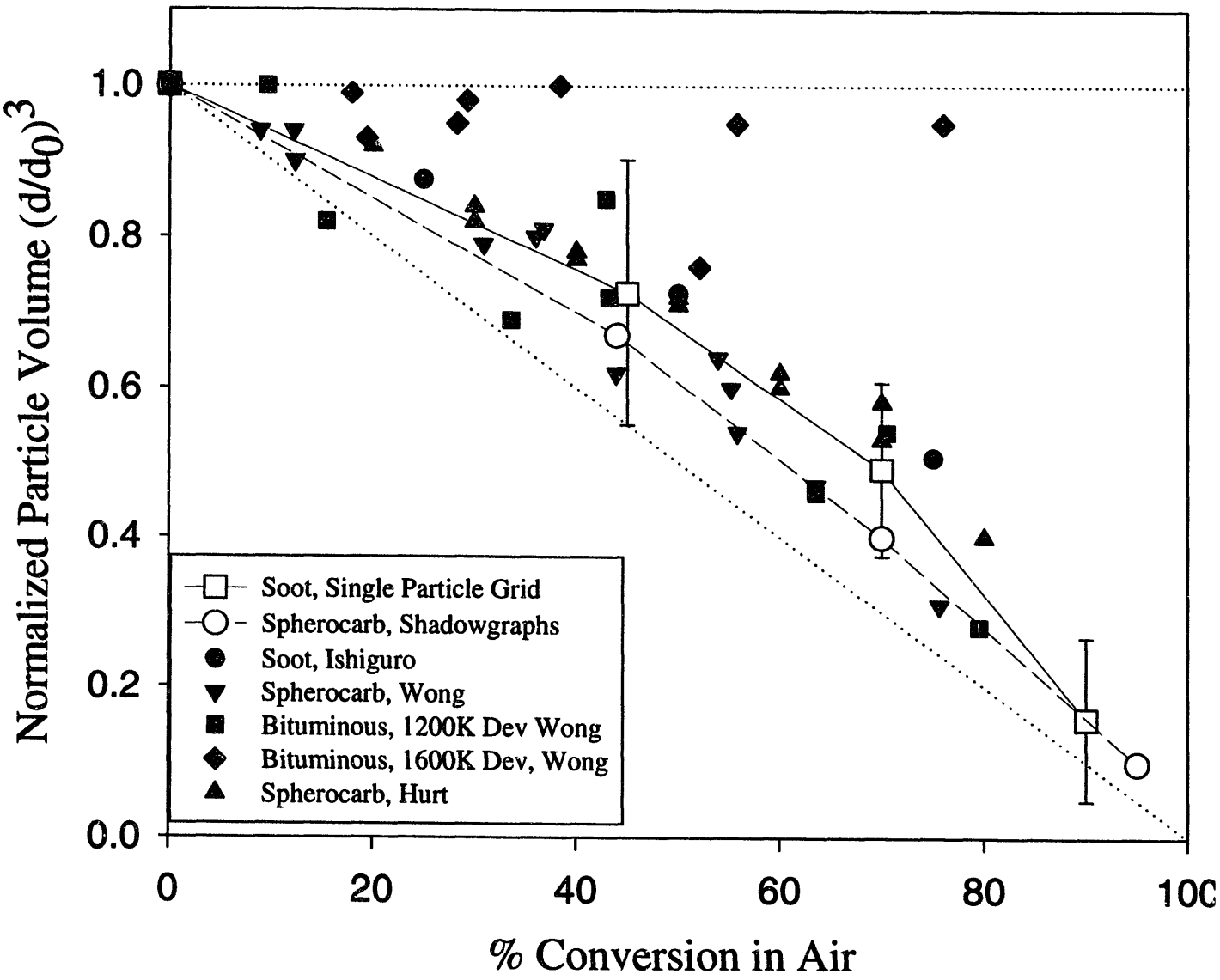

Figure 76. Variation in particle volume (densification) with conversion.

Appendix A. Summary of the Theory of HRTEM Light Imaging of Carbon

The study of carbons using the TEM is one of the principal methods used in this thesis. However, the science of carbon imaging with the TEM is quite diffuse, ranging over numerous fields. Issues such as the transfer function of the TEM, focusing, and astigmatism confuse an issue already made complicated by the inherent three-dimensional nature of carbon steriology. Complex methodologies such as defocusing, axial illumination, tilted illumination and the like often have been used to characterize the complex, randomly oriented crystals in carbons. However, despite its complexity, the TEM provides an excellent compliment to "blind" statistical methods such as x-ray diffraction and spectroscopy, as a picture is sometimes worth more than a thousand charts when understanding the nature of carbon. This appendix is an attempt to present some of the essential theory for imaging carbons, and some of its limitations. Much of this section is based on excellent reference series *Chemistry and Physics of Carbon,*[139,140] and works by Olander[109,140] and Marsh[9,10,122,124] that deal with carbon structure and microscopy.

To begin the examination of carbon, one must first understand the composition of carbon. All carbonaceous materials can be considered to be made up of similar building blocks arranged in different manners. This elemental unit is referred to in microscopy terms as the basic structural unit, BSU, and is thought to contain planar aromatic structures consisting of 10-20 rings arranged in parallel stack heights of two to four layers. There are only two symmetries that need be considered in carbon studies, spherical or cylindrical. For most turbostratic carbon

examples, spherical symmetry predominates, either in statically spherical symmetry with crumpled sheets or in the case of graphitic structures, infinite spherical radius.[140]

A.1 OPERATOR MICROCOPE PARAMETERS

Before proceeding to the theory involving the processing of TEM micrographs, one must first understand a typical TEM, a schematic of which is depicted in Figure 3. An excellent source for operating instructions is *Introduction to TEM*[141]. The most important factors that are subject to user control in generating a resolvable image are

(1) Accelerating Voltage: Simply put, the power of the microscope. The higher the voltage, the more the electrons will penetrate the sample, allowing for thicker samples. However, more sensitive samples are subject to damage from very energy electrons, so care must be taken. The wavelength of the electrons is given by

$$\lambda = \frac{h}{p} = h(2meE)^{-1/2} \qquad (42)$$

where h is Planck's Constant, p is the electron momentum, E is the accelerating voltage, and e and m are the electron charge and mass. Neglecting relativistic electrons, $\lambda = (150/E)^{1/2}$, or 0.37 nm for an accelerating voltage of 100 keV.

(2) Condenser Aperture: This device acts to make the beam of electrons of coherent energy to minimize variations in intensity from "spreading" of the source power.

(3) Objective Lens: The electron focusing point of the lens. Electromagnetic lenses are subject to high amounts of spherical aberrations that limit the resolution.

(4) Focusing/Astigmatism: The process of tuning the objective lens so that the object is in focus with no preferential alignments highlighted.

A.2 THEORY OF LIGHT FIELD IMAGING: OPTICAL DIFFRACTION

PATTERNS AND TRANSFER FUNCTIONS

From (002) light field micrographs, the length of a perfect fringe (L1) and the distorted fringes (L2) can be measured. The number, N, of fringes in a stack can also be measured. To simplify these measurements, Taylor and Lipson[142] and Ban[143] used laser sources to obtain optical diffraction patterns when laser light passed through a TEM negative. Classically, a He/Ne laser beam (λ= 632.8 nm) optical bench was used to obtain optical diffraction patterns (ODP), as shown Figure 77. The optical transform provided information, in the form of a spatial frequency intensity map, about the distribution of optical density on the electron micrograph, this is in turn directly related to the electron intensity distribution in the original image.

One of the problems encountered with the ODP system depicted in Figure 77 is the issue of magnification. Slight errors in placement of the negative can lead to large errors in magnification. However, modern computers and digital scanners have neatly solved this problem. One can use a modern digital scanner to obtain the pattern that would normally reach the diffraction lens. Once can then mimic the optic lens by performing the same function of the lens electronically, by taking the Fourier transform of the image mathematically. During the course of this thesis, performance of this operation (referred to previously as "taking a power spectrum") has improved from approximately 3 minutes (Intel 486DX66 microprocessor) for a 256 pixel radius scanned image to less than 15 seconds (Intel Pentium 133 MHz microprocessor).

An example of the differences and inherent limitations of TEM microscopy is shown in Figure 78. The electron micrographs (a-c) are from a focal series taken of a single region of a polyvinyl chloride (PVC) sample graphitized at 815°C. The general appearance of the image

fringes is similar at each focal position, but critical inspection shows many differences of detail. Unfortunately, one cannot quantify these differences without ODP techniques. Applying the ODP technique, the transform intensity of zero is indicated as black (0%) and increasing transmitted intensity is shown by increasing the grey level until complete transmittal is represented as white (100%). The scattered light intensity patterns are quite distinct in each of the three cases, and these differences can only result from dissimilarities in the information recorded on the respective electron micrographs. Clearly, if micrographs are used to characterize the specimen quantitatively, the answer obtained depends upon which original micrograph is chosen for analysis. Therefore, it is of utmost importance to critically assign which, if any, of the electron micrographs most closely represent the structure.

The relationship between fringes and the corresponding family of lattice planes depends on the transfer function of the lens, an essential concept in microscopy. The phase contrast transfer function $\sin \chi(s)$, assuming a thin phase/amplitude grating, is used in the following equation for electron microscopy

$$A_D(s) = \delta(0) - \sigma V(s) \sin \chi(s) \tag{43}$$

where A_D is the wave function in the back-focal (diffraction) plane of the imaging system and s represent the generalized reciprocal space coordinates. The symbol $\sigma = \pi/\lambda W$, where λ and W are the relativistically corrected values of the electron wavelength and acceleration potential. The Dirac delta function $\delta(0)$ represents the primary beam, while V(s) is a Fourier transform of the potential distribution in the object projected onto a plane normal to the optic axis of the microscope. The Fourier transform mathematically represents the process that electron lenses perform.

The transfer function, a.k.a. phase contrast function, sin $\chi(s)$, is a description of how accurately information is transferred from the object plane to the image plane. When sin $\chi(s) = 0$, no information is contained in the image related to the corresponding object structure. However, if sin $\chi(s) = 1$, the appropriate object detail is transferred with maximum contrast.

To demonstrate the importance of sin $\chi(s)$, consider the case of a perfectly ordered graphite crystal oriented for 002 lattice imaging (spacing 0.34 nm) and of effectively infinite lateral extent for a Phillips EM300 electron microscope ($C_s = 1.6$ mm) operating at 100kV. The electrons will be scattered at a precise angle corresponding to a single spatial frequency of 1/0.34 nm^{-1}. As shown in Figure 79, if the objective lens is not focused properly, the graphitic layer contrast will be quite weak. Proper focusing allows the lattice planes to be observed with the maximum achievable positive and negative contrast. This focusing must be done carefully, as seen in the 3-dimensional transfer function in Figure 82, where astigmatism would lead to improper reinforcing in one spatial direction.

Ideally, one wants a transfer function as seen in Figure 80, but with a "plateau," where sin $\chi(s)$ is near unity, broadened to encompass a wider range of spatial frequencies. One must examine the Scherrer equation for the instrumental phase factor $\chi(s)$ as a function of the scattering angle $\alpha(s)$ defined as

$$\chi(s) = \frac{2\pi}{\lambda}\left[\frac{1}{2}DF\alpha(s) - \frac{1}{4}C_s\alpha^2(s)\right] \tag{44}$$

to understand how to change $\chi(s)$.

There are three possible ways of affecting $\chi(s)$, the lens aberration defect of focus (DF), the spherical coefficient (C_s), and the wavelength, λ. To a first order approximation, the DF and

C_s terms are are inherent in the design of the TEM, while λ is a function of the accelerating voltage. The effect of improving the spherical aberration of the microscope is shown in Figure 80. The actual transfer function of the Akashi 002B used in this work is very close to the bottom of Figure 80. The vast improvements are due to a low C_s(0.5mm), a much smaller DF, and a higher accelerating voltage. The use of better electronic controls in future versions of TEM will undoubtedly improve this value further.

One must ask "why go into great detail about the transfer function?" The answer is that the transfer function of the microscope is directly related to the information content of the optical transform. To clarify this, one needs to examine the relationship between transform intensity and the original structure of the specimen investigated in the electron microscope.

In the optical diffraction system, we assume the electron micrograph is illuminated with a plane wave of unit amplitude. The intensity of the transmitted light through the object is governed by the distribution of transmissivity over the micrograph, so

$$I_0(r) = 10^{-D(r)} \tag{45}$$

Where D(r) is the distribution of optical density on the electron micrograph and $I_0(r)$ is the intensity of transmitted light. The wave amplitude of the light immediately after interaction with the electron micrograph may then be written as

$$\psi_0(r) = 10^{-D(r)/2} \tag{46}$$

Assuming that the plate acts as a pure amplitude object.

D(r) is linearly related by K to the time of exposure of the image intensity in the electron microscope, $I_I(r)$, or

$$D(r) = KI_I(r) \tag{47}$$

Giving

$$\psi_0(r) = \exp[-K'I_I(r)] \tag{48}$$

in exponential form.

When combined with a transformation of (41) and a convolution transform, the optical transform intensity, I_T, becomes

$$I_T(s) = \delta(0) + K'4\sigma^2 V^2(s)\sin^2\chi(s) \tag{49}$$

The feature of most importance in the above equation is that the optical transform intensity is a function of the square of the transfer function. The dependence on sin $\chi(s)$ may be observed in optical transforms prepared from electron micrographs of amorphous evaporated thin films of carbon. The distribution of electrons scattered by this carbon is fairly uniform over a wide range of frequencies and under ideal imaging conditions the optical transform will exhibit a corresponding distribution in optical intensity. In practice, image aberrations cause the transform intensity to by modulated by sin $\chi(s)$, and can be used to characterize the TEM.

Figure 81 demonstrates this effect, where the differences in a single region of a thin, evaporated carbon film are shown for various levels of defocus. Only image b can be thought of as "in focus." The rest of the images have periodic spacings that are related to the transfer function of the TEM system, and not the sample itself.

A.3 THEORY OF LIGHT FIELD IMAGING: SAMPLE THICKNESS AND LINE LENGTH

In the preceding discussion, the specimen was assumed to be thin enough to behave as a weak phase object, or in other words, the electrons are considered to be scattered once. In the general case, multiple scattering of electrons does occur, and is related to the thickness of the

sample. The most convenient way of modeling this effect is the multislice approach of Cowley and Moodie.[144] In this approach, the crystal is divided into slices that are thin enough so that multiple scattering within a slice is negligible. The potential within each slice is considered projected onto an internal plane, and the crystal is thus represented as a series of scattering planes separated by vacuum gaps. The electron wave effect is then simply a sum of the changes each phase brings about.

The studies of Jefferson and coworkers[145] in the formation of d_{002} lattice images of graphitic carbons showed that for linear transfer theory to be possible, the specimen thickness must be no more than 5 nm. In particular, secondary fringes predominate at thicknesses of 11.5 nm, and this result is repeated periodically for thick samples. However, Jefferson and Millward concluded that, provided that spherical aberration is low and defocus is appropriately chosen, the effect of multiple scattering on the information relating to the shape of the crystal is not particularly important. This is due to the weak nature of these interactions for thin sample thickness, and as a practical matter, modern instruments have a thickness limit of approximately 10 nm.

The limit of 10 nm on sample thickness is also a result of the limitation to the size of crystal domains. As the crystal size decreases, the Bragg condition (a function of the fact that the microscope only illuminates fringes that fulfill a narrow window of the Bragg angle given by $2d\sin\theta=\lambda$, where d is the distance between scatters) becomes less and less strict so that an increasing error relative to the Bragg angle becomes possible without losing too much of the scattered beam intensity. For example, for a 2 layer carbon particle with a 1 nm thickness, the intensity will reach a maximum when the angle reaches θ_{002} (~ 5×10^{-3} rad, about 10^{o}), as shown

in Figure 83. However, the beam will vanish if the specimen's tilt reaches an angle α of approximately $+d_{002}/2t$, or about $18x10^{-2}$ rad. A $2\theta_{002}$ tilting is negligible at this point, and a large degree of error is allowed. As the thickness increases to 10 nm, the maximum tilt, α, is approximately 10 times less, or $18x10^{-3}$ rad, or slightly more than 2θ. This is another reason the practical limit of carbon microscopy is about 10 nm. If α becomes less that 2θ, the ability to satisfy the practical limit of fulfilling the Bragg angle becomes too great.

The overlap is especially important to turbostratic carbon, where there are a large number of superimposed layers. Electron beams scattered from this material are close to each other and can pass through the aperture. For graphitic crystals superimposed at random one can develop rotational moires. These rotational moires are shown in Figure 84, showing the destructive interference that can occur with overlap. This limits turbostratic information to only mean length and distribution of fringes, and not shape.

The diffraction limitation of about 10° also becomes important in understanding a possible cause of the reported "hole" in many carbon blacks and soots,[146] as seen in Figure 86. The question is whether it is a hole, an amorphous or nearly amorphous region, or something else. One must first assume that the basic structural unit, BSU, of a particle is layered in concentric circles. Then, analysis must be made on two adjacent BSUs that form a basis for concentric shells within a soot primary particle, as shown in Figure 87.

Letting OB be the bisector of AOC, the angle CBO is then equal to angle ABO. If the BSU of AB fulfills the 002 Bragg condition, BOA is 10° at the maximum. Therefore, the BSU of CB cannot be imaged. The radius of the circle OA is then given by

$$\frac{AB}{OA} = \tan 10^{o} \tag{50}$$

Assuming that OA bisects the BSU, then the radius of OA is simply

$$OA = \frac{AB}{\tan 10^{\circ}} = \frac{0.5\,nm}{0.176} = 2.8\,nm \tag{51}$$

Therefore, there is a theoretical limit of 5.6 nm in sample width. For areas less than this limit, no TEM fringes will be observed.

However, the limit of 5.6 nm assumes that the onion-like structures proposed by Lahaye and Prado[147] for primary particles extends to the limit of the inner core of the particle. This clearly ignores the differences between the two principle mechanisms in the formation of primary particles, nucleation and deposition. There is no reason that the nucleation of the soot particle will be preferentially form the "onion" layers that later depositions will, as can been seen in Chapter 5, instead of flat platelletes. Therefore, the "hole" in the center, while non-imagable, is probably not a true hole, but representative of structural differences and a more amorphous carbon nature.

Another issue that one must deal with is steriology, the projection of the 3 dimensional geometric structure that makes up carbon unto the 2 dimensional image plane. The simplest way to deal with this structure is to assume that the basic aromatic structures that make up the carbon can be considered "lines" in space (The misorientation of the aromatic layers, due to the Bragg condition and simple contrast limitations, will force only relatively straight lines to appear). One can use the fundamental relationship for projected lines relating the mean projected length of a straight, randomly oriented line segment to the true length.

Since any line can be broken up into line segements of length δl, one can consider an elementary segment of length δl with one end fixed that is free to rotate in any direction θ or ϕ

(ie, anywhere in a sphere of radius δl). Figure 85 shows one octant of the surface. The average projected line length, $\overline{\delta l'}$, is then given by

$$\overline{\partial l'} = \frac{\int_0^{\pi/2}\int_0^{\pi/2} \delta l \sin\theta \, \delta l^2 \sin\theta \, d\theta d\phi}{\pi \delta l^2 / 2} \tag{52}$$

$$\overline{\partial l'} = \frac{2\delta l}{\pi}\int_0^{\pi/2}\int_0^{\pi/2} \sin\theta^{\,2} d\theta d\phi = \delta l \int_0^{\pi/2} \sin\theta^{\,2} d\theta = \frac{\pi}{4}\delta l \tag{53}$$

Since the line L can be represented by a series of elementary colinear segments, $L = \Sigma\delta l$ and

$$L = (\frac{4}{\pi})\overline{\delta L'} \tag{54}$$

Where $\overline{\delta L'}$ is the mean line length on the projected plane. This value provides an upper bound for the error, as the limitation of fulfilling the Bragg condition will limit the arc of the fringes to a narrow region, decreasing this difference.

Once the lattice fringe images has have been generated (checked with the ODP method or the Fourier transform), we are left with an image of the lattice fringes, as depicted in various figures throughout this thesis. Assuming that optimal defocus has been achieved and no other defects (such as astigmatism) are present, the most important question remains, what exactly do these fringes (lines) represent?

A.4 THEORY OF LIGHT FIELD IMAGING: INTERPRETATION OF FRINGE "LINES"

The following questions must be answered before any analysis of a distribution of lengths, and for simplicity, we will refer to Figure 88, which provides a grossly simplified image of an extracted pattern.:

What are the dark (light) lines?

The dark lines represent positions of potential, i.e. carbon atoms. Under most conditions, the dark lines represent absorption and scattering of electrons, indicating the presence of carbon atoms. However, a reversed contrast image function (see Figure 79d) would result in the opposite effect. In Figure 88, the dark lines represent carbon atoms lattice fringe structures (which we assume perfectly represent the sample).

Can the dark lines arise from inadequate resolution of small molecules?

All microscopes have a resolution limit, and it a key to understanding this question. In Figure 88, between lines C and D, there is a small gap. If this gap is larger than the resolution limit of the microscope, there will be a measurable gap in the system. However, if the gap is smaller than the resolution limit, than lines C and D will appear joined, with lengths approximately that of lines A and B.

The resolution of the Akashi 002B electron microscope used in this work is 0.16 nm. This resolution limit is larger than the average carbon-carbon aromatic bond (0.14 nm), and any defects smaller than this will not be observable. Localized defects such as a fault internal to a large molecule may be invisible, giving a dark line that is longer than the true length of the constituent segments. This effect suggests that annealing large internal defects in a "molecule" can produce long dark lines in images(i.e., pulling atoms into a more planar configuration will lead to "larger molecules".

Can lengthen dark lines appear from something other than lengthened molecules?

Marsh showed, using a multislice approach, that projection of a 15 carbon model compound (at maximum) showed no increase in lattice length, whereas a thickness of 32 atom

projected compound produced long, contorted lines. It should be noted that for most carbon systems, assuming an aromatic type structure, 15-carbon atom thickness represents a length of approximately 2.3 nm, while a length of 32 atoms represents lengths on the order of 5 nm. Lengths of the order 3 nm are seen in images of turbostratic carbons, but are rarely longer, indicating that is not of sizable concern.

Another factor that may arise is shown in the meeting of lines D and G in Figure 88. Clearly, the lattices are from separate systems, but in the microscope would appear to be one lattice. This illustrates the fact that such systems rarely show lines that are straight. However, as can be shown by numerous examples of graphitized carbon blacks and nanotubes, bends in continuous graphitic sheets are possible by inclusion of a single 5-member ring. Therefore, one must not separate out only the straight-line segments.

Can short lines arise from factors other than the predominance of short "molecules"?

A mechanism that can produce short dark lines arises from orientation effects of large molecules and simple absorption by carbon of electrons. Assuming no diffraction occurs, and carbon absorbs electrons linearly, then a system 20 atoms thick will absorb twice as many electrons, resulting in a line that is half as intense as a system that is 10 atoms thick. Marsh found that projections of greater than 14 atoms resulted in decreased spacing between dark lines, or the lengthening of existing dark lines. This mechanism should not be a large factor in turbostratic carbon, although the carbon thickness is usually above 3 nm (the thickness of required for a projection of greater than 14 atoms). This is because the layers are not oriented in a specific manner in turbostratic carbons. However, it does suggest that short images near the

edge of the material should be carefully examined to ensure that fringes do not to arise from simple thickness effects.

Overall, from the above discussion, light fringe imaging is a complex field of study. However, it allows one to examine turbostratic carbons in ways that are impossible with other methods, such as X-ray diffraction. In general, the true size of the constituent projections will tend to be overestimated. However, while the absolute size may be larger than in reality, the shorter fringes are a good estimate of disorder, while the lengthening of these lines is an important indicator of order

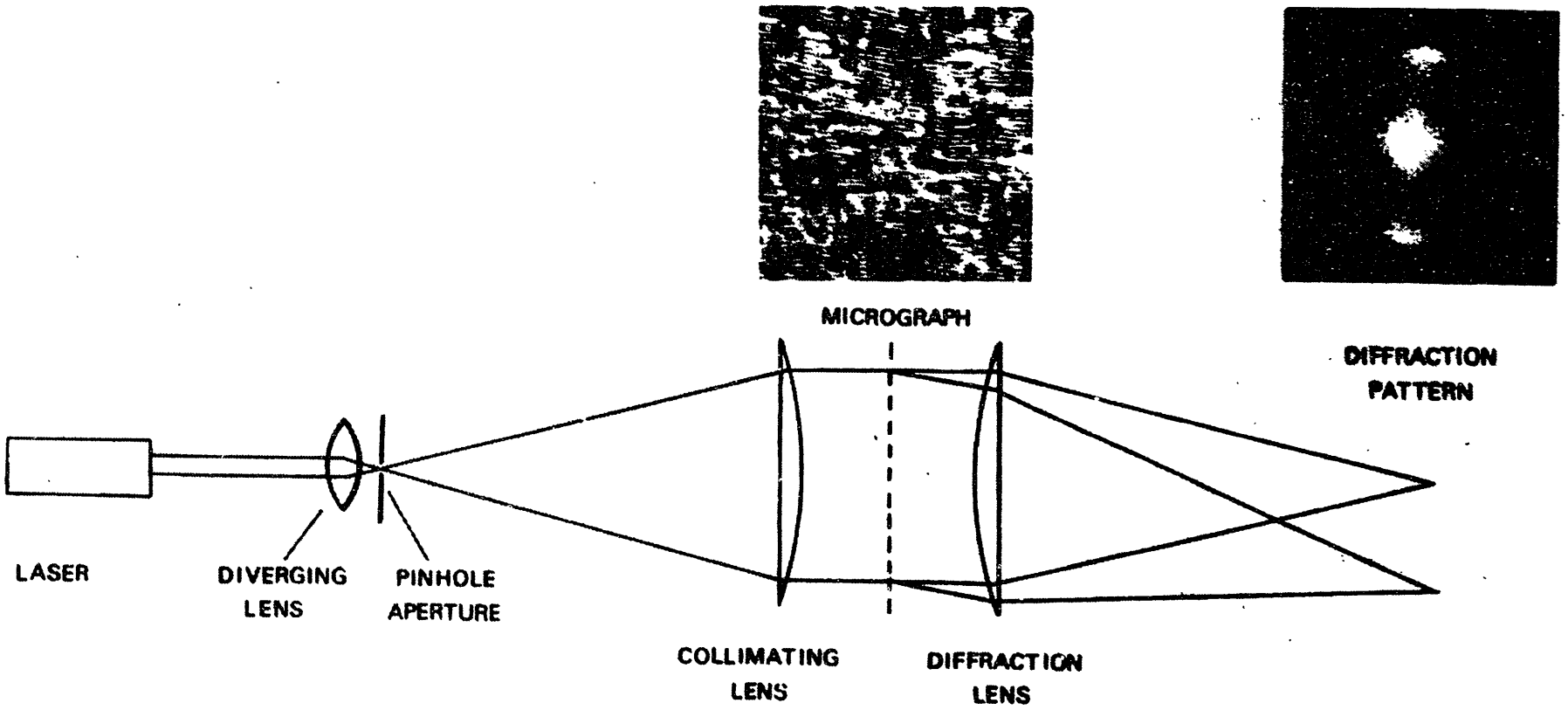

Figure 77. Schematic diagram of an optical diffractometer. The micrograph and diffraction patterns are rotated 90° for illustrative purposes.

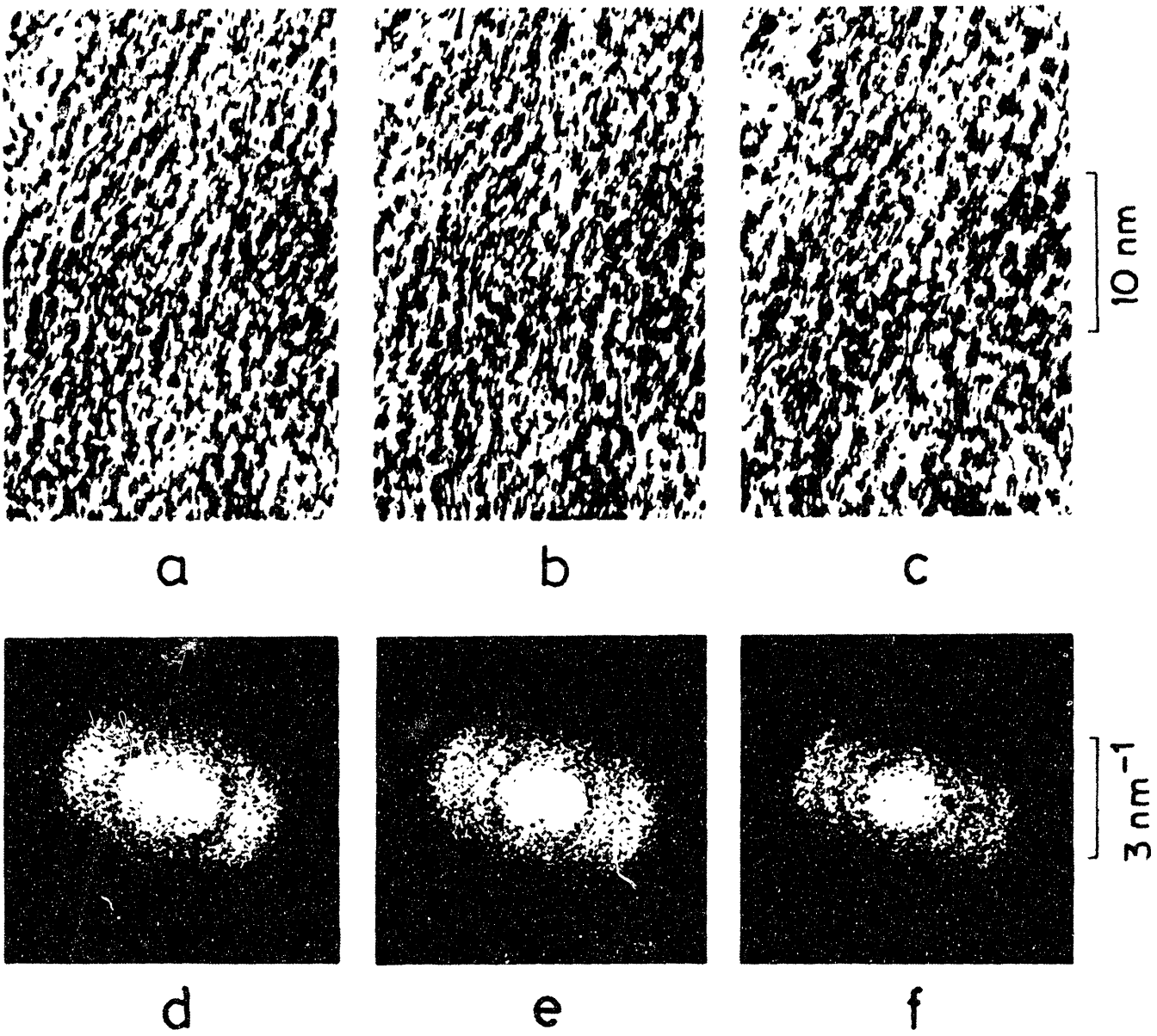

Figure 78. (a-c) 002 lattice images of the same regions of a polyvinyl chloride heat treated at 815°C under different underfocus settings of the objective lens. (d-f) are the corresponding optical transforms.

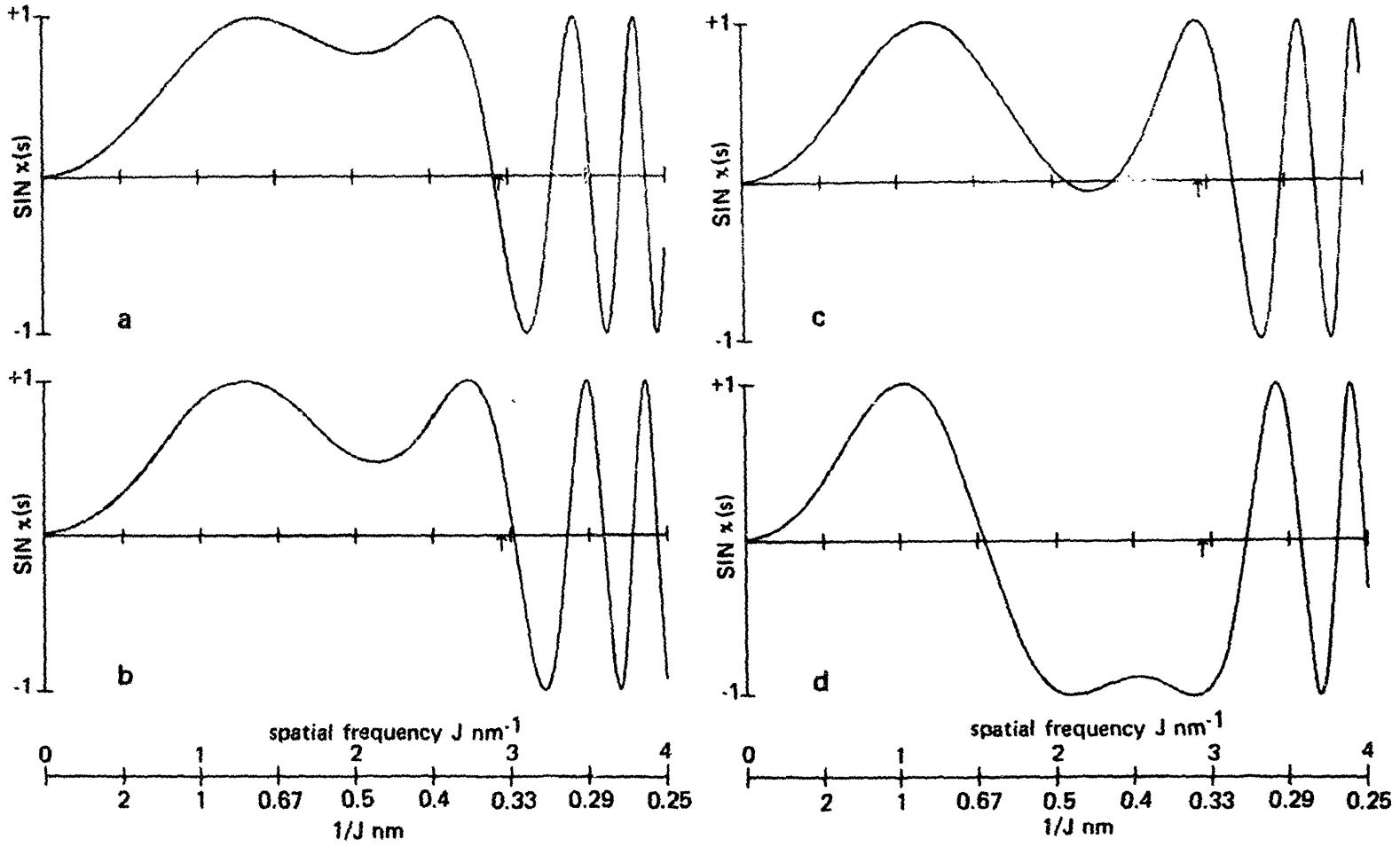

Figure 79. Phase-contrast transfer functions sin $\chi(s)$ for 100 keV electrons, C_s = 1.6 mm. Underfocus values are a) 92.5nm, b) 100 nm, c) 110 nm and d) 150 nm. The arrow corresponds to J = 1/0.34 nm^{-1}, the d_{002} spacing.

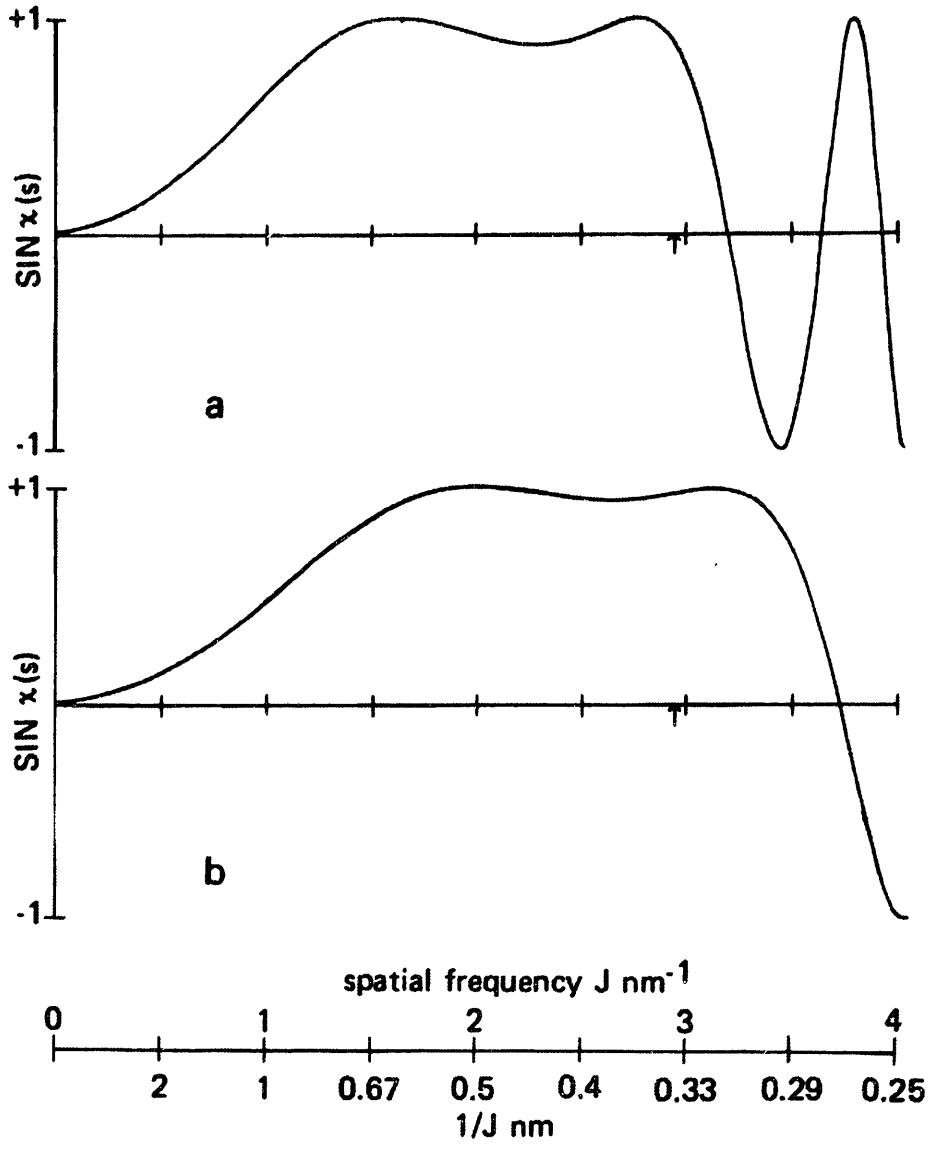

Figure 80. Phase-contrast transfer function sin $\chi(s)$ for 100 keV electrons. a) C_s = 1.0 mm and 70 nm underfocus, b) C_s=0.5 nm and 40 nm underfocus.

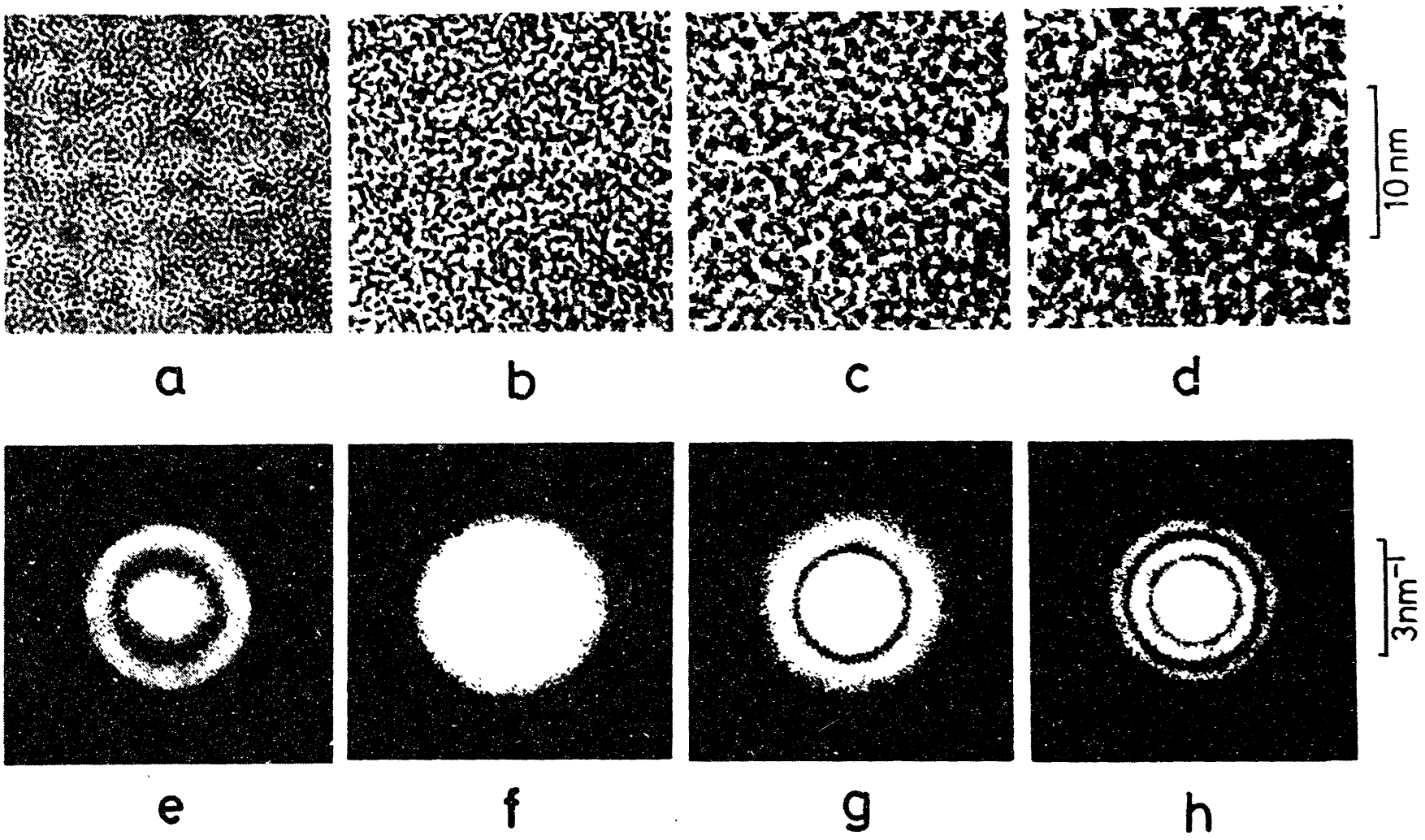

Figure 81. Single region of a thin film of evaporated carbon imaged at different levels of objective underfocus (a-d) with corresponding optical transforms (e-h).

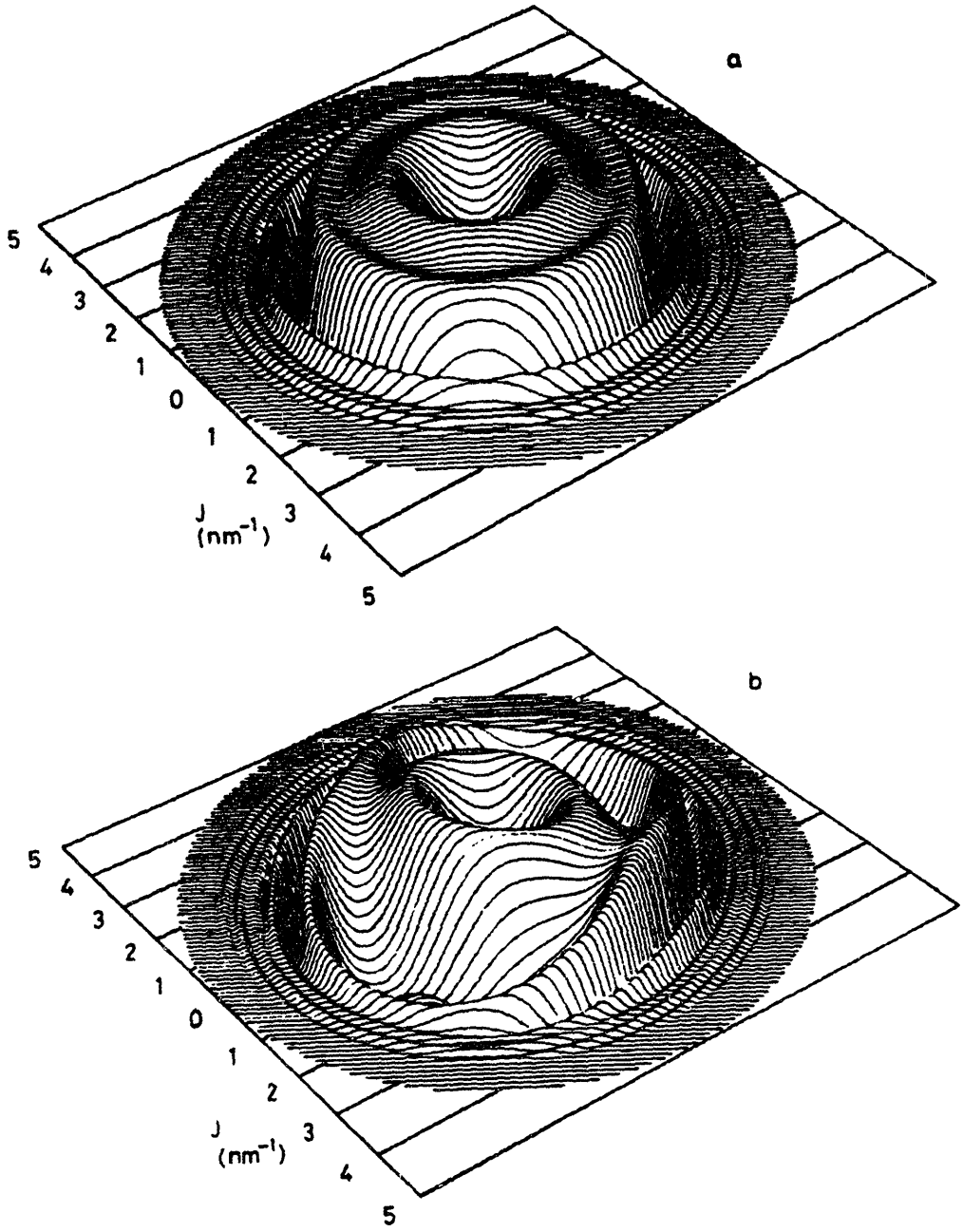

Figure 82. 3-D portrayal of the transfer function (a). In region (b), the same transfer function has not properly focused, resulting in astigmatism. The higher transfer function points will preferentially increase the contrast of the fringes that are diffracted in this region.

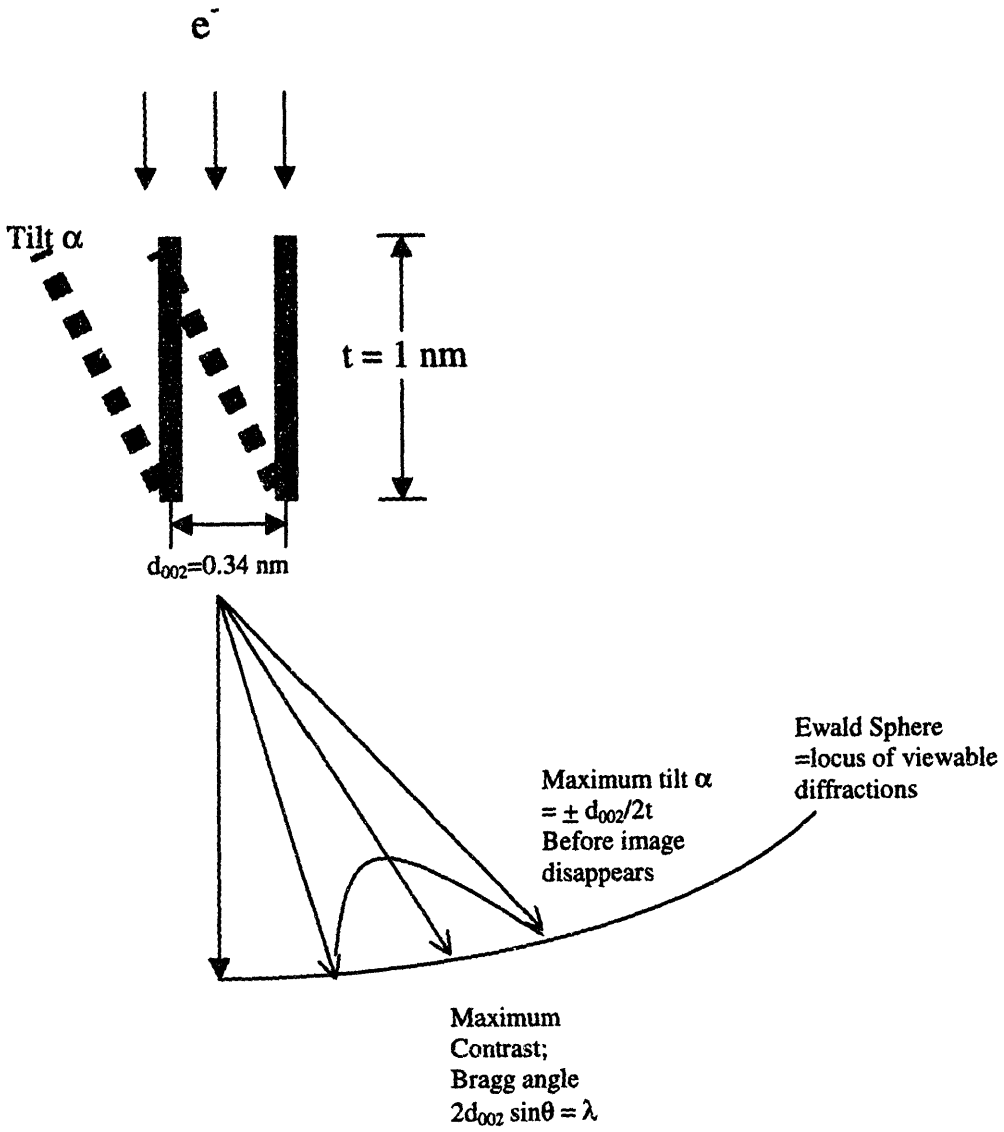

Figure 83. Illustration of maximum permissible tilt in electron microscopy.

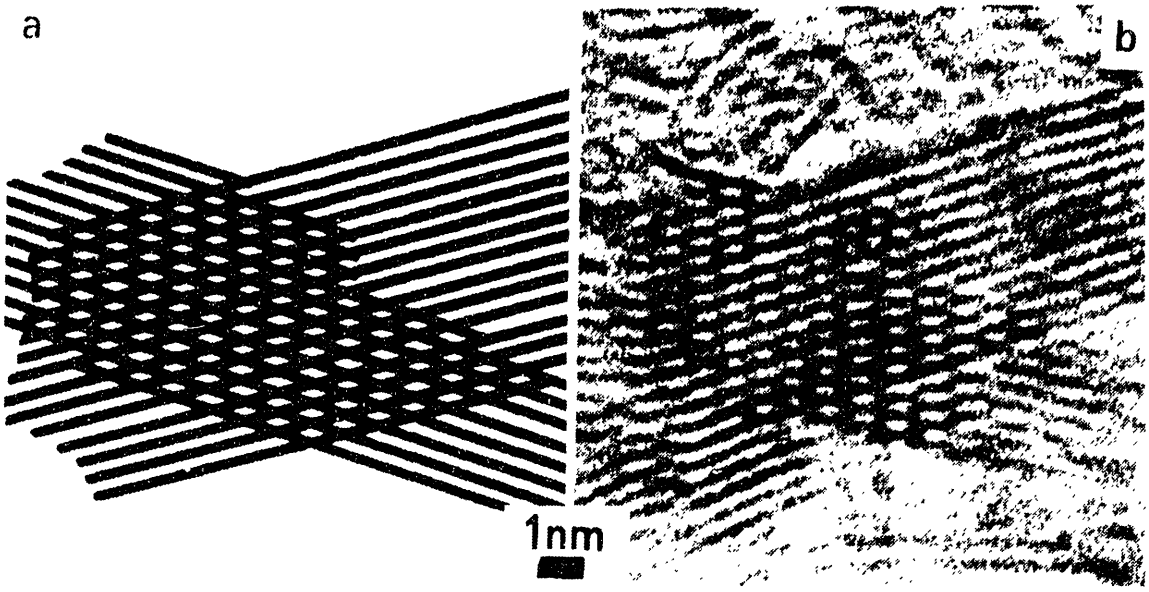

Figure 84. Rotation moires: a) sketch and b) image.

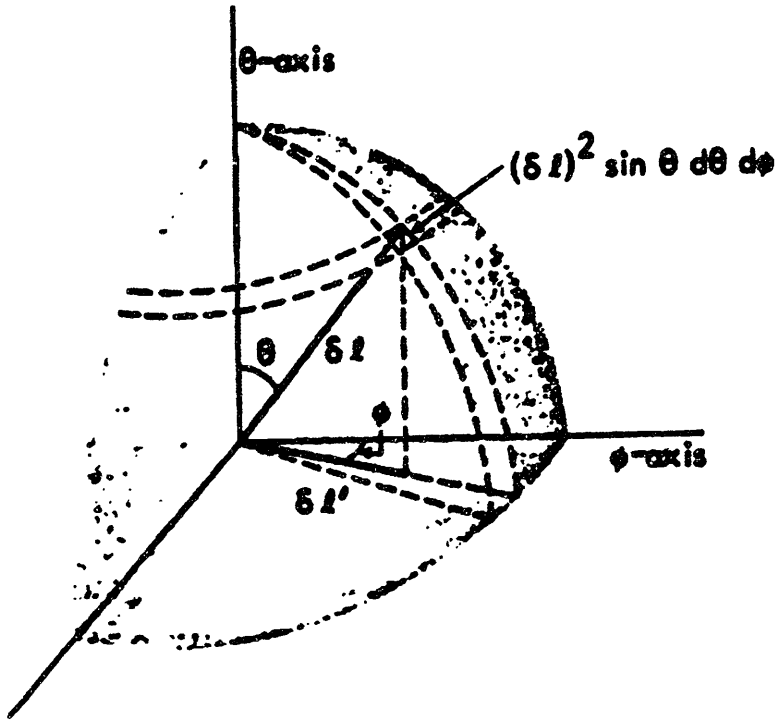

Figure 85. Mean projected length of a randomly oriented linear segment.

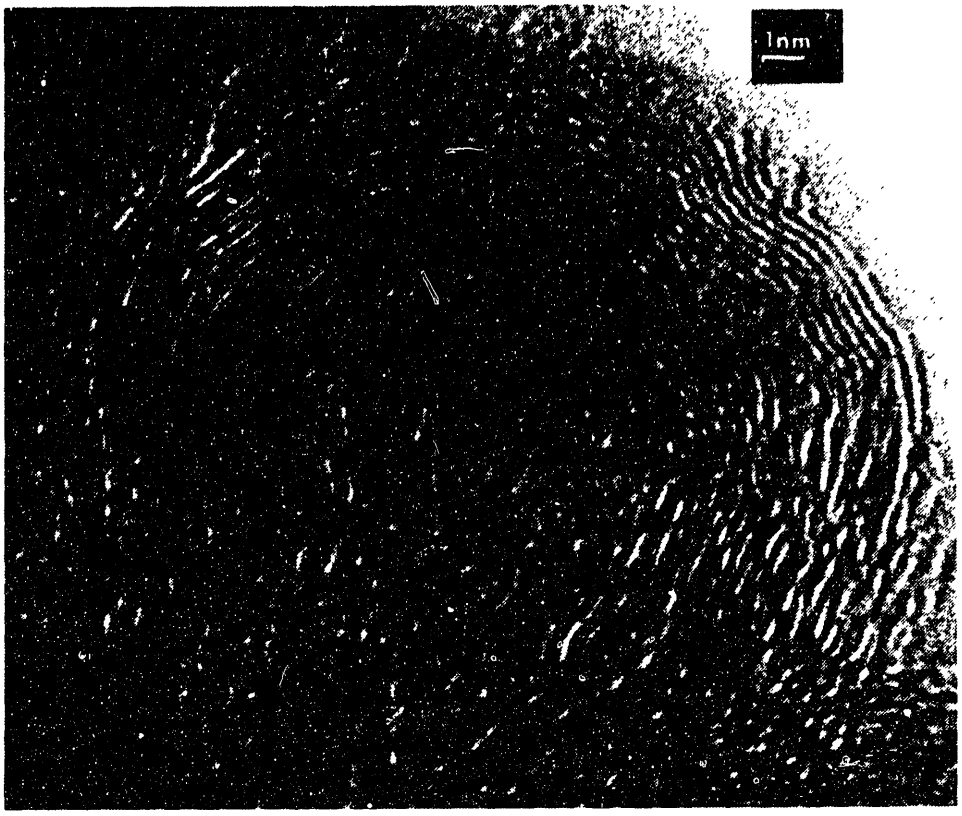

Figure 86. Example of diesel soot with a "hole" after 1 hour heat treatment at 1523K.

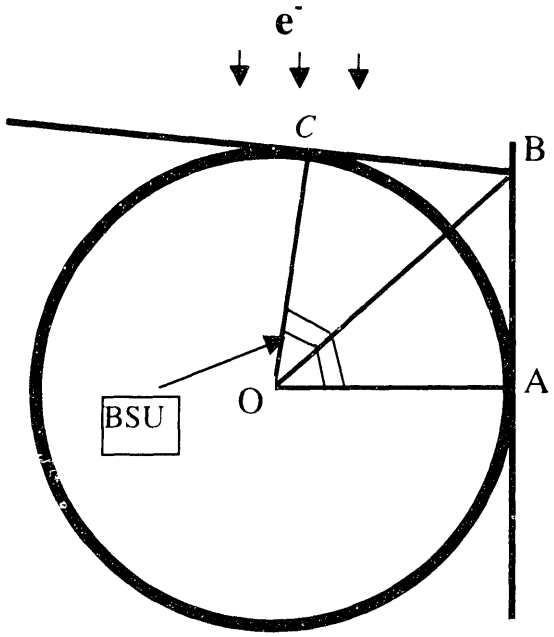

Figure 87. Calculation of the "empty" core radius.

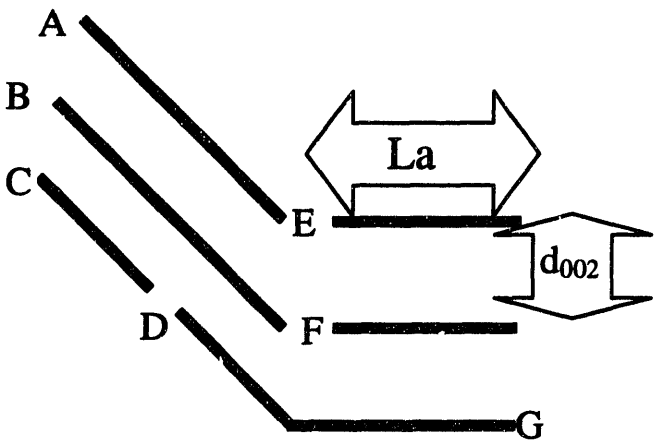

Figure 88. Simplified depiction of lattice and d_{002} fringe effects.

Appendix B: TEM Sample Preparation and Image Analysis Technique

Much of this work relies on image analysis of TEM micrographs. The analysis of TEM micrographs quantitatively for structural order and other characteristics has traditionally been quite difficult, especially when optical diffraction techniques are used, and many of the theoretical issues were discussed Appendix A. The technique presented in this appendix is based on the work of Palotás[128] on soot, extended to Spherocarb and other thicker samples of carbons that can be sectioned thin enough for TEM examinations.[148]

B.1 SAMPLE PREPARATION AND HARDWARE HANDLING

For the HRTEM observation a small portion of each sample of carbon was ultrasonically dispersed in ethanol. Generation of the samples thin enough for measurement in the TEM was accomplished by use of a ball mill for 5 minutes or a mortar and pestle for approximately 10 minutes. Figure 89 the analysis results of the extracted structure for each of the two grinding methods. No significant differences were found between the sample methods. Once a fine powder was generated, the dispersed suspension was deposited dropwise on a copper TEM grid coated with a lacy carbon film. The examination of the samples was carried out on material that extended over the holes in the supporting film in order to avoid interference from the amorphous carbon background film.

An Akashi/TOPCON 002B transmission electron microscope operated at 200 keV, with a LaB_6 filament was used to record high-resolution images of each sample, typically 590 kX for structural imaging. These images were then digitized with a VITEK™ image acquisition system equipped with a Kodak MEGAPLUS™ Model 1400 camera and stored as 1024×1024 pixel

computer images. The VITEK system was replaced by direct image scanning with UMAX POWERLOOK II digital scanner, operating at 993 dpi resolution, which offers significant improvements in ease of use and repeatability,. The 993 dpi resolution was calculated to give the same magnification as the original VITEK system. To confirm that the two different systems gave the same results, the same negative area was digitized. The subsequent analysis of the resulting images' fringe structure is given in Figure 90. The methods showed no significant differences in the resulting data except for differences to be expected from inexactly duplicating the same image.

The high degree of conformity exhibited in Figure 90 can also be used to surmise the degree of error inherent the digitization system. Using a bin average of 0.5 Å gave comparable results only if nearest neighbors ($\pm$ 0.5 Å) were included. This indicates that the analysis of fringes has an absolute minimum error in the range of 0.25 Å to 1.0 Å, although probably closer to the 0.25 Å region.

Analysis of the images was accomplished using the high-level language computer software, SEMPER6P® (Synoptics Ltd., Cambridge, UK), developed specifically for use with high-resolution electron microscopy to manipulate the stored images. Using SEMPER6P, pseudo-optical diffraction patterns were generated. The pseudo-optical diffractogram is a power spectrum calculated from the modulus of the Fourier Transform (FT). Intensity profiles characteristic of the range of contrast of the diffractograms were then produced. A sample power spectrum of Spherocarb is given in Figure 91. The diffraction pattern is a circular cloud as the fringes are approximately evenly distributed over all possible directions with a wide range of interlattice spacings for the randomly oriented Spherocarb structure. Figure 91 also shows the

effect of astigmatism on the power spectrum. The flattened power spectrum indicates no preferential ordering, but more likely, astigmatism.

Using a correlated gold standard, the number of pixels per Angstrom was found in the Fourier space. The relationship established using the oriented gold single crystal can be used to translate the length range of interest, $[d_1,d_2]$, in the scanned image, specified for pattern repetition, into a region in Fourier (reciprocal) space, $[r_1,r_2]$. The FT of the original image is then masked for $r<r_1$ and $r>r_2$ ($r_2>r_1$). The remaining annulus is then reverse transformed.[d] The integrated intensity profile of a FT image is shown in XXX as a function of the real (d) coordinates. The gray scale filtered is then transformed to a two color 'extracted structure' by establishing an intensity threshold value for the intensity of the pixels, separating the two colors (here selected as black and white). This extracted structure is the basis for analyses most of the previous Chapters (4-7), and complete details on the image properties tested may be found there or in Palotás[128]. A complete write up of an example SEMPER6P analysis code used to extract fringe structure is found in Appendix C.

B.2 SOFTWARE PARAMETERS

The software parameters chosen were based on the early work of Palotás[128] and experience, and should be valid for most thin edged carbons. However, an examination of the software parameters used in the analysis is warranted.

[d] Theoretically the center peak (corresponding to infinite distance on the original image) in the Fourier space is always needed for the reverse Fourier Transformation, therefore an annulus would be insufficient. Semper 6P retains the information content of the center peak and, even if the center is manually masked out, the reverse transform can be performed.

B.2.1 Filter Pass:

The Fourier transform is filtered (masked out) in the high and low bands by specifying the minimum and maximum layer spacing (d_{002}). The range chosen was 3.0 to 5.0 Angstrom in order to capture only fringes of reasonable interlattice spacing. This corresponds to the AA and BB parameters in Appendix B. The value of 3 Å corresponds to below the absolute limit of d_{002} fringe spacing reported, while 5 Å represents the maximum spacing between fringes for them to be considered to be part of the same pore system. The value of 235.62 was obtained by measuring the pixel distances between lattice points for the gold standard in Fourier space.

B.2.2 Threshold Intensity

This is the minimum in intensity of a pixel considered to be part of a fringe in the processed image. Figure 92 shows the results of varying the intensity threshold and filtering parameters. The lower the intensity, the fewer the number of fringes are seen as fewer pixels satisfy the intensity parameter. As can be seen in Figure 92, there is a great deal of variation in image with threshold intensity, which poses a problem due to varying thickness and microscope parameters. Every individual micrograph will have its own unique average intensity due to variations in these parameters, and one must identify the proper intensity value for each micrograph.

To solve for the optimum intensity, a plot of the fraction coverage versus intensity threshold is created for each image, as shown in Figure 93. As the minimum intensity accepted as part of a fringe increases, the fractional coverage decreases since fewer pixels satisfy the condition of having sufficiently high intensity to be counted in the fringe. At a low intensity threshold value the fringes are long and thick and become merged. As the threshold value

increases the fringes begin to separate and the total number of fringes increases. By increasing the threshold value even more the disappearance of the lower intensity group of pixels accelerates and the number of identified fringes levels off and in fact begins to decrease.[128] The intensity used in the analysis is chosen to be the intensity where the maximum number of lattice fringes can be found. This value usually is part of a relatively wide plateau, as depicted in the box of Figure 93.

B.2.3 Minimum Fringe Area

This is the filtering parameter for the minimum fringe size that will be considered in the extracted structure, and is specified to remove error that may arise from small fluctuations in intensity from a variety of sources. The minimum area used to define a fringe was determined by multiplying the width of graphitic/aromatic fringe in the microscope (approximately 0.15 nm, about ½ the d_{002} spacing) by the length of two aromatic units (approximately 0.5 nm). The width (0.15 nm) is much smaller than the characteristic d_{002} spacing (0.34 – 0.4 nm) due to the fact that the microscope will ideally only provide high image contrast where carbon atoms in a lattice network exist. This spacing is much smaller than the characteristic d_{002} spacing (in practical terms, roughly ½ of the space between planes will be excluded from the fringe due to contrast differences, resulting in thickness of 0.15 - 0.2 nm. Using the conversion ratio of 0.4336 Angstrom/pixel, this corresponds to a size of approximately 40-60 pixels. The elimination of noise to the maximum possible extent is vital, since it can falsify describing parameters, e.g., lattice length, orientation or fractional coverage distributions.

As the minimum area is of critical importance, a distribution of the lattice fringe length was obtained by varying the minimum size parameter, as shown in Figure 94. The absolute

number of lattice fringes is seen to increase in size as the minimum area considered a fringe increases. The minimum area used does not alter the number of larger lattice lengths to a significant extent past about 0.4 nm from the minimum fringe length specified. The fringe width assumption can be confirmed by comparing the maximum fringe hits for minimum areas of 20 and 60 pixels. For a 20 pixel minimum area, the maximum number of fringes is located at 0.4 nm, and assuming a square fringe structure, corresponds to a mean thickness of 0.104 nm. The 60 pixel length maximum is located at 1.0 nm, corresponding to a fringe thickness of approximately 0.12 nm.

For the basis of this analyses described in this thesis, a minimum area of 50 pixels was used in the calculations. This gives a minimum pixel fringe length corresponding to roughly 0.7 nm, which corresponds well to the minimum length that can reasonably be expected to measure for symmetric aromatic molecules, that of corenene (width 0.71 nm).

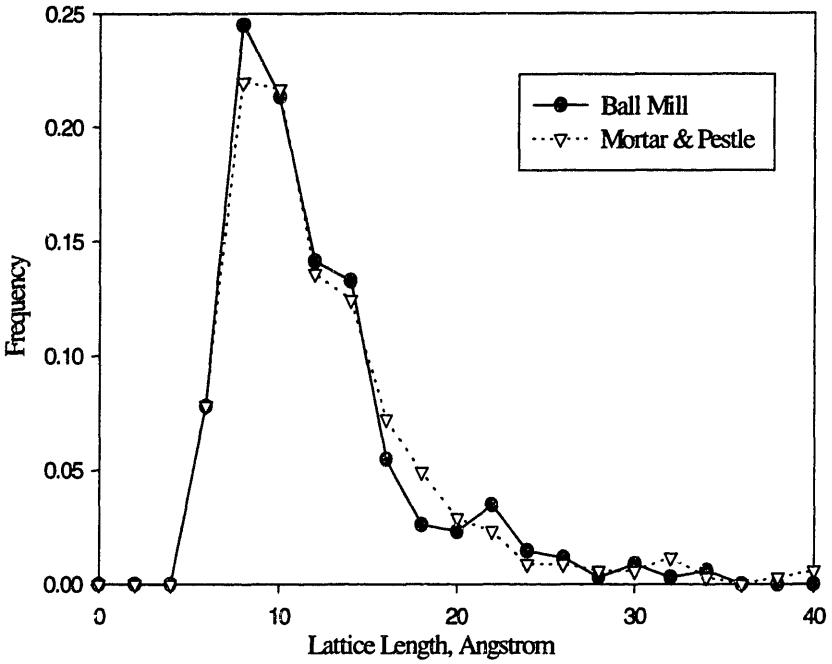

Figure 89. Comparison of the fringe length analysis of ground Spherocarb obtained by using two different powder preparation method

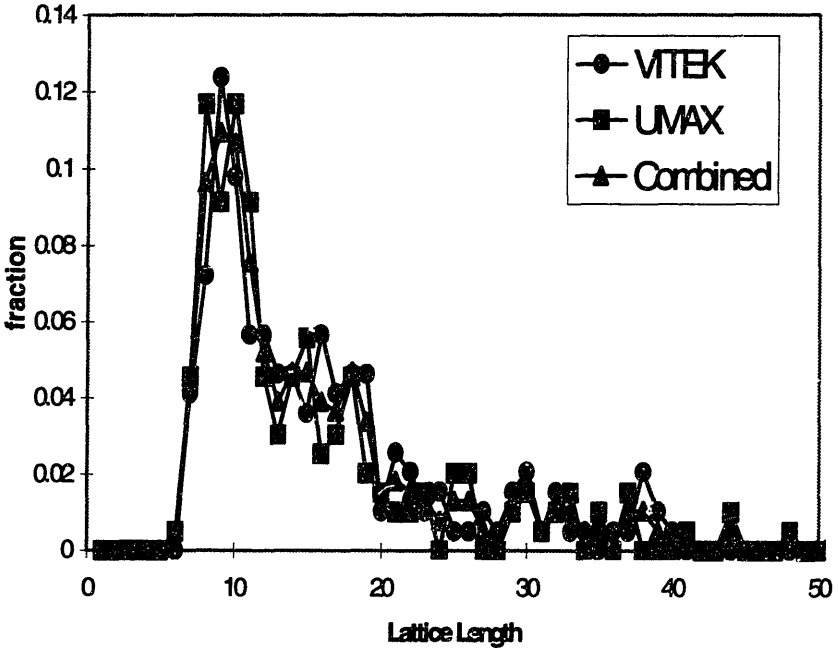

Figure 90. Comparison of Spherocarb particles and the subsequent analysis obtained by using two different methods to digitize the samples with the VITEK scanner and UMAX Powerlook II.

(A)

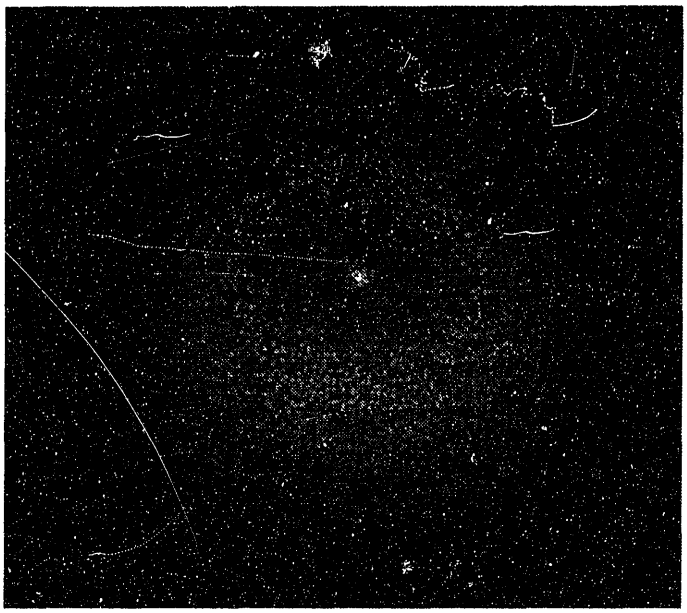

(B)

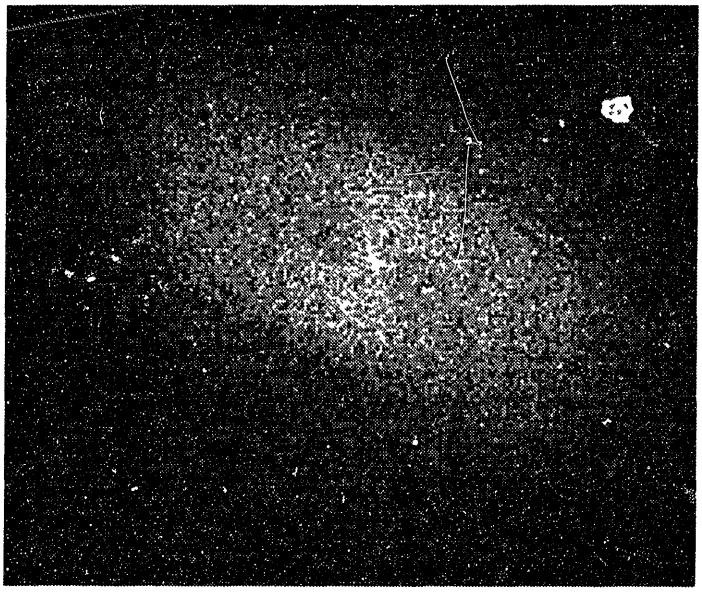

Figure 91. Sample power spectrum of Spherocarb depicted in Figure 5. The cloud like character (a) is due to the random distribution of different lattice lengths in the sample.

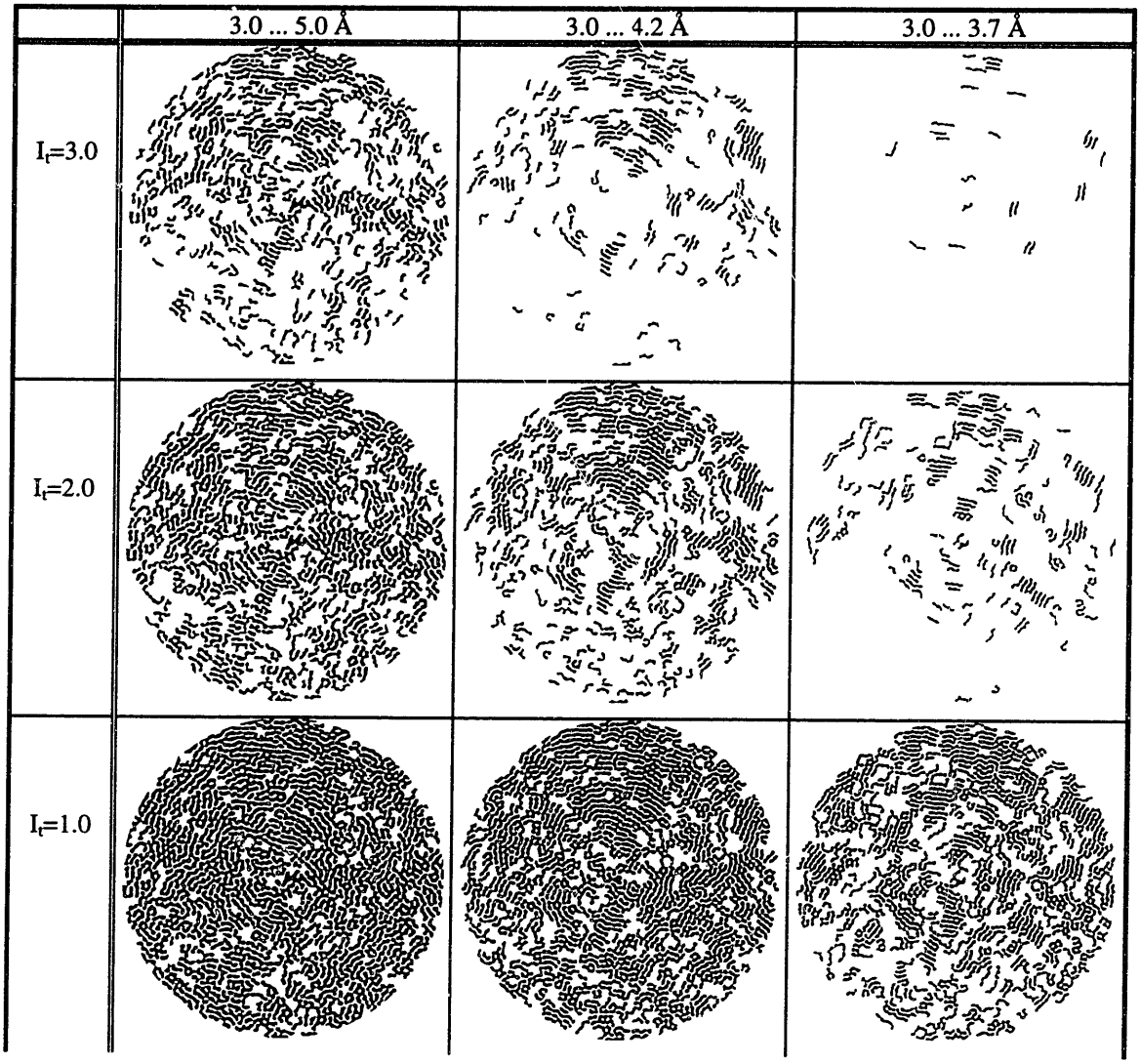

Figure 92. Effect of software parameters on the extracted pattern of carbon black. The horizontal axis shows the frequency window for the repeated pattern while the vertical axis is I_t , the intensity threshold value for the filtered image (from Palotas[128]).

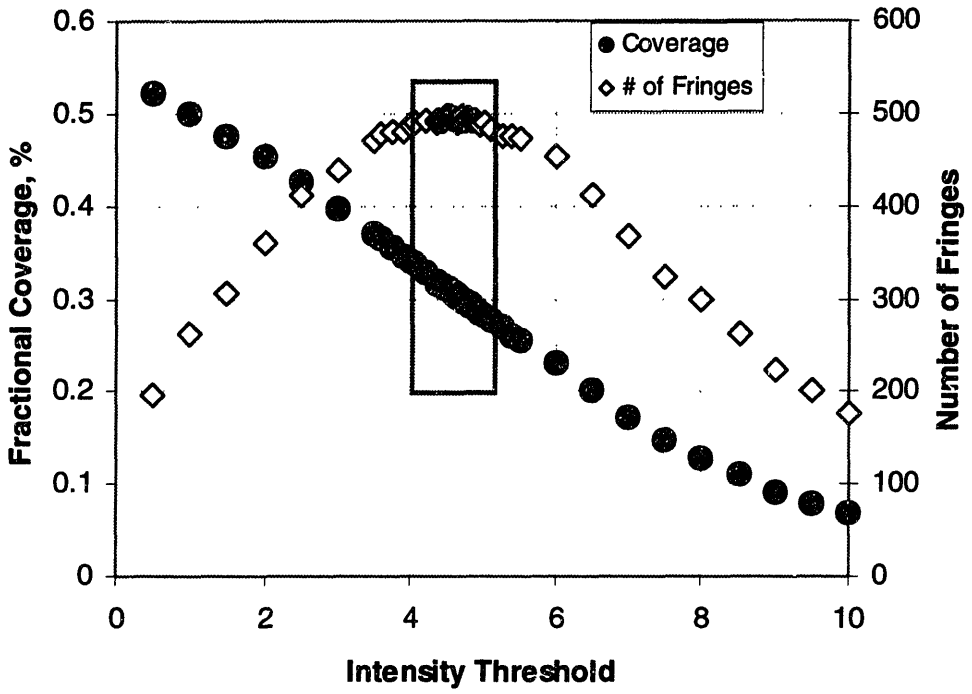

Figure 93. Effect of the intensity threshold value on the fractional coverage and on the number of lattice fringes found.

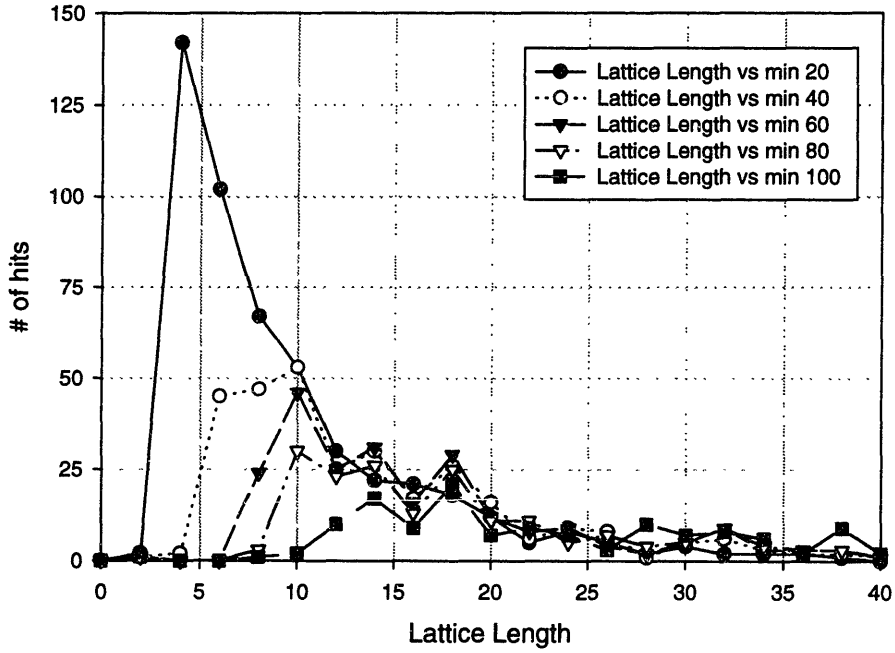

Figure 94. Variation in the number of fringes measured as a function of length for different size parameters.

Appendix C: Extracting structural data from TEM images with Semper 6P

This is a sample program needed to run Semper 6P to extract structural data, based on the program of Palotas[128].

How to extract the structure from the TEM image

```
copy 6800 3:1; cd=3; 1
```

This is the TEM image.

```
fourier 1 to 3; fullplane;

mask 3 radius 118; mask 3 inside radius 39;
```

$$r = \frac{235.62}{\text{distance in Å}}$$

```
halfplane; image; mask 3 radius 256
```

Masks out possible computational errors outside image after reverse Fourier.

```
analyse 3 5 le -3.0 area 30,10000 segment 4
```

The extracted pattern ("segmented image").

Maximum area to be considered as "particle" [pixels].

Minimum area for a "particle".

Intensity threshold: intensities above correspond to structure, pixels with intensities below this value are not element of the "structure" (do not form a "particle").

The Particle Parameter List (variable value: *ppl=5*).

```
pset count; TotalArea=0
```

Count the particles, and the result is stored in variable *n*.

```
for index=1,n; pset area;
```

The area of the actual "particle" (in pixels) is stored in variable *a*.

```
TotalArea=a+TotalArea; loop;
```

Closes the loop "for" started in the previous line.

Calculates Total Area of all the particles (if it is done more than once, it is important to annul it before the next loop).

```
type TotalArea
```

Types the numerical value onto the screen.

```
copy 4 to 6737 byte; copy 5 to 6738;
```

Saves the Particle Parameter List. If you need to analyze it later, don't forget to define the variable *ppl* (i.e. give value to it, before using any command related to the *ppl*: ppl=6738; pset count;...).

Saves the extracted pattern in byte format (byte requires less space on the hard drive).

```
calculate :4 >0 to 4;4 to 1
```

Makes the segmented image ("extracted structure") black and white (originally it is multi gray level, each "particle" has an intensity value equal to its sequential number.

Appendix D. Random Pore Model

```
*************************
*     Pore model program  *
*     version 3.0         *
*************************

      INTEGER I,ilow, NPORES, Nsteps
      INTEGER ARRYMAX
      REAL RPORE, RCHAR
      PARAMETER ( ARRYMAX = 3000000)
      PARAMETER (Nsteps = 1000)
      PARAMETER (POROSITY = 0.5)
      PARAMETER (RPORE =.05)
      PARAMETER (RCHAR = 3)

      REAL  X, DELTAX, time, vol, CO2
      REAL PORES(1:ARRYMAX)

      REAL DVDT, DRDT, DMDT, ppmCO2
      integer asspore
      external asspore

      real ran1
      external ran1

      real RAREA, carbon
      external RAREA

      open ( unit = 20 , file ="results", status = 'unknown')
      open (unit = 21, file = "model.log", status = 'unknown')

      print *, "Check pore routine"
      print *, RCHAR**3/Rpore**3
      print *, ran1(10)
      print *, "done checking"
      seed = 0.4
      write(21, *) " Going to assign Pores now"
      write(21, *) "   "
      print *, "HI"
      Npores =  asspore(arrymax, PORES, POROSITY, RPORE, RCHAR)
      print *, "I'm bacck"
      print *,Npores

      do 20 I = 1, Npores

 20   continue


*****  Char recesion rate(m/s)
* Data from Goeal
```

```
      DRDT = 2.736e-6
      carbon = 0

      R = RCHAR
      ilow = 1
      X = 0
      Time = 0.
      carbon = 0
 50   if ( R .gt. 0) then

        AREA = RAREA(arrymax, X, R,  PORES, RPORE, ilow, Npores)
        AREA = AREA/1e6

        DVDT = Area * DRDT
        DMDT= DVDT * 11.79

        ppmCO2 = 172308.6 * DMDT *1e6
        carbon = carbon + DMDT/.53*12.011/.486*1000

        DELTAX= (AREA-3.4156*4*R*R/1e6)*DRDT*11.79*172308.6*1e6

        write (20, *) time, R, ((Rchar-R)**3)/(Rchar**3),
     +    ppmCO2, carbon


        X = X+ DRDT*1000
         R = RCHAR - X
         Time = time + 1

         if (time .lt. 10) print *, X, R, Area, Vol, ppmCO2,
     +        DVDT, DMDT

         goto 50
       end if
       endfile 20
       close(unit = 20, status = 'keep')
       close(unit = 21, status = 'keep')

       END


**********
*  Subroutine to assign pores locations
***********

      integer function asspore(nmax, pores, eps, Rp, Rc)
      integer nmax, i, idum
      real pores(1:nmax)
      real eps, Rp, Rc, epsrun
      idum = 100
      seed = 0.597
      epsrun = 0
      write (21, *) "entered pore assignment routine"
      print *, "in pore assign routine"
```

```
 1000   if ( epsrun .LT. eps) then
         i = i + 1
*         print *, i
         pores(i) =Rc - ( ran1(idum) **(1./3.)) * Rc
*         print *,i, pores(i), "done with pores"
         epsrun = epsrun + (Rp**3)/(Rc**3)
*         print *, pores(i), epsrun
         if(epsrun .gt. .49 ) print *, i, epsrun
         goto 1000
       end if
       print *, "done with pore randomizer"
       write(21, *) "Pores succesfully randomized"
       write(21, *) "Pores used     =   ", i
       write(21, *) "Overall Porosity = ", i * Rp**3 / Rc**3
       write(21, *) " "

       call sort(nmax, i, pores)
       write(21, *) "Pores succesfully sorted"


       write (21,*) " "
       print *, nmax
       call porechk(nmax,i, Rp, Rc, pores)
       asspore = i
       end

*************
*  RANDOM FUNCTION 2
**************
       FUNCTION ran1(idum)
       INTEGER idum,IA,IM,IQ,IR,NTAB,NDIV
       REAL ran1,AM,EPS,RNMX
       PARAMETER (IA=16807,IM=2147483647,AM=1./IM,IQ=127773,IR=2836,
      *NTAB=32,NDIV=1+(IM-1)/NTAB,EPS=1.2e-7,RNMX=1.-EPS)
       INTEGER j,k,iv(NTAB),iy

       SAVE iv,iy
       DATA iv /NTAB*0/, iy /0/
       if (idum.le.0.or.iy.eq.0) then
         idum=max(-idum,1)
         do 11 j=NTAB+8,1,-1
           k=idum/IQ
           idum=IA*(idum-k*IQ)-IR*k
           if (idum.lt.0) idum=idum+IM
           if (j.le.NTAB) iv(j)=idum
11       continue
         iy=iv(1)
       endif
       k=idum/IQ
       idum=IA*(idum-k*IQ)-IR*k
       if (idum.lt.0) idum=idum+IM
       j=1+iy/NDIV
       iy=iv(j)
       iv(j)=idum
```

```
      ran1=min(AM*iy,RNMX)
      return
      END


**********
* Pore Checking subroutinte
**********

      subroutine porechk(nmax,i,Rp,Rc, pores)
      integer i, nmax, j
      real Rp, Rc, x, DELTAX
      real pores(1:nmax)
      real step, pvol

      step = 20
      deltax = Rc/step
      pvol = 0
      x = deltax

      write (21,*) "Checking Pore distribution"
      do 1050 j = 1, i
*         print *,"pores = ", pores(j)
 5       if (pores(j) .lt. x) then
            pvol =  pvol + (Rp**3)

         else
 6          eps = pvol/((Rc-x+DELTAX)**3-(Rc-x)**3)
            pvol = 0
            print *, x, eps
            write (21,*) x, eps
            x = x+Deltax
            if (pores(j) .gt. x) goto 6
            if ((j .eq. i) .and. (x .lt. Rc)) goto 6
            goto 5
         endif


 1050 continue
      write (20,*) " "
      end


**********
*  Array sorter
**********

      subroutine sort(nmax, i, pore)
      integer i, nmax
      real pore(1:nmax)
      real swapvar

      do 1100 j = 1, i
```

```
         do 1200 k = j, i
            if (pore(k) .lt. pore(j) ) then
               swapvar = pore(j)
               pore(j) = pore(k)
               pore(k) = swapvar
            endif
 1200    continue
 1100 continue

      end


**********************
* RAndom # generator
**********************


      subroutine random(x,xr)

      data k, j, m, rm / 5701, 3612, 566927, 566927.0 /

      ix = int( x*rm)
      kr = j * ix + k
      Irand = mod(kr, M)
      xr = (float(irand) + 0.5 ) / rm
      return
      end

*****************
*  Area computator
*****************

      real function RAREA(MAX, X, R, pores, Rp, ilow, Npores)
      real X,R, Rp
      INTEGER MAX, i, ilow, Npores
      real pores(1:MAX)
      REAL area


*  Spheroid area
      area = 4* 3.1456 * R*R
* Compensate for pores

      i = ilow

 1500 if ((pores(i) .le. X) .and. (i .le. Npores)) then

         if ( (pores(i) +2 *Rp) .le. X) then
            ilow = i
            i = i + 1

         else
            area = area + 3.1456 * (2*Rp - ( X -pores(i)))**2
            i = i + 1
```

```
   end if
   goto 1500
end if

RAREA = area

end
```

BIBLIOGRAPHY

1 Smith, I.W. "The Combustion Rates of Coals Chars: A Review," *Nineteenth Symposium (International) on Combustion,*" pp. 1045-1065, 1982.

2 Smith, I.W., "The Intrinsic reactivity of carbons to oxygen," *Fuel*, **57**, pp. 57, 1978.

3 Brunauer, S., Emmett, P. H., and Teller, E., *J. Am. Chem. Soc.*, **60**, pp 309, 1938.

4 Dubinin, M.M., "Porous Structure and Adsorption Propertis of Active Carbons," Chemistry and Physics of Carbon, vol. 2 (P.L. Walker, Jr., ed.) Marcel Decker Inc., N.Y., pp 51-120., 1966.

5 LaineN.R., Vatola, F.J., and Walker, Jr., P.L., "The role of the surface complex in the carbon-oxygen reaction." *Proceedings of the Fifth Conf. Carbon,* Vol 2., Pergamon Press, New York, pp. 211-219, 1963.

6 Sing, K.S.W., Everett, D.H., Haul, R.A.W., Moscou, L., Pierotti, R.A., Rouquerol, J. and Siemieniewska, T., *Pure and Applied Chemistry,* **57**, pp 603, 1985.

7 D'Amore, M.,Tognotti, L., Sarofim, A. F., "Oxidation Rates of a Single Char Particle in an Electrodynamic Balance." *Combustion and Flame,* **95**, pp. 374, 1993.

8 Jenkings, R.G., Nandi, S.P, and Walker, J.R., P.L., "Reactivity of heat -treated coals in air at 500oC," *Fuel*, **52** pp 288., 1973.

9 Marsh, H., ed., *Introduction to Carbon Science.* Butterworth & Co. LTD, London, pp 110, 1989.

10 Marsh, H., and Griffiths, J., "A high resolution electron-microscopy study of graphitization and graphitizable carbon," *Int. Symp. On Carbon*, Toyohashi, Japan, Kagaku Gijutsu-sha, Tokyo, 1982.

11 Baker, R. T. K., "The relationship between particle motion on a graphite surface and Tammann temperature,: *J. Catalysis*, **78,** pp 473, 1982.

12 Stein S.E., and Brown, R.L., "Chemical Theory of graphite-like molecules," *Carbon*, **23**, pp 105, 1985.

13 Acharya, T.R., and Olander, D.R., "The rate of oxidtion of the basal and prismatic surfaces of pyrolytic graphite in the transition regime between chemical and diffusional control," *Carbon*, **11**, pp 7-18, 1973.

14 Hurt, Robert H., "Chemical and Physical Phenomena Dettermining Carbon Gasification Reactivity," PhD Thesis, Dept. of Chemical Engineering, Massachusetts Institute of Technology, 1987.

15 Ishiguro, T., Suzuki, N., Fujitani, Y. and Morimoto, H., "Microstructural Changes of Diesel Soot During Oxidation," *Combustion and Flame*, **85**, pp 1-6, 1991.

16 Walker, P.L., and Mahajan, O.P., "Pore Structure in Coals," Energy and Fuels, **7**, pp. 559-560, 1993.

17 Wong ,B.A., Gavalas, G.R., and Flagan, R.C, "Effect of Char Formation Temperature on the Densification of a Bituminous Coal Char during Gasification," *Energy and Fuels*, **9**, pp 493-499, 1995.

18 Hurt, R. H, Davis, K. A., and Hardesty, D.R., *"Coal Combustion Science-quarterly Progress Report,"* Sandia Technical Report, October-December, 1993.

19 Davis, K.A.; Hurt, R.H.; Yang, N.Y.C.; Headley T.H.: "Evolution of char chemistry, cristallinity, and ultrafine structure during pulverized-coal combustion," *25th International Symposium on Combustion*, Irvine, CA, 1994

20 Sundback, C.A., Beer, J.M, and Sarofim, A.F., "Fragmentation Behavior of Single Coal Particles in a Fluidized Bed," *Twentieth Symposium (International) on Combustion*, pp 1495-1503, 1984.

21 Zygourakis, K. and Sandmann, C.W. Jr., "Discrete Structural Models and Their Application to Gas-Solid Reacting Systems," *AIChE Journal*, **34**, pp 2030-2040, 1988.

22 Zygourakis, K., "Effect of Pyrolysis Conditions on the Macropore Structure of Coal-Derived Chars," *Energy and Fuels*, **7**, pp 33-41 1993.

23 Zygourakis, K., Arri, L., and Amundson, N.R., "Studies on the Gasification of a Single Char Particle," *Ind. Eng. Chem. Fundam.*, **21**, pp 1-12, 1982.

24 Sundback, C.A., Fragmentation Behavior of Single Coal Particles in a Fluidized Bed, Ph.D. Thesis in Chemical Engineering, 1984.

25 Su, J.L., and Perlmutter, D.D., "Effect of Pore Structure on Char Oxidation," *AIChE Journal*, **31**, pp 973 -981, 1985.

26 Delikouras, E.A., and Perlmutter, D.D., "Combined Effects of Mass Transfer and Inaccessible Porosity in Gasification Reactions," *AIChE Journal*, **39**, pp 829-836, 1993.

27 Delikouras, E.A., and Perlmutter, D.D., "Inaccessible Porosity in Gasification Reactions under Kinetic Control," *AIChE Journal*, **37**, pp 1607-1612, 1991.

28 Goel, S. K., "Environmental problems : fundamental studies and global ramifications," PhD Thesis, Dept. of Chemical Engineering, Massachusetts Institute of Technology, 1996.

29 D'Amore, M.,Tognotti, L., Sarofim, A. F., "Oxidation Rates of a Single Char Particle in an Electrodynamic Balance." *Combustion and Flame,* **95**, pp. 374, 1993.

30 Lahaye, J., and Prado, G., "Mechanisms of Carbon Black Formation," Chemistry and Physics of Carbon, vol. 14 (P.L. Walker, Jr., ed.) Marcel Decker Inc., N.Y., pp 167-294, 1978.

31 Neoh, K.G., Howard J.B., and Sarofim A.F., "Effects Of Oxidation On The Physical Structure Of Soot," *Twentieth Symposium (International) On Combustion*, Am Arbor, MI, pp. 951-957, 1984.

32 Wicke, B.G., and Grady, K.A., *Carbon*, **25**, 6, pp. 791-797, 1981.

33 Smith, W.R., and Polley, M.H., "The oxidation of graphitized carbon black," *The Journal*, pp 689-91, 1956.

34 Due, Z., "Kinetic Modeling of Carbon Oxidation," MIT PhD Thesis, Mechanical Engineering, 1990.

35 Bonnefoy, F., Gilot, P., Stanmore, B.R., and Prado, G., "A Comparative Study of Carbon Black and Diesel Soot Reactivity in the temperature range 500-600°C - Effect of Additives", *Carbon*, **7**, pp 1333-1340, 1994.

36 Gilot, P. Bonnefoy, F., Marcuccilli, F., and Prado, G., "Determination of Kinetic Data for soot oxidation. Modeling of Competition Between Oxygen Diffusion and Reaction During Thermogravimetric Analysis," *Combustion and Flame*, **95**, pp 87-100, 1993.

37 Pfeifer, P, Preparative Chemistry Using Supported Reagents, Academic Press, New York , 1987, p 13.

38 Mandelbront, B.B., *Fractals – Form, Chance and Dimension*, Freeman, San Francisco, 1977.

39 Xu, W., Zerda, T.W., Yang, H., and Gerspacher, M., "surface Fractal Dimension of Graphatized Carbon Black Particles," *Carbon*, **34 #2**, pp 165-171, 1996.

40 Ismail, M.K., Pfeifer, P, "Fractal Analysis and Surface Roughness of Nonporous Carbon Fibers and Carbon Blacks," *Langmuir*, **10**, pp 1532-1538, 1994.

41 Darmstadt, H., Roy, C., and Kaliaguine, S. Sahouli, B., Blacher, S., Pirard, R., and Brouers, F., "Fractal Analysis of Commercial and Pyrolytic Carbon Blacks using Nitrogen Adsorption Data," *Rubber Chemistry and Technology, 68,* pp 330-341, 1995.

42 Ishiguro, T., Suzuki, N., Fujitani, Y. and Morimoto, H., "Microstructural Changes of Diesel Soot During Oxidation," *Combustion and Flame*, **85**, pp 1-6, 1991.

43 Hurt, R., H, Sarofim, A.F, and Longwell, J.P., "Gasification-Induced Densification of Carbons: From Soot to Form Coke," *Combustion and Flame*, **95**, pp 43-432, 1993.

44 Du, A., "Kinetic Modeling of Carbon Oxidation", Mechanical Engineering Ph.D. thesis, Massachusetts Institute of Technology, 1990.

45 Kofinas, P., "Shear - Induced Morphologies of Semicrystalline Block Copolymers," MIT Ph.D. Thesis, Dept. of Materials Science and Engineering, 1994.

46 Dubinin, M.M., and Astakov, V.A., "Description of Adsorption Equilibria of Vapors on Zeolites over Wide Ranges of Temperatures and Pressure," *Adv. Chem. Ser.*, **102**, pp 69-82, 1971.

47 Levendis, Y.A., Flagan, R.C., "Synthesis, Formation and Characterization of Micron-Sized Glassy Carbon Spheres of Controlled Pore Structure," *Carbon*, **27**, pp 265-283 1989.

48 Foster, M.D. and Jensen, K.F., "Small angle X-ray scattering investigations of pore structure changes during coal gasification," *Fuel*, **69**, 1990.

49 Foster, M.D., Jensen, K.F., "SAXS investigation of model carbon pore structure and its change with gasification," *Carbon* **29**, pp 272-282, 1991.

50 Guet, J.M, Lin, Q., Linares-Soland, A., and Salinas-Martinex de Lecea, "Characterization of Activated Carbon: An Approach to the Activation Process by SAXS and Optical Microscopy", Characterization of Porous Solids II, pp. 379-385, Elsevier, 1991.

51 Hua, D.W, D'Souza, Schmidt, P.W., and Smith, D.M., "Pore Structure Analysis Via Small Angle X-Ray Scattering and Contrast Matching," Characterization of Porous Solids III, pp. 255-261, 1994.

52 Porod, G., *Kolloid Zeitshrift.*, "Die Röntgenkleinwinkelstreung von dichtgepakten kolloiden systemen. I. Teil," **124**, pp. 83-114, 1951.

53 Kalliat, M., Kwak, C.Y., and Schmidt, P.W., "Small-Angle X-ray Scattering Investigation of the Porosity in Coals," *New Approaches in Coal Chemistry*, pp 1-12, ACS Symposium Series 169, 1981.

54 Pfeifer, P., Avnir, D., "Chemistry in noninteger dimensions between two and three. I. Fractal theory of heterogeneous surfaces," *J. Chem Phs,* **79**, pp. 3568, 1983.

55 Avnir, D., Farin, D., and Pfeifer, P.," Chemistry in noninteger dimensions between two and three. II. Fractal surfaces of adsorbents," *J. Chem Phys.*, **79**, pp. 3566, 1983.

56 Hoinkis, E., "Small-Angle Scattering of Neutron and X-rays from Carbon and Graphtites,"*Chemistry and Physics of* ***Carbon,*** vol 25, pp. 71, 1997.

57 Glatter, O.,"Determination of particle Size Distribution Functions from Small-Angle Scattering Data by Means of the Indirect Transformation Method," *Journal of Applied Crystallography*, **13**, pp 7-11, 1980.

58 Glatter, O.,"Comparison of Two Different Methods for Direct Structural Analysis from Small Angle Scattering Data," *Journal of Applied Crystallography*, **21**, pp. 886-890, 1988.

59 Donnet, J, Banal, R.C, and Wang, M, eds. *Carbon black : science and technology,* Dekker, New York1993.

60 Sahouli, B., Blacher, S., Brouers, F., Sobry, R., Vand Den Bossche, G., Darmstadt, H, and Roy, C., "SAXS Characterization of Pyrolytic Carbon Blacks," *Mat. Res. Soc. Symp. Proc.*, **407**, pp. 39-43, 1996.

61 Ehrburger-Dolle, F., Holz, M., and Lahaye, J., "Use of N2, Ar and CO2 adsorption for the determination of microporosity and surface fractal dimension of carbon blacks and silicas," *Pure and Appl. Chem.*, **65 #10,** pp 2223-2230, 1993.

62 Hurt, R. H., Dudek, D.R., Longwell, J.P, Sarofim, A.F., "The Phenomenon of Gasification-induced Carbon Densification and its Influence on Pore Structure Evolution," Carbon, **26**, pp. 433-449, 1988.

63 Bar-ziv, E., Jones, D.V., Spjut, R. E., Dudek, D. R., Sarofim, A.F., and Longwell, J.P., "Measurement of Combustion Kinetics of a Single Char Particle in an Electrodynamic Thermogravimetric Analyzer," Combustion *and Flame*, **75**, pp. 81-106, 1989.

64 Wong, B.A, Gavalas, G.R, and Flagan, R.C., "Effect of Char Formation Temperature on the Densification of a Bituminous Coal Char during Gasification," *Energy and Fuels*, **9:3**, pp. 493, 1995.

65 Walker, P.L., and Mahajan, O.P., "Pore Structure in Coals," *Energy and Fuels*, **7**, pp. 559-560, 1993

66 Ishiguro, T., Suzuki, N., Fujitani, Y. and Morimoto, H., "Microstructural Changes of Diesel Soot During Oxidation," Combustion *and Flame*, **85**, pp. 1-6, 1991.

67 Hurt, R.H, Sarofim, A.F., and Longwell, J.P., "Gasification-Induced Densification of Carbons: From Soot to Form Coke," *Combustion and Flame*, **95**, pp. 430-432, 1993.

68 Heckman, F.A., and Harling, D.F., "Progressive Oxidation of Selected Particles of Carbon Black: Further Evidence for a New Microstructural Model," Rubber *Chemical Tehnology*, 1967.

69 Heckman, personal commmunications, Nov. 17, 1993.

70 Baker, R.T.K., "In Situ Electron Microscopy Studies of Catalyst Particle Behavior," Cataly. Rev,-Sci. Eng., **19**, pp. 161-209, 1979.

71 Baker, R.T.K, "Metal Catalysed gasification of graphites", *Carbon and Coal Gasification*, Eds .Figueiredo, J., and Joulijn, J.A., Proc. NATO Advanced Science Institute, Alvar, Portugal, pp. 231-238, 1986.

72 Du, Z., Sarofim, A.F., Longwell, J.P., "Surface Area of Soot & Its Evolution During Oxidation" unpublished article, 1995.

73 Gilot P., Bonnefoy, F.rcuccilli, F. and Prado, G., "Determination of Kinetic Data for Soot Oxidation. Modeling Compettition Between Oxygen Diffusion and Reaction during Thermogravimetric Analysis." *Combustion and Flame*, **95(1-2)**, pp 87. 1993.

74 Gilot P., Bonnefoy, F.rcuccilli, F. and Prado, G., "Determination of Kinetic Data for Soot Oxidation. Modeling Compettition Between Oxygen Diffusion and Reaction during Thermogravimetric Analysis." *Combustion and Flame*, **95(1-2)**, pp 87. 1993.

75 Lahaye,J., Prado, G Mechanisms of Carbon Black Formation, *Chemistry and Phsycis of Carbon*, Vol 14, pp 167-294. P.L. Walker, Jr, and P. Thrower, Eds. Marcel Dekker, New York, NY (1978).

76 Rainey, L., Palotas, A. Bolsaitis, P, Vander Sande, J.B, and Sarofim, A.F., "Application of High Resolution Electron Microscopy for the Characterization and Source Assignment of Diesel Particulates," *Appl Occup Environ. Hyg* **11(7)**, pp 777-781, 1996.

77 Palotas, A. B., Rainey, L.C., Sarofim, A.F, Vander Sande, J.B., and Ciambelli, P., "Effect of Oxidation on the Microstructure of Carbon Blacks, *Energy and Fuels,* **10**, pp 254-259, 1996.

78 Palotas, A.B., Rainey, L.C., Feldermann, C.J., Sarofim, A.F., and Vander Sande, J.B., "Soot Morphology: An Application o Image Analysis in High-Resolution Transmission Electron Microscopy," *Microscopy Research and Technique,* **33**, pp 266-278, 1996.

79 Busek, Peter R., Huang, Bo-Jun, Keller, Lindsay P., "Electron Microscope Investigation of the Structures of Annealed Carbons," *Energy & Fuels*, 1, 1981.

80 Lahaye, J., Prado, G., Donnet, J.B., "Nucleation and Growth of Carbon Black Particle During Thermal Decomposition of Benzene," Carbon, **12**, pp 27, 1974

81 Kang, S.G., Helble, J.J., Sarofim, A.F., and Beér, *J.M., Twenty-Second Symposium (International) on Combustion*, The Combustion Institute, Pittsburgh, 1988, pp. 231-238.

82 Helble, J.J., and Sarofim, A.F., "Influence of char fragmentation on ash particle size distributions," *Combustion and Flame* ,**76**, pp. 183-196, 1989.

83 Davis, H., and Hottel, H.C., "Combustion Rate of Carbon, Combustion at a Surface Overlaid with a Stagnant Gas," *Ind. Eng. Chem.* **26**, pp 889-895, 1934.

84 Walker, P.L., Jr., Rusino, F., and Austin, L.G., "Gas Reactions of Carbon," *Advances in Catalysis and related subjects,*(Eley, D.D., Selwood, P.W., an d Weisz, P.B, eds.), Academeic Press, Vol 11, pp. 133-221, 1957.

85 Dutta, S., Wen, C.Y., and Belt, R.J., *Ind. Eng. Chem. Proc. Des. Dev.* 16: 20, 1977.

86 Kerstein, A.R., and Niksa, S., "Fragmentation During Carbon Conversion: Predictions and Measurements," *Twentieth Symposium (International) on Combustion*, The Combustion Institute, Pittsburgh, pp. 941-949, 1984.

87 Weiss, Y. and Bar-Ziv, E., "Observation of Nonuniform Shrinkage and Activation of Highly Porous Chars during Combustion in an Improved Electrodynamic Chamber," *Combustion and Flame* 95:362-373,1993.

88 Zhang, X., Dukhan, A., Kantorovich, I.I., and Bar-Ziv, E., "Bulk Fragmentation of Highly Porous Char Particles in Regime I," *Combustion and Flame* (in Press)..

89 Salatino, P., and Massimilla, L., "Modeling fragmentation by percolation in combustion of carbons," *Powder Technology* 66: 47-52, 1991.

90Miccio, F., and Salatino, P., *Twenty-Fourth Symposium (International) on Combustion*, The Combustion Institute, Pittsburgh, pp. 1145-1151, 1992.

91 Salatino, P., Miccio, F., and Massimilla, L., "Modeling fragmentation by percolation in combustion of carbons," *Combustion and Flame,* **95**, pp. 342-350,1993.

92 Kantorovich, I.I., and Bar-Ziv, E., "Microstructural Evolution of Char under Oxidation Induced by Uneven Heating," Combustion and Flame (In press).

93 Kantorovich, I.I., and Bar-Ziv, E., "Processes in Highly Porous Chars under Kinetically Controlled Conditions: I. Evolutions of the Porous Structure." *Combustion and Flame,* **97**, pp. 61-78, 1994.

94 Hurt, R.H., Ph.D. Chemical and physical phenomena determining carbon gasification reactivity, Thesis, Department of Chemical Engineering, Massachusetts Institute of Technology, Cambridge, MA, 1987.

95 Bar-Ziv, E. and Sarofim, A. F., "The electrodynamic chamber: A tool for studying high temperature kinetics involving liquid and solid particles," *Progress in Energy and Combustion Science,* **17**, pp. 1-65,1991.

96 Weiss, Y. and Bar-Ziv, E., "Observation of Nonuniform Shrinkage and Activation of Highly Porous Chars during Combustion in an Improved Electrodynamic Chamber,"*Combustion and Flame* 101: 452-460,1995.

97 Weiss, Y., Benari, Y., Kantorovich, I.I., Bar-Ziv, E., Krammer, G., Modestino, A., and Sarofim, A.F., "Evolution of Porosity and Thermal Conductivity during Char Oxidation," *Twenty-Fifth Symposium (International) on Combustion,* The Combustion Institute, Pittsburgh, pp. 519-525, 1994.

98 D'Amore, M., Donsi, G., Giordano, P., and Raso, G., "Single Particle Operations by LDAA-Assisted Electrodynamic Thermogravimetry," Seventh Int. Symp. on Application of Laser Techniques to Fluid Mechanics, Lisbon, Portugal, July, 1994.

99 Palotas, A. B., Rainey, L. C. Feldermann, C. J., Sarofim, A. F., and Vander Sande, J. B., "Soot Morphology: An Application of Image Analysis in High-Resolution Transmission Electron Microscopy", *Microscopy Research and Techniques*, **33:3**, pp. 266, 1996.

100 Hurt, R. H., Dudek, D.R., Longwell, J.P, Sarofim, A.F., "The Phenomenon of Gasification-induced Carbon Densification and its Influence on Pore Structure Evolution," *Carbon*, **26**, pp. 433-449, 1988.

101 Weiss, Y. and Bar-Iv, E., "Further Development of the Electrodynamic Chamber for Studying Single-Particle Oxidation and Nonuniform Shrinkage of Char Particles," *Combustion and Flame,* **95**, pp 362-373, 1993.

102 Weiss, Y., Benari, Y., Kantorovich, I.I., Bar-Iv, E., Krammer, G., Modestino, A., Sarofim, A.F, "Evolution of Porosity and Thermal Conductivity during Char Oxidation" 1993.

103 Waters, B.J., Squires, R.G., Laurendreau, N.M., Mitchell, R.E., "Evidence for formation of CO2 in the vicinity of Burning Pulverized Carbon Particles," *Combust. Flame.*, **74**, 1988, pp 91-106.

104 Hurt, R. H., , Sarofim, A.F., and Longwell, J.P, "Gasification-Induced Densification of Carbons: From Soot to Form Coke" *Comb. Flame*, **95**, pp 430, 1993.

105 Ishigiro, T., Suzuki, N., Fujitani, Y. and Morimoto, H., "Microstructural Changes of Diesel Soot During Oxidation," *Combustion and Flame*, **85**, pp 1-6, 1991.

106 Easler, T.E., Bradt, R.C., and Walker, P.L., "Gasification induced densification of form coke" *Fuel*, **69**, pp 124, 1990.

107 Levendis, Y.A., Flagan, R.C., Gavalas, G.R. "Oxidation Kinetics of Monodisperse Spherical Carbonaceous Particles of Variable Properties," *Combustion and Flame,* **76** pp 221-241, 1989.

108 Herein, D., Find., J., Herzog, B., Kollman, H., Schmidt, R., Schogl, R., Barl, H., and Troyer, Ch. "On the relation between structure and reactivity in the carbon oxygen reaction," *Issues in Gasification of Carbon,* NATO, pp 148-153, 1990.

109 Acharya, T.R., and Olander, D.R. "The Rate of Oxidation of the Basal and Prismatic Surfaces of Pyrolytic Graphite in the Transition Regime Between Chemical and Diffusional Control," *Carbon*, **11**, pp 7-18, 1972.

110 Davis, K.A., Hurt, R.H., Yang, N.Y.C., and Headley, T.H., "Evolution of Char Chemistry, Crytallinity, and Ultrafine Structure during Pulverized Coal Combustion," Submitted Report to Sandia National Labs, 1996.

111 Lee, Chun Hyuk, "Modeling of Single Char Combustion, Including CO Oxidation in its Boundary Layer," Ph.D. Thesis, Dept. of Chemical Engineering, Massachusetts Institute of Technology, 1994.

112 Dudek, David R., "Single Particle, High Temperature, Gas-Solid Reactions in an Electrodynamic Balance," Ph.D. Thesis, Dept. of Chemical Engineering, Massachusetts Institute of Technology, 1988.

113 Floes, Joachim K., "The effect of Calcium on the Gasification Reactions of Cabon," Ph.D. Thesis, Dept. of Chemical Engineering, Massachusetts Institute of Technology, 1985.

114 Millward and Thomson, *Chemistry and Phsycis of Carbon*, Vol 3, pp 167-294. P.L. Walker, Jr, and P. Thrower, Eds. Marcel Dekker, New York, NY (1967).

115 Crawford, D., and Marsh, H., "High Resolution Electron microscopy of disorder carbons," *Fuel*, **55**, pp 251-253, 1976.

116Johnson, D.J., and Crawford, D., "Defocusing Phase contrast effects in electron microscopy," *Journal of Microscopy,* Vol. **98**, pp. 313-324, 1973.

117 Palotás, Á. B., Rainey, L.C., Felderman, C.J., Sarofim, A.F., and Vander Sande, J.B., "Soot Morphology: An Application of Image Analysis in High-Resolution Transmission Electron Microscopy," *Microscopy Research and Technique*, **33**, pp. 266-278, 1996.

118 Dudek, D.R., "Single Particle, High Temperature, Gas-Solid Reactions in an Electrodynamic Balance," PhD Thesis, Chemical Enginering, Massachusetts Institute of Technology, 1988.

119 Weiss, Y., Benari, Y., Kantorovich, I., Bar-ziv, E., Krammer, G., Modestino, A., and Sarofim, A.F., "Evolution of Porosity and Thermal Conductivity during Char Oxidation," 1993.

120 Mitchell, personal communications. June 5, 1996

121 Anderson, S., Radovic, L., and Hatcher, P., "Effects of Surface Chemistry on the Porous Structure of Coal," University Coal Research Project Meeting, Pittsburgh, Pa, 1996.

122 Marsh, H. and Crawford, D., "Structure in Graphitizable Carbon from Coal-Tar Pitch HTT 750-1148K. Studied Using High Resolution Electron Microscopy," *Carbon* **4/5**, pp 413-422, 1984.rd.

123 Levendis,Y.A., Flagan, R.C., Gavalas, G.R., "Oxidation kinetics of carbanaceious Spheres," Combustion and Flame, **76**, pp 221-241, 1989.

124 Marsh, P.A., Voet, A., Mullens, T.J., and Price, L.D., "Quantitative Micrography of Carbon Black Microstucture," *Carbon*, **9**, pp. 797-805, 1971.

125 Kawamurea, K., Lachter, J., and Bragg, R.H., Lawrence Berkley Laboratory Technical Report, No LBL,-17982..

126 Aladekomo, J.B., and Bragg, R.H., "Structural transformations induced in graphite by grinding: Analsyis of 002 X-ray diffraction line profiles, *Carbon*, **28**, pp. 897, 1990.

127 Ciambelli, Personal communications, 1996.

128 Palotás, Á. B., Quantitative Measures of Carbon microstructure, Masters of Chemical Engineering Thesis, Massachusetts Institute of Technology, 1995.

129 Randolph, A.D., and Larson, M.A., Theory of Particulate processes: Analysis and Techniques of Continuous crystallization," Academic Press Inc, San Diego, 1988

130 Hulburt & Katz, *Chem. Eng. Science*, **19**, pp. 555., 1964(1961).

131 Suuberg, E.M., "Thermally Induced Changes in Reactivity of Carbons," Fundamental Issues in Control fo Carbon Gasification Reactivity, Kluwer Academic Publishers, Netherlands, pp 269-305, 1991.

132 Schlogl, R., Loose, G., and Wesemann, M., "On the mechanism of the oxidation of graphite by molecular oxygen," *Solid State Ionics*, **43**, pp 183-192, 1990.

133 Yang, R.T., and Wong, C., "Kinetics and Mechanism of oxiationof basal plane on graphite," *J. Chem. Phys.*, **75**, pp 4471-4476, 1981.

134 Olander, E.R., Siekhaus, W., Jones, R., and Schwarz, J.A., "Reactions of Modulated Molecular Beams with Pyrolytic Graphite, I. Oxidation of the Basal Plane," *The Journal of Chemical Physics*, **57** #1, pp 408, 1972.

135 Sahu, R., Levendis. Y., Flagan, R.C., and Gavalas, G.R., "Physical properties and oxiation rates of chars from three bituminous coals," *Fuel*, **67**, pp. 275-283, 1988.

136 Ballas, G., and Zygourakis, K., Évolution of Pore Surface Area during Noncatalytic Gas-Solid Reactions. 2. Experimental Results and model validation," *Ind. Eng. Chem. Res.*, **26**, pp 1787-1796, 1987.

137 Levendis, Y.A., Nam, S.W., Lowenberg, M., Flagan, R.C., and Gavalas, G.R., "Catalysis of the Combustion of Synthetic Char Particles by Various Forms of Calcium Additives," *Energy & Fuels*, **3**, pp. 28-37, 1989.

138 Wong, B.A., Gavalas, G.R., and Flagan, R.C., "Effect of Char Formation Temperature on the Densification of a Bituminous Coal Char during Gasification," *Energy & Fuels*, **9**, pp. 493-499, 1995.

139 Millward, G.R., and Jefferson, D.A., "Lattice Resolution of Carbons by Electron Microscopy," in *Chemistry and Physics of Carbon,* Vol. 14, Marcel Dekker, Inc., New York, 1978.

140 Oberlin, A., "High-resolution TEM studies of Carbonization and Graphitization, " *Chemistry of Carbon,* Vol 22, Marcel Dekker, Inc., New York, 1989.

141 Flegler, Stanley L. Scanning and transmission electron microscopy : an introduction, New York, W.H. Freeman, 1993.

142 Taylor, C.A., Lipson, H. Optical transforms, Cornell University Press, Ithaca, NY, 1965.

143 Ban, L.L. in Surface and defect properties of solids, (Roberts, M.W., Thomas, J.M. Eds), The Chemical Society London, Vol 1, p.54-94., 1972.

144 Cowley, J.M., Moodie, A.F., "The scattering of electrons by atoms and crystals. I. A new theoretical approach," *Acta Crystallogr.*, **10**, pp 609, 1957.

145 Jefferson, D.A., Millward, G.R., and Thomas, J.M., "The role of multiple scattering in the study of lattice images of graphitic carbon," *Acta Crystallogr.*, **A32**, pp 832, 1976.

146 Heidenreich, R.D., Hess, N.M., and Ban, L.L., *J. Appl. Crystallography,* **1:1**, 1968.

147 Lahaye, J., and Prado, G., "Mechanisms of Carbon Black Formation," Chemistry and Physics of Carbon, vol. 14 (P.L. Walker, Jr., ed.) Marcel Decker Inc., N.Y., pp 167-294, 1978.

148 Davis, K.A.; Hurt, R.H.; Yang, N.Y.C.; Headley T.H.: Evolution of char chemistry, cristallinity, and ultrafine structure during pulverized-coal combustion. 25th International Symposium on Combustion, Irvine, CA, 1994